Indian Institute of Metals Series

Amber Shrivastava · Amit Arora ·
Chandan Srivastava · Nikhil Dhawan ·
Sudhanshu Shekhar Singh *Editors*

# New Horizons in Metallurgy, Materials and Manufacturing

IIM
Metallurgy
Materials Engineering

Springer

# Indian Institute of Metals Series

**About the Book Series:**

The study of metallurgy and materials science is vital for developing advanced materials for diverse applications. In the last decade, the progress in this field has been rapid and extensive, giving us a new array of materials, with a wide range of applications, and a variety of possibilities for design of new materials, processing and characterizing the materials. In order to make this growing volume of knowledge available, an initiative to publish a series of books in Metallurgy and Materials Science was taken during the Diamond Jubilee year of the Indian Institute of Metals (IIM) in the year 2006, and has been published in partnership with Springer since 2016.

This book series publishes different categories of publications: textbooks to satisfy the requirements of students and beginners in the field, monographs on select topics by experts in the field, professional books to cater to the needs of practising engineers, and proceedings of select international conferences organized by IIM after mandatory peer review. The series publishes across all areas of materials sciences and metallurgy. An panel of eminent international and national experts serves as the advisory body in overseeing the selection of topics, important areas to be covered, and the selection of contributing authors.

Amber Shrivastava · Amit Arora ·
Chandan Srivastava · Nikhil Dhawan ·
Sudhanshu Shekhar Singh
Editors

# New Horizons in Metallurgy, Materials and Manufacturing

IIM
Metallurgy
Materials Engineering

Springer

*Editors*
Amber Shrivastava
Department of Mechanical Engineering
Indian Institute of Technology Bombay
Mumbai, Maharashtra, India

Chandan Srivastava
Department of Materials Engineering
Indian Institute of Science
Bengaluru, Karnataka, India

Sudhanshu Shekhar Singh
Department of Materials Science
and Engineering
Indian Institute of Technology Kanpur
Kanpur, Uttar Pradesh, India

Amit Arora
Department of Materials Engineering
Indian Institute of Technology Gandhinagar
Gandhinagar, Gujarat, India

Nikhil Dhawan
Department of Metallurgical and Materials
Engineering
Indian Institute of Technology Roorkee
Roorkee, Uttarakhand, India

ISSN 2509-6400 ISSN 2509-6419 (electronic)
Indian Institute of Metals Series
ISBN 978-981-19-5569-3 ISBN 978-981-19-5570-9 (eBook)
https://doi.org/10.1007/978-981-19-5570-9

© The Editor(s) (if applicable) and The Author(s), under exclusive license to Springer Nature
Singapore Pte Ltd. 2023
This work is subject to copyright. All rights are solely and exclusively licensed by the Publisher, whether the whole or part of the material is concerned, specifically the rights of translation, reprinting, reuse of illustrations, recitation, broadcasting, reproduction on microfilms or in any other physical way, and transmission or information storage and retrieval, electronic adaptation, computer software, or by similar or dissimilar methodology now known or hereafter developed.
The use of general descriptive names, registered names, trademarks, service marks, etc. in this publication does not imply, even in the absence of a specific statement, that such names are exempt from the relevant protective laws and regulations and therefore free for general use.
The publisher, the authors, and the editors are safe to assume that the advice and information in this book are believed to be true and accurate at the date of publication. Neither the publisher nor the authors or the editors give a warranty, expressed or implied, with respect to the material contained herein or for any errors or omissions that may have been made. The publisher remains neutral with regard to jurisdictional claims in published maps and institutional affiliations.

This Springer imprint is published by the registered company Springer Nature Singapore Pte Ltd.
The registered company address is: 152 Beach Road, #21-01/04 Gateway East, Singapore 189721, Singapore

# Series Editor's Preface

The *Indian Institute of Metals Series* is an institutional partnership series focusing on metallurgy and materials science and engineering.

## About the Indian Institute of Metals

The Indian Institute of Metals (IIM) is a premier professional body (since 1947) representing an eminent and dynamic group of metallurgists and materials scientists and engineers from R&D institutions, academia and industry, mostly from India. It is a registered professional institute with the primary objective of promoting and advancing the study and practice of the science and technology of metals, alloys and novel materials. The institute is actively engaged in promoting academia-research and institute-industry interactions.

## Genesis and History of the Series

The study of metallurgy and materials science and engineering is vital for developing advanced materials for diverse applications. In the last decade, the progress in this field has been rapid and extensive, giving us a new array of materials, with a wide range of applications and a variety of possibilities for processing and characterizing the materials. In order to make this growing volume of knowledge available, an initiative to publish a series of books in metallurgy and materials science and engineering was taken during the Diamond Jubilee year of the Indian Institute of Metals (IIM) in the year 2006. IIM entered into a partnership with Universities Press, Hyderabad, and as part of the IIM book series, 11 books were published, and a number of these have been co-published by CRC Press, USA. The books were authored by eminent professionals in academia, industry and R&D with an outstanding background in their respective domains, thus generating unique resources of validated expertise of interest in metallurgy. The international character of the authors and editors has enabled the books to command national and global readership. This book series includes different categories of publications: textbooks to satisfy the requirements of undergraduates and beginners in the field, monographs on select topics by experts in the field and proceedings of select international conferences organized by IIM, after mandatory peer review. An eminent panel of international and national experts constitutes the advisory body in overseeing the selection of topics, important areas to be covered, in the books and the selection of contributing authors.

## Current Series Information

To increase the readership and to ensure wide dissemination among global readers, this new chapter of the series has been initiated with Springer in the year 2016. The goal is to continue publishing high-value content on metallurgy and materials science and engineering, focusing on current trends and applications. So far, four important books on state of the art in metallurgy and materials science and engineering have been published, and during this year, three more books are released during IIM-ATM 2021. Readers who are interested in writing books for the series may contact the Series Editor-in-Chief Dr. U. Kamachi Mudali, Former President of IIM and Vice Chancellor of VIT Bhopal University at ukmudali1@gmail.com, vc@vitbhopal.ac.in or the Springer Editorial Director Ms. Swati Meherishi at swati.meherishi@springer.com.

## About *New Horizons in Metallurgy, Materials and Manufacturing*

The book *New Horizons in Metallurgy, Materials and Manufacturing* presents an overview of the evolution and opportunities associated with promising upcoming fields in materials, metallurgy and manufacturing. There are a lot of interesting fields at this tri-junction, such as alloy design, bio-materials, composites, high entropy alloys, sensors, electronic materials, recycling and materials degradation. The progress in these fields is further fueled by the advances in the analysis and fabrication techniques such as correlative microscopy, additive manufacturing and surface engineering. The book discusses the above topics/fields covering advanced analysis techniques, fabrication methods and various technological applications. Each chapter provides the basics of the respective field and comprehensively discusses the current developments and future avenues, to arrive at a point where the reader acquires an overall view of the field. Special emphasis is given on the scientific fundamentals and application potential, in a way that readers of all backgrounds can get benefited.

The editors Dr. Amber Shrivastava, Indian Institute of Technology, Bombay; Dr. Chandan Srivastava, Indian Institute of Science, Bangalore; Dr. Sudhanshu Shekhar Singh, Indian Institute of Technology, Kanpur; Dr. Amit Arora, Indian Institute of Technology, Gandhinagar; and Dr. Nikhil Dhawan, Indian Institute of Technology, Roorkee, have made excellent efforts to coordinate with specialists in the respective field to provide ten articles of high relevance. These chapters in the most advanced areas of materials engineering have been prepared by the well-experienced authors meticulously for a reader to pursue research in those areas. This book will be a treasure for those who are interested in learning everything about advanced materials and manufacturing technologies and pursuing a career and study in the area of advanced materials and manufacturing. The IIM-Spring Series gratefully acknowledge the editors and authors for the excellent chapters covering a wide range of information on the subject matter of interest to the readers.

Dr. U. Kamachi Mudali
Editor-in-Chief
Series in Metallurgy and Materials
Engineering
Vice Chancellor
VIT Bhopal University
Bhopal, India

# Foreword

Materials and manufacturing is a discipline as old as human civilization; yet, the subject keeps reinventing itself year to year such that one longs to—and needs to—explore new horizons and the opportunities and challenges that lie ahead. Metallurgy is an evolving subject which has got developed by mergers and differentiation of various sub-disciplines. The impact that metallurgical industries have made on the economies of countries, including India, has been significant.

Like a biologist, metallurgists and materials scientists need to deal with several levels of organization of knowledge among which microstructure is central to the subject. The understanding and application of the relationships between processing (or synthesis), composition, microstructure, properties and performance distinguish metallurgy from other branches of science and engineering. As Robert Cahn wrote, "materials science has emerged by the process of integration rather than by splitting of larger disciplines but, in practice, doubles up as a multi-discipline."

The role of other disciplines in shaping metallurgy cannot be overemphasized. For example, metal extraction, thermodynamics, transport phenomena and corrosion are intertwined with chemical engineering and chemistry. Manufacturing engineering grew out of the synergy between mechanical and metallurgical engineering. The field of functional materials and devices stands on the foundation of physics, electronics and instrumentation. Computer science provides the tool to practically implement Integrated Computation Materials Engineering. Likewise, statistics and data science are the essential ingredients of the materials genome initiative which promises to reduce materials development cycle from around 20 years to as low as five years. In future, materials engineers may need to be even more inclusive in the development of smart and novel materials and related devices if these are to be produced at economically competitive prices.

Another way to look at materials, as Prof. P. Rama Rao once said, is to deal with "materials as a system," where skills and knowledge across hierarchies are integrated to meet system objectives. The materials engineer may, therefore, assume the roles of design, integration of knowledge and testing, to deliver products to the specified properties.

Finally, the practicing metallurgist needs to develop the skill of looking at industrial problems beyond the traditional boundaries of knowledge and specializations; otherwise, metallurgy will remain only as an academic subject.

I am happy to see that young academics of our country decided to come together and prepare a volume on the subject of metallurgy, materials and manufacturing. For these are the leaders of tomorrow, and their perspectives on the subject matter with regard to the future of the materials discipline.

Amol A. Gokhale
Former President
Indian Institute of Metals
Professor
Indian Institute of Technology Bombay
Mumbai, India

# The Indian Institute of Metals: Technical Books—Editorial Advisory Board (2020–2022)

# Contents

Advanced Characterization and Calphad in Design and Development of Advanced High Strength Steels . . . . . . . . . . . . . . . . . . 1
R. Veerababu, R. Balamuralikrishnan, and S. Karthikeyan

Correlative Electron Microscopy and Atom Probe Tomography—Experimental Techniques and Its Applications . . . . . . . . . 17
Surendra Kumar Makineni

Additive Manufacturing: Bringing a Paradigm Shift . . . . . . . . . . . . . . . . . . 35
C. P. Paul and A. N. Jinoop

Multiscale Modeling in Arc Welding Using Secondary Thermal Cycle . . . . . . . . . . . . . . . . . . . . . . . . . . . . . . . . . . . . . . . . . . . . . . . . . . . . . 51
Deepu Mathew John and Gandham Phanikumar

Material Recycling: Unearthing Metals from Anthropogenic and Industrial Resources . . . . . . . . . . . . . . . . . . . . . . . . . . . . . . . . . . . . . . . . 69
Pratima Meshram and Abhilash

Process Development and Stability Modeling of High-Speed Micromachining . . . . . . . . . . . . . . . . . . . . . . . . . . . . . . . . . . . . . . . . . . . . . 91
Rinku Kumar Mittal, Kundan Kumar Singh, and Ramesh Kumar Singh

Materials Degradation: Metallic Materials . . . . . . . . . . . . . . . . . . . . . . . . . . . 107
Amulya Bihari Pattnaik and Smrutiranjan Parida

Frontiers in Multi-functional Biomaterials for Hip Joint Application . . . . . . . . . . . . . . . . . . . . . . . . . . . . . . . . . . . . . . . . . . . . . . . . . . 123
Chinmayee Nayak and Kantesh Balani

Bacterial Cellulose for Drug Delivery: Current Status and Opportunities . . . . . . . . . . . . . . . . . . . . . . . . . . . . . . . . . . . . . . . . . . . . . . 137
Shivakalyani Adepu, Sailaja Bodrothu, and Mudrika Khandelwal

**An Odyssey from High Entropy Alloys to Complex Concentrated Alloys** . . . . . . 159
Jitesh Kumar, Saumya R. Jha, N. P. Gurao, and Krishanu Biswas

# About the Editors

**Professor Amber Shrivastava** is assistant professor in mechanical engineering department at IIT Bombay, since 2016. Previously, Prof. Shrivastava worked at Corporate Technology Centre of A O Smith at Milwaukee, USA. Dr. Shrivastava received his Ph.D. in mechanical engineering from the University of Wisconsin-Madison. He received M.S. in mechanical engineering from Idaho State University. He graduated with Bachelor's in Marine Engineering from Marine Engineering and Research Institute, Kolkata. Thereafter, he worked as a licenced marine engineer for 4 years. His current research interest lies in the area of joining processes in manufacturing, friction stir technologies, joining of dissimilar materials, additive manufacturing, manufacturing process automation, and sustainable manufacturing. As principal investigator, Dr. Shrivastava has received and led sponsored projects from government agencies like DST, ISRO, etc. as well as industries.

**Professor Amit Arora** is an Associate Professor of Materials Engineering at the Indian Institute of Technology Gandhinagar (IITGN), India. He leads the Advanced Materials Processing Research Group at IITGN. Prof. Arora received his Ph.D. in Materials Science and Engineering from The Pennsylvania State University, University Park, USA, in 2011. He worked on heat transfer and material flow modeling of friction stir welding process and developed several numerical models for simulation of this solid-state welding method. Before joining the doctoral program, he was working with IBM India Pvt Ltd as Associate System Engineer. Prof. Arora received B.Tech. (Hons.) in Metallurgical and Materials Engineering and M.Tech. in Metallurgical Engineering (Dual Degree) in 2005 from Indian Institute of Technology (IIT) Kharagpur. The broad research area of Prof. Arora includes various advanced material processing and simulation, such as friction stir welding and processing, additive manufacturing, laser material interaction, surface modification. Prof. Arora has worked on several sponsored projects from SERB, BRNS, DST, DTE-Gujarat, and MHRD. He has also been awarded Excellence-in-Research Award from IIT Gandhinagar and Dept. of Atomic Energy Young Scientist Research Award from the Board for Research in Nuclear Sciences. Prof. Arora was also awarded Indian Patent for fabrication process of polymer reinforced metal matrix composites.

Dr. Amit Arora completed his B. Tech. and M. Tech. (Dual Degree) in Metallurgical and Materials Engineering from IIT Kharagpur in 2005. He received Ph.D. in Materials Science and Engineering from The Pennsylvania State University in August 2011. He has worked on heat transfer and material flow modeling of friction stir welding for his Ph.D. thesis. His main research focus is physical understanding of the joining processes, heat transfer and material flow modeling, and advanced material processing. Currently, Dr. Arora is working as Assistant Professor of Materials Science and Engineering at IIT Gandhinagar and leading Advanced Materials Processing Research Group.

**Chandan Srivastava** received Ph.D. (2009) in Materials Science from the University of Alabama, Tuscaloosa, Alabama, USA. He is currently working as a Professor in the Department of Materials Engineering at the Indian Institute of Science, Bangalore, India. Prof. Chandan Srivastava's research focuses on microstructure-property correlations in metallic systems. Three representative research topics of his work are: (a) understanding the evolution of morphology, microstructure, texture, and corrosion behavior of electrodeposited metallic coatings as a function of the deposition variables, additive volume fraction, and alloying additions, (b) understanding the atomistic mechanism of degradation of compositionally complex multi-component alloys in severely corrosive environments, and (c) size-dependent phase stability and microstructures in nano-solids.

**Professor Nikhil Dhawan** is working as Associate Professor at the Department of Metallurgical and Materials Engineering, Indian Institute of Technology, IIT-Roorkee, INDIA. He received Outstanding Young Faculty award from the Indian Institute of Technology, Roorkee. He was awarded Mineral Engineering International (MEI) global Young Person award for his work in recycling electronic waste to recover metals. Nikhil Dhawan obtained a Bachelor of Engineering (Metallurgical Engineering) with First Class Honors from Punjab Engineering College, Chandigarh, in 2008. His Ph.D. in Metallurgical Engineering (Modeling of crushed ore agglomeration for heap leach operations, AMIRA P-986 project) was conferred by the University of Utah, the USA, in 2013. He has his credit to seven sponsored research projects funded by various government organizations and has authored 90 referred international journal articles and 25 international conference papers) and 2 book chapters with an h-index of 20. His research work is focused on the extraction of bases and rare earth values from red mud, fly ash, electronic waste (discarded CFLs, hard disks), lithium and cobalt from lithium-ion batteries, copper and gold values (printed circuit boards), potassium values from silicate rocks, and enrichment/hydrogen reduction of low-grade banded iron ores for steel vision 2030. He has been elected as a Member of the Indian National Young Academy of Sciences (INYAS). He has received the AC Datta MESA Award (Institution of Engineers, 2016) and Khare award (2016) from the Indian Institute of Mineral Engineers (IIME) in the research domain. Received the IOM3 Billiton Gold Medal for the best paper published in Transactions C: Mineral Processing & Extractive Metallurgy. He was a Member of the Technology Information, Forecasting, and Assessment Council study steering committee on “Technology solutions for maximum value recovery from Electronic Wastes" approved by NITI Aayog, Government of India (2018–2020); Bureau of Indian Standards for aluminum and other nonferrous metals division.

**Dr. Sudhanshu Shekhar Singh** is an associate professor in the Department of Materials Science and Engineering at Indian Institute of Technology (IIT) Kanpur. Dr. Singh received his Ph.D. in Materials Science and Engineering from Arizona State University, USA in 2015. Prior to joining IIT Kanpur in Dec 2015, he was a postdoctoral researcher at Arizona State University. Dr. Singh received his B. Tech degree in Metallurgical and Materials Engineering from Indian Institute of Technology (IIT) Kharagpur in 2008. After his undergraduate studies, Dr. Singh joined Tata Steel (Jamshedpur) and worked there for three years. The broad area of his research includes mechanical behaviour of materials at different length scales, 3D/4D materials science, and laser-assisted processing of materials. Dr. Singh has been awarded sponsored projects from various agencies (such as DST, SERB, ISRO). He has co-authored over 80 papers in international peer-reviewed journals. Dr. Singh is a recipient of several awards, including P. K. Kelkar Young Fellowship (IITK), INYAS Member, NASI Young Scientist platinum jubilee award, Young Metallurgist of the Year by the Ministry of Steel, and IEI Young Engineer award.

# Advanced Characterization and Calphad in Design and Development of Advanced High Strength Steels

**R. Veerababu, R. Balamuralikrishnan, and S. Karthikeyan**

## 1 Introduction

### *1.1 Microstructure at Different Length Scales*

Understanding the microstructure at different length scales plays an important role in the design and development of new alloys or improving the performance of existing alloys. The microstructure can be characterized at different levels viz., optical, scanning and transmission electron microscopies and 3D atom probe. Figure 1 shows the microstructures of high strength naval steels (HSNS) using different microscopy techniques. At optical level (Fig. 1a), the microstructure shows the presence of banding of microstructure, grain size, types of phases, e.g., ferrite and pearlite. Finer details of the phases, relatively coarse precipitates along with their chemical compositions, can be obtained in scanning electron microscopy (SEM) (Fig. 1b). At electron back scattered diffraction (EBSD) level (Fig. 1c), microstructural features like different phases, grain size and its distribution, orientation of different grains, etc. can be characterized. Very fine microstructure details like dislocations, inter-and intra-lath particles of more than 5 nm size along with their chemistry and crystal structure can be obtained from transmission electron microscopy (TEM) (Fig. 1d and e). All the above microscopy techniques provide microstructural information in the lateral direction. 3D atom probe (3DAP), with its single atom resolution, provides the microstructural information in the depth direction [1]. It helps in obtaining elemental distribution in different phases, various attributes of clusters and their evolution with processing and chemistry (Fig. 1f).

---

R. Veerababu (✉) · R. Balamuralikrishnan
Defense Metallurgical Research Laboratory (DMRL), Kanchanbagh, Hyderabad, India
e-mail: veera.dmrl@gov.in

R. Veerababu · S. Karthikeyan
Department of Materials Engineering, Indian Institute of Science, Bangalore, India
e-mail: karthik@materials.iisc.ernet.in

A. Shrivastava et al. (eds.), *New Horizons in Metallurgy, Materials and Manufacturing*,
Indian Institute of Metals Series, https://doi.org/10.1007/978-981-19-5570-9_1

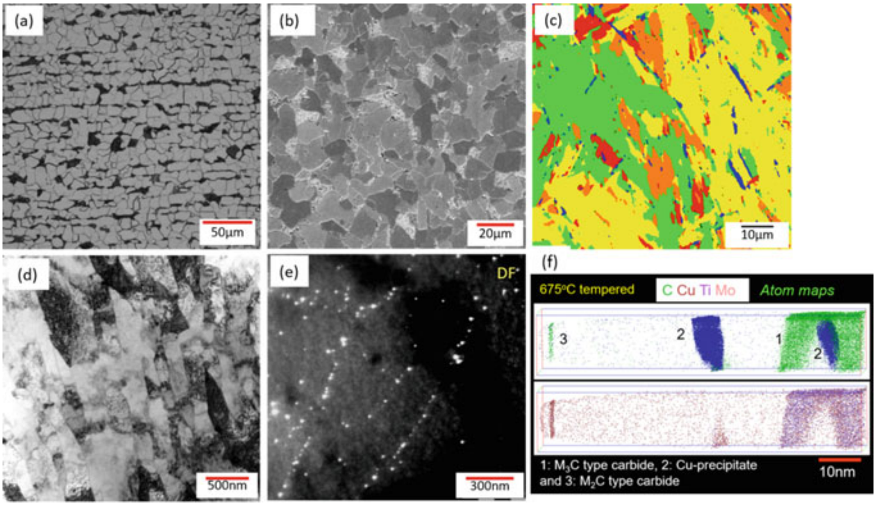

**Fig. 1** Microstructure of high strength naval steels (HSNS) at different length scales; **a** optical, **b** SEM, **c** EBSD, **d** and **e** TEM and **f** 3D atom probe

If one understands the microstructure of a given material at these different levels as a function of composition and processing windows and its correlation to the obtained mechanical properties of the material, one would be able to design a new composition or processing windows or modify the existing composition to achieve improved mechanical properties. This approach for alloy design has been employed in design and development of secondary hardening ultra-high strength (SHUHS) steels through balancing of strength and fracture toughness. This book chapter describes our efforts in minimizing the number of experiments in improving the strength of existing DMRL UHS steel without compromising the toughness. Initially, a brief background (Sect. 2) on the development of typical SHUHS steels and the current understanding of the microstructure of these steels has been presented followed by recent developments in understanding the microstructure using 3D atom probe with reference to DMRL UHS steel (Sect. 3.1). Since the objective of the work is to minimize the number of experiments through thermodynamic calculations, ThermoCalc has been used extensively to understand the phase stability and its correlation to the achieved mechanical properties in typical SHUHS steels and DMRL steel. ThermoCalc findings and understanding of the microstructure in typical SHUHS steels and the DMRL steel have been used to select few alloys for experimental validation using thermodynamic calculations on DMRL steel by varying Cr and Mo contents and are presented in Sects. 3.2, 3.3, 3.4, 3.5, 3.6, and 3.7. Finally, before presenting the conclusions of the present work in Sect. 5, the opportunities and challenges associated with the use of semi-empirical approach in alloy design have been presented in Sect. 4.

**Table 1** Nominal composition and mechanical properties of standard SHUHS steels

| Steel | C | Co | Ni | Cr | Mo | Fe | Mechanical properties | | |
|---|---|---|---|---|---|---|---|---|---|
| | | | | | | | YS, MPa | UTS, MPa | $K_{IC}$, MPa $\sqrt{m}$ |
| HY180 | 0.10 | 8.0 | 10.0 | 2.00 | 1.00 | Bal | 1250 | 1380 | 233 |
| AF1410 | 0.16 | 14.0 | 10.0 | 2.00 | 1.00 | Bal | 1533 | 1675 | 158 |
| Aermet100 | 0.24 | 13.4 | 11.5 | 3.00 | 1.20 | Bal | 1724 | 1965 | 126 |
| Aermet310 | 0.25 | 15.0 | 11.0 | 2.40 | 1.40 | Bal | 1896 | 2172 | 71 |
| Aermet340 | 0.33 | 15.6 | 12.0 | 2.25 | 1.85 | Bal | 2068 | 2379 | 37 |

# 2 Background

## 2.1 *Secondary Hardening Ultra-High Strength (SHUHS) Steels*

SHUHS steels possess excellent combination of high strength, fracture toughness and stress corrosion cracking resistance, which make them candidate materials for niche applications such as aircraft landing gear and armor [2]. Table 1 shows the composition and mechanical properties of the standard SHUHs steels in typical heat treatment conditions [3]. Chronologically, the standard SHUHS steels have been developed in the order: HY180, AF1410, AerMet100, AerMet310 and AerMet340. It can be seen that, except for Cr, amounts of all other alloying elements have been increased progressively from HY180 to AerMet340 steels. Cr has been increased to 3wpct in AerMet100, decreased to ~2wpct and maintained in the vicinity of 2wpct in the later grades of steels. Mo and C have shown a continuous increase from HY180 to AerMet340 steel. Co was increased significantly from HY180 to AF1410 and maintained at that level in the later grades, while Ni was increased steadily from HY180 to AerMet340. With increase in the amount of total alloying elements from HY180 to AerMet340, strength properties have also been increased with concomitant decrease in fracture toughness.

## 2.2 *Tempering Response of SHUHS Steels*

The microstructure of these steels in the as-quenched condition consists essentially of lath martensite along with small amounts of undissolved primary carbides such as MC, $M_6C$ and $M_{23}C_6$ [4, 5]. The typical tempering behavior of these steels (Fig. 2) reveals that [4, 6–11] during low temperature tempering (200–300 °C), the strength of the steel drops slightly with an increase in tempering temperature, it increases to reach a peak in the range 450–600 °C and tempering beyond this temperature results in a decrease in strength/hardness. In contrast, toughness increases marginally in the 200–300 °C tempering range, decreases to a minimum in the vicinity of 425 °C and increases significantly when tempered beyond 425 °C. The toughness minimum at 425 °C has been attributed to the formation of coarse cementite (Fig. 3a). Tempering beyond 425 °C, typically in the range 450–600 °C, results in the dissolution of this coarse cementite and provides carbon for the formation of fine dislocation nucleated $M_2C$ alloy carbides, which is associated with the peak hardness/strength of these steels. At even higher tempering temperatures, needle-shaped $M_2C$ precipitates begin to coarsen resulting in a slight loss of strength but accompanied by a disproportionate increase in toughness (Fig. 3b). For this reason, all secondary hardening steels are put into service in this slightly overaged condition.

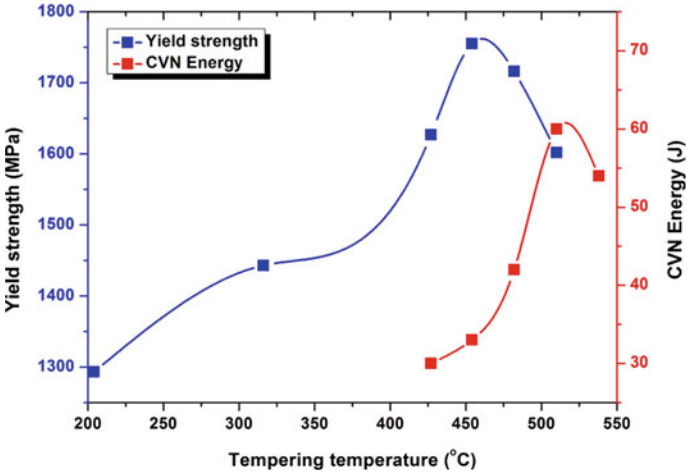

**Fig. 2** Tempering response of AerMet100 steel [4]

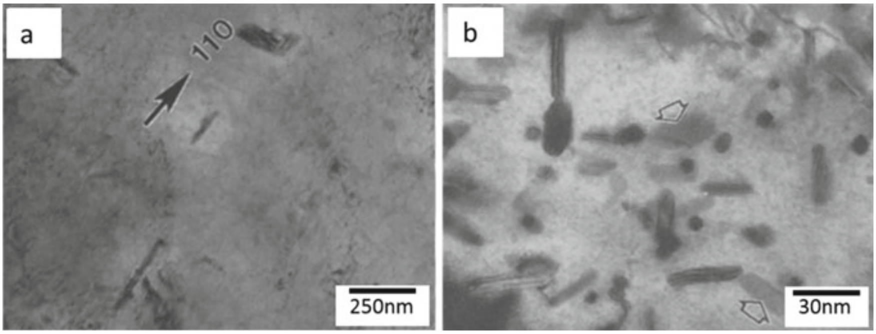

**Fig. 3** TEM micrographs of Aermet 100 steel at **a** 427 °C and **b** 566 °C tempering treatments [4]

# 3 Recent Developments and Current Status

## *3.1 DMRL UHS Steel*

Steel similar to typical SHUHS steels, designated as DMRL UHS steel, is being developed at DMRL with a nominal composition (in wt. %) of 0.37C, 14.8Co, 13.7Ni, 2Cr, 1Mo and Fe (bal.). Typical mechanical properties in different heat treatment conditions are shown in Table 2. This table shows that at similar strength levels, the samples tempered for 8 h at a given tempering temperature of either at 485 °C or 495 °C show nearly 50% improvement on fracture toughness. Microstructural characterization at SEM (Figs. 4a and b) and TEM (Figs. 4d and e) scales shows no apparent differences, and differences in cluster size and number density have been observed in 3D atom probe (Figs. 4c and f). The sample tempered for 8 h shows significantly higher fraction of clusters compared to 4 h sample. It has been reported that clusters have the potential to significantly improve both strength and toughness simultaneously [12, 13]. In addition to this, significant fractions of clusters were found to be deficient in carbon along with clusters close to $M_2C$ stoichiometry [14]. To understand the influence of composition on the amount of $M_2C$ and the presence of carbon-deficient clusters, composition of $M_2C$ has been examined—to form $M_2C$, two metal atoms (Cr, Mo and V) and one carbon atom are required. DMRL SHUHS steel contains (in at. %) 2.16Cr, 0.58Mo, 0.22 V and 1.73C. The total amount of carbide forming elements (Cr + Mo + V) is 2.96at. %. If we assume that the entire amount of carbide forming elements are consumed in forming $M_2C$ carbides, it would have only used up1.48at. % C, resulting in the availability of excess 0.25at. % C. Moreover, in spite of the availability of this excess carbon, carbon-free clusters consisting of Cr, Mo and Fe have been observed in DMRL SHUHS steels [14]. This loss of M to such clusters results in a lesser fraction of $M_2C$ than is possible if all available carbide forming M elements were used to form $M_2C$. In contrast, in standard SHUHS steels as summarized in Table 1, there is excess amount of carbide forming elements and hence increased strength. Therefore, it is hypothesized that by increasing the amount of carbide forming elements (Cr and Mo), one may be able to utilize all the excess carbon and maximize the amount of $M_2C$ and perhaps increase strength further. This understanding has been utilized as the basis for modification of the composition of DMRL UHS steel. The question then arises as to how much the amount of Cr and Mo can be increased over and above the levels of DMRL UHS steel. It is well known that experimental design of alloys following empirical trial and error approaches, particularly of the multi-component steels containing 6–10 alloying elements, is rather expensive, time consuming and involves enormous efforts before realizing a promising composition with desired set of mechanical properties. Therefore, a semi-empirical approach involving both computations using ThermoCalc [15] and experiments has been adopted in this work.

**Table 2** Mechanical properties of the DMRL SHUHS at different tempering temperatures

| Heat treatment condition (Temp., °C/time) | Yield strength, MPa | UTS, MPa | Elongation, % | $K_{IC}$, MPa$\sqrt{m}$ |
|---|---|---|---|---|
| 485/4 h | 1855 | 2105 | 12.6 | 45.0 |
| 485/8 h | 1825 | 2040 | 13.4 | 66.0 |
| 495/4 h | 1825 | 2050 | 14.0 | 60.5 |
| 495/8 h | 1775 | 2030 | 15.0 | 87.0 |

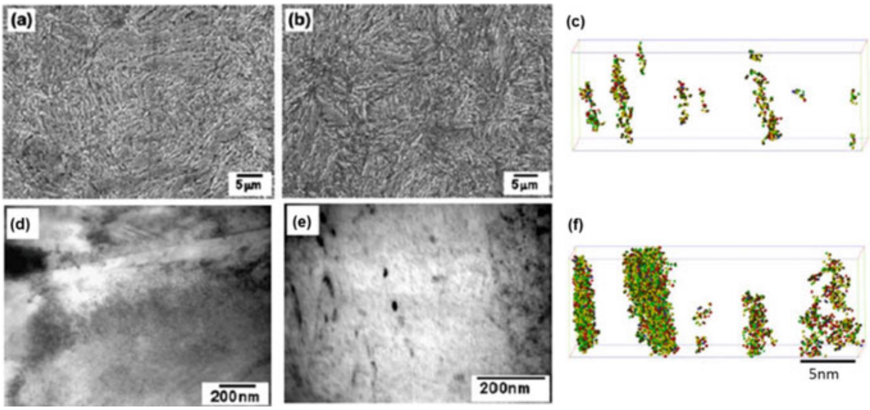

**Fig. 4** Microstructure of DMRL UHS steel tempered at 485 °C for—4 h **a** SEM, **d** TEM and **c** atom map of clusters and—8 h **b** SEM, **e** TEM and **f** atom map of clusters

## 3.2 Validation of ThermoCalc for Design of SHUHS Steels

Initially, ThermoCalc has been used to predict the equilibrium phase fractions and their compositions as a function of temperature in typical SHUHS steels for which experimental data is available. These calculations suggest that ThermoCalc can be used to investigate phase equilibria in standard SHUHS steels, especially if corrections are made by suppressing the stable carbide phases that are typically not observed experimentally for kinetic and other reasons. A typical phase fraction calculation depicting the comparison of $M_2C$ phase fraction in standard SHUHS steels as a function of temperature in the tempering regime is shown in Fig. 5. The predicted maximum amount of $M_2C$ increases (in mole %) from ~1.4 in HY180 to 2.3 in AF1410 and further to 3.4 in AerMet100. The temperature at which complete dissolution of a given precipitate occurs is called the maximum dissolution temperature, $T_d$, and this temperature also follows the same trend, i.e., increasing from 740 °C in HY180 to 770 °C in AF1410 to 825 °C in AerMet100. The higher mole fraction and $T_d$ for $M_2C$ in AF1410 steel may be attributed to higher carbon content in AF1410 relative to HY180 (Table 1). The amount of $M_2C$ in AerMet100 steel is significantly higher than the other two due to higher amounts of all carbide forming

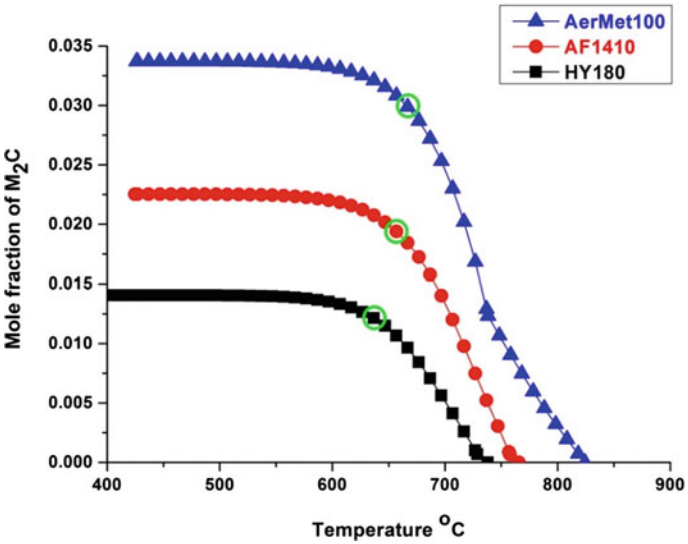

**Fig. 5** $M_2C$ phase fraction in standard SHUHS steels as a function of temperature in the tempering regime

elements (Table 1). It can be seen from Fig. 5 and Table 1 that the predicted $M_2C$ phase fractions of the steels correlate well with the observed mechanical properties: AerMet100 with highest $M_2C$ carbide fraction exhibits the highest strength. This suggests that if one were to design a new alloy with enhanced strength, one could do so by increasing the amount of $M_2C$ carbides, which in turn could be achieved by modifying the composition.

### *3.3 Calculations Based on DMRL UHS Steel*

Based on the understanding of the ThermoCalc predictions in standard SHUHS steel, similar calculations have been extended to DMRL UHS steel through variations of Cr and Mo and keeping the other alloying elements same as those in DMRL steel except Fe. Contour plots of $M_2C$ phase fraction and Cr/Mo ratio in $M_2C$ carbide at a typical tempering temperature of 450 °C are shown in Fig. 6. The reason for mapping the Cr/Mo ratio of $M_2C$ carbide is that this ratio influences the coarsening resistance of the carbide during tempering and it is desirable to keep this ratio at minimum to obtain maximum coarsening resistance for the $M_2C$ carbide and hence higher strengthening [16, 17]. DMRL composition is indicated with dark spot in both these maps. The most desirable region in the phase fraction map (Fig. 6a) is red color region with maximum $M_2C$ phase fraction and the desirable region in Cr/Mo ratio map (Fig. 6b) is gray color region.

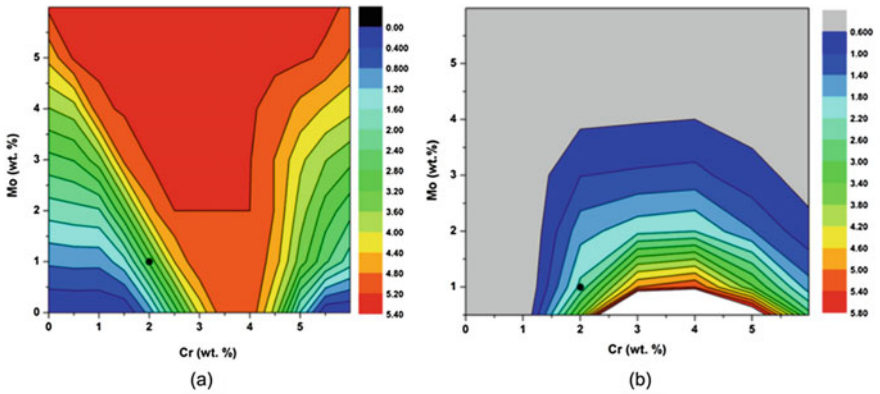

**Fig. 6** Contour maps with variation of Cr and Mo in DMRL UHS steels at 450 °C; **a** $M_2C$ phase fraction and **b** Cr/Mo ratio of $M_2C$ carbide

## 3.4 *Design Criteria*

Initially, the $M_2C$ fraction and Cr/Mo ratio have been considered to select the alloys. The design criteria has been arbitrarily chosen such the model alloys shall have at least 50% higher $M_2C$ phase fraction ($\geq$4.32%) than the DMRL steel with 2.88 mol.% and Cr/Mo ratio of the $M_2C$ carbide shall be at least 50% lower ($\leq$1.16) than that of the DMRL steel with 2.31. Based on these two criteria, a combined contour map of $M_2C$ fraction and Cr/Mo ratio at 450 °C tempering temperature has been plotted as shown in Fig. 7. The *maroon* color line and the horizontally hatched region in *maroon* indicate the range of compositions where the $M_2C$ fraction is equal to lesser than the desired target ($\geq$4.32%). Similarly, the *green* color line and the vertically hatched region in *green* represent the range of compositions where the Cr/Mo ratio of the carbide is equal to or higher than the target ($\leq$1.16). The *white* unhatched region is the most desirable region which indicates the compositions where the $M_2C$ fraction is at least 50% higher and the Cr/Mo ratio in $M_2C$ is at least 50% lower than that in DMRL UHS steel. Three model alloys, $C_{21}$, $C_{23}$ and $C_{55}$, indicated with black spots, have been selected for experimental validation. The first and second subscripts denote the nominal weight percent of the Cr and Mo, respectively. Other alloying elements such as C, Co and Ni are kept at the levels of DMRL UHS steel, i.e., C: 0.37, Co: 15 and Ni: 14.

## 3.5 *Experimental Results on Model Alloys*

The selected model alloys have been melted as 500gms pancakes, rolled to 3-mm-thick sheets and subjected to a series of austenitizing treatments between 1000 and 1150 °C to optimize the austenitizing temperature [18]. These results suggest that the

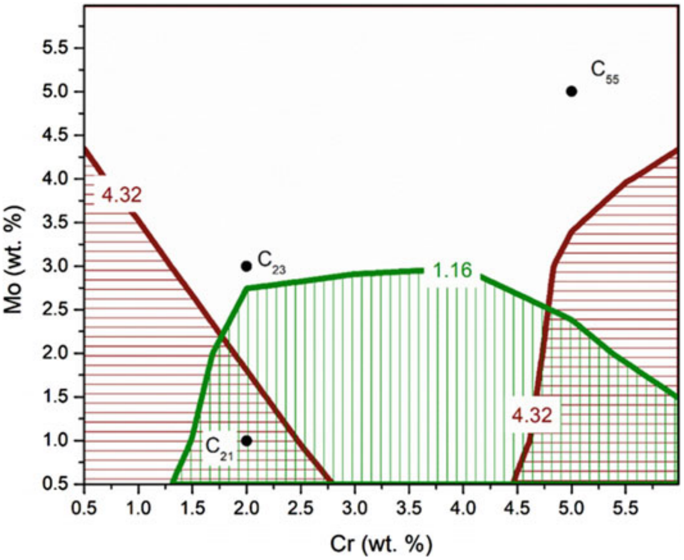

**Fig. 7** Combined contour map of both $M_2C$ fraction and Cr/Mo ratio in $M_2C$ carbide at 450 °C with variation of Cr and Mo concentrations. The three model alloy compositions are indicated with filled black circles

hardness is relatively insensitive to austenitizing temperature when the temperature is increased from 1000 to 1150 °C, whereas the hardness is decreased in $C_{23}$ steel and more drastically decreased in $C_{55}$ steel with increase in austenitizing temperature. Further, it has been found that the $C_{21}$ steel exhibited highest hardness followed by $C_{23}$ and $C_{55}$ in spite of higher Cr and Mo levels in the latter steels. Microstructural origin for the lower hardness in $C_{23}$ and $C_{55}$ steels at 1000 °C and 1150 °C at different length scales reveals the presence of higher fraction of retained austenite as shown in Fig. 8. Quantification of amount of retained austenite (RA) of samples subjected to oil quenching and $LN_2$ ($OQ + LN_2$) treatment following austenitizing using EBSD (Table 3) suggests that with increase in Cr and Mo contents and austenitizing temperature, austenite has become more stable and the fraction of RA in $C_{55}$ steel is more than 50%. Further, it has been observed that $C_{55}$ retained significant fraction of undissolved precipitates even after austenitizing at 1150 °C (Fig. 9). Based on these experimental results, $C_{55}$ was not studied further since it is not fulfilling the design criteria of having maximum amount of martensite for matrix strengthening and retaining higher faction of undissolved precipitates which minimizes the amounts of alloying elements participating in secondary hardening reaction to form strengthening precipitates and hence reducing the strength of the steel. Therefore, all the further studies were concentrated on $C_{23}$ and compared against the $C_{21}$ steel, being the base composition above which the composition is modified for improved performance.

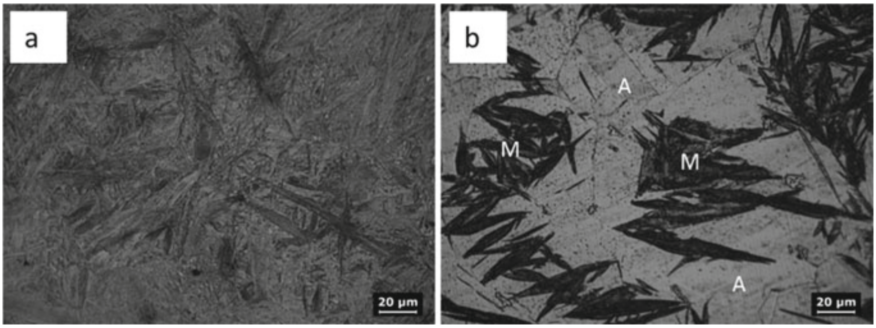

**Fig. 8** Optical micrographs of samples austenitized at 1150 °C; **a** $C_{23}$ and **b** $C_{55}$

**Table 3** Relative amounts of retained austenite in $C_{23}$ and $C_{55}$ subjected to austenitizing at 1000 °C and 1150 °C followed by OQ + $LN_2$ treatment

| Steel | Austenitizing temperature, °C | Area % of austenite |
|---|---|---|
| $C_{23}$ | 1000 | 2.08 |
| | 1150 | 8.69 |
| $C_{55}$ | 1000 | 40.70 |
| | 1150 | 56.30 |

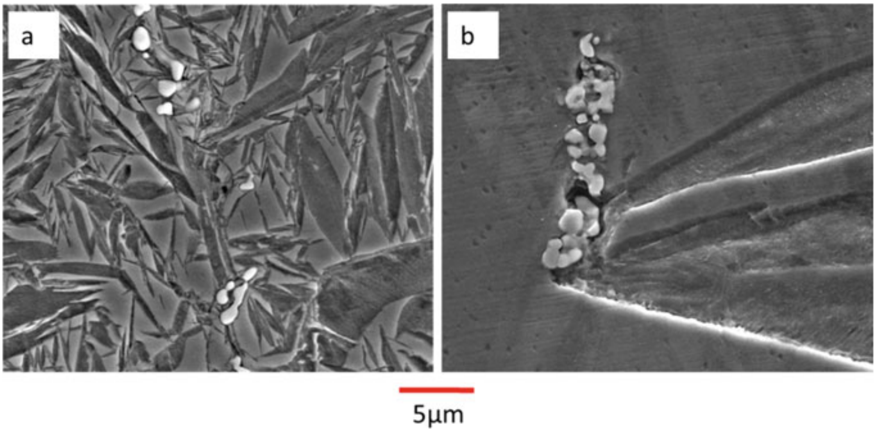

**Fig. 9** SEM micrographs of samples subjected to 1150 °C, followed by OQ + $LN_2$ treatment; **a** $C_{23}$ and **b** $C_{55}$ [18]

## 3.6 Comparison of $C_{21}$ and $C_{23}$ Alloys

Both $C_{21}$ and $C_{23}$ steels exhibit similar tempering response, which shows that the hardness increases slowly at lower tempering temperatures of nearly 300 °C, reaches a peak at 450 °C and then falls sharply when tempered at temperatures beyond 450 °C. However, the hardness of $C_{23}$ was found to be significantly higher than $C_{21}$ at all tempering temperatures, reaching a maximum difference of 90VHN at 450 °C. Detailed microstructural characterization of both $C_{21}$ and $C_{23}$ steels suggests similar microstructural features, as observed in typical SHUHS steels [4, 16, 19–24], showing the presence of alloy cementite at lower tempering temperatures of 400 °C (Fig. 10). This alloy cementite was found to be dissolved and replaced by fine $M_2C$ carbides when tempered at tempering temperatures of above 500 °C. However, at peak aged (450 °C) and slightly over aged (500 °C) conditions, it was rather difficult to establish the type of precipitates due to fine nature of the precipitates and high dislocation density of the martensitic matrix [4, 25, 26]. 3D atom probe, with single atom atomic resolution [1], has been used to identify the nature of these fine precipitates. In these aged conditions, extremely fine precipitates and numerous atomic clusters have been observed using atom probe as shown in atom map of 450 °C tempered sample (Fig. 11). Detailed quantitative analysis of these clusters in terms of cluster composition, size, number density and volume fraction has been carried out. When the composition of these clusters in terms of (Cr+Mo)/C ratio is plotted as a function of size in the form of a contour map, three individual peaks in number density have been observed for both $C_{21}$ and $C_{23}$ steels suggesting three different types of clusters (Fig. 12) [27].

Based on the observation of three peaks and the type of carbides typically formed in this class of steels, clusters have been classified into three types, namely *Type I* (carbon-rich clusters, (Cr+Mo)/C ratio $< 1.5$), *Type II* (clusters close to $M_2C$ stoichiometry, (Cr+Mo)/C ratio $= 1.5$–$3.25$) and *Type III* (metal-rich clusters, (Cr+Mo)/C ratio $> 3.25$). Evolution of cluster composition and volume fraction ($V_f$) of the clusters (Fig. 13) with aging temperature in $C_{21}$ steel suggest that *Type I* clusters dissolve initially to form *Type II* and *Type III* clusters at lower aging temperatures of 400 °C, and when the samples are tempered at relatively higher temperatures, *Type III* clusters also gets dissolved and are replaced by the *Type II* clusters. Cluster

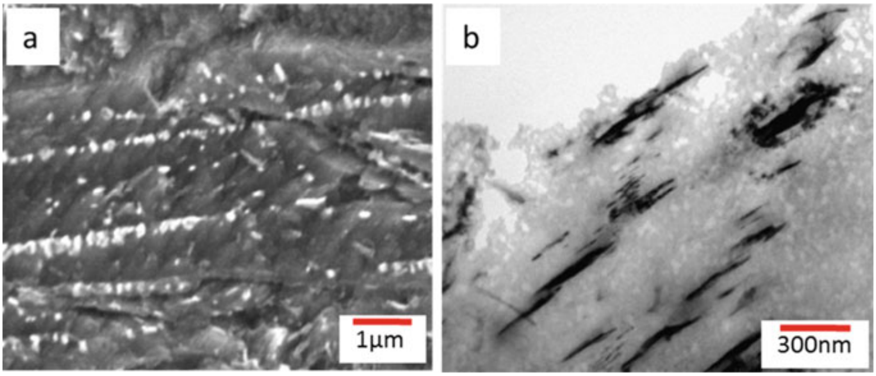

**Fig. 10** Micrographs of $C_{23}$ steel tempered at 400 °C; **a** SEM and **b** bright field TEM image

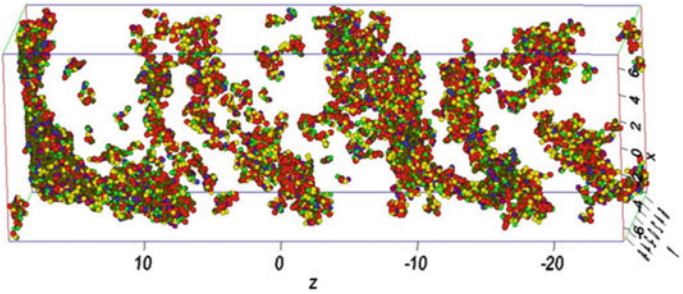

**Fig. 11** Atom map showing the presence of fine precipitates and clusters in $C_{23}$ tempered at 450 °C

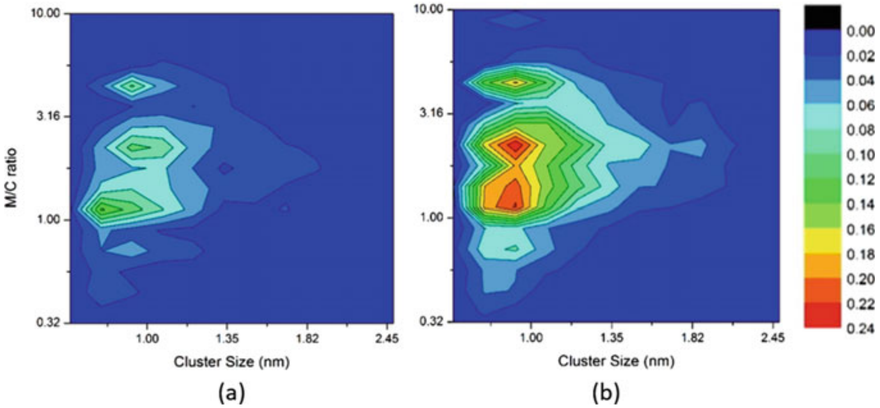

**Fig. 12** Contour maps in terms of number density, (Cr+Mo)/C ratio and size of clusters in 400 °C tempered samples; **a** $C_{21}$ and **b** $C_{23}$ [27]

composition evolution in $C_{23}$ was found to be slightly different. When the samples are aged at 400 °C or beyond, both *Type I* and *Type III* clusters get dissolved and replaced by *Type II* clusters. Further, $C_{23}$ was found to contain more numerous *Type II* clusters compared to $C_{21}$ which can be attributed to higher Mo content. In both steels, the size of *Type II* clusters has been increased with increase in aging temperature and M/C ratio of the clusters approaches close to 2 with increase in size of the clusters suggesting that these clusters are either fine $M_2C$ carbides or precursors to the formation of $M_2C$ carbides. Timokhina et al. [28] also reported similar results in Ti-Mo steel which suggests that the composition of Ti-Mo-Fe clusters approaches equilibrium composition of MC precipitates as the size of the clusters is increased.

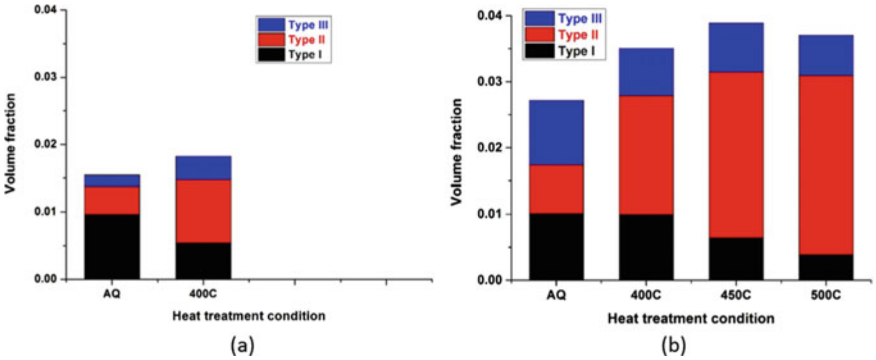

**Fig. 13** Volume fraction of various types of clusters under different heat treatment conditions; **a** $C_{21}$ and **b** $C_{23}$ [27]

**Table 4** Comparison of $M_2C$ fraction and Cr/Mo ratio from ThermoCalc and 3D atom probe

| Steel | Mole fraction of $M_2C$ | | Cr/Mo ratio | |
|---|---|---|---|---|
| | ThermoCalc | 3DAP | ThermoCalc | 3DAP |
| $C_{21}$ | 2.58 | 0.93 | 2.46 | 0.97 |
| $C_{23}$ | 5.09 | 1.80 | 0.98 | 0.60 |

### *3.7 Comparison of ThermoCalc and Experimental Results*

The observed hardness differences between $C_{21}$ and $C_{23}$ can be correlated to microstructural features, especially *Type II* clusters ($M_2C$ type) which in turn can be attributed to higher Mo content in $C_{23}$ relative to $C_{21}$. Summary of mole fraction and Cr/Mo ratio of $M_2C$ carbide predicted from ThermoCalc and the measured volume fraction and Cr/Mo ratio from 3DAP experiments is shown in Table 4. The predicted mole fraction of the $M_2C$ carbide from ThermoCalc in $C_{23}$ is almost double that of $C_{21}$. 3D atom probe results also suggest that the measured volume fraction of $M_2C$ type clusters is also double that of $C_{21}$. Similarly, the Cr/Mo ratio predicted by ThermoCalc and measured by 3D atom probe is close to half in $C_{23}$ compared to that in $C_{21}$. Although the absolute values of $M_2C$ phase fraction and the Cr/Mo ratio of the $M_2C$ carbide may not be the same in ThermoCalc predictions and 3D atom probe, the trends predicted by both theoretical calculations and experimental measurements are the same.

## 4 Opportunities and Challenges

The design approach adopted in this work involves understanding the existing the experimental data in the field of SHUHS steels and applying the computational tools such as ThermoCalc for alloy designing. Though the methodology was explained with reference to SHUHS steels, the general principles elucidated here, in general, are applicable to other steels as well as other alloy systems. This approach provides ample opportunities in alloy designing. One can theoretically verify several combinations of alloying elements with varying amounts and understand the influence of these alloying elements on phase stability, amounts of phases and their composition as a function of temperature without going for experimental validation of multiple alloys. The objective of the present work is not to replace the experiments completely. Instead, design multiple alloys theoretically and experimentally process very few alloys that appear to be more promising. This approach not only reduces the number of alloys for experimental validation but also can be used to predict the processing windows for the selected alloys, which would in turn further reduce the experimental efforts. Therefore, this approach significantly reduces the more expensive experiments, saves time and efforts in developing new alloys or improving the performance of existing alloys.

Though this approach significantly reduces the experimental efforts and reduces the alloy development time, it also poses several challenges. One should have a thorough knowledge of the alloy systems in terms of formation of different phases, approximate temperature ranges for their formation and so on. For example, in the current work, $M_6C$ and $M_{23}C_6$ are predicted as stable phases when both these phases were allowed to form in the calculations, and the strengthening precipitate in this class of steels, $M_2C$, has not been predicted. However, extensive literature suggests that $M_2C$ is the strengthening precipitate in this class of steels [4, 10, 16, 19, 20]. Since $M_6C$ and $M_{23}C_6$ are thermodynamically more stable carbides and hence were predicted in the calculations instead of meta-stable $M_2C$ carbide. However, experimentally, $M_6C$ and $M_{23}C_6$ normally do not form in the typical tempering regimes in these steels for kinetic reasons. Therefore, these carbides have been suppressed in the calculations. Unless one has a fair knowledge of formation of different phases in a given alloy system, there is every chance that the results can be misinterpreted. However, it is often difficult to obtain prior knowledge on all alloy systems of interest, especially in the absence of extensive experimental work. In such cases, caution must be exercised while interpreting the results predicted from the calculations.

## 5 Conclusions

This work has clearly demonstrated that understanding the microstructure at different length scales can play a major role in the design and development of a new set of alloys with improved performance or designing new alloys. A semi-empirical approach using ThermoCalc calculations has been employed to improve the performance of the secondary hardening ultra-high strength steels. ThermoCalc has been used to select two new alloys ($C_{23}$ and $C_{55}$) based on DMRL steel with higher $M_2C$ phase fraction and lower Cr/Mo ratio. Experimental validation of these two alloys suggests that $C_{55}$ steel contains significant fraction of undissolved precipitates and more than 50%

austenite even after 1150 °C austenitizing treatment. Tempering studies on $C_{21}$ and $C_{23}$ reveal that $C_{23}$ was stronger than $C_{21}$ by more than 10%. Microstructural studies tempered samples at optical, SEM and TEM level reveal the presence of typical lath martensite and fine precipitates in both $C_{21}$ and $C_{23}$ steels. Advanced characterization using 3DAP suggests that $C_{23}$ contained a significantly higher fraction of clusters close to $M_2C$ stoichiometry, with a lower Cr/Mo ratio than $C_{21}$. This is in accordance to the design objective for this alloy. Therefore, the design objective of increasing the strength of the existing DMRL SHUHS steel through alloy modifications for achieving higher $M_2C$ fraction was realized successfully. This work has confirmed that a judicious use of ThermoCalc with an emphasis on qualitative trends can be used for designing new alloy compositions in this class of SHUHS steels.

**Acknowledgements** This research was funded by the Defense Research and Development Organization (DRDO), India. Dr. G Madhusudhan Reddy, OS and Director, Defense Metallurgical Research Laboratory (DMRL), Hyderabad, to publish this work is gratefully acknowledged. The authors wish to thank Dr. M. Srinivas, retired scientist from DMRL and extensively worked on UHS steels for fruitful discussions. The authors are grateful to Professor T. A. Abinandanan, former Chairman, Dept. of Materials Engg., IISC, Bangalore, Dr. K. Muraleedharan, Director (retd.), CGCRI, Kolkata, Dr. G. Malakondaiah, former Director, DMRL and former Chief Controller (HR&D) at DRDO Headquarters, Dr. S. V. Kamat, DS and former Director, DMRL and DG (NS&M) for their constant encouragement and support.

## References

1. D.N. Seidman, Three-dimensional atom-probe tomography: advances and applications. Annu. Rev. Mater. Res. **37**, 127–158 (2007)
2. J.M. Dahl, P.M. Novotny, Airframe and landing gear alloy. Adv. Mater. Processes **155**(3), 23–25 (1999)
3. R. Veerababu, in *Microstructural Studies on High Cr-Mo Secondary Hardening Ultra-High Strength Steels* (Indian Institute of Science, 2015)
4. R. Ayer, P.M. Machmeier, Transmission electron microscopy examination of hardening and toughening phenomena in Aermet 100. Metall. Trans. A **24**(9), 1943–1955 (1993). https://doi.org/10.1007/BF02666329
5. M. Grujicic, Thermodynamics aided design of high Co-Ni secondary hardening steels. Calphad **14**(1), 49–59 (1990). https://doi.org/10.1016/0364-5916(90)90039-3
6. K.S. Cho, J.H. Choi, H.S. Kang, S.H. Kim, K.B. Lee, H.R. Yang, H. Kwon, Influence of rolling temperature on the microstructure and mechanical properties of secondary hardening high Co–Ni steel bearing 0.28wt% C. Mat. Sci. Eng.: A **527**(27–28), 7286–7293 (2010). https://doi.org/10.1016/j.msea.2010.07.069
7. L.E. Iorio, J.L. Maloney, W.M. Garrison Jr., 40th Mechanical Working and Steel Processing Conf. Proc., ISS-AIME, Warrendale, PA, 901–920 (1999)
8. P. Machmeier, T. Matuszewski, R. Jones, R. Ayer, Effect of chromium additions on the mechanical and physical properties and microstructure of Fe-Co-Ni-Cr-Mo-C ultra-high strength steel: Part I. J. Mater. Eng. Perform. **6**(3), 279–288 (1997). https://doi.org/10.1007/s11665-997-0091-3
9. J.S. Montgomery, G.B. Olson, Proc. G.R. Speich Symp., ISS, Warrendale, PA,177–214 (1992)
10. G.R. Speich, D.S. Dabkowski, L.F. Porter, Strength and toughness of Fe-10ni alloys containing C, Cr, Mo, and Co. Metall. Trans. **4**(1), 303–315. https://doi.org/10.1007/BF02649630

11. H.R. Yang, K.B. Lee, H. Kwon, Effects of Ni additions and austenitizing temperature on secondary hardening behavior in high Co-Ni steels. Metall. and Mater. Trans. A. **32**(9), 2393–2396 (2001). https://doi.org/10.1007/s11661-001-0213-8
12. E.V. Pereloma, A. Shekhter, M.K. Miller, S.P. Ringer, Ageing behaviour of an Fe–20Ni–1.8Mn–1.6Ti–0.59Al (wt%) maraging alloy: clustering, precipitation and hardening. Acta Mat. **52**(19), 5589–5602 (2004). https://doi.org/10.1016/j.actamat.2004.08.018
13. A. Shekhter, H.I. Aaronson, M.R. Miller, S.P. Ringer, E.V. Pereloma, Effect of aging and deformation on the microstructure and properties of Fe-Ni-Ti maraging steel. Metall. and Mater. Trans. A. **35**(3), 973–983 (2004). https://doi.org/10.1007/s11661-004-0024-9
14. R. Veerababu, R. Balamuralikrishnan, K. Muraleedharan, M. Srinivas, Three-Dimensional Atom Probe Investigation of Microstructural Evolution during Tempering of an Ultra-High-Strength High-Toughness Steel. Metall. and Mater. Trans. A. **39**(7), 1486–1495 (2008). https://doi.org/10.1007/s11661-007-9333-0
15. B. Sundman, B. Jansson, J.-O. Andersson, The Thermo-Calc databank system. Calphad **9**(2), 153–190 (1985). https://doi.org/10.1016/0364-5916(85)90021-5
16. R. Ayer, P.M. Machmeier, Microstructural basis for the effect of chromium on the strength and toughness of AF1410-based high performance steels. Metall. and Mater. Trans. A. **27**(9), 2510–2517 (1996). https://doi.org/10.1007/BF02652345
17. L.E. Iorio, in *The Effect of Increasing Carbon Level on Titanium Carbosulfides and Their Influence on Toughness in Ultra-high Strength Steels,* 5–10 (Carnegie Mellon, 2000)
18. R. Veerababu, K. Satya Prasad, S. Phani, K., Balamuralikrishnan, S. Karthikeyan, Austenite stability and M2C carbide decomposition in experimental secondary hardening ultra-high strength steels during high temperature austenitizing treatments. Mater. Charact. **144**, 191–204 (2018). https://doi.org/10.1016/j.matchar.2018.07.013
19. H. Kwon, J.H. Lee, K.B. Lee, C.M. Kim, H.R. Yang, Effect of alloying additions on secondary hardening behavior of Mo-containing steels. Metall. and Mater. Trans. A. **28**(3), 621–627 (1997). https://doi.org/10.1007/s11661-997-0047-0
20. H. Kwon, J.H. Lee, K.B. Lee, H. Kwon, C.M. Kim, H.R. Yang, Effects of Co and Ni on secondary hardening and fracture behavior of martensitic steels bearing W and Cr. Metall. and Mater. Trans. A. **29**(1), 397–401 (1998). https://doi.org/10.1007/s11661-998-0191-1
21. H.M. Lee, S.M. Allen, Coarsening resistance of M2C carbides in secondary hardening steels: Part III. Comparison of theory and experiment. Metall. Trans. A, **22**(12), 2877–2888 (1991). https://doi.org/10.1007/BF02650249
22. H.M. Lee, S.M. Allen, M. Grujicic, Coarsening resistance of M2C carbides in secondary hardening steels: Part I. Theoretical model for multicomponent coarsening kinetics. Metall. Trans. A, **22**(12), 2863–2868 (1991a). https://doi.org/10.1007/BF02650247
23. H.M. Lee, S.M. Allen, M. Grujicic, Coarsening resistance of M2C carbides in secondary hardening steels: Part II. Alloy design aided by a thermochemical database. Metall. Trans. A, **22**(12), 2869–2876 (1991b). https://doi.org/10.1007/BF02650248
24. K.B. Lee, H. Kwon, H. Kwon, H.R. Yang, Secondary hardening and impact fracture behavior in isothermally aged Mo, W, and Mo-W steels. Metall. and Mater. Trans. A. **32**(7), 1862–1866 (2001). https://doi.org/10.1007/s11661-001-0163-1
25. J. Akré, F. Danoix, H. Leitner, P. Auger, The morphology of secondary-hardening carbides in a martensitic steel at the peak hardness by 3DFIM. Ultramicroscopy **109**(5), 518–523 (2009). https://doi.org/10.1016/j.ultramic.2008.11.010
26. K. Stiller, L.-E. Svensson, P.R. Howell, W. Rong, H.-O. Andrén, G.L. Dunlop, High resolution microanalytical study of precipitation in a powder metallurgical high speed steel. Acta Metall. **32**(9), 1457–1467 (1984). https://doi.org/10.1016/0001-6160(84)90092-0
27. R. Veerababu, R. Balamuralikrishnan, S. Karthikeyan, Nanoscale clusters in secondary hardening ultra-high strength steels with 1 and 3 wt% Mo: An atom probe investigation. J. Mater. Res. **35**(14), 1763–1776 (2020). https://doi.org/10.1557/jmr.2020.145
28. I. Timokhina, M.K. Miller, J. Wang, H. Beladi, P. Cizek, P.D. Hodgson, On the Ti-Mo-Fe-C atomic clustering during interphase precipitation in the Ti-Mo steel studied by advanced microscopic techniques. Mater. Des. **111**, 222–229 (2016). https://doi.org/10.1016/j.matdes.2016.08.086

# Correlative Electron Microscopy and Atom Probe Tomography—Experimental Techniques and Its Applications

**Surendra Kumar Makineni**

## 1 Introduction

Correlative use of electron microscopy techniques and atom probe tomography (APT) has shown a great promise in understanding and reveal atomic-scale mechanisms related to material behavior. The former provides structural while the latter gives atomic-scale compositional information. Now, it is possible to get both the data from the same region or feature of interest using special sample preparation techniques. This enables an understanding of the complete nature of the nanoscale features that directly impact the macroscopic material behavior.

Electron microscopes (EMs), such as scanning electron microscopes (SEMs) and transmission electron microscopes (TEMs, both analytical and aberration-corrected), are excellent tools that provide scope to use different methods to obtain crystallographic and structural information from macro- to the atomic scale. The methods include electron backscattered and transmission Kikuchi diffraction (EBSD and TKD) for grain orientation mapping, conventional electron diffraction, and imaging to identify the phases and their structure, high angle annular dark field imaging (HAADF) of individual atomic columns (atomic structure) of phases, interfaces, defects and dislocations, planar faults, etc. In EMs, the local chemical information from a material region can be obtained using energy-dispersive-X-ray spectroscopy (EDS) and electron energy loss spectroscopy (EELS). In EDS, the sensitivity toward elemental detection depends on the atomic number (Z) and concentration of elements present in the material [1, 2]. More specifically, low Z-elements (whose K-shell peaks are spaced narrowly) and elements with low concentration (whose EDS signal has a low signal/background ratio) will have a poor measurement accuracy (>10%). Hence, the concentration measurement of low Z-elements is preferred to be carried

---

S. K. Makineni (✉)
Department of Materials Engineering, Indian Institute of Science Bangalore, Bangalore, India
e-mail: skmakineni@iisc.ac.in

A. Shrivastava et al. (eds.), *New Horizons in Metallurgy, Materials and Manufacturing*,
Indian Institute of Metals Series, https://doi.org/10.1007/978-981-19-5570-9_2

out using EELS in TEMs. However, this technique is not appropriate for quantifying high Z-elements due to the overlap of element-specific edges with a strong background [1].

In contrast, APT provides a three-dimensional (3D) compositional map and accurate quantification near the atomic scale [3–5]. It offers a combination of high mass resolution (10 parts per million) and high elemental sensitivity, irrespective of the Z (atomic number) of the element, for example, details of atomic arrangement in solid solutions [6, 7], chemical composition gradients across different phases [8, 9], interfacial segregations [10–12], and misorientation of crystals [13, 14]. APT provides a mass spectrum from a local region that consists of counts of ionic species (y-axis) appearing at their different mass-to-charge ratios (x-axis) measured by the time-of-flight of the ions [15]. More details related to the working principle of APT can be found elsewhere [16]. However, it has poor spatial resolution [17] due to the aberrations related to the specimen geometry [18, 19], local compositional inhomogeneity [16, 20], and distribution of electrostatic field near the specimen surface [21] that affects the evaporation sequence of atoms and hence disturbs the actual atomic positions after reconstruction.

Correlative APT and other EM techniques can bring together their specific strengths to obtain more robust data related to a material microstructure that can be conclusively connected to the material properties. In this chapter, some methodologies are presented with relevant examples. Figure 1 shows a flowchart diagram comprising the sequential use of several advanced EM techniques before field evaporation in APT. A brief description of sample preparation, EM techniques, and APT analysis will be presented with some recent examples in relevant sections.

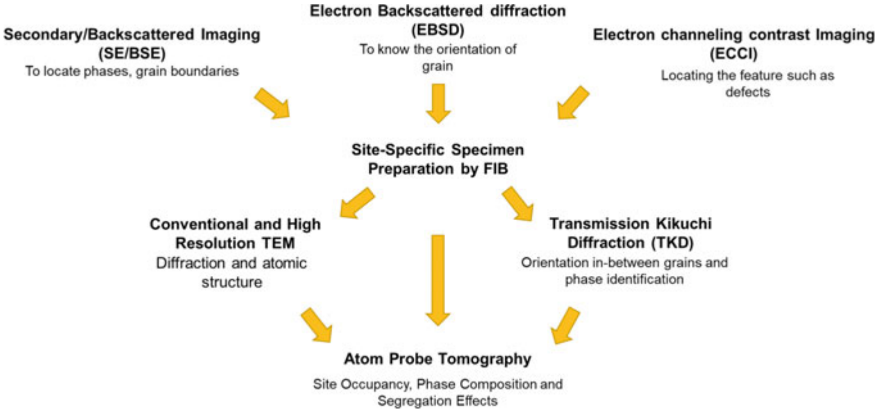

**Fig. 1** Flowchart showing sequential use of some advanced electron microscopy techniques before field evaporation in an atom probe

## 2 Sample Preparation

Atom probe specimens from the bulk metallic samples can be prepared by electrochemical polishing with alkaline or acidic solutions [22, 23] or dual-beam SEM/focused-ion-beam (FIB) systems. The former method involves extraction or preparation of a thin wire or a blank from the bulk sample and subsequently moved back and forth across a thin layer of solution until the wire end cross section reduces to a needle shape having an approximate end radius < 100 nm. This method makes site-specific target preparation from a microstructural feature of interest challenging and complex [24, 25]. Liquid ion source technology led to the development of FIB systems where a beam of ions is used to mill or remove the unwanted sample material from the surface via a sputtering process [26]. The milling can be performed with nanoscale precision by controlling the energy and intensity of the ion beam. Additionally, the ion beam can also assist chemical vapor deposition of a precursor gas on the sample surface. Most of the FIBs use Ga as the source of ions since it exists in the liquid state near room temperature (melting point—9.8 °C), and it can be focused to a fine probe size (<10 nm in diameter). The FIB system became more powerful when combined with an SEM, i.e., a dual beam SEM/FIB instrument that enables a more robust and convenient way of preparing site-specific targeted needle-shaped specimens [27]. Figure 2 shows schematic diagrams with three step-by-step protocols that can be followed for site-specific specimen preparation for APT analysis using dual-beam SEM/FIB instrument [28].

The first method, Fig. 2a, is a site-specific conventional lift-out protocol by using the standard Cameca flat-top Si coupons [27, 29]. Consider a region of interest (ROI) as a grain boundary (white line) located from the e-beam (electron beam in SEM) image acquisition. A thin layer of Pt is deposited (~200 to 500 nm) using an e-beam on the GB region for identification and protection against the Ga-ion damage during milling in later steps. The stage is tilted to 22°. The first cut was made near the GB region (~1000 nm away from ROI) using the Ga-ion milling. The sample was rotated (about Z-axis) to 180°, and a second cut was made as shown in the figure, such that a V-shaped cross-sectional lamella could be separated from the bulk sample. The cut lamella is adhered to the tip of a micro-manipulator by Pt-deposition, and a cut was made to another end of the lamella such that it is free to be lifted out from the surface. The end of the cut-lamella is kept on the apex (diameter ~2 μm) of a Si-post and adhered using Pt-deposition (red color area). Subsequently, the rest of the lamella is separated from the attached part by a cut using Ga-ion milling. Similarly, the rest of the lamella regions are adhered to other Si-posts, as shown in the figure. The stage is tilted to 52° such that the Ga-ion source is perpendicular to the plane of the lamella top surface and ion-milled by keeping the ROI at the center. Milling was performed step by step using a voltage of 30 kV and different current values ( 1.6 nA to 80 pA) until the adhered regions became a needle-shaped specimen with a tip radius of < 100 nm and the ROI approximately passing through the axis of the needle [30].

The second method, Fig. 2b, is a site-specific in-plane lift-out method that is a special technique for analyzing surface features [31]. First, the surface features

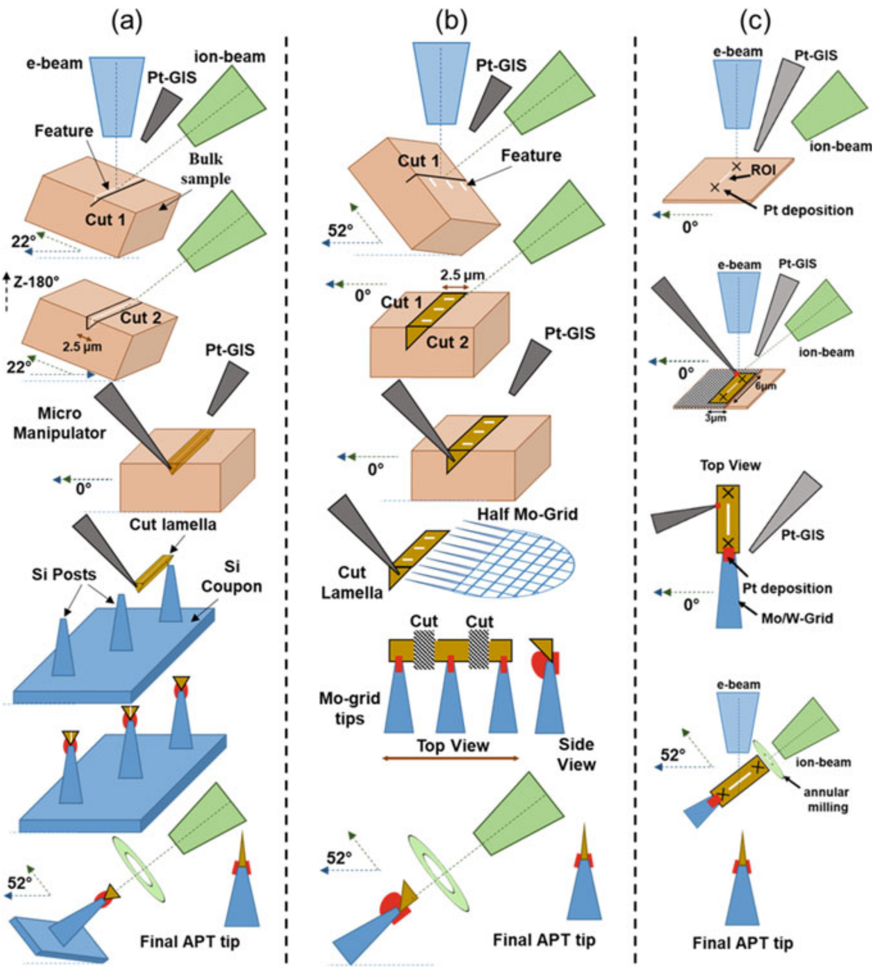

**Fig. 2** Schematic representation of step by step protocols for needle specimen preparation from bulk sample: **a** Conventional lift-out [27, 29], **b** in-plane lift out [31], **c** from TEM lamella [28, 32]. **b** and **c** were adapted from reference [28] (open access article under the terms of Creative Common CC BY license)

are marked by Pt-deposition by e-beam, and the stage is tilted to 52° such that the ion-beam is perpendicular to the sample surface. A first cut was made using Ga-ion milling near the ROI (~1000 nm away). The sample is titled to 0° and rotated 180° about Z-axis. A second cut was made at 0° (~1000 nm away from ROI), as shown in the figure, until the lamella region was separated from the bulk. The cut lamella is lifted out using a micro-manipulator, as described in the first method, and attached to the posts of an electropolished half-cut Mo/Cu grid that are held by special correlative holders [31, 33, 34]. Subsequently, the grid is placed perpendicular to the plane of the stage. The adhered regions were ion-milled to a needle shape by keeping the

ROI at the center until the feature was between 100 to 200 nm from the apex of the specimen [30].

The third method, Fig. 2c, is preparing APT needles from a TEM lamella [28, 32]. First, a site-specific TEM lamella was lifted out from the bulk sample containing a specific interest feature [35, 36]. The feature is identified using e-beam imaging and marked with Pt-deposition, as shown in the figure. A lamella region centered on the feature is cut out using an ion beam and attached to the micro-manipulator. The cut lamella region adhered to a Si-post or an electropolished tip of a half-cut Mo/Cu/W grid. Finally, the attached lamella region was ion-milled to get a needle-shaped specimen [29]. Before field evaporation in an atom probe, a final cleaning procedure at low voltage (2–5 kV) and using currents between 8 to 15 pA is necessary to remove the high energy Ga-ion beam damage and contamination from the needle specimen surface.

## *2.1 Applications*

In this section, several examples will be introduced, centered on the experimental techniques used as depicted in Fig. 1.

### 2.1.1 SE/BSE—FIB (Needle)—TEM—APT

This example demonstrates the correlative use of EM techniques and APT on an aluminum alloy (Al-3.1Ni-0.15Zr, at.%) [37]. Aluminum alloys are critical for automotive applications due to their lightweight and high specific strength. Here, the role of Zr in addition to a binary Al-3.1Ni (at.%) eutectic cast alloy was probed, leading to a remarkable yield strength increment at 250 °C and improved microstructural stability even after exposure to 400 °C. Figure 3a shows a SE image of the binary as-cast Al-3.1Ni-0.15Zr alloy with eutectic microstructure having $Al_3Ni$ (bright contrast) intermetallic rods embedded within the α-Al (gray) phase. Figure 3b shows a HAADS TEM image taken from the sample region after 10 h of annealing at 400 °C that demonstrates the Z-contrast between $Al_3Ni$ rods and α-Al matrix. Additionally, α-Al (see inset of Fig. 3b) contains coherent nano-metric $L1_2$ ordered $Al_3Zr$ precipitates.

A needle-shaped specimen was prepared according to the procedure described in Fig. 2a. A HAADF-STEM image of the needle specimen (Fig. 3d) and the corresponding APT reconstruction shows the distribution of Al atoms (yellow color) and iso-composition interfaces with a threshold value of 16 at.% Zr (red color) that depicts the presence of spherical $L1_2$ ordered $Al_3Zr$ precipitates in the α-Al matrix. In addition, an iso-composition interface with a threshold value of 19 at.% Ni (green color) also shows a Ni-rich region (green color) corresponding to part of an $Al_3Ni$ rod. The composition profiles (Fig. 3e) across the Ni-rich region and α-Al that shows the Ni-rich region are close to the stoichiometry of $Al_3Ni$ intermetallic. Figure 3f

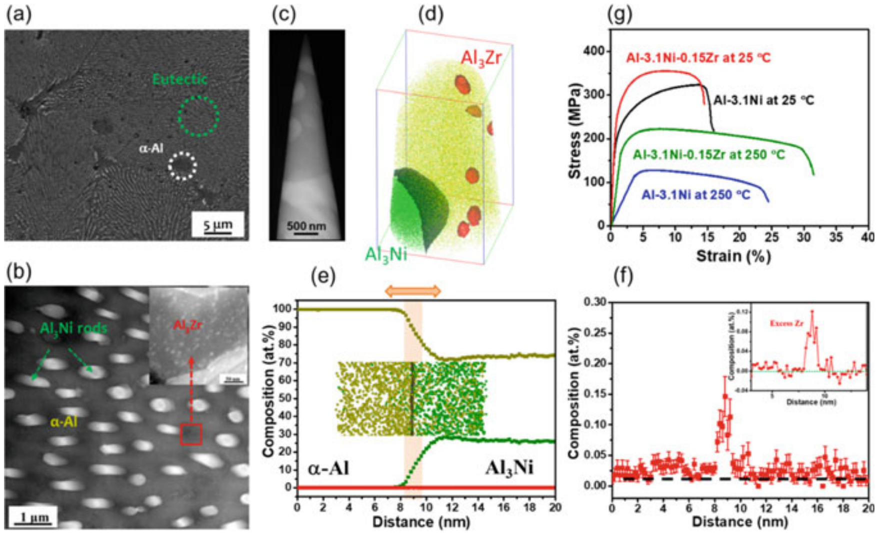

**Fig. 3** **a** Secondary electron (SE) image of as-cast Al-3.1Ni-0.15Zr alloy showing eutectic microstructure containing bright contrast $Al_3Ni$ rods embedded in the α-Al matrix. **b** HAADF-STEM image of the alloy after heat treatment (annealed at 400 °C for 10 h) showing $Al_3Ni$ rods in the α-Al matrix. The inset reveals the presence of $Al_3Zr$ precipitates distributed uniformly in the α-Al matrix. **c** HAADF-STEM image of a needle specimen from the heat-treated alloy showing bright $Al_3Ni$ rods in the gray α-Al matrix. **d** APT reconstruction shows several spherical Zr-rich (red color) precipitates and Ni-rich (green color) regions. **e** The composition profiles across the interface between α-Al and Ni-rich region reveal the $Al_3Ni$ phase with negligible solubility of Zr. **f** The composition profile of Zr (red color) across the α-Al/$Al_3Ni$ interface shows interfacial segregation of Zr. **g** Tensile stress vs. strain plots at temperatures of 25 °C and 250 °C for the as-cast Al-3.1Ni alloy and annealed Al-3.1Ni-0.15Zr alloy (after isothermal annealing at 400 °C for 10 h). The figures are adapted with permission from reference [37]

shows a magnified view of the Zr profile from the interface region that clearly reveals enrichment of Zr up to 0.16 at.% at the α-Al/$Al_3Ni$ interface relative to either α-Al or $Al_3Ni$ phase.

The interfacial segregation of a solute species $i$ can be quantified by Gibbsian interfacial excess at any interface for a solute species $i$ given as [11].

$$\Gamma_i = \frac{N_i^{\text{int}} - N_i^0}{A_{\text{int}}} \tag{1}$$

where $N_i^{\text{int}}$ and $N_i^0$ are the number of atoms $i$ at the interface and the number of atoms $i$ in the matrix per unit area, $A_{\text{int}}$. The Gibbsian interface excess for solute Zr was estimated in the range between +0.54 and +1.07 atoms/nm$^2$. Hence, this interfacial excess led to the reduction of $\gamma/\gamma'$ interfacial energy that provided the high-temperature stability of the eutectic microstructure.

Figure 3g also shows the tensile test curves of the Al-3.1Ni-0.15Zr and Al-3.1Ni alloys at room and 250 °C temperatures. The yield strength significantly drops for binary Al-3.1Ni alloy at 250 °C which is due to the higher coarsening rate of eutectic in Al-3.1Ni alloy at 250ºC compared to Al-31Ni-0.15Zr alloy. The Ni diffusivity in Al, at 250 °C, is calculated to be $\sim 1.15 \times 10^{-18} m^2/s$ [38] while the Zr diffusivity is much lower ~$4.92 \times 10^{-26} m^2/s$ and hence, at the α-Al/$Al_3Ni$ interface, Zr obstructs the diffusion of Ni atoms and resist the coarsening of $Al_3Ni$ rods. Additionally, Zr has very high binding energy of ~0.24 eV in aluminum alloys [39] that effectively acts as trapping sites for a large number of vacancies at the interface that will also contribute to retard the solute mass transport across the α-Al/$Al_3Ni$ rod interface.

### 2.1.2 SE/BSE—FIB (Needle)—TKD—APT

This example will showcase the application of TKD [40–42] to identify the specific grain boundaries (GBs) and study their intergranular corrosion behavior in a 316L stainless steel [43]. 316L steel is widely used in industrial pipes due to its excellent corrosion and creep performance. However, at higher temperatures and under corrosive environments, they show intergranular corrosion (IGC) and intergranular stress corrosion cracking (IGSCC) that usually takes place at GBs. Figure 4a shows a BSE image of the steel microstructure containing ∑5 and ∑7 GBs. It was observed that after solutionizing at 1000° for 30 min followed by quenching and sensitizing at 700 °C for 10 h, both the GBs exhibited significantly different corrosion behavior in 10 vol.% HF + 90 vol% $H_2O_2$ solution. The ∑5 show no evidence of GB corrosion even after 2 h of exposure, while the ∑7 show severe GB corrosion.

To understand the corrosion mechanism, needle-shaped specimens were prepared from both ∑5 and ∑7 GBs with the procedure outlined in Fig. 2b. Figure 4b shows a TKD map on the a needle specimen from the solution-annealed Σ5 GB. Figure 4c shows the APT reconstruction with the distribution of Fe atoms (golden color) and with a 2.2 at.% iso-surface of Mo (red color) depicting the ∑5 GB. A 3D top view of the iso-surface is also shown that reveals Mo is distributed homogeneously across the ∑5 boundary planes. Figure 4d shows the composition profiles for the trace elements (Mo, Si, Mn, P, C, Cu, B). The reader can refer to [43] for the profiles of major elements (Fe, Cr, and Ni). The profiles indicate depletion of Fe and Ni at ∑5 GB while Cr is enriched up to ~ 24 at.%. The profile in Fig. 4d shows Mo and Si are enriched to 4.7 at.% and 3.7 at.% while P, C, and B are also slightly enriched at the GB. Hence, the segregation of Cr and Mo is directly related to more corrosion resistance of ∑5 GB than the matrix.

Similarly, a needle specimen guided by TKD, is prepared from a Σ7 GB of the solution-annealed sample. Figure 4e shows the APT reconstruction with the distribution of Fe atoms (golden color). Interestingly, at ∑7 GB i.e., Mo segregates in a stair-like feature running parallel across the GB indicated by the 2.2 at.% Mo iso-surface (red color). The stair-like feature is clearer from the top and edge-on view. It reveals strongly faceted GB, giving a rough inter-facet distance of 13 nm. The composition profile across one stair-like feature is shown in Fig. 4f, which reveals

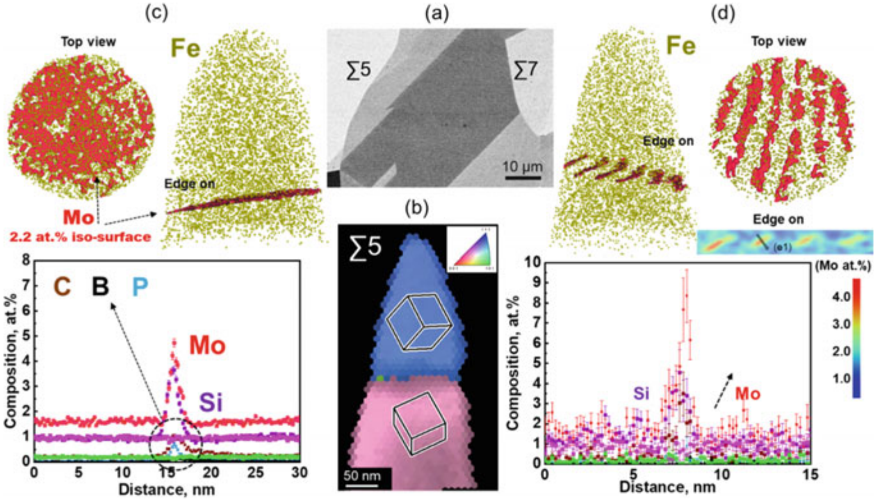

**Fig. 4** Backscattered electron (BSE) image of annealed 316L stainless steel showing Σ5 and Σ7 grain boundaries. **b** Inverse pole figure (IPF) overlapped with image quality (IQ) map of a Σ5 GB needle specimen using transmission Kikuchi diffraction (TKD) method. APT reconstruction with the distribution of Fe atoms and an iso-surface delineated by 2.2 at.% Mo that represents **c** Σ5 GB and **d** Σ7 GB. The top views and one-dimensional composition profiles of trace elements across both Σ5 and Σ7 GBs are also shown

a higher degree of segregation of Cr, Mo, Si, P, and C than for Σ5 GB. The reader should refer to the reference [43] for the profiles of other elements. For example, Mo is enriched up to 8.4 at.%, almost six times the nominal composition. In contrast, the composition profile taken in between the two stair-like features is virtually free of segregation.

The observed different types of segregation behavior between ∑5 and ∑7 GBs were linked to having a weak GB energy anisotropy for ∑5 while strong GB energy anisotropy for ∑7. More specifically, in ∑7, the GB energies of the facets (stair-like features) can be dramatically reduced by the accommodation of the segregating elements (Cr, Mo, C, P, Si) as compared to the regions (in-between facets) that are un-segregated and lead to a strong GB energy anisotropy. After sensitization (annealed at 700 °C) and APT analysis on the ∑7 reveals an additional Cr-depleted zone adjacent to both sides of the GB. The observed segregation behavior of elements and strong GB anisotropy of ∑7 were directly correlated to the nucleation and formation of Mo-rich Laves and $M_{23}C_6$ carbide phases. It was shown that the former phase promotes pit corrosion while the latter phase results in a huge crevice (trench-like corrosion). Hence, conclusions were made using correlative experiments that ∑7 GBs are prone to IGC while ∑5 GBs are immune to it.

### 2.1.3 EBSD—FIB (Needle)—APT

In this section, the application of APT in revealing the site occupancy of solutes in an ordered lattice will be discussed, and its direct influence on the microstructure of the alloy. Figure 5a shows an SE image of a Co-12Ti (at.%) superalloy with $\gamma/\gamma'$ microstructure [44, 45]. Here, the $\gamma'$ is $L1_2$ ordered block-shaped precipitates ($Co_3Ti$ stoichiometry) that are coherently embedded in the face-centered-cubic (fcc) $\gamma$-Co matrix. In Fig. 5b a schematic of the $\gamma'$ $L1_2$ unit cell is shown with the site occupancy of Co (golden color) and Ti (green color) and a lattice parameter of 0.36 nm ($a = b = c = 0.36$ nm). Note that all the Co atoms are in face-centered positions {1/2,1/2,0} while Ti atoms are at corner positions {0,0,0} of the unit cell. Hence, in <00 > directions, the {002} planes contain only Co atoms while {001} planes contain mixed Co and Ti atoms. A correlative use of EBSD and APT can give information related to the site occupancy of elements in $Co_3Ti$ (or any $A_3B$) $L1_2$ ordered compounds.

Figure 5c shows an EBSD orientation map for the Co-12Ti superalloy and its respective inverse pole figure (IPF) as an inset. The red color grains in the map indicate their orientation near to [001] direction. A needle specimen was lifted out from the red

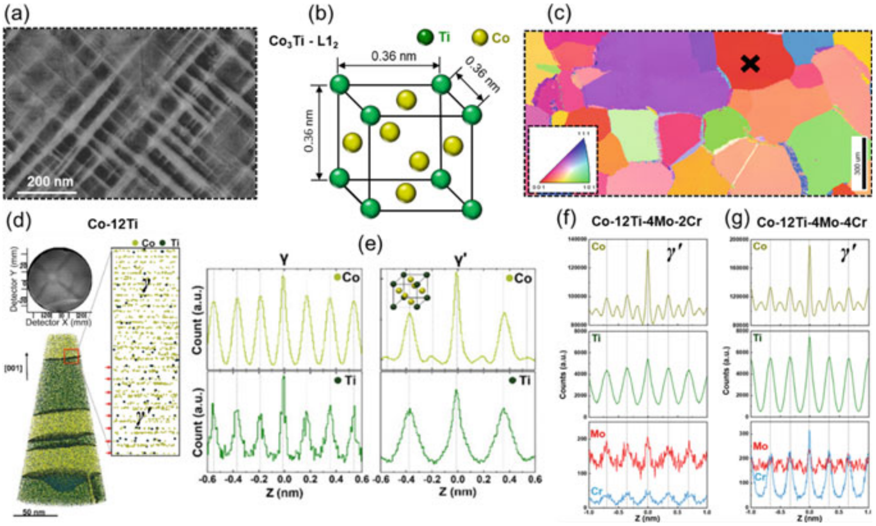

**Fig. 5** BSE image of aged Co-12Ti alloy. **b** A schematic of $L1_2$ $Co_3Ti$ unit cell with Co occupying {1/2,1/2,0} positions and Ti on {0,0,0} positions. **c** An EBSD orientation color map of aged Co-12Ti alloy. **d** A field desorption map acquired from the APT data set of a needle specimen lifted out from the [001] oriented grain (cross mark in **c**) of the aged Co-12Ti alloy. APT reconstruction of the needle specimen aligned along the [001] direction with their $\gamma/\gamma'$ interfaces highlighted by 12.65 at.% Ti iso-surface. The resolved [001] lattice planes in $\gamma$ and $\gamma'$ across the interface are also shown. **e** Spatial distribution maps (SDMs) of Co and Ti in $\gamma$ and $\gamma'$ generated along the [001] direction. Comparison of SDMs of Co, Ti, Mo, and Cr in $\gamma'$ generated along the [001] direction for **f** Co-12Ti-4Mo-2Cr and (g) Co-12Ti-4Mo-4Cr alloys

color region (cross mark), i.e., [001] oriented grain, as per the procedure described in Fig. 2a. The specimen was field evaporated in an atom probe. Figure 5d shows the field desorption map (i.e., cumulative histogram of the ion impact positions on the position-sensitive detector of the atom probe) that indicates a fourfold symmetrical [001] pole nearly parallel to the axis of the needle specimen. Figure 5e shows the APT reconstruction with the distribution of Co atoms (golden color) and Ti atoms (dark green color). The $\gamma/\gamma'$ interfaces are represented by iso-surfaces delineated by 12.65 at.% Ti. Figure 5f shows the (001) lattice planes along [001] direction from the $\gamma/\gamma'$ interface region. In an atom probe, the field evaporated ions are detected as one atomic layer at a time on multi-channel plate (MCP) detector. Hence, along a specific crystallographic direction, the depth resolution can be achieved in the order of inter-planer spacing, as shown in Fig. 5f. It is clearly seen that the Ti atoms occupy every second plane in $\gamma'$ as marked by the red arrows.

For more insights, element-specific spatial distribution maps (SDMs) are generated along [001] direction from the APT data set. Through SDMs, accurate identification and characterization of atomic planes can be made. The SDMs are a combination of two radial distribution functions: the average distribution of interatomic spacing of atoms in the $z$-direction and a two-dimensional map showing average atomic positions in the $x$–$y$ lateral plane [46]. Hence, element-specific SDMs can be generated by adjusting the specific crystallographic direction ([001] in the present case) along the $z$-direction. Figure 5g shows the SDMs generated along [001] direction from the $\gamma$ and $\gamma'$ regions. In the $\gamma$-Co region, the SDMs for Co and Ti show the appearance of peaks at an average interatomic spacing of ~ 0.18 nm that indicating the Co and Ti atoms are randomly distributed and can occupy both the lattice positions {0,0,0} and {1/2,1/2,0} without any preference. In the $\gamma'$-$Co_3Ti$ region, The SDM for Co shows alternating high and low-intensity peaks appearing at every 0.18 nm distance, whereas the SDM for Ti indicates peaks at every ~0.36 nm distance. This shows that the Co occupies {1/2,1/2,0} positions while Ti preferentially occupies {0,0,0} positions indicating a stoichiometry of $Co_3Ti$ for $\gamma'$ i.e., $L1_2$ unit cell. Hence, the element-specific SDMs can detect site occupancy or change in site occupancy after alloying in ordered structures. For example, Fig. 5h shows the SDMs for the solutes Cr and Mo in the $\gamma'$ precipitate region added to the Co-Ti binary alloy. In Co-12Ti-4Mo-2Cr alloy, the SDMs for Mo and Cr show their occupancy in {0,0,0} lattice positions as for the Ti. However, with an increase in Cr composition in the alloy, i.e., Co-12Ti-4Mo-4Cr, the SDM of Mo shows the additional occupancy of Mo atoms in {1/2,1/2,0) lattice positions. It indicates the additional Cr atoms prefer to replace Mo atoms from {0,0,0} positions and occupy them. This change in site occupancy by alloying addition is shown to directly influence the lattice parameter of $\gamma'$ (and hence $\gamma/\gamma'$ lattice misfit) and the $\gamma'$ volume fraction in the alloy. Since these two microstructural characteristics in $\gamma/\gamma'$ superalloy control their high-temperature mechanical behavior, tuning of site occupancy by alloying can be used for optimizing the alloy properties.

In the same context, another example is shown in Fig. 6 for a $\gamma/\gamma'$ Co-30Ni-10Al-2Mo-2Ta-2Ti-XCr (X – 0 to 8)-based superalloy [47]. Cr is one of the crucial alloying additions in superalloys that impart high-temperature oxidation and corrosion resistance. In addition, Cr also alters the $\gamma/\gamma'$ lattice misfit and hence, controls the $\gamma'$ morphology. Figure 6a and c show SEM images for 0Cr and 8Cr added alloys that reveal the $\gamma'$ morphology changes from cuboidal to a spherical shape due to the reduction of $\gamma/\gamma'$ lattice misfit with an increase in Cr addition (Fig. 6b). Similar coupled EBSD and APT experiments are performed to understand the site occupancy effect on the $\gamma'$ morphological change. Figures 6d and e shows the (001) planes across $\gamma$ and $\gamma'$ with the distribution of Co + Ni (golden), Al + Ti + Ta (green), Cr (blue), and Mo (red) atoms for both 5Cr and 8Cr added alloys. The figure also shows the respective Cr SDMs in $\gamma'$ that clearly reveal an additional occupancy of Cr atoms at {1/2,1/2,0} positions along with the Co + Ni atoms in 8Cr as compared to 5Cr. The Cr site occupancy change results in the reduction of $\gamma/\gamma'$ lattice misfit that lowers the strain energy contribution to the total free energy. This leads to the morphological transition of $\gamma'$ from cuboidal to spherical shape.

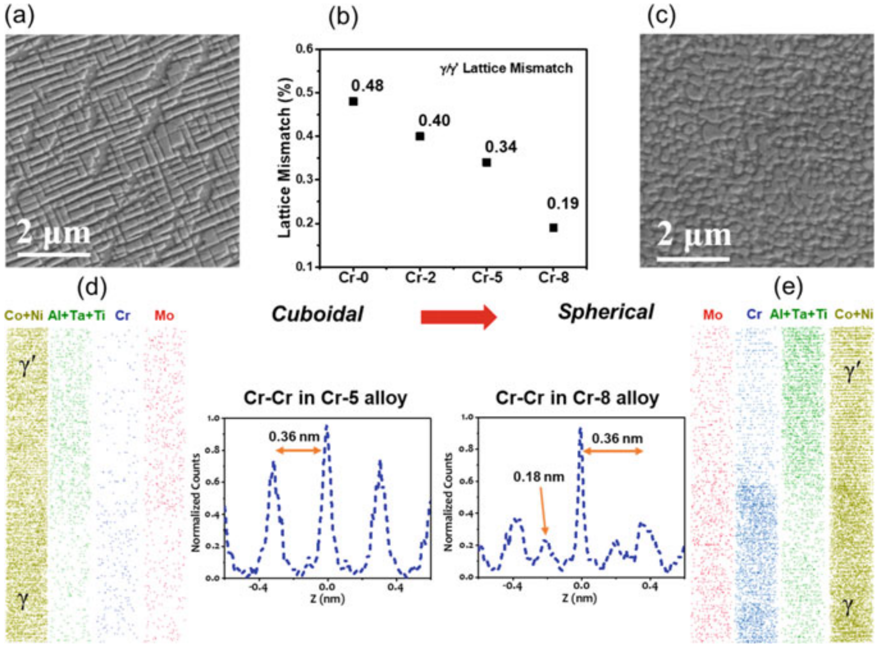

**Fig. 6** SE images for aged Co-30Ni-10Al-5Mo-2Ta-2Ti after **a** 0Cr, **c** 8Cr addition. **b** Change in $\gamma/\gamma'$ lattice misfit with an increase in Cr composition in the alloy. The atomically resolved lattice plane along [001] direction for **d** 5Cr **e** 8Cr added alloy. Corresponding spatial distribution maps (SDMs) from successive {100} planes of $\gamma'$ are also shown. Adapted with permission from reference [47]

### 2.1.4 ECCI—FIB (Needle)—TEM/STEM—APT

This section will demonstrate an example comprising correlative use of electron-channeling-contrast-imaging (ECCI), analytical and high-resolution TEM, and APT. ECCI is a powerful microscopy technique to observe crystalline defects such as dislocations, stacking faults (SFs), anti-phase boundaries (APBs), twins and grain boundaries in a bulk sample using SEM [48]. In ECCI, the primary beam of electrons is channeled through the crystal, i.e., minimum backscattering. This is done by orienting the crystal such that the primary beam exactly is in the Bragg condition with one of the lattice planes. In the presence of defects, the coherency of the channeled primary beam is disturbed and leads to a strong backscattering from the position of the defect. Hence, the defect becomes brighter in a darker contrast background when imaged using a BSE detector. More details related to ECCI can be found in the following reference [48]. Controlled ECCI (cECCI) can be performed using a combination of EBSD orientation mapping and simulation of electron channeling pattern (ECP) at different sample tilts and rotations using Tools for Orientation Determination and Crystallographic Analysis (TOCA) [49] or CrystalMaker software [50]. First, EBSD is performed on the surface of the bulk sample to get the orientation of grains. A region of interest is selected as per the grain orientation required for the analysis. The crystal orientation information of the chosen grain is fed into either TOCA or CrystalMaker software that provides the simulated Kikuchi patterns as per the orientation of the selected grain. The software is used to calculate the tilt and rotation angles to reach exact 2-beam conditions. The bulk sample is given with these tilt and rotation angles, and the BSE detector is used to get the ECC images from the selected grain.

Figure 7a shows an cECC image of a single crystal CoNi-based superalloy bulk sample surface after creep deformation with its crystal orientation near to the [110] direction [51]. The image was acquired in a two-beam Bragg's diffraction condition with $g = 00\bar{2}$ (where $g$ is the diffraction vector) by controlling the rotation/tilt of the crystal. Figure 7b shows the corresponding stereogram. The image clearly distinguishes the fcc $\gamma$ (dark regions) and the rafted $L1_2$ $\gamma$' (gray regions) phases by atomic density contrast. In addition, a significant channeling contrast from the defect regions appears as bright intensity-oscillating areas inside the rafted $\gamma$' regions. According to their crystallographic orientation, these correspond to stacking faults (SFs) represented by *A*, *B*, *C*, and *D*, respectively. From the stereogram, the traces reside on {111} cubic planes with displacement vectors of the type $R = \pm\frac{1}{3}112$. The faults *A*, *B*, *C*, and *D* are lying on the $\left(11\bar{1}\right)$, $\left(\bar{1}11\right)$, $\left(\bar{1}1\bar{1}\right)$, and (111) planes, respectively. Figures 7c–e show ECCI micrographs taken using two-beam $\bar{1}11$, $\bar{1}1\bar{1}$ and $\bar{2}20$ conditions near the [110] zone direction, respectively. It is noticeable that the SFs become invisible at specific diffraction conditions.

A needle specimen was prepared from a SF region using the protocol described in Fig. 2b. Figure 7f shows a bright field (BF.) TEM of the needle specimen taken in [110] zone axis. Two darker contrast lines are visible inside the needle specimen that originated from the intersection of the SF plane across the curved surface of the

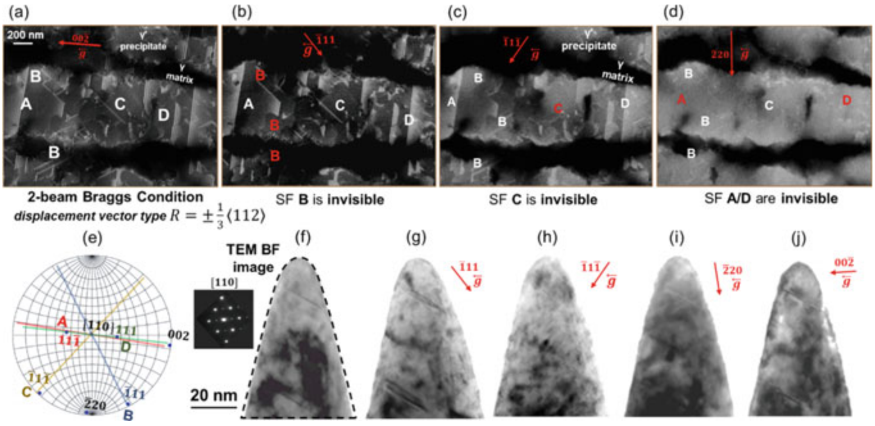

**Fig. 7** High magnification cECC images of the crept CoNi-based superalloy taken under different two-beam diffraction conditions **a**–**d** near the [110] pole showing bright regions corresponding to SFs inside rafted $\gamma'$ and **e** corresponding stereogram of plane normals viewed in the same orientation as the specimen's surface. **f** A brightfield (BF.) TEM image of a needle specimen taken along [110] zone direction showing two dark contrast lines corresponding to planar stacking faults **g**–**j** BF images of the needle specimen taken in different two-beam conditions. Adapted with permission from reference [51]

needle specimen. Figure 7g–j shows BF micrographs of the same tip imaged under different two-beam diffraction conditions. By comparing the invisibility of these SFs with ECCI results (figure (a-e)), the SFs inside the needle specimen is identified as C type.

Figure 8a shows a low-magnification HAADF-STEM image of the needle specimen taken close to the [110] cubic zone axis that reveals a stacking fault in the edge-on condition. The stacking fault region has a bright contrast compared to the surrounding regions, shown in Fig. 8b. Figure 8c depicts the atomic-column resolution that reveals atomic Z-contrast along the fault, showing a slight increase in the Z-contrast intensity. This indicates the segregation of heavier alloying elements at the fault plane. The change in stacking sequence across the fault shows a local D0$_{19}$ structure corresponding to a superlattice intrinsic stacking fault (SISF) coherently embedded in an L1$_2$ ordered lattice. A schematic view of the atomic structure of the SISF with DO$_{19}$ ordering [52, 53] embedded in the L1$_2$ ordered $\gamma$' phase is also shown along [110] projection.

Subsequently, the needle specimen was field evaporated in LEAP 5000 XHR to get near-atomic scale compositional information. Figure 8d shows APT reconstruction with the distribution of Co atoms (golden color). A confined linear enrichment of Cr is highlighted by an iso-surface with a threshold of 5.6 at.% Cr (pink color) is seen. The overlay of the 3D atom map and the BF image indicates the linear Cr enrichment occurs along with the associated partial dislocation. The 2D elemental composition maps projected onto the faces (xy, xz, yz) of a cuboidal region-of-interest centered on the feature shown in Fig. 8e confirms the observation, i.e., the

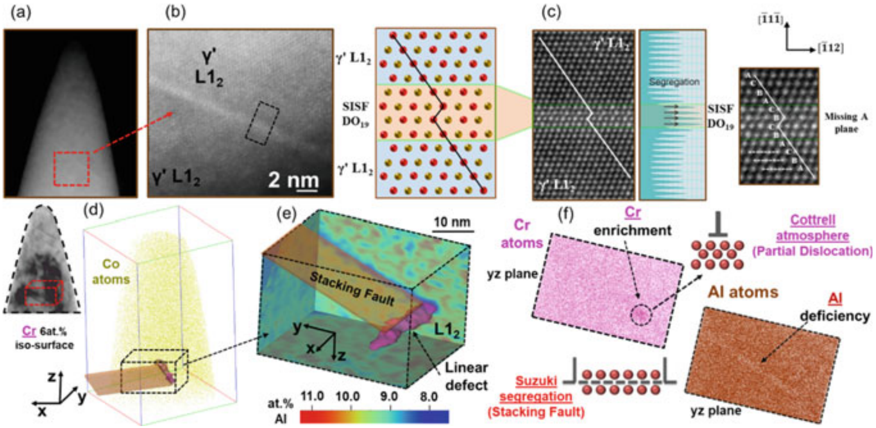

**Fig. 8** **a** STEM HAADF image of the needle specimen taken along [110] zone axis showing bright line corresponding to a planar SF and **b** a higher magnification image centered on the SF showing higher Z-contrast at SF region. **c** The HR-STEM image is showing slightly increased intensity (Z-contrast) in SF indicating segregation of heavy elements. The sequence of atomic planes across the SF showing the intrinsic nature of the fault plane (missing A plane). Simulated atomic structure of the SF with $D0_{19}$ structure coherently embedded in $L1_2$ ordered lattice **d** BF TEM image and the APT reconstruction of the same needle specimen showing confined linear Cr decoration. **e** 2D elemental compositional maps projected onto the xy, xz, and yz planes as faces of a cuboidal ROI centered on the SF for the solute Al with the corresponding composition color-scale. The distribution of Al (brown) and Cr (pink) atoms viewed perpendicular to the yz plane is also shown. Adapted with permission from reference [51]

linear enrichment of Cr is along with the partial dislocation that is attached to a stacking fault. Figure 8f shows the distribution of Cr and Al projected on yz plane that clearly shows local Al depletion along a specific plane and ends precisely at the location of Cr segregation. This plane corresponds to the SISF attached to a Cr enriched leading partial dislocation (LPD). The SISF composition is enriched with W and Co while Al and Ni are depleted relative to the composition of the surrounding $\gamma'$ lattice. In contrast, the bounding LPD is enriched with Cr and Co while Al and Ni are depleted. By taking a composition profile measured along the SISF plane and across the LPD shows that in the adjoining γ' planes, the composition in Al increases ahead of the LPD over approx. 4 nm and decreases after that, in contrast with the W content that first drops and then increases. This 3D compositional information led to the proposal that the solute diffusion occurs in-plane during the movement of LPD and is assisted by stress on {111} planes [51].

### 2.1.5 FIB (TEM Lamella)—STEM TEM/SEM—FIB (Needle)—APT

This example shows the correlative use of TEM and APT by the protocol described in Fig. 2c [28, 32]. Figure 9a shows STEM images taken in TEM and SEM of a TEM lamella lifted out from a bulk sample of CoNi base single crystal superalloy using

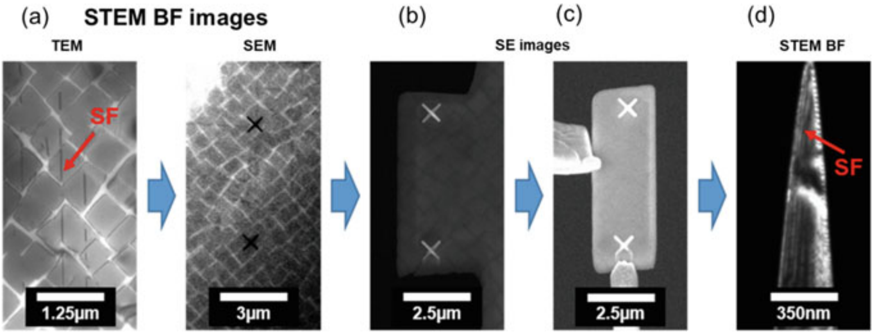

**Fig. 9** **a** STEM BF image centered on a region of interest (ROI) with stacking faults (SFs) from a TEM lamella taken in TEM and SEM. Note that in SEM, the SF region is marked by cross marks through Pt-deposition. **b** Ion-beam image of the ROI with cross marks. **c** Welding of the ROI on a pre-sharpened Mo post using Pt-deposition. **d** Sharpened specimen with the SF inside the needle. Adapted with permission from reference [28]. (open access article under the terms of Creative Common CC BY license)

FIB. A clear contrast of SFs can be seen inside the cuboidal $\gamma'$ precipitates (marked by a red arrow). In dual beam, SEM/FIB, the SF region was marked by Pt-deposition or by putting cross marks using Ga-ion beam. Figure 9b shows the SE image taken in SEM with the cross markers. The SF region was cut from the TEM lamella and finally attached to a pre-sharpened Mo post and subsequently milled such that the SF region remains at the center of the axis of the needle. The APT of the needle was successful, and a planar SF with a different composition was imaged in the APT reconstruction. The data is not shown here.

## 2.2 Challenges

While performing these experiments, one of the main challenges is the formation of oxides and absorption of species from the air, such as hydrogen, on the surface of needle specimens, which occurs mainly during handling and transport between the used instruments. Additionally, a large amount of carbon contamination occurs on the surface of needle specimens by electron beam interaction during EM experiments. Another issue is the implantation and diffusion of Ga-ions into the needle specimens during FIB preparation, which causes liquid metal embrittlement leading to brittle fracture during field evaporation. This is more detrimental in the case of Al-alloys [54]. The consequence of these directly affects the yield of the APT run, i.e., the needle specimen may develop cracks during field evaporation and fracture early, leading to failure of the correlative experiment. Sometimes the failure can be avoided if the needle specimen is cleaned after FIB preparation (removal of Ga-ion damaged areas) and after each EM technique by the use of an ion beam operating at a low accelerative voltage (2–5 kV) and low currents (9–23 pA). But the researcher should be careful that the feature of interest should be well below (~200 nm) such that it should not be lost during cleaning before field evaporation. Another option for cleaning is to use low-energy sputtering using argon gas in a precision-ion-polishing system (PIPS) [55]. However, the parameters related to voltage and currents should be optimized according to the needle specimen material. Ga-ion damage of needle specimens can also be minimized if the FIB preparation is carried out in cryogenic temperatures using a cryo stage [56] or alternatively using plasma-based sources such as Xe ions [57, 58]. Another issue is the field-induced low-temperature oxidation that damages the top region of the needle specimen [59]. This can be avoided if proper grounding of all parts that come in contact with the needle specimen.

## 3 Summary and Future Scope

In this chapter, the use of a different combination of EM techniques with APT was discussed with relevant examples. The use of the number of EM techniques with APT is not limited to the ones introduced here. Other EM techniques such as precision electron diffraction (PED) using TEM [12, 60], electron holography in TEM [61, 62], etc., on needle specimens before field evaporation in APT were also demonstrated by several groups. It is also expected that, in the future, any new EM techniques for bulk or TEM samples can also be utilized for needle specimens. This may require the indigenous design of special correlative holders that can be used in any instrument for correlative experiments.

**Acknowledgements** The author is grateful to the workshop organizers for their invitation to contribute to this book. The author also acknowledges electron microscopy, atom probe tomography, and ion beam facilities in IISc Bangalore and MPIE. The author is thankful to Professor Baptiste Gault, Professor Dierk Raabe, Professor Kamanio Chattopadhyay, and Professor Dipankar Banerjee for their constant support and encouragement. The authors also acknowledge the financial support from SERB India, IISc for SEED Grant, and MPG-IISc Partner Group.

## References

1. D.B. Williams, C.B. Carter, *Transmission Electron Microscopy: A Textbook for Materials Science*, 2nd edn. (Springer, US, 2009)
2. R.F. Egerton, *Physical Principles of Electron Microscopy: An Introduction to TEM, SEM, and AEM* (Springer, US, 2005)
3. F. De Geuser, B. Gault, Acta Mater. **188**, 406–415 (2020)
4. T.F. Kelly, D.J. Larson, Annu. Rev. Mater. Res. **42**, 1–31 (2012)
5. E.W. Müller, J.A. Panitz, S.B. McLane, Rev. Sci. Instrum. **39**, 83–86 (1968)
6. R.K.W. Marceau, G. Sha, R.N. Lumley, S.P. Ringer, Acta Mater. **58**, 1795–1805 (2010)
7. S. Medrano, H. Zhao, F. De Geuser, B. Gault, L.T. Stephenson, A. Deschamps, D. Ponge, D. Raabe, C.W. Sinclair, Acta Mater. **161**, 12–20 (2018)
8. D. Palanisamy, S. Ener, F. Maccari, L. Schäfer, K.P. Skokov, O. Gutfleisch, D. Raabe, B. Gault, Phys. Rev. Materials **4**, 054404 (2020)

9. S. Meher, L.J. Carroll, T.M. Pollock, M.C. Carroll, Scripta Mater. **113**, 185–189 (2016)
10. P. Pandey, A.K. Sawant, B. Nithin, Z. Peng, S.K. Makineni, B. Gault, K. Chattopadhyay, Acta Mater. **168**, 37–51 (2019)
11. O.C. Hellman, D.N. Seidman, Mater. Sci. Eng., A **327**, 24–28 (2002)
12. M. Herbig, D. Raabe, Y.J. Li, P. Choi, S. Zaefferer, S. Goto, Phys. Rev. Lett. **112**, 126103 (2014)
13. B. Gault, M.P. Moody, J.M. Cairney, S.P. Ringer, Mater. Today **15**, 378–386 (2012)
14. V.J. Araullo-Peters, B. Gault, S.L. Shrestha, L. Yao, M.P. Moody, S.P. Ringer, J.M. Cairney, Scripta Mater. **66**, 907–910 (2012)
15. T.F. Kelly, P.P. Camus, D.J. Larson, L.M. Holzman, S.S. Bajikar, Ultramicroscopy **62**, 29–42 (1996)
16. B. Gault, M.P. Moody, J.M. Cairney, S.P. Ringer, *Atom Probe Microscopy* (Springer-Verlag, New York, 2012)
17. B. Gault, M.P. Moody, F.D. Geuser, A.L. Fontaine, L.T. Stephenson, D. Haley, S.P. Ringer, Microsc. Microanal. **16**, 99–110 (2010)
18. J.M. Hyde, A. Cerezo, R.P. Setna, P.J. Warren, G.D.W. Smith, Appl. Surf. Sci. **76–77**, 382–391 (1994)
19. B. Gault, S.T. Loi, V.J. Araullo-Peters, L.T. Stephenson, M.P. Moody, S.L. Shrestha, R.K.W. Marceau, L. Yao, J.M. Cairney, S.P. Ringer, Ultramicroscopy **111**, 1619–1624 (2011)
20. E.A. Marquis, F. Vurpillot, Microsc. Microanal. **14**, 561–570 (2008)
21. A.J.W. Moore, J.A. Spink, Surf. Sci. **44**, 198–212 (1974)
22. A.J. Melmed, J. Vacuum Sci. Tech. B: Microelect. Nanometer Struct. Process., Measurement, Phenomena **9**, 601–608 (1991)
23. A. Eades, Microsc. Res. Tech. **20**, 217–217 (1992)
24. J.M. Papazian, J. Microsc. **94**, 63–67 (1971)
25. H. Nordén, K.M. Bowkett, J. Sci. Instrum. **44**, 238–240 (1967)
26. A.R. Waugh, S. Payne, G.M. Worrall, G.D.W. Smith, J. Phys. Coll. **45**, C9-C9–209 (1984)
27. K. Thompson, D. Lawrence, D.J. Larson, J.D. Olson, T.F. Kelly, B. Gorman, Ultramicroscopy **107**, 131–139 (2007)
28. S.K. Makineni, M. Lenz, P. Kontis, Z. Li, A. Kumar, P.J. Felfer, S. Neumeier, M. Herbig, E. Spiecker, D. Raabe, B. Gault, JOM, 1–8 (2018)
29. M.K. Miller, K.F. Russell, G.B. Thompson, Ultramicroscopy **102**, 287–298 (2005)
30. D.J. Larson, D.T. Foord, A.K. Petford-Long, H. Liew, M.G. Blamire, A. Cerezo, G.D.W. Smith, Ultramicroscopy **79**, 287–293 (1999)
31. P.J. Felfer, T. Alam, S.P. Ringer, J.M. Cairney, Microsc. Res. Tech. **75**, 484–491 (2012)
32. S.-I. Baik, D. Isheim, D.N. Seidman, Ultramicroscopy **184**, 284–292 (2018)
33. M. Herbig, P. Choi, D. Raabe, Ultramicroscopy **153**, 32–39 (2015)
34. M. Herbig, Scripta Mater. **148**, 98–105 (2018)
35. M.H.F. Overwijk, F.C. van den Heuvel, C.W.T. Bulle-Lieuwma, Journal of Vacuum Science & Technology B: Microelectronics and Nanometer Structures Processing. Measurement, and Phenomena **11**, 2021–2024 (1993)
36. L.A. Giannuzzi, F.A. Stevie, Micron **30**, 197–204 (1999)
37. P. Pandey, S.K. Makineni, B. Gault, K. Chattopadhyay, Acta Mater. **170**, 205–217 (2019)
38. K.E. Knipling, D.C. Dunand, D.N. Seidman, MEKU **97**, 246–265 (2006)
39. S. Özbilen, H.M. Flower, Acta Metall. **37**, 2993–3000 (1989)
40. K. Babinsky, R. De Kloe, H. Clemens, S. Primig, Ultramicroscopy **144**, 9–18 (2014)
41. R.R. Keller, R.H. Geiss, J. Microsc. **245**, 245–251 (2012)
42. T. Schwarz, G. Stechmann, B. Gault, O. Cojocaru-Mirédin, R. Wuerz, D. Raabe, Prog. Photovoltaics Res. Appl. **26**, 196–204 (2018)
43. S.-P. Tsai, S.K. Makineni, B. Gault, K. Kawano-Miyata, A. Taniyama, S. Zaefferer, Acta Mater. **210**, 116822 (2021)
44. H.J. Im, S.K. Makineni, B. Gault, F. Stein, D. Raabe, P.-P. Choi, Scripta Mater. **154**, 159–162 (2018)

45. H.J. Im, S.K. Makineni, C.-S. Oh, B. Gault, P.-P. *Choi, Microscopy and Microanalysis* (undefined/ed), 1–5
46. B.P. Geiser, T.F. Kelly, D.J. Larson, J. Schneir, J.P. Roberts, Microsc. Microanal. **13**, 437–447 (2007)
47. P. Pandey, S.K. Makineni, A. Samanta, A. Sharma, S.M. Das, B. Nithin, C. Srivastava, A.K. Singh, D. Raabe, B. Gault, K. Chattopadhyay, Acta Mater. **163**, 140–153 (2019)
48. S. Zaefferer, N.-N. Elhami, Acta Mater. **75**, 20–50 (2014)
49. S. Zaefferer, J Appl Cryst **33**, 10–25 (2000)
50. http://crystalmaker.com/
51. S.K. Makineni, A. Kumar, M. Lenz, P. Kontis, T. Meiners, C. Zenk, S. Zaefferer, G. Eggeler, S. Neumeier, E. Spiecker, D. Raabe, B. Gault, Acta Mater. **155**, 362–371 (2018)
52. M.S. Titus, A. Mottura, G. Babu Viswanathan, A. Suzuki, M.J. Mills, T.M. Pollock. Acta Mat. **89**, 423–437 (2015)
53. Y.M. Eggeler, J. Müller, M.S. Titus, A. Suzuki, T.M. Pollock, E. Spiecker, Acta Mater. **113**, 335–349 (2016)
54. B.A. Benson, R.G. Hoagland, Scr. Metall. **23**, 1943–1948 (1989)
55. M. Herbig, A. Kumar, Microsc. Res. Tech. **84**, 291–297 (2021)
56. L. Lilensten, B. Gault, PLoS ONE **15**, e0231179 (2020)
57. R. Estivill, G. Audoit, J.-P. Barnes, A. Grenier, D. Blavette, Microsc. Microanal. **22**, 576–582 (2016)
58. B. Gault, A.J. Breen, Y. Chang, J. He, E.A. Jägle, P. Kontis, P. Kürnsteiner, A.K. da Silva, S.K. Makineni, I. Mouton, Z. Peng, D. Ponge, T. Schwarz, L.T. Stephenson, A. Szczepaniak, H. Zhao, D. Raabe, J. Mater. Res. **33**, 4018–4030 (2018)
59. C. Nowak, G. Schmitz, R. Kirchheim, Surf. Sci. **604**, 641–648 (2010)
60. E.F. Rauch, M. Véron, Mater. Charact. **98**, 1–9 (2014)
61. L. Amichi, I. Mouton, E. Di Russo, V. Boureau, F. Barbier, A. Dussaigne, A. Grenier, P.-H. Jouneau, C. Bougerol, D. Cooper, J. Appl. Phys. **127**, 065702 (2020)
62. V. Migunov, A. London, M. Farle, R.E. Dunin-Borkowski, J. Appl. Phys. **117**, 134301 (2015)

# Additive Manufacturing: Bringing a Paradigm Shift

**C. P. Paul and A. N. Jinoop**

## 1 Introduction

A paradigm shift from the sellers' market to the buyers' market in the past two decades changes the mode of operation for most industries [1]. The industries are pushed to move from customer satisfaction to customer delight by providing product value addition. One of the techniques that considerably enhances the product value is additive manufacturing (AM). ISO/ASTM 52,900 defines additive manufacturing as the "process of joining materials to make parts from 3D model data, usually layer upon layer, as opposed to subtractive manufacturing and formative manufacturing methodologies" [2]. AM converts an *abstract idea* to a *tangible component* using a three-step process called pre-processing, processing, and post-processing [3]. The pre-processing stage involves developing 3D model data, which can be a computer-aided-design (CAD) model or a result of numerical analysis or a model generated using 3D scanning. The developed 3D model will be converted to machine-specific file formats (e.g.: stl,.amf,.obj, etc.), which is followed by slicing of the 3D model into different layers and tool path generation for each layer. The processing stage in AM involves the addition of material in a layer-by-layer fashion to convert the 3D design to the 3D component. The final stage in AM is the post-processing stage, where the built feature is tailored as per the customer requirements by using secondary treatments, like machining, painting, heat-treatment etc. [4].

AM can influence the complete product value addition by giving superior flexibility at several stages of manufacturing, as it includes direct action on the digital data.

---

C. P. Paul (✉) · A. N. Jinoop
Laser Technology Division, Raja Ramanna Center for Advanced Technology, Indore 452013, India
e-mail: paulcp@rrcat.gov.in

A. N. Jinoop
e-mail: jinoop@rrcat.gov.in

Homi Bhabha National Institute, Anushakti Nagar, Mumbai 400094, India

A. Shrivastava et al. (eds.), *New Horizons in Metallurgy, Materials and Manufacturing*, Indian Institute of Metals Series, https://doi.org/10.1007/978-981-19-5570-9_3

**Fig. 1** AM disrupting the conventional production route

It is one of the disruptive technologies that provides a paradigm shift in design and manufacturing by enabling the manufacturing of new-to-market, mass-customized and smarter products. The major difference between AM and conventional manufacturing is the approach used to build a structure. AM adds material in a layer-by-layer fashion instead of material removal in subtractive manufacturing and material shaping in formative manufacturing. In addition, as presented in Fig. 1, AM brings a significant disruption in industrial manufacturing by changing the product flow path from design to the component. In the conventional manufacturing route, the product is made first, followed by its appreciation of novelty by the customer, and lastly, its sale to the customer. However, AM disrupts the conventional route by understanding the feel first using digitization/digital model followed by selling of product and finally making it.

## 2 Freedoms and Need for AM

The various freedoms offered by AM as compared to conventional manufacturing techniques are:

(a) **Shape design freedom**: As AM uses a layer-by-layer approach to building the components, the technology provides unlimited design flexibility. During the pre-processing stage of AM, a complex 3D part is converted into simple 2D sketches, like line, circle, etc., or even a single point. Thus, the technology provides shape design freedom to build components with sophisticated geometries, hollow interior parts, irregular shapes, undercuts, etc. Besides the above, the cost-per-part remains constant with an increase in the design complexity in AM as opposed to conventional manufacturing. The increase in the complexity of the component can lead to an increase in the machining time, requirement for customized tooling, increase in documentation, etc. However, an increase in design complexity does not invite extra costs in AM as the cost is always a function of build time in AM [5]. In addition, any customization can be made digitally without additional tooling and cost. Thus, AM gives "complexity for free" through "shape design freedom," allowing the fabrication of superior and intricate components [4].

(b) **Material design freedom**: AM involves selective addition of materials as per the requirement, which provides the extra space of adding different materials at different locations within a single component. For example, if an engineering application demands higher thermal conductivity at one end and higher mechanical strength at another end, it is advisable to build a multi-material component involving copper and nickel. Copper can be used in those regions where conductivity is critical, and nickel can be used as a building material in regions where strength is critical. In addition, AM also gives us the freedom to have a transition in the composition to avoid steep joints. Even though copper and nickel are metallurgically compatible, the difference in thermophysical properties can yield weak joints when the component is put into actual loading conditions [6]. AM allows having a smoother transition in composition between the material, which enables the building of strong joints. In addition, the process also provides the freedom to join two metallurgically incompatible materials by adding a buffer layer (metallurgically compatible to both materials) of a third material in between the two materials to build a defect-free joint [7].

(c) **Logistics freedom**: As the input for AM is the 3D model, the input file can be sent through cyber systems, and manufacturing can be carried out remotely by eliminating the direct contact between manufacturer and customer. Thus, AM can decrease the stages involved in the supply chain, and the manufacturer can respond to customer requirements quickly and thus decreases the lead time [1].

(d) **Post-processing freedom**: The components built by AM can be post-processed to tailor their properties and surface quality as per the user requirements. Building strategy can be established as per the post-processing requirements, and dimensionally critical parts can be developed using machining, for which machining allowance can be provided during the design stage itself.

Figure 2 presents the different stages involved in product development, which include the various stages from concept to final product development. The product development cycle has a number of steps, and the three main stages are design, production, and application. The design stage starts with synthesis, where the need for the product/ design is analyzed using information obtained from the market survey or customer feedback. This stage also involves "concept design," in which different concepts are selected and analyzed. After a comprehensive analysis, the best concept is selected for design modeling and simulation, which is carried out in the analysis stage. It involves design optimization and performance evaluation. The last stage of the design stage is the development of finalized design, and it will be sent to the production stage after preparing the documentation and drawing. Once the design stage is finished, the production stage starts, which includes planning, material procurement, tool procurement, and generation of numerical code for machining, etc. This is followed by manufacturing, quality checking, and packing if the quality is satisfactory. The full product is shipped and delivered to the customers, and the feedback obtained from the customer is again used for concept design, which helps to achieve continuous quality improvement.

It can be seen in Fig. 2b that the use of AM in the product development cycle eradicates some of the stages either fully or partially. The 3D model developed during the synthesis and analysis stage is used as a reference document and thus eliminates the drawing and documentation stages. The planning stage is completely avoided as the AM system automatically performs the planning operations. One significant advantage brought by AM is that the material procurement is not dependent on the design and size of the component, as AM uses shapeless materials. The raw material purchase can be carried out before finalizing of the design of the component. The tool procurement stage is also avoided in AM as it does not require any special tooling, and hence, the tool procurement stage is also eliminated. Thus, the use of AM process leads to considerable savings in expenditure and time, making it feasible for several applications, especially for product development [8].

Some of the advantages of AM that attract its use in several industries are:

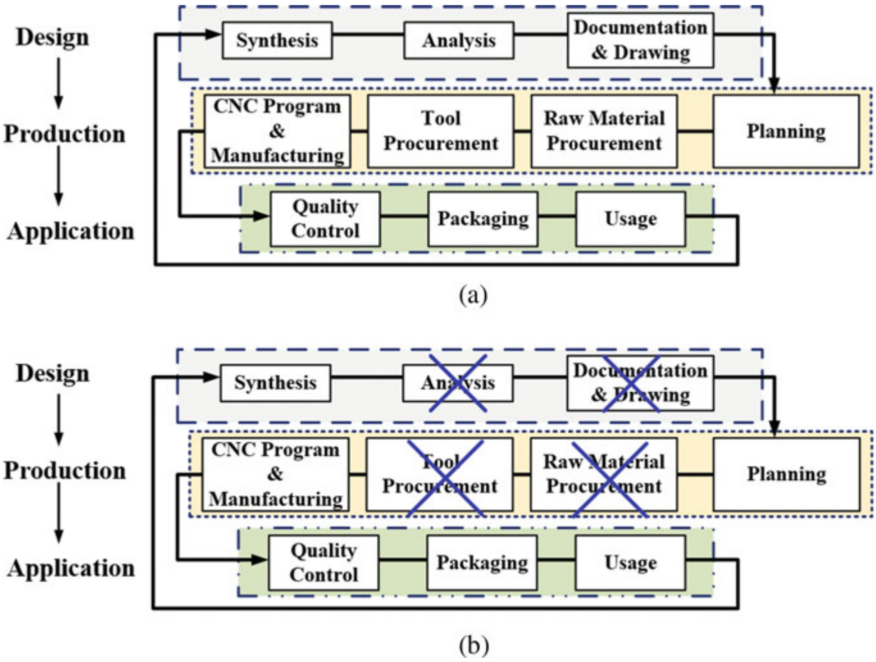

**Fig. 2** Stages in product development: **a** conventional manufacturing and **b** additive manufacturing

(a) **Customized components**: Several sectors, like aerospace, bio-medical, jewelry, and power sector, require customized components for various applications. In the case of the aerospace sector, the internal cabin design is one of the areas where a high level of customization is required. In the aerospace and power sector, there is always a need for high-performance components in limited quantities, which makes the deployment of AM suitable for these applications. In the case of the biomedical sector, the need for patient-specific implants is one of the major requirements. Jewelry sector requires designs that are customer-specific, which attracts the use of AM for such applications.

(b) **Low buy-to-fly ratio**: The buy-to-fly ratio refers to the ratio of material purchased/ used for developing a component to the amount of material used in the final part. A high value of the buy-to-fly ratio shows that a greater portion of the procured raw material is not used to develop the final component. The typical buy-to-fly ratio is close to 10 or higher in conventional manufacturing, which indicates large wastage of material. The use of AM in the manufacturing cycle reduces the ratio and brings it close to 1, as the wastage of raw material is reduced considerably [9].

(c) **Pre-surgical planning and Education**: In the medical sector, AM helps to give a surgeon with the physical 3D model of the required patient anatomy prior to surgery, which aids the doctor to precisely plan the surgery. This will help the doctor to have an improved understanding of complex anatomy unique to each patient, which can help to have patient-specific pre-surgical planning. This can reduce the time to be spent inside the operating room and complications during the surgery [10].

(d) **Integrated Components**: AM technology allows to build components with less assembly components, which improves the flexibility of the built components. With AM, all the parts required for building a functional component like springs, joints, actuators, etc., can be built in a single step, which aids in reducing a large number of assembly steps. This can save money and reduces the probability of production errors. In addition, AM also allows the fabrication of smart components by building sensor embedded components [11].

## 3 Limitations of AM

The various limitations offered by the technology are:

(a) **High production costs**: The cost of high-quality AM systems and materials are very high, which limits its wide adoption. This issue is more significant in the case of metal AM (MAM) processes, which involve the use of high energy sources, like – lasers, electron beam,etc., to melt metallic materials. As some of the techniques are patented by the industries, the cost of AM systems is higher due to domination by machine manufacturers. Further, the restrictions generally imposed by the machine manufacturers to use proprietary materials for fabrication also increases the production cost. However, in the last few years, some machine manufacturers have become lenient in terms of material usage and started allowing the use of open raw materials.

(b) **Mechanical properties**: During AM, the material addition takes place in a layer by layer fashion, and thus, layering and multiple interfaces are seen, which causes defects like – porosity, cracks, delamination, etc., in the component. Further, during MAM, the use of high energy sources results in more significant residual stresses in the built structures, which can reduce the life of AM-built components, especially in dynamic loading conditions. In addition, the use of different rastering/ scanning patterns, building directions, and process parameters can cause variation in the solidification pattern, cooling rates, and microstructure evolution, which eventually leads to variation in mechanical properties and anisotropy in the build material [12, 13].

(c) **Need for post-processing**: AM-built components attract the use of post-processing treatments to bring the properties and quality as per the user requirements and standards. In the case of surface finish and dimensional accuracy, AM-built components are inferior to conventionally built components due to layer-wise build, presence of partially melted powders, surface texture due to scan pattern, etc. These can be reduced by using treatments like—conventional machining, polishing, sanding, sandblasting, etc. Further, post-processing techniques like shot peening, heat treatment, etc., are necessary for improving the properties of the built components. The post-processing stage in AM is both a resource and time-consuming stage [4].

(d) **Limited component size/small build volume**: The limited machine size is one of the major limitations of AM, which prevents the use of the technology for building significant size engineering components generally used in aerospace and power sectors. Thus, researchers are attempting to understand the welding behavior of AM-built components to check the feasibility of joining parts built by AM to develop large components.

## 4 Evolution and Future Projections of AM

The first commercial AM process emerged in the year 1987 with the stereolithography process developed by Charles Hull. The process was commercialized by 3D Systems. In 1991, Stratasys developed the fused deposition modeling (FDM) technique, and Helisys developed the laminated object manufacturing (LOM) process. In 1992, DTM Corp. introduced the selective laser-sintering (SLS) process. In the year 1993, Soligen brought direct shell production casting (DSPC), which uses the inkjet mechanism. Germany-based EOS GmbH commercialized EOSINT using laser-sintering technology in the year 1994. In 1995, direct metal laser-sintering (DMLS) system was launched by the EOS for building metallic toolings for injection molding applications. In 1998, laser-engineered net shaping (LENS) was brought to market by Optomec, and in April 1999, the Extrude Hone additive manufacturing business (presently ExOne) introduced ProMetal RTS-300, a MAM system based on inkjet-printing technology. In 1999, Fockele & Schwarze introduced its selective laser melting system. In 2000, the world's first multi-color additive manufacturing system was introduced by Z Corp. Andersson and Larsson patented and licensed electron beam melting (EBM) based AM in the year 2000. In 2002, the first commercial EBM system was introduced by Arcam. In 2015, continuous liquid interface production (CLIP) technology was developed by Carbon 3D to generate smooth-sided solid objects using a photopolymer solution and UV radiation [14].

Figure 3 presents the evolution of AM in the last three decades and the future projections for the following two decades. AM technology started as the process for faster conversion of 3D model data to physical prototypes for a quick decision on product feasibility, and it was widely known as rapid prototyping (RP). Subsequently, the technology was extended to the fabrication of patterns for mold development in which the pattern is burned out later to fill the mold with molten material. The technique was popular with the name rapid casting. Besides the above, RP is used to build fixtures, and toolings for formative techniques, like injection molding, and the process is named "rapid tooling." After this stage, MAM processes started contributing to the automotive, aerospace, and medical industries in the late 1990s and early 2000s. In addition, polymer-based materials were also deployed for biomedical applications in the mid-2000s.

AM also started developing in micro and nano-manufacturing, and during the last decade, a lot of progress in various sectors such as fashion, jewelry, medical, aerospace, automotive, food, constructions, etc., were observed. AM is noticeably venturing in two major sectors: aerospace and biomedical, where quantity is very limited in numbers. The typical examples are the fabrication of satellite parts and customized prosthetics. It is forecasted that by the early 2030s, human body organs could be printed directly using AM techniques [15].

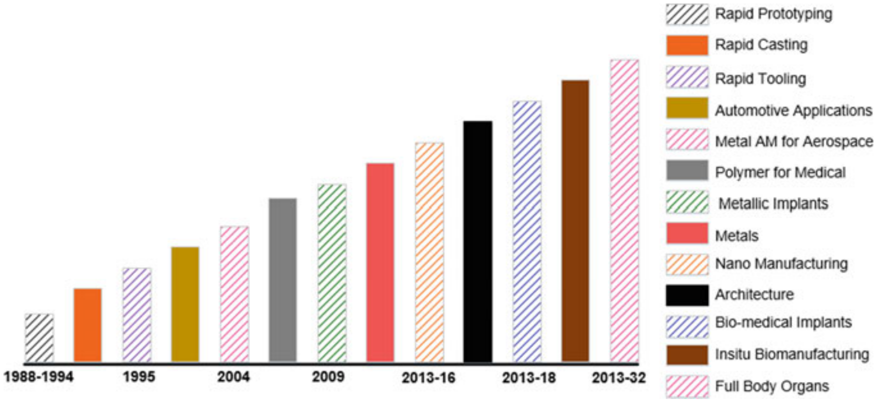

**Fig. 3** AM evolution and future projections

## 5 AM Processes

AM was classified by several research groups from the early days of inception based on materials (solid, liquid or powder) and energy sources (laser, electron, jetting, etc.). ISO/ASTM 52,900 classified additive manufacturing into seven different classes as explained below:

(a) **Vat photopolymerization (VP)**: VP is defined as "*An additive manufacturing process in which liquid photopolymer in a vat is selectively cured by light-activated polymerization*" [2]. In the process, the curing of a liquid resin (photosensitive) is carried out using a light source, usually in the ultraviolet range. The process starts by spreading a layer of liquid resin on the build platform. The light source follows the path obtained for each layer from the sliced 3D model and cures the liquid resin. The depth of curing should be in such a way that there is good adherence of solidified part with the build platform. With the first layer deposited, the build platform moves down by a value equal to the layer thickness, and new layer of liquid resin is spread over the previous layer. The light source scans the liquid resin as per the drawing of the second layer. Thus, the material added for the second layer is completed. These steps are repetitive till the final 3D component is built [16]. The main advantages of the VP process are high accuracy, simplicity, ability to process multi-materials, etc. The main limitations are slower fabrication rate, need for post-curing, and material limitations. The major applications include medical applications for surgical planning, tooling applications, and micro-fluidics.

(b) **Material Jetting (MJ)**: MJ is defined as **"** *An additive manufacturing process in which droplets of feedstock material are selectively deposited*" [2]. Similar to other AM processes, MJ starts with 3D model data, and it is sliced into several layers along the build direction. During the process, photopolymer droplets are deposited using a deposited head at locations where material addition is required on a particular layer (XY plane). Based on the requirement, the deposition head can have a single nozzle or multiple nozzles. Subsequent to material deposition, a UV light source is used for the polymerization reaction. This is followed by the downward movement of the build platform at a distance equal to layer thickness. The process is repeated till the final component is built [17]. Sacrificial support structures are also deposited for building overhang geometries. The advantages of MJ techniques are high accuracy, ability to build multi-material components, and the removable nature of supports. The limitations of MJ techniques include poor mechanical properties, the slow nature of the process, material limitations, and the high cost of materials and machines. The major applications of MJ are in the medical, automotive, jewelry, electronics and medical sectors.

(c) **Material Extrusion (ME)**: ME is defined as "*An additive manufacturing process in which material is selectively dispensed through a nozzle or orifice*" [2]. ME is the most commonly used AM process globally. In this process, feedstock material in wire form, generally called filaments, is fed to a hot end extruder, which heats the material to a semi-molten state. Further, the material passes through the outlet of a nozzle and gets extruded. The material after extrusion gets cooled rapidly. The temperature used for heating the material is generally fixed based on the material. The extrusion head deposits the material in the XY plane as per the geometry in a single layer. After the deposition of a layer, the next layer is deposited on top of the previous layer by either moving the platform down or moving the nozzle head up [3]. The layer thickness is adjusted by precisely maintaining the gap between the nozzle and the previously deposited layer. The advantages of ME process include low cost, simplicity, lack of material wastage, easy material storage, possibilities to use new materials, easy support removal, accessibility, etc. The limitations of ME include low surface finish and accuracy, low build rate, need for support structures, and anisotropy in mechanical properties. The applications of ME process are generally seen in prototyping, concept modeling, aerospace, tooling, medical, automotive, and education.

(d) **Binder Jetting (BJ)**: BJ is defined as " *An additive manufacturing process in which a liquid bonding agent is selectively deposited to join powder materials*" [2]. The process uses powder as the raw material, and the powder is spread on the build platform using a powder spreader. A print head carrying the binder selectively deposits binder at regions in a particular layer, where the bond is required as per the tool path generated from the input 3D model [18]. Thus, a 2D pattern is obtained in a single layer. Further, the binder is dried to avoid its diffusion to other regions of the powder bed. Once the layer is solidified, the next layer of powder is spread on top of the previous layer, and process continues till the final part is built, which is generally known as the "green part." The built part requires curing operation for densification if the part has to be used for engineering applications. If metallic/ ceramic powders are used as feed material, green parts are cured and sintered in a furnace for burning of binder and joining the powder particles together. The process of burning the binder is called debinding [19]. The advantages of BJ are no need for support structures, no need for high energy sources, ability to build support structures, high build rate (if multiple nozzles are used), use of a variety of powders, etc. The limitations of BJ include low strength, need for post-processing, shrinkage due to debinding, etc. The typical applications of BJ are the development of colored prototypes, metallic components, tooling, etc.

(e) **Sheet Lamination (SL)**: SL is defined as "*An additive manufacturing process in which sheets of material are bonded to form a part*" [2]. During the process, an adhesive-backed sheet of a particular layer thickness is placed on the surface of a build plate. Further, a heated roller is moved over the sheet to melt the adhesive and bond the sheet with the build plate. Once bonding is achieved, the $CO_2$ laser is used to cut the sheet as per the required geometry up to a depth equal to the layer thickness. Unused materials are diced into cubes, and they act as support material. Once a layer is built, the platform with the built layer moves down, and a new layer of material is placed by advancing the sheet. The process continues till the final part is built. Once the build is completed, wood carving tools are used to remove the unused excess material [3]. The process is also used to build metallic components by using metallic sheets as the feedstock material. In the case of the metallic SL process, the sheet materials are joined by using ultrasonic welding, and shaping is carried out by a CNC machining operation. This process is commonly known as ultrasonic consolidation [20]. The advantages of the SL process include the following: no thermal stress, ability to build integrated components, capacity to build colored and multi-material parts, no need for support structures, and low cost. The limitations of the process include dependency of resolution on the sheet thickness, material wastage, and difficulty in removing materials trapped inside cavities. The typical applications of the process have the development of sensor integrated components, prototyping, etc.

(f) **Powder Bed Fusion (PBF)**: PBF is defined as "*An additive manufacturing process in which thermal energy selectively fuses regions of a powder bed*" [2]. In PBF, a thin layer of powder (metal or polymer) is laid as a bed on the top surface of the build plate, and focused thermal energy (laser or electron beam) is used to selectively melt or sinter the layer of a powder bed as per required geometry. A number of layers built one over the other generates the required 3D component as per the design [21]. The process can be primarily classified into laser PBF and electron beam-based PBF based on the energy source used for consolidation. The advantages of PBF systems are the ability to build components with high complexity and minor features, higher mechanical strength, better dimensional accuracy than other MAM processes, etc. The limitations of PBF include limited multi-material capability, chances of porosity, low build rate, high thermal stress, and low build volume. The applications of PBF include the fabrication of complex components for various sectors, like aerospace, medical, automotive, tooling, power sectors, etc.

(g) **Directed Energy Deposition (DED)**: DED is defined as *"An additive manufacturing process in which focused thermal energy is used to fuse materials by melting as they are being deposited*" [2]. DED process can be primarily of two types: powder fed deposition (PFD) or wire fed deposition (WFD). The process uses thermal energy sources, like -laser, electron beam, or arc, to create a melt-pool on the surface of a substrate. Once the melt-pool is completed, the feedstock material (powder or wire) will be fed into the melt-pool for deposition. The movement of the deposition head or work station as per the trajectory provides the deposition in a single layer. Subsequently, the deposition head moves up, and the next layer is deposited on the surface of the previously deposited layer. Thus, a 3D component is built as per the requirement [4]. The significant advantages of the DED process are high build rate, capability to build multi-material components, high density, large size components, easy material change, etc. The limitations of DED are low dimensional accuracy, relatively limited shape design freedom as compared to PBF, thermal distortions, etc. The applications of DED are the fabrication of near-net-shaped components, feature addition, repairing and remanufacturing, cladding, etc.

## 6 Additive Manufacturing and Industry 4.0

Industry 4.0 is a blend of cyber and physical systems [22] to form smart factories, and the physical part of the factories will be insufficient with the capacities of the conventional manufacturing techniques. This attracts AM as one of the significant elements of Industry 4.0. Industry 4.0 allows for quicker manufacturing and improved customization by using digital production techniques. It attempts for "mass customization," which can only be possible through advanced manufacturing techniques, like AM. The combination of Industry 4.0 and AM allows for the development of first-to-market, completely customized, and dynamic components. AM enables the combining of two extremes of manufacturing, i.e., mass production and customization. It also permits "just in time manufacturing" and "onsite manufacturing" of components in industries. AM allows industries to assemble and understand data/ information across several machines, which permits fast, flexible and efficient processes to build features at higher quality and low cost [1]. AM also enables sharing the of manufacturing capabilities among different industries for the finest use of resources. The technology also allows the development of components at remote locations, which permits product distribution. AM also reduces material wastage by adding materials at specified locations as per the digital model data. AM is also a seamless tool for satisfying the increasing customer requirements and for building more competent components. As discussed earlier, AM can help the customers by responding swiftly to customer requirements for customization as it requires only editing in the digital model used for AM. The technology also allows to decrease the transportation distances and costs and reduces inventory management by storing 3D models instead of physical parts. Thus, AM is an important part of the next movement in industries called Industry 4.0 and is changing continuously as an essential digital manufacturing technique in the period of smart manufacturing.

## 7 Additive Manufacturing at RRCAT

Realizing the significance of AM and allied technologies, comprehensive research, and development program in laser additive manufacturing (LAM) was initiated at Raja Ramanna Center for Advanced Technology (RRCAT), India, in the year 2003. A number of components for engineering and prosthetic applications are manufactured using the LAM system integrated at the RRCAT's LAM Laboratory. RRCAT has two indigenously developed LAM systems in laser PBF (LPBF) and laser DED (LDED) categories. Figure 4a presents the LDED system integrated with a five-axis workstation for job manipulation. The five axes of the LDED system are X, Y, Z, V and W. The effective stroke length of the X, Y, and Z axis is 250 mm. The angular tilt of the V axis is ± 110°, while the W axis can have a 360° continuous rotation. The manipulator is interfaced with a standard CNC for workstation manipulation.

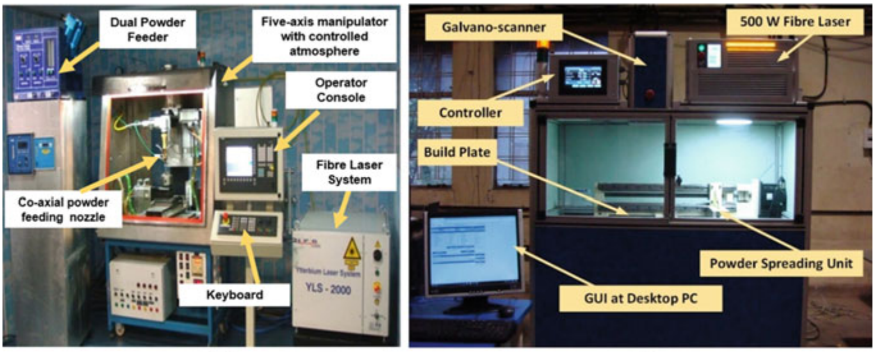

(a) (b)

**Fig. 4** LAM systems developed at RRCAT: **a** PFD-based LAM-DED with processing volume of 250 × 250 × 250 mm$^3$, **b** LAM-PBF with build volume 250 mm × 250 mm × 250 mm

The glove box is essentially required for maintaining controlled atmospheric conditions during processing. Oxygen and moisture analyzers are also integrated with the system. High purity grade argon gas is used for attaining the desired purity levels [4]. Figure 4b presents the LPBF system using a 500 W fiber laser, Galvano-scanner, powder spreading mechanism, built-plate, and hopper plate to cater to the fabrication need of complex geometries. A solid model of the engineering component to be built is made using computer-aided-design software. The model is sliced into thin layers at various sections along the vertical axis, and each slice is converted into the corresponding file in.dxf format, and these files are transferred to the desktop computer attached with the system. Mitsubishi's programmable logic controller (PLC) and servo-package are used along with a 7–inch HMI for data entry to PLC. Fiber laser, galvano-scanner, and servo-package are connected with PLC. The system is capable of fabricating components having a size within 250 mm × 250 mm × 250 mm and builds it with the slice-layer thickness of 25 microns or more.

Figure 5 presents the recent applications of LAM at RRCAT. Figure 5 (a) illustrates a porous structure fabricated by LAM using titanium as the raw material for potential biomedical applications. Figure 5b illustrates the deposition of Tribology-700 on valve spools for direction control applications of high-pressure, high flow hydraulic fluid using newly designed vertical LAM head to improve the helpful life of valve spools [4]. Figure 5c presents the stainless steel-titanium (SS-Ti) transition joint for joining chemical reactor vessels with transfer lines yielding economic advantage. It is developed by introducing friendly materials between the two incompatible materials at the identified process parameter combination. Figure 5d presents Dolero-50 bushes fabricated for transfer arm gripper subassembly of safety devices, which require materials with galling resistance, like Colmonoy-6, Deloro-50, etc. [4]. Figure 5e presents the fabrication of low-cost tools using LAM. The LAMed cutting tool is observed to have 80% performance as compared to conventional means. Figure 5f presents the honeycomb shape orifice grid plate for pressure drop devices intended for appropriate flow distribution in significant heat generation sources [4]. Figure 5g presents a bi-metallic wall fabricated with Stellite-21on on one side and AISI type 316L stainless steel on the other side. Figure 5h illustrates LAM fabricated die with the conformal cooling channel for uniform temperature distribution. These cooling channels find huge applications in the tooling sector. Figure 5i presents the prototype hip implant fabricated using LAM for bio-medical applications. It started with the making of a solid model with stem length 125 mm and proximal widths at mediolateral and anterior–posterior planes of 19 and 29 mm, respectively. The tool paths are generated using CAD/CAM software UG NX 6.0, modified into customized G&M code and transferred to the CNC controller of LAM system [4].

**Fig. 5** Recent applications of LAM at RRCAT

## 8 Summary and Future Scope

The industries are pushed to move from customer satisfaction to customer delight by providing product value addition. One of the techniques that considerably influences the product value addition is AM. AM converts an abstract idea to a tangible component by using a three-step process called pre-processing, processing, and post-processing. AM brings a major disruption in industrial manufacturing by changing the product flow path from design to component. The various freedoms offered by AM are shape design freedom, material design freedom, logistics freedom, and post-processing freedom. The various limitations of AM are high production cost, inferior mechanical properties, the requirement for post-processing, and limited component size. In the industrial scenario, AM reduced the number of steps in the product development cycle by eradicating some of the stages either fully or partially. The seven AM processes as per ISO/ASTM 52,900 are vat photopolymerization, material jetting, material extrusion, binder jetting, sheet lamination, powder bed fusion, and directed energy deposition. Further, AM is an essential part of the next movement in industries called Industry 4.0 and is changing continuously as a crucial digital manufacturing technique in the period of smart manufacturing.

The manufacturing of complex engineering components in a swift manner with low cost is one of the visions of developing industries. This is significant in the present industrial scenario because the industries are pushed to build high-performance components with a faster delivery period. The various research areas that are being explored/ have to be explored globally for the further growth of AM are presented in Table 1.

The present status of AM is the beginning of a new voyage toward Industry 4.0, and many more unanswered curiosity and technological challenges are ahead to be explored. The efforts are promising for a better future by investigating science and deploying innovative technology with sustained academia-industry collaborations.

**Table 1** R&D opportunities in the area of additive manufacturing

| S. no | Research opportunities in AM | Description |
|---|---|---|
| 1 | Machine/software development | • Machine and software development is costly<br>• Indigenous development of machines and software are necessary |
| 2 | Process development and control | • Limited to certain materials and more materials should be explored<br>• More repeatability is required |
| 3 | Material/feedstock development | • Presently, industries are using standard materials available in market<br>• Need to produce application-specific alloys and materials for AM |

(continued)

**Table 1** (continued)

| S. no | Research opportunities in AM | Description |
|---|---|---|
| 4 | Design for AM | • AM is now considered as a technology that can replace conventional manufacturing<br>• The advantage of AM should be used to the fullest by modifying designs for AM |
| 5 | Modeling and simulation | • Several analytical and numerical models are available for AM. However, analytical models are suitable for simple geometries, and numerical models take a long time to obtain results<br>• Need to develop modeling tools for better understanding of AM process |
| 6 | Characterization and testing | • More advanced characterization tools should be used<br>• Testing should be done at simulated conditions for qualification |
| 7 | Quality control and assurance | • Need for design codes and standard operating procedures |
| 8 | Application development | • Qualify AM components for applications<br>• AM should enter into new domains<br>• Capability should be demonstrated for new domains |
| 9 | Education and training | • Curriculum development<br>• Training for industrialists and academicians<br>• More undergraduate and postgraduate courses |

**Acknowledgements** The authors express their sincere gratitude to Mr. Debashis Das, Director RRCAT, for his constant support and encouragement. Thanks to Mr. S. V. Nakhe, Director—Laser Group, and Dr. K. S. Bindra, Associate Director—Laser Group, for constant encouragement in this evolving program at RRCAT. The authors are also thankful to our collaborators and colleagues at Laser Additive Manufacturing Laboratory for their support. A N Jinoop acknowledges the financial support of RRCAT, Department of Atomic Energy, Government of India, and HBNI, Mumbai.

## References

1. C.P. Paul, A.N. Jinoop, S.K. Nayak, A.C. Paul, Laser additive manufacturing in industry 4.0: Overview, applications, and scenario in developing economies, in *Additive Manufacturing Applications for Metals and Composites*, ed. K.R. Balasubramanian, V. Senthilkumar (IGI Global, Hershey, PA, 2020), pp. 271–295
2. International Organization for Standardization—American Society for Testing and Materials International, ISO/ASTM 52900:2015(en) Additive manufacturing—General principles—Terminology (2015)
3. I. Gibson, D.W. Rosen, B. Stucker, in *Additive Manufacturing Technologies 3D Printing, Rapid Prototyping, and Direct Digital Manufacturing* (Second). (Springer, New York, NY, 2015). Retrieved from http://lib.ugent.be/catalog/ebk01:2670000000006827

4. C.P. Paul, A.N. Jinoop, K.S. Bindra, Metal Additive Manufacturing using Lasers, in *Additive Manufacturing Applications and Innovations (First*. ed. by R. Singh, J.P. Davium (CRC Press, Boca Raton, 2018), pp.37–94
5. A.J. Pinkerton, [INVITED] Lasers in additive manufacturing. Optics & Laser Tech. **78**, 25–32 (2016). https://doi.org/10.1016/j.optlastec.2015.09.025
6. S. Yadav, A.N. Jinoop, N. Sinha, C.P. Paul, K.S. Bindra, Parametric investigation and characterization of laser directed energy deposited copper-nickel graded layers. Int. J. Adv. Manuf. Tech. **108**(11), 3779–3791 (2020). https://doi.org/10.1007/s00170-020-05644-9
7. L.D. Bobbio, B. Bocklund, R. Otis, J.P. Borgonia, R.P. Dillon, A. Shapiro, et al., Characterization of a functionally graded material of Ti-6Al-4V to 304L stainless steel with an intermediate V section. J. Alloys Comp. **742**, 1031–1036 (2018). https://doi.org/10.1016/j.jallcom.2018.01.156
8. C.P. Paul, *Parametric Studies of Laser Metal Deposition for Fabrication Engineer-ing Components* (Devi Ahilya Vishwavidyalaya, Indore, India, 2005)
9. R. Liu, Z. Wang, T. Sparks, F. Liou, J. Newkirk, 13–Aerospace applications of laser additive manufacturing, in *Woodhead Publishing Series in Electronic and Optical Materials*, ed. M.B.T.-L.A.M. Brandt (Woodhead Publishing, 2017), pp. 351–371. https://doi.org/10.1016/B978-0-08-100433-3.00013-0
10. S.K. Malyala, Y. Ravi Kumar, L. Kankanala, P. Vasamsetty, A. Alwala, Assessment and treatment planning in maxillofacial surgery by using additive manufacturing technology. Mat. Today: Proc. **5**(2, Part 1), 4162–4166 (2018). https://doi.org/10.1016/j.matpr.2017.11.678
11. M. Binder, L. Kirchbichler, C. Seidel, C. Anstaett, G. Schlick, G. Reinhart, Design concepts for the integration of electronic components into metal laser-based powder bed fusion parts. Procedia CIRP **81**, 992–997 (2019). https://doi.org/10.1016/j.procir.2019.03.240
12. B.E. Carroll, T.A. Palmer, A.M. Beese, Anisotropic tensile behavior of Ti–6Al–4V components fabricated with directed energy deposition additive manufacturing. Acta Mat. **87**, 309–320 (2015). https://doi.org/10.1016/j.actamat.2014.12.054
13. N.S. Hmeidat, R.C. Pack, S.J. Talley, R.B. Moore, B.G. Compton, Mechanical anisotropy in polymer composites produced by material extrusion additive manufacturing. Additive Manuf. **34**, 101385 (2020). https://doi.org/10.1016/j.addma.2020.101385
14. T. Wohlers, T. Gornet, Wohlers Report 2016 (2016)
15. Royal Academy of Engineering, Additive manufacturing: opportunities and constraints (2013)
16. N.A. Chartrain, C.B. Williams, A.R. Whittington, A review on fabricating tissue scaffolds using vat photopolymerization. Acta Biomat. **74**, 90–111 (2018). https://doi.org/10.1016/j.actbio.2018.05.010
17. P. Gay, D. Blanco, F. Pelayo, A. Noriega, P. Fernández, Analysis of factors influencing the mechanical properties of flat PolyJet manufactured parts **132**, 70–77 (2015). https://doi.org/10.1016/j.proeng.2015.12.481
18. I. Rishmawi, M. Salarian, M. Vlasea, Tailoring green and sintered density of pure iron parts using binder jetting additive manufacturing. Additive Manuf. 24, 508–520 (2018). https://doi.org/10.1016/j.addma.2018.10.015
19. C.L. Cramer, P. Nandwana, J. Yan, S.F. Evans, A.M. Elliott, C. Chinnasamy, M.P. Paranthaman, Binder jet additive manufacturing method to fabricate near net shape crack-free highly dense Fe-6.5 wt.% Si soft magnets. Heliyon **5**(11), e02804 (2019). https://doi.org/10.1016/j.heliyon.2019.e02804
20. A. Bournias-Varotsis, R.J. Friel, R.A. Harris, D.S. Engstrøm, Ultrasonic additive manufacturing as a form-then-bond process for embedding electronic circuitry into a metal matrix. J. Manuf. Proc. **32**, 664–675 (2018). https://doi.org/10.1016/j.jmapro.2018.03.027
21. S.K. Nayak, S.K. Mishra, C.P. Paul, A.N. Jinoop, K.S. Bindra, Effect of energy density on laser powder bed fusion built single tracks and thin wall structures with 100 μm preplaced powder layer thickness. Optics & Laser Tech. **125**, 106016 (2020). https://doi.org/10.1016/j.optlastec.2019.106016
22. P.J. Mosterman, J. Zander, Industry 4.0 as a cyber-physical system study. Software & Systems Model. **15**(1), 17–29 (2016). https://doi.org/10.1007/s10270-015-0493-x

# Multiscale Modeling in Arc Welding Using Secondary Thermal Cycle

**Deepu Mathew John and Gandham Phanikumar**

## 1 Introduction

Welding and joining are processes that involve various aspects of metallurgy. An integrated approach is necessary to ensure weldability and final strength and ductility of the weldments. This is particularly important for heat treatable alloys where the microstructure is carefully engineered after thermo-mechanical treatment. Trial-and-error approach to determine optimal process parameters for weldability of special alloys will lead to significant cost and time.

Integrated Computational Materials Engineering (ICME) approach is emerging as a widely accepted means to reduce the cycle time for the development of new engineered products. In this approach, multiscale modeling is an important aspect which can help in bridging the length scales and providing insights into the structure–property correlations. The concept of multiscale modeling deals with the integration of simulations or models at different length scales, which is also known as the vertical integration in the ICME approach [1]. The original definition of ICME does not prescribe how exactly the integration of models or simulations at different length scales can be performed [2]. These details are important as the time taken for the simulation at each length scale is large and the data transferability between the length scales is not obvious [3].

Several attempts have been made by industry and academia to use multiscale modeling aspect of ICME approach to accelerate materials development and manufacturing [4–6]. QuesTek® Innovations LLC has used ICME approach for the fast development of materials for landing gears and high-performance materials for gas

---

D. M. John · G. Phanikumar (✉)
Department of Metallurgical and Materials Engineering, Indian Institute of Technology Madras, Chennai, India
e-mail: gphani@iitm.ac.in

D. M. John
e-mail: mm14d207@smail.iitm.ac.in

A. Shrivastava et al. (eds.), *New Horizons in Metallurgy, Materials and Manufacturing*,
Indian Institute of Metals Series, https://doi.org/10.1007/978-981-19-5570-9_4

turbines [7]. Motaman et al. [8] attempted an ICME approach in additive manufacturing for design optimization. In their work, a process–structure–properties–performance (PSPP) chain for metal additive manufacturing (AM) was implemented using multiscale modeling. Calculation of Phase Diagrams (CALPHAD) approach and Density Functional Theory (DFT) were used for the alloy design. Phase field simulation (PFS) with Micress® software [9] was used to study the evolution of microstructure during AM process. Crystal plasticity simulations could take orientation of phases while evaluating overall properties of the material. Finite element simulation was used to simulate AM process at the macroscale. Savic et al. [10] developed an ICME-based multiscale model for transformation-induced plasticity (TRIP) steels. The properties obtained via crystal plasticity were used for macroscale FEM simulations of forming process. Ridgeway et al. [11] implemented a multiscale modeling approach by combining cellular automaton and finite element method (FEM) to predict the mechanical properties of aluminum casting based on location-specific microstructure.

Application of physics-based simulations as part of multiscale modeling introduces challenges at the mesoscale such as microstructure to be integrated with the macroscale simulation. Simulation of microstructure in steel requires handling multiple phase transformations such as the transformation of austenite ($\gamma$) to ferrite ($\alpha$), martensite as well as bainite. The simultaneous nature of these transformations renders the simulation a complex process. Multiscale modeling can integrate structural features at the mesoscale with the macroscale simulation using finite element (FE) methods. Commercial FE tools currently available use many assumptions and simplifications based on semiempirical models to assess the microstructure and the resultant mechanical properties. Often, rule of mixtures is used to average the properties. Rahul and Phanikumar [12] proposed a pragmatic workflow for ICME using a case study of welding of titanium alloy with finite element method. They extracted thermal profiles from calibrated simulation of welding process and used those for physical simulation in Gleeble 3800®. Use of techniques like PFS and virtual test in a multiscale framework can help in considering the effect of microstructure on the averaged properties used for macroscale FEM simulation.

## *1.1 Overview*

The following sections will review some of the developments in the areas of PFS- and FEM-based virtual test which are important components in a multiscale model. These simulations are applied to welding of steels to illustrate the emerging trends in this domain. With PFS, the evolution of microstructure during macroscale processes can be simulated, and with the help of virtual test, the macroscale effective properties can be estimated from the microstructure. Usually, a commercial welding software uses simplified models to estimate phase transformation effects to take stresses due to those for consideration. Typically, Leblond model [13] is used for diffusive transformations. Koistinen and Marburger model [14] is used for diffusionless transformations. The phase transformation strains are added to the thermal strains while performing the thermal–mechanical simulation of the weld.

However, an actual simulation of microstructure is useful in bringing out the morphological aspects and configuration of phases as part of the phase evolution. Such a simulation will also reduce empirical parameters for the phase transformation model. Phase field models rely on thermodynamic and kinetic parameters which are more fundamental and would allow for minor changes in the alloy composition to enable prediction of microstructure. This section reviews some of the works in PFS of microstructure evolution by focusing on the $\gamma \rightarrow \alpha$ and bainite transformation in steel. The range of cooling rates experienced by steels during welding necessitate that these two transformations are considered simultaneously.

## 1.2 Phase Field Simulation of Austenite to Ferrite Transformation

Phase field modeling has been used by several researchers to simulate the $\gamma \rightarrow \alpha$ transformation in steel. For the case of multi-component steel, carbon is a fast-diffusing species whereas the other alloying elements are slow diffusing. Hence, a redistribution criterion is needed. Para-equilibrium (PE) and local equilibrium negligible partitioning (LENP) are the two most popularly used redistribution criteria. In the case of para-equilibrium, it is assumed that only carbon diffuses at the microscale. Hence, for the calculation of transformation kinetics, the contribution of only the fast-diffusing elements is taken into consideration. In the case of LENP, it is considered that full diffusion with local equilibrium occurs at the atomic scale, whereas at the microscale, no partitioning occurs [15]. The α phase can exhibit vermicular, lacy, acicular or globular morphology. Vermicular and lacy morphologies are associated with delta ferrite that forms during solidification.

Several works have attempted the simulation of $\gamma \rightarrow \alpha$ transformation with in-house codes. Such studies could be traced back to 2001. Yeon et al. [16] developed a 1D phase field model for a ternary system. Their evolution equation was coupled with concentration equation to solve for the diffusion of species during phase transformation. Para-equilibrium (PE) condition was simulated for a Fe-Mn-C system, and local equilibrium (LE) condition was simulated for a Fe-Cr-Ni system. The study concludes that phase field modeling is a suitable technique to deal with systems containing substitutional and interstitial elements. In those systems, the interfacial mobility and the solute diffusivities determine the kinetics of transformation.

Other works in this aspect include a 1D phase field model for binary alloy developed by Bhattacharya et al. [17] which was used to simulate the formation of α in steels. Ginzburg–Landau equation was solved by coupling with concentration equation. A mixed mode of growth was considered. This work was later extended to simplified geometry shapes in 2D [18]. Several other attempts were made to address various issues in $\gamma \rightarrow \alpha$ transformation in steel. A recent attempt was made by Kohtake et al. [19] to study the growth stagnation of α during $\gamma \rightarrow \alpha$ transformation. Experimentally, the growth of α stagnates after some time, during the $\gamma \rightarrow \alpha$ transformation in multi-component steels. The stagnation in growth was attributed to the formation of a peak in the substitutional solute concentration at the boundary of $\gamma$ and $\alpha$ phases. Zhu et al. also developed a code for phase field modeling of cyclic phase transformation in low carbon steel [20, 21]. LENP criteria were used for simulation of elemental redistribution.

A major development in the domain of PFS for $\gamma \rightarrow \alpha$ transformation was accomplished after the launch of Micress® software. With the help of this software, overall phase transformation kinetics could be simulated and experimentally validated. Micress® software uses the multi-phase field approach [22, 23] for performing PFS. Micress® has the capability to communicate with Thermo-Calc® database using TQ® interface for obtaining the thermodynamic and diffusion data needed for PFS. This allows for realistic simulations for technical alloys. The multiphase-field equation solved by Micress® is as follows:

$$\frac{\partial \Phi_\alpha}{\partial t} = \sum_{\beta=1,\ldots,N} \mu_{\alpha\beta} \left\{ \begin{array}{l} \sigma_{\alpha\beta}\left[\Phi_\beta \nabla^2 \Phi_\alpha - \Phi_\alpha \nabla^2 \Phi_\beta + \dfrac{\pi^2}{2\eta^2}\left(\Phi_\alpha - \Phi_\beta\right)\right] \\ +\dfrac{\pi}{\eta}\sqrt{\Phi_\alpha \Phi_\beta} \end{array} \right\} \tag{1}$$

where $\mu_{\alpha\beta}$ is the interfacial mobility, $\sigma_{\alpha\beta}$ is the interfacial energy, $\eta$ represents the interfacial thickness, $\Phi_\alpha$ is the order parameter for α phase and similarly for other phases. Micress® has OpenMP® parallelization inbuilt, and it uses a modified finite difference method that requires lesser number of finite difference grids at the interface to obtain a good accuracy for the PFS. In 2001, Pariser et al. [24] used Micress® software to simulate the overall transformation kinetics of $\gamma \rightarrow \alpha$ transformation during continuous cooling in ultra-low-carbon (ULC) and interstitial-free (IF) steels. 2D PFS studies of $\gamma \rightarrow \alpha$ transformation were performed with Micress® software. Only the three major components (Fe–C-Mn) were considered while performing the PFS. Linearized phase diagram obtained from Thermo-Calc® was used for obtaining the thermodynamic data while the diffusion data was taken from the literature. Similar 2D calculations were performed by Meccozzi et al. [25]. In their work, an attempt was made to simulate the $\gamma \rightarrow \alpha$ transformation during continuous cooling in Nb micro-alloyed Fe–C-Mn ternary alloy steel. The effect of NbC precipitates on kinetics was incorporated into the simulation by adjusting the phase field interfacial mobility to calibrate against the experimental phase evolution kinetics. Mobility was assumed to be temperature-dependent according to Eq. 2, where $Q = 140\ \mathrm{kJmol}^{-1}$ is the activation energy. The kinetics can be calibrated using the pre-exponential factor here. In this work, the interfacial mobility increases with increase in austenitization temperature. Mecozzi et al. extended this work later [26] and observed that the nature of phase transformation is influenced by NbC precipitates.

$$\mu_{(\alpha\gamma)}(T) = \mu^{0}_{(\alpha\gamma)} exp\left(\frac{-Q}{RT}\right) \tag{2}$$

The first attempt to simulate the transformation of $\gamma \rightarrow \alpha$ in 3D with Micress® software was by Militzer et al. [27]. In this work, the $\gamma \rightarrow \alpha$ transformation was simulated in both 2D and 3D by considering a ternary Fe-C-Mn steel. Comparisons were made between 2D simulation and 2D cuts from 3D simulations. A recent study on this topic was attempted by Farahani et al. [28]. 3D PFS were performed with Micress® software, and the microstructures were validated with the help of in-situ high-temperature 2D electron backscattered diffraction (EBSD). The overall phase transformation kinetics from EBSD were qualitatively similar to dilatometry.

For all the simulations of $\gamma \rightarrow \alpha$ transformation cited above, the globular morphology of α was considered for PFS. There were also several attempts to simulate the acicular morphology of α, with and without the consideration of stress fields. The first attempt in this direction was in 2003 by Loginova et al. [29]. Phase field method was applied to investigate the transition between diffusive and massive transformation in a binary Fe–C system. 1D PFS were performed for an interfacial thickness of 1 nm. Since the simulation was 1D, the authors were able to apply phase field method for a small interface thickness of 1 nm within reasonable computation time. Loginova et al. [30] further extended their phase field model to 2D and applied it to simulate colonies of acicular ferrite (Widmanstätten ferrite). For the simulations, the interfacial energy and interfacial thickness were considered anisotropic. The anisotropy was taken as a factor of amplitude that relates the minimum and the maximum interfacial energy.

A recent attempt was made by Bhattacharya et al. to simulate the formation of Widmanstätten ferrite in 2D using phase field modeling. Bhattacharya et al. [31] simulated the formation of Widmanstätten ferrite plates using a multiphase-field model. Their formulation was based on the grand chemical potential approach. Anisotropy in interfacial energy was considered for the simulation. The modeling of Widmanstätten ferrite can also be carried out by considering the stress fields in the microstructure during the phase transformations. In this type of approach, the phase field interfacial parameters will be a function of the stress fields in the microstructure. The first work in this aspect can be traced back to 2008. Yamanaka et al. [32] simulated the morphology of acicular α by combining PFS- and FEM-based homogenization theory. Their formulation for phase field model was similar to that of Loginova et al. [30], but the method of introducing anisotropy was different. Yamanaka et al. considered anisotropy to be dependent on strength. Finite element method based on mathematical homogenization theory was used to obtain the microscopic and macroscopic deformation behavior. The interfacial mobility was taken as dependent on strength. Kubendran Amos et al. [33] used a similar phase field formulation that combines chemical and elastic fields in a thermodynamically rigorous manner to simulate the growth of Widmanstätten ferrite plates. Zhang et al. [34] used the anisotropy of elastic effects to simulate the formation of Widmanstätten ferrite plates in 2D. The morphology and growth kinetics are influenced greatly by the elastic energy anisotropy. Song et al. [35] used a combination of multiphase-field method and nudged elastic band method to investigate the shape of critical nucleus. The results were compared with molecular dynamics simulation. The driving force for nucleation as indicated by undercooling determines the shape of the critical nucleus.

## *1.3 Simulation of Transformation of Austenite to Bainite*

Though there were earlier works on PFS of martensitic transformation in steel, those on bainite transformation works were not reported until 2010. This was perhaps because of the mechanism of bainite transformation being still open for discussion to be diffusional or displacive [36, 37]. There were several attempts to model the $\gamma$ to bainite transformation in steel using phase field modeling. Some of these works attempted to develop phase field models and used in-house codes for the simulations [38, 39]. These works tried to address the coupled diffusional and displacive mechanisms that act during bainite transformation. The displacive mechanism was modeled in a phenomenological manner. There were also several attempts to simulate the bainite formation with Micress® software [37, 40, 41]. There are often limitations in a phase field implementation that can readily account for the displacive mechanisms for bainite formation. Hence, in these works, it was assumed that only diffusional mechanism acts for the bainite formation. Bainite was considered as a α phase but with anisotropy in interfacial energy as well as interfacial mobility. Different anisotropy functions were used in different works, and the selection is mainly based on comparison of morphology of bainite with experimentally observed morphology.

Attempts were made to develop phase field model to simulate the bainite transformation with a single order parameter model. Arif and Qin [39, 42] developed a phase field model that considers both diffusive and displacive mechanisms in a coupled manner. A phenomenological (shape-based) displacive transformation theory was added to the classical phase field formulation to achieve the new phase field model. A single order parameter was used to model the bainite transformation with reduced computation time. With the help of a transformation matrix, multiple bainite sheaves were simulated. The developed phase field model was coupled with Cahn–Hilliard diffusion equation to solve for the carbon concentration field during the bainite growth.

Several studies have attempted the simulation of bainite formation with Micress® software. The first work in this aspect could be traced back to 2010. Mukherjee et al. [40] simulated the $\gamma \rightarrow \alpha$ and bainite transformation during gas metal arc welding (GMAW) in DP 600 sheets. The thermal cycles in the material during welding were simulated using macroscale welding simulation tool SimWeld® and the thermal cycles from these simulations were validated with experimental weld trials. For these thermal cycles, the phase transformation was simulated using Micress®. 2D simulations of transformation of $\gamma \rightarrow \alpha$ and bainite were carried out. Bainite phase was considered as ferrite phase with faceted anisotropy description. A similar work was performed by Ramazani et al. [41] using slightly different numerical parameters.

A constant value was used for interfacial mobility, whereas Mukherjee et al. [40] used a temperature-dependent interfacial mobility.

Cementite precipitation during bainite transformation was not considered in the phase field simulation studies mentioned above. Capturing the cementite precipitation requires a very small grid size in PFS and will be computationally expensive. There were attempts to simulate a single bainite sheaf formation with consideration of cementite precipitation also. In 2016, Düsing et al. [43] formulated a phase field model for the simulation of lower bainitic transformation. A coupled Cahn–Hilliard multiphase-field model was used. The concept of generalized stresses and microforce balance was introduced in this work to model the displacive mechanism in a phenomenological manner. The multiphase-field model was used to describe the bainitic ferrite evolution and the precipitation of carbide. The Cahn–Hilliard equation was used to simulate the carbon diffusion within the bainitic ferrite. The interfacial energy was considered anisotropic. The work was later extended to simulate both upper and lower bainite transformation [44].

Song et al. (2018) [45] attempted to simulate the formation of lower bainite with cementite precipitation in a 2 μm × 8 μm domain, with a refined grid spacing of 2 nm. Multi-phase field model implemented in the software Micress® was used to simulate the isothermal lower bainitic transformation. A faceted anisotropy model was used for interfacial energy (Eq. 3) and interfacial mobility (Eq. 4). The thermodynamic data was described with para-equilibrium linearized phase diagram from Thermo-Calc® software, and the diffusion data was fed manually. A fully diffusional mechanism was considered for the bainite formation. Periodic boundary condition was considered in all directions for the 2D simulations preformed. The simulations were compared with the experimental data, and a good agreement was obtained in terms of the morphology and phase fractions.

$$\sigma = \sigma_0 k_{st}^2 \left(k_{st}^2 cos\beta^2 + sin\beta^2\right)^{-1.5} \tag{3}$$

where $\sigma_0$ is the interfacial energy coefficient, $k_{st}$ is the static anisotropy coefficient of the facet, and $\beta$ is the misorientation between normal vector of interface and normal of nearest facet.

$$\mu = \mu_0 \left[ k_{\text{kin}} + (1 - k_{\text{kin}}) \cdot \tan\left(\frac{\kappa}{\tan\beta}\right) \cdot \frac{\tan\beta}{\kappa} \right] \tag{4}$$

where $\mu_0$ is the interfacial mobility coefficient,$k_{\text{kin}}$ is the kinetic anisotropy coefficient, and $\kappa$ is value that describes the degree of anisotropy. $\kappa$ varies between 0 and 1 where 1 indicates isotropic growth.

## 1.4 Simulation of Simultaneous Transformation to Ferrite and Bainite

The study of Toloui and Militzer [37] was the first to use the multi-phase field model implemented in Micress® to simulate the simultaneous formation of α and bainite. Diffusional bainite growth was assumed, and the formation of upper bainite was simulated in 2D. Crystalline faceted anisotropy model (Eqs. 5 and 6) was used to describe the anisotropy of bainite sheaf growth, whereas the α growth was considered as isotropic. A good agreement was obtained between the simulated and experimental bainite kinetics. There were several reviews [36, 46, 47] that cover some of the above works. Those on the use of phase field simulation for bainite transformation have not been reviewed so far in a comprehensive manner.

$$\sigma^{*} = \sigma_0^{*} k_{st}^2 \left(k_{st}^2 \cos^2\theta + \sin^2\theta\right)^{-1.5} \tag{5}$$

$$\mu = \mu^{\mathrm{eff}} \left( k_{\mathrm{kin}} + \frac{1 - k_{\mathrm{kin}}}{\kappa} \tan h\left(\frac{\kappa}{\tan\theta}\right) \tan\theta \right) \tag{6}$$

Deepu and Phanikumar [48] used Micress® software to simulate the simultaneous phase transformations, namely of $\gamma$ to bainite and α during cooling at heat-affected zone of DP980 GMA weld. Tetragonal anisotropy functions were used for simulating the bainite morphology. The final phase fractions and the kinetics of phase transformation of bainite simulated with phase field simulation agreed well with experiments. Figure 1 shows the microstructure simulated using phase field technique.

## 1.5 Other Thermodynamic-Kinetic Tools

Some of the other simulation tools that can be used for simulation of phase transformation in steel are DICTRA and JMatPro® [49]. DICTRA is a module in Thermo-Calc® software [50] that uses sharp interface approach for simulation of phase transformation. One-dimensional phase transformation simulation can be performed with DICTRA module. It uses the thermodynamic and mobility databases from Thermo-Calc® software for obtaining the thermodynamic and diffusion data needed for phase transformation simulation. JMatPro® is a software tool that can be used for different purposes like thermodynamic calculation, simulation of phase transformation and calculation of thermo-mechanical properties of a material. JMatPro® uses databases in the background that contain free energy functions. It uses the CALPHAD approach. For the simulation of phase transformation, JMatPro® uses the Johnson–Mehl–Avrami–Kolmogorov (JMAK) equation.

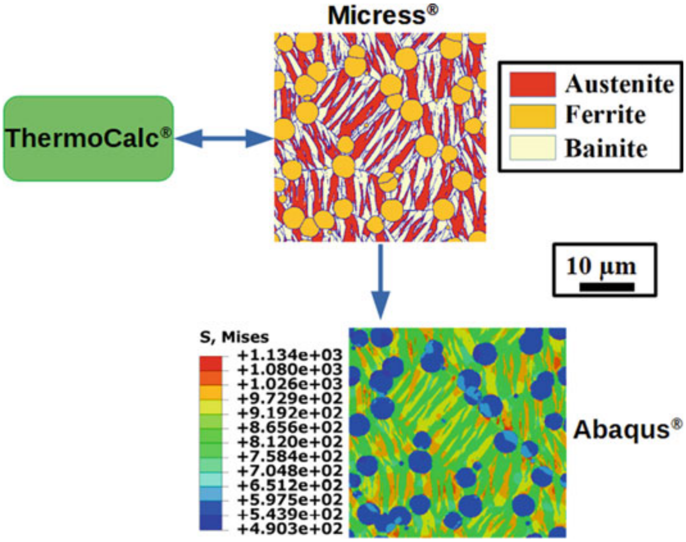

**Fig. 1** Phase field simulated microstructure for DP 980 steel, using Thermo-Calc coupling. The phase simulated microstructure was used for performing virtual test. The figure shows the stress distribution in the microstructure at 2% strain

## *1.6 Estimation of Microstructure-Dependent Effective Properties*

Several techniques can be used to estimate effective properties from the microstructure of the material. Several analytical techniques are available such as Voigt and Reuss bounds, self-consistent methods, Hashin and Shtrikman's bounds, and Mori–Tanaka method. These analytical techniques face the limitation that the morphology information of microstructure is not taken into account. Asymptotic homogenization is an efficient numerical technique for the calculation of averaged macroscale properties. These can take as input either representative experimental microstructures or those simulated using the phase field technique. Laschet [51] used asymptotic homogenization to derive the effective thermo-elastic properties from material microstructure. Based on these works, a tool HOMAT® was developed for evaluation of averaged properties taking configuration of phases in the microstructure into account. Laschet et al. [52] simulated microstructure of steels in three dimensions using phase field technique and performed homogenization for thermal and elastic properties. Laschet et al. [53] also used the representative volume element (RVE) to calculate the averaged mechanical properties of a pipeline steel as part of the simulation of the forming process. Effective flow curves from an RVE can also be used in a virtual test based on FEM. Ramazani et al. [54] calculated the effective macroscale flow curve of dual phase steels using FEM-based virtual test on different RVEs. They also proposed a correlation to relate the flow curves obtained using different virtual tests. Deepu et al. used asymptotic homogenization with HOMAT® and virtual test with FEM implemented in Abaqus® software to calculate the effective properties from PFS microstructure for DP980 steel. Figure 1 shows the distribution of stress during virtual test at 2% strain.

## 2 Case Studies

In this section, we take up two case studies, namely multi-pass welding of structural steel, using a trailing heat sink and welding of DP steel using a trailing heat source. These examples illustrate the importance of phase transformations during welding simulation. Figure 2 shows the schematic thermal profiles considered for these two examples.

### 2.1 *Multi-pass Welding of Steel Using Trailing Heat Sink*

Kala [55–58] has worked on the use of trailing heat sink to control the distortion in IS1020 steel with a composition close to S355J2G3, a DIN standard structural steel for which the material database is available with the commercial welding software used. Autogenous welds were used for the purpose of studying the effect of thermal profiles on distortion. Figure 3a shows a cylindrical tube being welded along the axial direction. The tube has been instrumented with thermocouples for thermal profile measurement. This data is used to calibrate the heat source models with the experiments. Figure 3b shows the distortion along the axial direction with and without a trailing heat sink. It is clear from the data that trailing heat sink reduced the distortion. The simulations consider the phase transformations into the model, and this has helped in bringing the simulation runs closer to the experimental values. Microstructure analysis of the welds showed that the final microstructure contained both bainite and martensite. Evolution of microstructure will thus affect the strains due to the

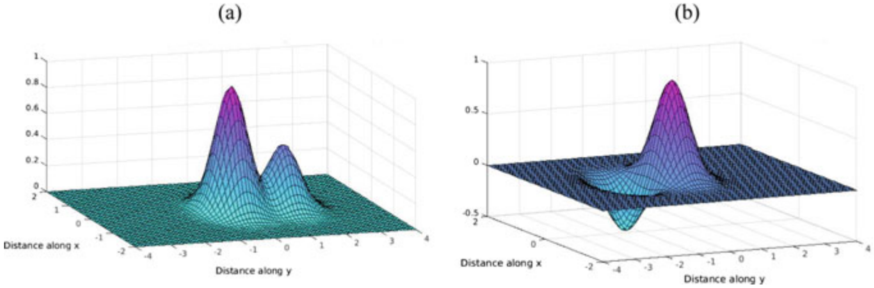

**Fig. 2** Superposition of two thermal profiles in the case studies being presented here: **a** trailing heat source and **b** trailing heat sink

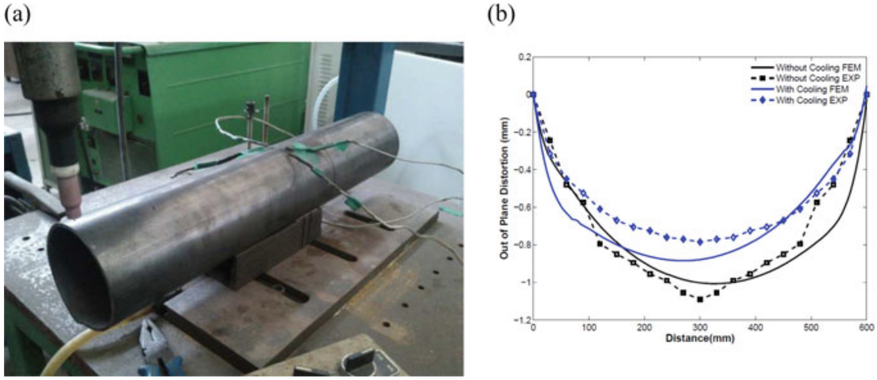

**Fig. 3** **a** Welding of cylindrical pipe with thermocouple measurements **b** Distortion along the axial direction of the pipe with and without cooling by a trailing heat sink [55]

phase transformation. These early studies showed that coupling the microstructure evolution models with welding simulations is important in understanding the evolution of residual stress and distortion. These studies also highlighted the possibilities of microstructure modification through superposition of thermal profiles during welding.

## *2.2 Multiscale Model for DP980 Steel GMA Welding*

Deepu and Phanikumar [48] attempted to implement a multiscale model for DP980 steel GMA welding. To address the weldability of newly developed alloys, an integrated two-stage workflow was proposed. Figure 4 shows the implemented multiscale model workflow. The thermal profile experienced by a location in the HAZ is used for validation with the simulation.

The same location is used for thermo-mechanical simulation during cooling and microstructure characterization as well. In the first stage of the workflow, prediction of phase fractions was performed using semiempirical models implemented in JMatPro® software. A scaling factor available in the software was used to calibrate one set of experimental data to adjust for the deviations. Effective macroscale properties were obtained using a linear rule of mixture. The mechanical properties of participating phases were obtained from the material models of the commercial software.

PFS runs are time-consuming and hence were included as a separate group of tasks in the workflow. These simulations use the thermal profile at a location in the HAZ of a DP980 steel GMAW. In addition to the asymptotic homogenization, to obtain the effective macroscale properties, a virtual test was also used. Thus, in stage 2, the estimation of effective properties takes the orientation information and morphology of DP 980 steel microstructure into account. The broken arrow connector in Fig. 4

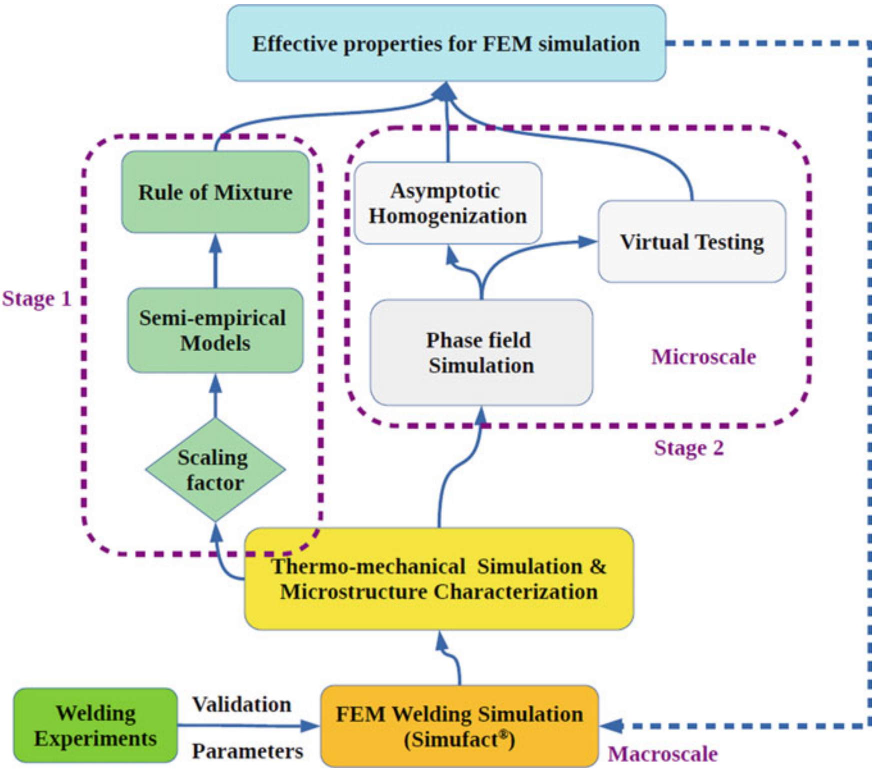

**Fig. 4** Multiscale modeling in an ICME framework implemented by Deepu and Phanikumar. The figure was adapted from Deepu et al. [48]

illustrates the workflow iteration that could eventually result in a comprehensive dataset for system-scale FEM simulation of the joining process by using different thermal profiles in the entire weld region as inputs. Where necessary, such a comprehensive dataset of homogenized properties can provide effective material properties and has the capability of including the role of process parameter-dependent evolution of microstructure.

## *2.3 Tandem Torch Welding for DP980 Steel*

A second heat source can be added to GMA welding for DP steel to decrease the cooling rate in the weld zones. This can affect the microstructure and thus affect the hardness variation across the weld. To study this, a tandem torch arrangement was used during GMA welding of DP980 steel sheet. For this purpose, a gas acetylene flame was attached to the trailing end of GMA weld torch. Figure 5 shows the welding

**Fig. 5** Tandem torch arrangement with gas acetylene flame at the trailing end of GMA welding torch

arrangement with the usage of tandem torch. Multiple thermocouples were used to measure the thermal profiles experienced by locations away from the center of the weld. The proportion of the gas mixture was selected to obtain sufficient heat at the trailing end to reduce the cooling rate of cooling after GMA welding. The flame was also adjusted so that the thermocouples were not melted during the welding process. Also, the peak temperature obtained from the gas acetylene flame was kept below the peak temperature obtained from the GMA weld torch. The objective of the trial was to reheat the melt pool to lower the cooling rate at the weld zones particularly in the HAZ. In this way, the gas acetylene flame acts as a second heat source.

Figure 6a shows the time–temperature profile obtained after tandem welding, compared to that of regular GMA welding. The label ‘$t1$’ is for a thermocouple placed 5 mm away from the weld center line. The label ‘$t2$’ is for the thermocouple fixed 10 mm away from the weld center line. Using the tandem torch welding, the cooling rate in the HAZ was decreased and this could in turn help in decreasing the hardness at the HAZ. Figure 6b compares the microhardness profiles across the weld between regular GMA weld and tandem torch enabled GMA weld. The hardness variation between the HAZ and remaining areas decreased during the tandem welding. The width of the HAZ also decreased during the tandem welding.

Such secondary thermal cycles are very relevant for DP steel. The reason for this is that DP steel is produced with carefully controlled heat treatments. The faster cooling rate introduced by welding processes often brings about a larger fraction of hard phase. Processes such as welding can thus modify the microstructure leading to gradients in local hardness that pose a problem during subsequent deformation processes. Introduction of secondary thermal source for DP steel welding effectively reduces the cooling rates. This increases the chances of α formation or martensite reduction in the weld HAZ which leads to decrease in hardness difference across the HAZ. This can be advantageous in further processing involving deformation of welded plates.

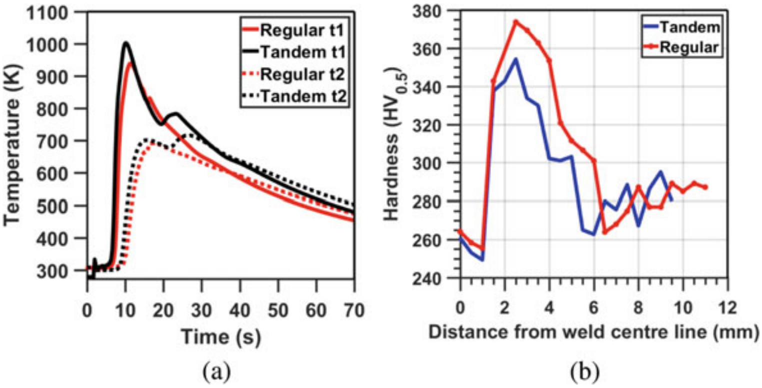

**Fig. 6** **a** Comparison of thermal profiles between tandem GMA welding and regular torch GMA welding. Thermocouples '*t*1' and '*t*2' are fixed 5 mm and 10 mm, respectively, away from the weld center line. **b** Comparison of microhardness profile between a regular GMAW and a tandem torch GMAW

## 3 Opportunities

The current implementation of secondary thermal cycle used gas acetylene flame. This can lead to increase in carbon in the weld zones, which leads to increase in hardness. Use of heat sources such as infrared (IR) heat source can eliminate this problem. Such implementations can potentially lead to further reduction of hardness difference across the HAZ.

In an integration scheme of multiscale models, phase field modeling is often seen as the slowest work element due to the large number of grid points and time steps involved. But this is not always the case. In the case of simulation chain shown in Fig. 1, the phase field simulations took only ~15 min to complete on 8 threads in an Intel Xeon® E5-2630 processor. The virtual test simulations turned out to be more time-consuming in the multiscale model chain currently implemented. The reason for it being the fact that the phase field grid size was taken forward while mapping the finite element meshes. This resulted in a very fine mesh size for finite element simulation. Future work can be thought of with adaptive meshing in the virtual test simulation domain so that the multiscale chain can be accelerated.

## 4 Challenges

One of the major challenges in the multiscale modeling approach is the material property input for virtual test. In order to consider anisotropy better, the input material property of individual phases must be anisotropic. Obtaining the anisotropic properties for each phase is a challenge with experiments. A combination of models and experiments can be thought of as a possible solution for this problem. The currently available commercial software JMatPro® has the capability to calculate the isotropic properties for individual phases with semiempirical approaches. Such a feature is much needed for obtaining the anisotropic material properties for individual phases in materials.

Another main challenge in multiscale modeling is to answer the question of how to integrate the simulation techniques and models at different length scale. Seamless integration of models and simulations at multiple length scales is still a challenge. In the proposed workflow of multiscale models shown in Fig. 4, the link between microscale simulation and macroscale simulation is obtained with the help of a virtual test. The phase field simulated microstructure is exported to finite element software for performing the virtual test. On repeating such a workflow, the complete set of material property input for macroscale FEM simulation can be obtained. But repeating such a workflow for every finite element mesh or region for every time step is unnecessary and time-consuming. Selective regions and selective time steps can be considered in the finite element macroscale model for property update using multiscale model. The decision on which regions in the model need such a multiscale chain property update and in what interval the property needs to be updated depends on the problem being studied. For cases like welding, the time taken for the process is short, and hence, the property update with multiscale model needs to be done at short time step intervals but that will not be the case with processes like heat treatment that take hours to complete. In order to accelerate the property update in FEM simulation with multiscale models, techniques such as look-up tables and machine learning can be used.

## 5 Summary and Future Scope

This chapter presented a detailed overview of microstructure simulation and virtual tests which are important steps in the integration of models in an ICME approach for welding processes. Two case studies of the use of secondary thermal profile during welding process were described. The first example using a trailing heat sink illustrated the importance of phase transformation in the control of residual stress and distortion. In the second example, a detailed multiscale model was implemented for regular GMA welding in DP980 steel along with a trailing heat source. The hardness difference decreased across the weld after the use of secondary heat source. Heat sources such as IR can be used as a future work to eliminate the effect of carbon on hardness of the weld regions. Multiscale model chain implemented in the present work can be used to simulate welding with secondary heat sources as a future work.

**Acknowledgements** The authors would like to acknowledge the financial support from the UAY project ‘Understanding the Evolution of Residual Stress During Repair and Refurbishment of Gas Turbine Components via Laser Additive Manufacturing.’ The authors would also like to acknowledge ‘The Center for Excellence in Iron and Steel Technology’ (CoExiST) at IITM for supporting this work. The financial support from Indo-German Science and Technology Centre (IGSTC) project ‘DP-Forge’ is also acknowledged for some of the ICME tools.

## References

1. A.B. Nellippallil, V. Rangaraj, B.P. Gautham, A.K. Singh, J.K. Allen, F. Mistree, J. Mech. Des. Trans. of the ASME **140** (2018). https://doi.org/10.1115/1.4041050
2. S.F. Ghoreishi, A. Molkeri, A. Srivastava, R. Arroyave, D. Allaire, J. Mech. Des. Trans. ASME **140** (2018). https://doi.org/10.1115/1.4041034
3. J.H. Panchal, S.R. Kalidindi, D.L. McDowell, CAD Comp. Aided Des. **45**, 4–25 (2013). https://doi.org/10.1016/j.cad.2012.06.006
4. Gupta, S. Goyal, K.A. Padmanabhan and A.K. Singh, Int. J. Adv. Manuf. Tech. **77**, 565–572 (2015). https://doi.org/10.1007/s00170-014-6464-5
5. R. Shukla, N.H. Kulkarni, B.P. Gautham, A.K. Singh, F. Mistree, J.K. Allen, J.H. Panchal, JOM **67**, 94–107 (2015). https://doi.org/10.1007/s11837-014-1216-4
6. U. Singh, R. Anapagaddi, S. Mangal, K.A. Padmanabhan, A.K. Singh, Metall. Mater. Trans. B **47**, 1804–1816 (2016). https://doi.org/10.1007/s11663-016-0620-2
7. J. Gong, D. Snyder, T. Kozmel, C. Kern, J.E. Saal, I. Berglund, J. Sebastian, G. Olson, JOM **69**, 880–885 (2017). https://doi.org/10.1007/s11837-017-2300-3
8. S.A.H. Motaman, F. Kies, P. Köhnen, M. Létang, M. Lin, A. Molotnikov, C. Haase, JOM **72**, 1092–1104 (2020). https://doi.org/10.1007/s11837-020-04028-4
9. Micress, https://micress.rwth-aachen.de/ (2020) (accessed 26 April 2020)
10. V. Savic, L. Hector, U. Basu, A. Basudhar, I. Gandikota, N. Stander, T. Park, F. Pourboghrat, K.S. Choi, X. Sun, J. Hu, F. Abu-Farha and S. Kumar, SAE Technical Papers 2017-March (2017). https://doi.org/10.4271/2017-01-0226
11. C.D. Ridgeway, C. Gu, K. Ripplinger, D. Detwiler, M. Ji, S. Soghrati, A.A. Luo, Materials Des. **194** (2020). https://doi.org/10.1016/j.matdes.2020.108929
12. M.R. Rahul, G. Phanikumar, Mat. Perform. Charact. **4**, 381–398 (2015). https://doi.org/10.1520/MPC20140065
13. J.B. Leblond, J. Devaux, Acta Metall. **32**, 137–146 (1984). https://doi.org/10.1016/0001-6160(84)90211-6
14. D.P. Koistinen, R.E. Marburger, Acta Metall. **7**, 59–60 (1959). https://doi.org/10.1016/0001-6160(59)90170-1
15. J. Rudnizki, B. Böttger, U. Prahl, W. Bleck, Metall. Mater. Trans. A **42**, 2516–2525 (2011). https://doi.org/10.1007/s11661-011-0626-y
16. D.-H. Yeon, P.-R. Cha, J.-K. Yoon, Scripta Mater. **45**, 661–668 (2001). https://doi.org/10.1016/S1359-6462(01)01077-6
17. A. Bhattacharya, C.S. Upadhyay, S. Sangal, Metallurgical and Materials Transactions A: Physical Metallurgy and Materials Science **46**, 926–936 (2015). https://doi.org/10.1007/s11661-014-2665-7
18. A. Bhattacharya, C.S. Upadhyay, S. Sangal, Metallurgical and Materials Transactions A: Physical Metallurgy and Materials Science **48**, 4929–4942 (2017). https://doi.org/10.1007/s11661-017-4225-4
19. T. Kohtake, A. Yamanaka, Y. Suwa, Metall. Mater. Trans. A **49**, 5023–5034 (2018). https://doi.org/10.1007/s11661-018-4829-3
20. Zhu, M. Militzer, Metall. Mat. Trans. A: Phys. Metall. Mat. Sci. **46**, 1073–1084 (2014). https://doi.org/10.1007/s11661-014-2698-y
21. B. Zhu, H. Chen, M. Militzer, Computational Materials Science **108**, 333–341 (2015). https://doi.org/10.1016/j.commatsci.2015.01.023
22. F. Steinbach, B. Pezzolla, M. Nestler, R. Seeßelberg, G.J. Prieler, Schmitz, J.L.L. Rezende, Phy. D: Nonlinear Phen. **94**, 135–147 (1996). https://doi.org/10.1016/0167-2789(95)00298-7
23. Steinbach, Modelling Simul. Mat. Sci. Eng. **17** (2009). https://doi.org/10.1088/0965-0393/17/7/073001
24. G. Pariser, P. Schaffnit, I. Steinbach, W. Bleck, Steel Research **72**, 354–360 (2001). https://doi.org/10.1002/srin.200100130
25. M.G. Mecozzi, J. Sietsma, S. van der Zwaag, Comput. Mater. Sci. **34**, 290–297 (2005). https://doi.org/10.1016/j.commatsci.2005.03.002

26. M.G. Mecozzi, J. Sietsma, S. Van Der Zwaag, Acta Mater. **54**, 1431–1440 (2006). https://doi.org/10.1016/j.actamat.2005.11.014
27. M. Militzer, M.G. Mecozzi, J. Sietsma, S. van der Zwaag, Acta Mater. **54**, 3961–3972 (2006). https://doi.org/10.1016/j.actamat.2006.04.029
28. H. Farahani, G. Zijlstra, M.G. Mecozzi, V. Ocelík, J.T.M. De Hosson, S. van der Zwaag, Microsc. Microanal. **25**, 639–655 (2019). https://doi.org/10.1017/S143192761900031X
29. I. Loginova, J. Odqvist, G. Amberg, J. Ågren, Acta Mater. **51**, 1327–1339 (2003). https://doi.org/10.1016/S1359-6454(02)00527-X
30. I. Loginova, J. Ågren, G. Amberg, Acta Materialia **52**, 4055–4063 (2004). https://doi.org/10.1016/j.actamat.2004.05.033
31. A. Bhattacharya, K. Ankit, B. Nestler, Acta Materialia **123**, 317–328 (2017). https://doi.org/10.1016/j.actamat.2016.10.035
32. A. Yamanaka, T. Takaki, Y. Tomita, Materials Science and Engineering A **480**, 244–252 (2008). https://doi.org/10.1016/j.msea.2007.08.066
33. P.G. Kubendran Amos, E. Schoof, D. Schneider, B. Nestler, J. Alloys Comp. **767**, 1141–1154 (2018). https://doi.org/10.1016/j.jallcom.2018.07.138
34. L. Zhang, Y. Shen, H. Wan, X. Xiong, L. Zhang, J. Alloy. Compd. **650**, 239–247 (2015). https://doi.org/10.1016/j.jallcom.2015.07.278
35. H. Song, R. Shi, Y. Wang, J.J. Hoyt, Metall. Mater. Trans. A **48**, 2730–2738 (2017). https://doi.org/10.1007/s11661-016-3711-4
36. M. Militzer, Curr. Opin. Solid State Mater. Sci. **15**, 106–115 (2011). https://doi.org/10.1016/j.cossms.2010.10.001
37. M. Toloui, M. Militzer, Acta Mater. **144**, 786–800 (2018). https://doi.org/10.1016/j.actamat.2017.11.047
38. M. Düsing, R. Mahnken, Comput. Mater. Sci. **111**, 91–100 (2016). https://doi.org/10.1016/j.commatsci.2015.08.043
39. T.T. Arif, R.S. Qin, Advanced Mat. Res. **922**, 31–36 (2014)
40. K. Mukherjee, U. Prahl, W. Bleck, U. Reisgen, M. Schleser, A. Abdurakhmanov, Materialwiss. Werkstofftech. **41**, 972–983 (2010)
41. A. Ramazani, Y. Li, K. Mukherjee, U. Prahl, W. Bleck, A. Abdurakhmanov, M. Schleser, U. Reisgen, Computational Materials Science **68**, 107–116 (2013)
42. T.T. Arif, R.S. Qin, Comput. Mater. Sci. **77**, 230–235 (2013). https://doi.org/10.1016/j.commatsci.2013.04.044
43. M. Düsing, R. Mahnken, Arch. Appl. Mech. **86**, 1947–1964 (2016). https://doi.org/10.1007/s00419-016-1161-5
44. M. Düsing, R. Mahnken, Int. J. Solids Struct. **135**, 172–183 (2018). https://doi.org/10.1016/j.ijsolstr.2017.11.018
45. W. Song, U. Prahl. Y. Ma, W. Bleck, Steel Res. Int. **89**, 1800028 (2018). https://doi.org/10.1002/srin.201800028
46. NaMin Xiao, Y. Chen, DianZhong Li, YiYi. Li, Progress in mesoscopic modeling of microstructure evolution in steels. Sci. China Technol. Sci. **55**, 341–356 (2012). https://doi.org/10.1007/s11431-011-4699-z
47. M. Gouné, F. Danoix, J. Ågren, Y. Bréchet, C.R. Hutchinson, M. Militzer, G. Purdy, S. van der Zwang, H. Zurob, Mater. Sci. Eng. R. Rep. **92**, 1–38 (2015). https://doi.org/10.1016/j.mser.2015.03.001
48. M.J. Deepu, G. Phanikumar, Integrating Mat. Manuf. Inno. **9**, 228–239 (2020). https://doi.org/10.1007/s40192-020-00182-4
49. JMatPro, https://www.sentesoftware.co.uk/jmatpro (2020) (accessed 11 May 2020)
50. ThermoCalc, https://thermocalc.com/ (2020) (accessed 30 May 2020)
51. G. Laschet, Comput. Methods Appl. Mech. Eng. **191**, 4535–4554 (2002). https://doi.org/10.1016/S0045-7825(02)00319-5
52. S. Rex, D. Bohn, Norbert Moritz and Laschet G. Numer. Heat Transfer, Part A **42**, 91–106 (2010). https://doi.org/10.1080/10407780290059440

53. G. Laschet, P. Fayek, T. Henke, H. Quade, U. Prahl, Mater. Sci. Eng., A **566**, 143–156 (2013). https://doi.org/10.1016/j.msea.2012.12.064
54. A. Ramazani, K. Mukherjee, H. Quade, U. Prahl, W. Bleck, Materials Science and Engineering A **560**, 129–139 (2013). https://doi.org/10.1016/j.msea.2012.09.046
55. S.R. Kala, Studies on distortions and residual stresses in weldment with trailing heat sink, Ph.D. thesis, IIT Madras (2013)
56. S. Kala, N. Siva Prasad, G. Phanikumar, Studies on multipass welding with trailing heat sink considering phase transformation. J. Mater. Process. Technol. **214**(6), 1228–1235 (2014). https://doi.org/10.1016/j.jmatprotec.2014.01.008
57. S. Kala, N. Prasad, G. Phanikumar, Numerical study of welding with trailing heat sink considering phase transformation effects. Adv. Mat. Res. **875–877**, 2118–2122 (2014). https://doi.org/10.4028/www.scientific.net/AMR.875-877.2118
58. S. Kala, N. Prasad, G. Phanikumar, Numerical studies on effect of interpass time on distortion and residual stresses in multipass welding. Adv. Mat. Res. **601**, 31–36 (2013). https://doi.org/10.4028/www.scientific.net/AMR.601.31

# Material Recycling: Unearthing Metals from Anthropogenic and Industrial Resources

**Pratima Meshram and Abhilash**

## 1 Introduction

Earth's crust is the source of metals. After mining, depending on the grade, the ores (if lean) are processed by beneficiated to generate a concentrate and a gangue fraction. The rich ore of the concentrates upon sizing is processed by various pre-pyroprocessing steps like drying, roasting, calcination, etc., to obtain a modified concentrate. This modified feed serves as the raw material for the extraction of metals by pyrometallurgy/hydrometallurgy/electrometallurgy/biohydrometallurgy to yield the desired metal and generate slag/residue. The extracted metals can be separated and purified to obtain marketable products. However, the gangue and slag/residue although dumped or landfilled serve as an important resource for metal extraction/replenishment.

The mining operations world over are witnessing the challenge of declining grade of primary reserves. As the exploration exceeds, the number of reserves increases geometrically but the grade of metals in these reserves is declining. For example, to produce 1 ton of copper required only 55 tons of copper ore in 1950; which is now of the order 6 times in 2020. India lacks any primary resources for critical metals. Of the 30 CRMs, India possesses some distinctive figures in reserves of graphite, rubber, and a few critical rare earth elements embedded in beach sand minerals. These critical metals have huge demand in low carbon technologies. Thus, dependence on secondaries can't be ignored.

The energy requirement in primary production of virgin copper and aluminium is 70 and 218 MJ/kg, which can be reduced by 75–85% using secondaries of these metals, thereby reducing energy consumption to 17.5 and 28.8 MJ/kg. Concurrently, the $CO_2$ emission reduces from 3.83 kg $CO_2$/kg to 0.96 kg $CO_2$/kg in the case of copper and 11.46 kg $CO_2$/kg to 1.69 kg $CO_2$/kg in the case of Al. Apart from $CO_2$,

---

P. Meshram (✉) · Abhilash
CSIR-National Metallurgical Laboratory, Jamshedpur, India
e-mail: pratima@nmlindia.org

A. Shrivastava et al. (eds.), *New Horizons in Metallurgy, Materials and Manufacturing*, Indian Institute of Metals Series, https://doi.org/10.1007/978-981-19-5570-9_5

emissions like $SO_2$ and usage of land and water can be effectively curbed. Mining has been causing damage to the environment also by its deleterious operations like blasting and acid mine drainage. A comprehensive approach is required to mitigate such post-operational challenges faced in mining, metallurgical, and metal manufacturing processes by a holistic waste management approach that results in lower waste generation, process in-built recycling, and opens vistas for innovative markets and applications in other sectors of the economy.

The magnitude of the waste generation problem in India is quite pronounced. The per capita waste generation has shot by > 2% per annum due to the rise in urban population by 3-4% per annum (e.g. nearly 42 million tons of MSWs are produced annually in India). With a 5% annual increase in waste generation, recyclability–recycling–reuse has been identified as the imperative step towards sustainability.

Given the need to achieve sustainability in material processing, the present chapter emphasizes exploring secondary resources as sustainable alternates to primary ores via replenishment cum recycling of anthropogenic and industrial wastes. These resources often contain metals in lower values except in a few cases like WEEEs, but processing of such is benign to the environment, economical, and ensures extended producer responsibility.

## 2 Material Resources

Waste generation is mainly associated with industrialization, economic development/urbanization, increase in population, and affluence. In Asia, with increasing population, prosperity, and urbanization, problem related to the expanded consumption and depletion of resources, a wide range of wastes are becoming major challenges. A material that either needs to be discarded/ disposed of is termed waste, and its non-reversible recuperation in an environmentally benign mode is the main objective of waste management processes [1]. About 7–10 billions ton per year of waste is generated globally, out of that 47% is dumped in deep pits, 31% is reprocessed, and 22% is subjected to high-temperature deashing. A major loss of values is contemplated with nearly 70% of waste being unreused or not recycled worldwide [2]. These are the wastes generated during mining, mineral industries as a sidestream, and also anthropogenic wastes which contain valuable metals and can be used as secondary resources.

The recent advent to extract metals from secondary resources is primarily due to its environmentally favourable processing that tackles hazardous heavy metals, economics is attractive due to the depletion of primaries, and is a valuable element in extended producer responsibility (EPR). These material resources are widely classified as anthropogenic wastes and wastes from mining-cum-metallurgical processing (Fig. 1). Wastes can be classified according to their states, viz., solid, liquids, or gaseous, or based upon their source of generation as municipal/household wastes (anthropogenic wastes), industrial wastes, or metallurgical wastes. Here in this review, we will focus mainly on recycling of these wastes for improved economics and ecological conservation. By recycling, these wastes/ discarded products or materials are recovered or reclaimed, refined or reprocessed, and converted into new or different products. Recycling these wastes is beneficial not only as it saves the natural resources but also it reduces the need for landfills, reduces $CO_2$/greenhouse gas emissions, and thereby protects the environment. Recycling also creates new industries, business opportunities, and employment for many and thereby leading to a circular economy. Among the methods practised, hydrometallurgical processing is considered more precise, foreseeable, and easy to deal with, making it a pertinent choice in valuable metal recovery from such resources (especially WEEEs) for over two decades. However, they owe the demerit in being acid consuming, stretched over longer durations, and quite often incomplete separation among precious metals. The use of harsh or noxious reagents, such as aqua regia, nitric acid, cyanide, and halides, produces large magnitudes of lethal and corrosive liquid or gaseous effluents. Consequently, it is obligatory to pursue a more environmentally friendly scheme to replenish metals from such resources. However, hybrid hydrometallurgical methods are an indispensable choice in the refining phase of a recycling process.

This review mainly focuses on the recycling of secondary resources for metals which are either anthropogenic or industrial wastes. The anthropogenic or household waste covered aluminium cans, cells, and batteries; and electrical and electronic wastes (e-wastes) while different metallurgical plant wastes, viz., iron and steel plant wastes, zinc plant wastes, aluminium plant wastes will be mainly covered.

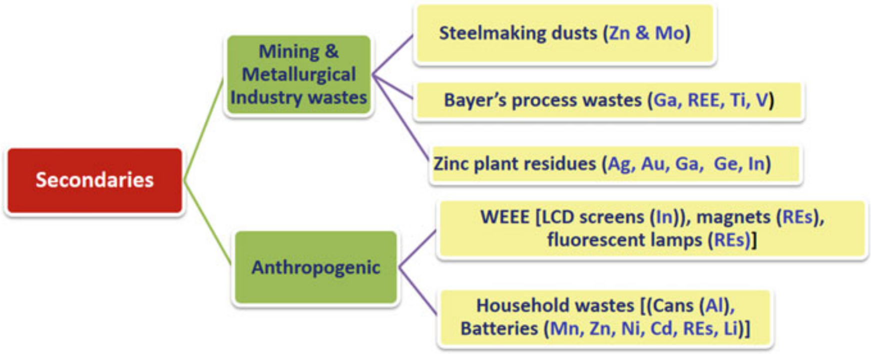

**Fig. 1** Classification of material wastes

# 3 Anthropogenic Wastes

## *3.1 Household Metal Wastes*

Household metal wastes are also called home generated or retail wastes. It includes household substances and chemicals that are no longer in use and such products either contain valuable metals or reactive, corrosive, or toxic substances that may cause land pollution if not recycled. Therefore, recycling this waste is necessary to save energy or protect the environment and for economic advantages. The term household metal waste more accurately identifies a broader range of appliances/items that are targeted as recyclable and should not be disposed of in a landfill, viz., aluminium and steel cans and containers, wirings, television, computer, and cell phones.

### 3.1.1 Cans and Containers

Every day we use different sorts of cans and containers to keep various household and food items. Steel containers, tin, aluminium cans, and foils are usually employed for these purposes. Disposal of this material not only harms the environment as they are not naturally degraded but also recycled to save energy and reduce emissions. Because of the considerable lower energy used, each ton of aluminium can recycling evades 9 tons of $CO_2$ equivalent emissions thus saving 97% GHG emissions as against the primary aluminium making. Aluminium can recycling to generate metal uses only 5% of the energy when compared to its initial extraction and processing (mine to metal) and 10% of the capital costs.

There are mainly two types of packaging employed for household items, rigid and semi-rigid packing, which is generally used for packaging food items, beverage, and aerosol cans, closures containers, and trays; while flexible packing is usually used as foil or laminated materials for plastics or cardboard. Cans are made up of steel, copper, tin, and aluminium which are used for rigid or semi-rigid packing. These cans contain high metal values and are therefore recycled directly as scrap in the smelter and then fabricated directly as wrought products. The aluminium cans are mostly Al-based but contain Mg and Mn as additives to improve the strength and ductility of cans. These cans comprise of metals in varying composition (95.1–98% Al, 1.15–4.65% Mg, 0.25–0.9% Mn) in the body and lid [3].

In flexible packaging, about 6 $\mu$m aluminium or copper foil is used which is generally laminated to paper or plastics. Hence, the flexible packaging waste contain fewer metals that can be generally extracted by pyrolysis and thermal plasma techniques. Oxidation of aluminium and purity of recycled aluminium are the major challenges in its recycling [4]. To overcome these challenges, Risonarta et al. [5] suggested a method by using drossing flux and applied an improved melting strategy and decorating cans before melting it [5]. The coating contains $Cr_2O_3$ and $TiO_2$ which cause aluminium oxidation resulting in slag formation and consequently its loss to form slag resulting its loss. Drossing flux added paved way for disunion of Al from the slag, thus preventing its loss. Another improvement was in terms of the decrease in the melting duration. These improvements helped in increasing the recycling yield by ~5% [5].

### 3.2 Waste Electrical and Electronic Equipments (WEEEs)

Due to industrialization and revolution in information and telecommunication industries, the demand for electric and electronic equipment is rising which results in increasing generation of hazardous and other wastes. These wastes consist of the equipment and its parts which are rejected or discarded during its manufacture or after use. These wastes are termed electronic waste or waste electrical and electronic equipment (WEEE), e-waste, or e-scrap. It includes a wide range of products viz., computers, laptops, television sets, VCRs, washing machines, refrigerators, air conditioners, stereos, copiers, fax machines, and electrical lamps. There exists a huge possibility of reusing, refurbishing or recycling these products after their shelf life in an environmentally benign mode. Of the MSWs generated, above 5% by weight worldwide is contributed as scrap WEEEs. It has been estimated that the quantity of WEEEs discarded in Asia amounts to nearly 12 million tons every year [6].

The Global E-waste Monitor [7] presents the continent data on electronic waste generation in 2019. Out of the globally spawned 53.6 million metric tons (Mt) WEEEs, only 17.4% were properly collected and recycled. In 2019, Asia generated 24.9 Mt of electronic wastes, followed by the USA (13.1 Mt) and European nations (12 Mt), while only 2.9 Mt and 0.7 Mt were emanated from Africa and Oceania, respectively. However, the statistics varied when accounted on a per capita basis where European nations topped the list with 17 kg generation per capita, Oceania countries being second (16 kg per capita), followed by the USA (13 kg per capita), while Asia and Africa spawned approximately 5.5 and 3.0 kg per capita, respectively [7]. Having the quantity of accumulated wastes in the background, a value-based assessment of the metals presents an attractive estimate of producing 120-140 kg copper, 2.75–4.25 kg silver, and 0.15–0.40 kg gold and palladium from 1000 kg mobile phones. The worldwide e-waste scrap market has generated a yearly revenue worth approximately 63 billion USD in 2020–2021 [8].

E-waste is a complex waste stream that comprises precious, critical, and non-critical metals that can be used as an alternate or secondary source for the production of metals; therefore, this waste is also called an urban mine/ ore. Table 1 shows the different electronic wastes and their metal content. More than 60 different elements can be found in electronic waste; some of them are precious, a few hazardous and some are both [9].

**Table 1** Metal content in various e-wastes

| Element | Source | Typical composition | References |
|---|---|---|---|
| Copper | PCBs | 83.42% Cu, 2.72% Sn, 2.36% Pb, 1.96% Al, 0.96% Zn, 0.23% Fe, 0.48% Ba, 0.11% Bi, 0.039% Ni | [10, 11] |
| | Flue dust of E-waste | 3.2% Cu, 0.8% Pb, 0.5% Ni, 27.2 Fe, 6% Mn, 4.9% Al, 0.7% Ca, 0.3% Mg, 114 ppm Au | [12] |
| | Wires | 80.4% Cu, 19.6% plastics | [13] |
| Gold | Mobile PCB | 66% Cu, 2.30% Ni, 0.045% Au | [14] |
| | Contractors | 40 ppm-1.04% Au | [15] |
| | ICs | 289–3386 ppm Au, 471–6590 ppm Ag | [16] |
| Silver | Mobile PCB | 39.86% Cu, 0.457% Zn, 0.396% Ni, 0.0043% Au, 0.054% Ag | [17] |
| | Photovoltaic cells | 0.13% Ag, 0.41% Cu, 5.27% Al, 0.15% Pb, 0.004% Fe, 2.31% others, 91.73% Si | [18] |
| Cobalt | Batteries | 15–55% Co, 3–7% Li, 5–40% Ni, 10–35% Mn | [19] |
| Tin | Solders | 63–97% Sn, 0.14% Ge | [20] |
| Lead | Solders | (63–37%) Sn–Cu, (60–37–3%)Sn–Cu–Ag | [21] |
| Bismuth | Gas safety valves | 1.48% Bi, 1.08% Pb, 5.14% Cu, | [22] |
| Selenium | Solar cells | 34.6% Se, 13.8% Zn, 25.7% Cu, 25.9% Sn | [23] |
| Indium | LCD glass | 69.78% Si, 14.37% Al, 9.59% Ca, 3.45% Sr, 0.9% Ba, 0.35% Fe, 0.90% As, 0.34% K, 0.18% Zn, 0.13% Ti, 0.06% In, 0.02% Cu, 0.01% Sn, 0.01% Cr | [24] |

### 3.2.1 Liquid Crystal Displays

Technology improvement has resulted in the replacement of old cathode-ray tubes (CRTs) with liquid–crystal display (LCDs) and is now a vital component in electronics like televisions, desktops, laptops, tablets, and other visual-cum-communication devices [25]. Indium, a critical metal, used as indium tin oxide (ITO) comprising of indium oxide and tin oxide in flat-screen liquid–crystal display technology and represents 84% of indium's total demand (Umicore). Due to its economic importance and supply risk, it comes under critical metals. There is no primary source of indium, and its concentration is one-sixth of gold in the earth crust. Indium is a by-product of zinc and lead processing industries and exists in a concentration range of 10–20 mg/kg [26]. To use this high resource potential in terms of high indium content and environmental issues due to the presence of mercury-like hazardous elements, recycling LCD is essential. LCD monitors are constituted of an LCD panel, a lightning source, a printed circuit board, and an optical system. The LCD panel is the most important component of LCD monitors where indium is present in ITO electrodes; apart from that, the light source consists of cold cathode fluorescent lamps containing mercury [24].

Different types of acid and acid mixtures viz., $HNO_3$, HCl, and $H_2SO_4$ with varying strength have been tested for extraction of indium from scrap LCDs. Sulphuric acid is mostly used due to its higher efficiency, low cost, and easy control during the process [24]. To remove liquid crystals from glass substrate, Li et al. [27] use a series of steps including thermal shock (to separate film), and ultrasonic cleaning-cum-dissolution.

An integrated process involving acid leaching with precipitation and cementation has been developed to recover indium from scrap ITO [27]. By employing concentrated sulphuric acid (100 g/L) with 10–12% pulp density at 90 °C in 2 h, ~99% In and only 8% Sn were extracted. The impurity of tin in liquor was removed by sulphide precipitation using 1.01 bar at 60 °C for 10 min. The raffinate (purified $In_2(SO_4)_3$ solution) was cemented on a zinc plate to obtain high pure sponge indium at pH 1–1.5 and 65 °C. To recover In from scrap TFT-LCDs post-sulphuric acid leaching, solvent extraction was employed to selectively load indium with 30% D2EHPA at an organic (1): aqueous (5) ratio in 5 min. The loaded D2EHPA was completely stripped by 4 M HCl with an aqueous (1): organic (5) ratio, resulting in ~97% In separation efficiency [27].

Table 2 presents the summary of recycling works executed for recycling LCD panels by various researchers, and the main focus is on indium recovery. The common processing options to recover indium from the LCD panel are pyrometallurgy, hydrometallurgy, vacuum metallurgy, and chlorination. Among these, hydrometallurgical recycling process is a widely used technique because the recovery rate is higher as compared to other processes. Most of the researchers used energy-intensive pre-treatment or high acid to process scrap LCD panels for indium extraction, and hence, most of these processes were not addressing the circular economy concept, but using high process throughput is also critical to achieving the economics required for the indium recovery process.

### *3.3 Printed Circuit Boards (PCBs)*

PCBs account 3–7% of the mass of almost all electrical and electronic equipment. PCBs are mainly constituted of conducting (tracks and components) fractions straddled on a laminated or non-conducting surface. The surface (specifically termed as substrate) is characteristically a glass fibres embedded on epoxy resin or paper on phenolic resin, intrinsically mixed with bromine-based retardants [33]. PCBs consist of ~ 54 different metals, and hence, the separation of these metals, especially Pt, Pd, Au, and Ag, is very complicated. PCBs are constituted of 40% metals, 30% organics, and 30% ceramics. PCBs comprises of 70% non-metallic fractions, apart from 10–20% copper, 0.9–6% solder (Pb), 0.5–4% iron, 1–3%, nickel, 400–500 ppm Ag, 250–350 ppm Au, 75–150 ppm Pd, etc. [34, 35]. Hence, it is not only containing hazardous substances but also a lot of precious metals by a factor of 10 when compared with their primary resources [35]. The metal fraction available in PCBs is variable based on the category of e-waste as shown in Table 3. PCBs

**Table 2** Recycling processes for LCD panels

| Source and Composition of LCD | Recovery process and parameters | | | | | Highlights | References |
|---|---|---|---|---|---|---|---|
| | Process | Parameters | | | | | |
| | | Concentration | Temp ($^oC$) | Time (min) | S/L | | |
| Scraped LCD glass (80–90% $In_2O_3$, 10–20% $SnO_2$) | Leaching | 100 g/l $H_2SO_4$ + 2 g $MnO_2$ as oxidant | 25 | 120 | 1:1 | 74.38% recovery<br>Very High Acid concentration vis-à-vis Low Recovery | [25] |
| 35.6 cm (14-in.) LCD screen (102 ppm In in ITO glass) | Pre-treatment (Thermal shock and ultrasonic cleaning) + Acid Leaching | 5.4 M HCl + 0.8 M $HNO_3$ | 60 | 30 | 2:1 g /mL | 92% In | [27] |
| ITO sample (95.65% $In_2O_3$, 4.35% $SnO_2$) | Chloride-induced Vaporization<br>$N_2$ Atm | 6 N HCl | 700 | 90 | 0.5 g/5 mL | 96.2% In | [26] |
| LCD scrap | | | 400 | 90 | 14 g/5 mL | 86.6% In | |
| Indium rich ITO bearing LCD (90% of $In_2O_3$ and 10% of $SnO_2$) | Leaching | 5 M HCl | 75 | 120 | 500 g/L | In (76.16 g/L) and Sn (10.24 g/L) | [29] |
| End-of-life LCD panels | Shredding, Milling, Leaching | 2 M $H_2SO_4$, 3-step cross current | 80 | 17 | 0.1 kg/L | 1st step: 35 ppm In<br>2nd step: 100 ppm In<br>3rd step: 160 ppm | [30] |

from desktops contain about 15–30% Cu and ~200–300 g/ton Au, while handset PCBs contain 12–15% Cu and 275–400 g/ton Au [36]. The extraction of gold from used PCBs is meritorious owing to nearly 100 × higher quantity of gold in PCBs when compared with its ore. Recycling of waste PCBs not only conserves primary resources by recovering valuable metals but also addresses the environmental pollution by treating hazardous substances. Lot of research has been envisaged on the extraction of copper which constitutes 34–35% of total metal content in PCBs [37, 38].

The polymer coating over PCBs inhibits the chemical reaction of lixiviant and metals, which according to Jadhav and Hocheng [47], can be removed by soaking in NaOH at ambient temperature for 22 h and slow stirring, as a pre-treatment step before leaching with hydrochloric acid [47]. Recovery of copper from WPCBs using the electrolysis process was investigated by Kumar et al. [48]. They reported that the 5 h as the maximum duration for the dissolution process of 132 g of PCBs compounds and the maximum duration of electrolysis for deposition of copper was 2 h for 14.86 g by using 0.0214 kWh [48]. Liu et al. [11] also proposed an efficient process that avoids acid leaching and recovers copper by direct electrolysis [11]. It was illustrated that 97.32% copper can be reclaimed with the increase in the concentration of copper sulphate, sodium chloride, sulphuric acid, and up to 90 g/L, 40 g/L, 118 g/L, respectively, and the apparent current density of 80 mA/cm$^2$, after which recovery diminished. The purity of copper recovered through this process was 99.86%.

The recovery method used depends upon the metal, the efficiency of the process, and the costs involved. The pyrometallurgical treatment of electronic wastes has demerits due to the loss of aluminium and iron into the slag, in addition to the release of dioxins from the brominated compounds in the PCBs. Also, the separation of precious metals is very poor.

### *3.4 Magnets*

The shift to green and carbon–neutral technologies has resulted in increased electrification, and thus, the application of rare earth-based magnets in energy storage/conversion devices has also shot up. These magnets are primarily found in motors, generators, medical equipment, consumer appliances, hybrid and electric vehicles (EVs), wind turbines, electrified marines, aircraft, etc. Neodymium-iron-boron (NdFeB) magnets have the highest demand due to the highest value of magnetic field per unit volume which is imperatively needed in mobility and wind turbines. NdFeB magnets are a potent resource of rare earth elements (REEs) with 28–35 wt% metal concentration (Pr, Nd, Tb, and Dy), of which Nd constitutes 15–30% and the remaining being iron [49]. With the highest CAGR of magnets in green energy transition, recycling of magnets shall help in alleviating Nd supply risk. However, the major challenges encountered are the sourcing mechanism and holistic recycling pathway.

**Table 3** Metal content in WPCBs depending on the type of WEEE

| Source/type of WEEE | Composition | | | | | | | | | | | References |
|---|---|---|---|---|---|---|---|---|---|---|---|---|
| | Cu | Fe | Al | Sn | Zn | Pb | Ni | Au | Ag | Pt | Pd | |
| | % | | | | | | | mg/kg (ppm) | | | | |
| Mobile phones | 34.49 | 10.57 | 0.26 | 3.39 | 5.92 | 1.87 | 2.63 | 0 | 2100 | 0 | 0 | [39] |
| | 20.6–45.1 | 0.5–4.84 | 0.89–2.01 | 1.3–6.3 | 0.23–6.7 | 0.1–2.7 | 1.1–5.9 | 17–2900 | 170–8300 | 7–50 | 0–82 | [40] |
| | 38.57 | 4.27 | 0.64 | 2.58 | 2.07 | 1.22 | 2.15 | 800 | 600 | 0 | 0 | [41] |
| | 41.76 | 44.76 | 1.13 | – | 0.33 | 0.12 | 2.92 | 113 | 140 | – | – | [42] |
| | 43.19 | 13.9 | 2.78 | – | 14.25 | 11.83 | 13.44 | 310 | 10 | 6.3 | – | [43] |
| | 29.37–42.85 | – | 2.28–2.95 | 1.8–2.64 | 0.94–1.38 | 0.73–1.78 | 2.76–3.13 | 724 | 331.5 | – | 0 | [38] |
| | 46.3 | – | 3.84 | 15.18 | 0.97 | 0.9 | 1.03 | – | 2534 | – | – | [44] |
| PCs | 50.52–61.5 | – | 2.54–7.71 | 5.7–8.71 | 0.2–0.63 | 0.13–0.5 | 0.85–9.99 | – | 1390–1683 | – | – | |
| | 20.19 | 7.33 | 5.7 | 8.83 | 4.48 | 5.53 | 0.43 | 1300 | 1600 | 0 | 0 | [39] |
| | 11.09–24.69 | 0.22–7 | 4.94 | 1.1–5.62 | | 0.6–2.96 | 0.11–1.65 | 76–347 | 45–363 | – | 27–220 | [45] |
| | 17.9–26.2 | – | 4.02–4.34 | 2.3–2.42 | 1.45–3.8 | 1.6–1.74 | 0.5–0.9 | 125–147 | 171–330 | – | 5.9–31.5 | [38] |
| TV PCBs | 44.58 | – | 3.84 | 32.58 | 3 | 2.46 | 1.24 | – | 1038 | – | – | [44] |
| Copier PCBs | 48.09 | – | 3.43 | 16.55 | 0.99 | 1.07 | 1.33 | – | 2260 | – | – | |
| Fax machine PCBs | 44.32 | – | 3.89 | 18.57 | 1.26 | 1.36 | 2 | – | 2307 | – | – | |
| CRTs | 8.41 | – | 4.84 | 0.83 | 1.46 | 1.32 | 1.42 | 63.8 | 223.8 | – | 0 | [38] |
| LCDs | 19–26.4 | – | 4.3–7.65 | 0.84–1.08 | 1.16–1.84 | 1.3–1.4 | 0.87–0.89 | 62.9–143.8 | 225.34–321.43 | – | 7.53–25.99 | |
| TVs | 9.23 | 0.04 | 0.75 | – | 0.47 | – | – | 3.01 | 86.3 | – | – | [46] |

There are two main techniques widely used for spent magnet recycling, viz., pyrometallurgy and hydrometallurgy (Table 4). The pyrometallurgical processes operate at high temperatures and are thus energy-intensive while hydrometallurgical processes are the most prominent among other alternatives mostly because of their applicability to varying magnet chemistries. Computer HDDs contain small magnets (weighing 50–70 g) which can be shredded as a whole for further use in metal extraction techniques [54]. The magnets used in wind turbines and EV motors are for comparatively larger in size and thus have to pre-treated before subjecting to recycling [55]. Demagnetization is required to remove the strong magnetic field before dismantling. There are two processes that are mostly used for demagnetization, namely thermal and non-thermal treatment. In thermal treatment, the spent magnet is heated above the Curie temperature of NdFeB magnets (400–500 °C) where magnetic properties disappear.

### *3.5 Phosphors*

Phosphors are an important component in lamps/lighting and display (CRT, LCD, and plasma screen). Fluorescent lighting mainly relies on REEs like yttrium, lanthanum, europium, cerium, terbium, and gadolinium. In addition to rare earth, the fluorescent tubes also contain Al, Cu, and glass, apart from mercury which terms these wastes as hazardous. Due to the wearing out of CRT display devices, the proportion of phosphor used in fluorescent lamps has risen sharply by 90% since 2011 and thus the demand for REEs [56]. Waste CRTs are a huge resource of REEs, with each CRT contributing to approximately 1-10 g phosphor which thereby accounts for 15% REEs embedded. The growth in demand for REE in phosphors is approximate > 9% per annum.

In India, ~ 690 million units of FLs/CFLs were produced in 2016 at a CAGR of 27%. The irony stays with the poor recycling rate (<30%) of these wastes, which, however, accounts for 2400 tons per year of phosphor powder. Fluorescent lamps contain 3% (w/w) phosphor powder as a thin layer coated inside a glass tube, which constitutes half by weight percentage halo-phosphate phosphor, 1/5th by weight fine glass powder and silica, 1/10th by weight alumina as well as rare earths phosphors [57]. Numerous methods have been adopted to recover metals from phosphor powders viz., simple distillation, pyro metallurgy, hydrometallurgical processes, or combination of all [53, 55].

### *3.6 Batteries*

Lithium-ion batteries (LIBs) have been the secret sauce fuelling the explosion of super portable, wireless electronics such as smartphones, laptops, tablets, and tiny wireless products such as Bluetooth headphones. They are also what make the modern

**Table 4** Recycling of magnets and phosphors for metal extraction

| Magnet source and Composition | Pre-treatment | Leaching process and parameters | | | | | Recovery | References |
|---|---|---|---|---|---|---|---|---|
| | | Size | Lixiviant | Time | Temp | PD | | |
| 0.95% Al, 1% B, 1.42% Co, 0.22% Cu, 1.08% Dy, 61.09% Fe, 0.15% Mn, 25.38% Nd, 2.03% Ni, 2.62% Pr, 0.02% Si | – | 50–100 µm | Stage 1: 4 M $HNO_3$ | 24 h | 25 °C | 20 g/L | 100% | [50] |
| | | | Stage 2: Aqua Regia | 1 h | 80 °C | | | |
| 61.1% Fe, 25.3% Nd, 2.62% Pr, 1.08% Dy, 1.42% Co, 1% B | Roasting and demagnetization | 50–100 µm | 1 M $CH_3COOH$ | 24 h | 25 °C | 30 g/L | > 95% REEs, Fe & Co | [51] |
| | | | 1 M $C_6H_8O_7$ | | 25 °C | 30 g/L | 100% REEs, > 95% Fe & Co | |
| 25.81 Nd, 62.67 Fe, 0.96 B, 6.1 Pr, 1.8 Dy, 0.19% Gd and 0.87 Co, | Roasting at 800 °C, 120 min | < 160 µm | 0.6 M HCl + 2 g/L $NaNO_3$ | 2 h | 180 °C | 100 g/L | 98% REEs. < 0.1% Fe | [44] |
| 38.46% Fe, 16.33% Nd, 4.61% Pr, 0.24% Dy, 3.72% Al, 0.42% Co, 2.45% B, 0.06% Cu, 0.08% Ga, 2.17% C, | – – | – - | 2 M $H_2SO_4$ | 24 h | 25 °C | 10 g/L | 62.69%Fe, 27.88% Nd, 6.87% Pr, 0.15% Dy, 0.64% Al, 0.8% Co, 0.97% B | [52] |
| 30.2% $Y_2O_2S$:Eu , 60.4% ZnS , 4.3% $SiO_2$ , 0.98% PbO , 2.63% Al , 0.325% BaO , 0.552% $K_2O$ , 0.613% Others | – – | – — | 3 M $H_2SO_4$ + 4 vol.% $H_2O_2$ | 1 h | 55 °C | 5% | 99% Y and Eu | [53] |

electric vehicle viable and able to feature ranges of 500 km and more. Lithium-ion batteries have enabled electric vehicles such as the Tesla Model X to boast ranges above 500 km and are a big part of the success of EVs. But what to do with the mounting heap of spent batteries coming from electronics and EVs. But increasingly people are worried about what to do with the mounting heap of spent lithium-ion batteries that are full of things like nickel, cobalt, and lithium and if mishandled can catch fire. Automakers who have pledged $300 billion towards the development of 700 new models of electric cars, mostly by 2025, need a secure supply of those raw materials. Recycling of the critical materials from spent LIBs not only addresses demand but also eliminates the deleterious effects of mining, brine extraction, transportation of precursors, energy consumption, GHG emissions, thereby making cost imbalance settled [58].

Lead-acid batteries dominate the global rechargeable battery market, followed by LIBs, nickel-metal hydride (NiMH), nickel–cadmium (NiCd), and lithium polymer. Table 5 depicts the metal content in various batteries. To achieve sustainability in the processing of LIBs with different battery chemistries, various recycling flowsheets have been developed globally by leading industrial players like Umicore, Recupyl, Toxco, Batrec, Sumitomo, Duesenfeld, etc. Battery recycling is divided into three segments, viz., dismantling, leaching, and separation. Dismantling involves the crushing, shredding, flotation by vibratory separator, followed sieve-based separation of electrode material from the less desired components like case, fluff, etc. Leaching is carried using hydrometallurgy/pyrometallurgy/both [19]. Among these, hydrometallurgy employs acids for solubilization of Li, Ni, Co, and Mn followed by solvent extraction, precipitation, crystallization without residue/slag as depicted in various studies (Table 6).

## 4 Industrial Wastes

### 4.1 *Ferrous Waste Recycling*

Iron making involves various unit processes like agglomeration, sintering, blast furnace; and steel making uses basic oxygen furnaces and electric arc furnace, steel refining, that generates voluminous wastes, largely governed by physico-chemical factors like design, operational methods and feed material [68, 69]. Blast furnace operations generates hazardous wastes, viz., dusts, slag, which contain lead, chromium, zinc, cadmium and possess difficulty for processing or handling. Although these wastes are rich in metal values, their recycling faces constraints due to accumulation of harmful metals in the process [68]. Recycling of ferrous dusts is restricted due to volatile compounds of Zn, Cd, As, and Pb. Zinc occurs as zinc oxide and zinc ferrite in steelmaking wastes based on the use of galvanized steel scrap as feed which can be processed by carbothermic reduction followed by zinc condensation [70].

**Table 5** Material composition in secondary batteries by weight (%)

| Materials | Secondary Batteries | | | | | | | |
|---|---|---|---|---|---|---|---|---|
| | Ni–Cd | NiMH | | | | Li-ion | Li-Polymer | $LiFePO_4$ |
| | | Button | Cylindrical | Prismatic | HEV | | | |
| Fe | 40–45 | 31–47 | 22–25 | 6–9 | 36 | 24.5 | 1 | 30–35 |
| Ni | 18–22 | 29–39 | 36–42 | 38–40 | 23 | | 2 | – |
| Zn | – | – | – | – | – | – | – | – |
| Mn | – | – | – | – | – | – | – | – |
| Cd | 16–18 | – | – | – | – | – | – | – |
| Co | | 2–3 | 3–4 | 2–3 | 4 | 27.5 ($LiCoO_2$) | 35 ($LiCoO_2$) | – |
| Li | – | – | – | – | – | | | 3.5–5.2 |
| REE | | 6–8 | 8–10 | 7–8 | 7 | – | 16 | – |
| Cu | – | – | – | – | – | 14.5 | 15 | 2.8–5.2 |
| Al | – | – | – | – | – | | – | 1.8–2.8 |
| K | | 1–2 | 1–2 | 3–4 | – | – | – | – |
| Trace metals | – | – | – | – | 2 | – | 15 | 17–18 (P) |
| Graphite/carbon | – | 2–3 | <1 | <1 | | 16 | – | >3 |
| Plastics/Polymer | – | 1–2 | 3–4 | 16–19 | 18 | 14 | 3 | – |
| $H_2O$ | – | 8–10 | 15–17 | 16–18 | – | – | – | – |

Among these, the high content of 28–30% Zn, 8–14% Pb makes EAF dust attractive for devising processing options. Generically, the zinc oxide is amenable to acid leaching but the process does not dissolve zinc ferrite due to its refractory nature. Zinc ferrite can be only dissolved in reducing environment but results in iron contamination in liquor [70]. The sinter plant dust also can serve as a resource of potassium for applications in fertilizer manufacturing [71].

## *4.2 Aluminium Associated Wastes*

The process of aluminium production generates huge quantity of dross which is a suitable raw material for recycling/replenishment of left over metal values [72]. Dross is hazardous and hence recycling of this waste is very essential. Drosses are generally differentiated as white and black dross based on metal quantity. White dross produced during skimming of molten metal in primary and secondary smelters as a fine powder contain 15–17% extractable aluminium. Black dross generated during aluminium recycling contains lesser metal content (11–16% Al) due to slag and above 40% salt in comparison to white dross.

Aluminium is extracted from the dross via the rotary salt furnace process [72, 73] in presence of salt flux (ratio of dross to flux being 1:2). Saline slags containing low metallic aluminium and high ratios of $Al_2O_3$, NaCl, KCl and traces of AlN, $AlC_3$

**Table 6** Acid leaching of spent LIBs in metal extraction from various sources

| Material | Leaching conditions | | | | Extraction/separation-parameters | Process features | References |
|---|---|---|---|---|---|---|---|
| | Acid concentration | Temp (K) | Time (h) | S/L ratio (g/L) | | | |
| Ash from LIBs | 4 M HCl | 363 | 18 | 50 | NaClO precipitation at pH 3 and NaOH addition at pH 11 | 100% Co, 99.99% Ni extraction | [59] |
| Spent LIBs of mobile | 3 M HCl + 0.3 M $H_2O_2$ | 353 | 1.5 | 20 | – | 99.4% Li extraction | [60] |
| Spent LIBs | 1 M $H_2SO_4$ + 30% $H_2O_2$ | 353 | 2 | 714 | 1 M citric acid Precipitation in 2 h, 278 K; calcined at 723 K, 4 h | 88.3% Co extraction; Crystalline $LiCoO_2$ synthesized | [61] |
| | 4 M $H_2SO_4$ + 10% $H_2O_2$ | 358 | 2 | 100 | SX by 25% P507; $(NH_4)_2C_2O_4$ precipitation at pH 1.5 | 98% Co, 97% Ni and Li separation | [62] |
| Spent laptop LIBs | 2 M $H_2SO_4$ + 0.075 M $NaHSO_3$ | 368 | 2 | 100 | Precipitation by Oxalic acid, NaOH, $Na_2CO_3$ | 92–99% Co, Ni, Mn and Li extraction. Products of $MnCO_3$, $NiCO_3$, $CoC_2O_4$, $Li_2CO_3$ | [63] |
| Scrap LIBs | 1 M $HNO_3$ + 1% $H_2O_2$ | 353 | 1 | 20 | 100% Co and Li extraction | Nitrous gas generated | [64] |
| Cylindrical spent LIBs of mobile phone | 1.25 M ascorbic acid | 343 | 0.33 | 25 | 94.8% Co and 98.5% Li extraction | Ascorbic acid replaces use of $H_2O_2$ | [65] |
| Spent LIBs | 0.4 M tartaric acid and 0.02 M ascorbic acid | 353 | 5 | 2 | >95% Li, Co extraction | Cobalt precipitated as Co-oxalate | [66] |

(continued)

**Table 6** (continued)

| Material | Leaching conditions | | | | Extraction/separation-parameters | Process features | References |
|---|---|---|---|---|---|---|---|
| | Acid concentration | Temp (K) | Time (h) | S/L ratio (g/L) | | | |
| Spent LIBs | 0.5 M citric acid with 0.55 M $H_2O_2$ + 90 W ultrasonic power | 333 | 5 | 25 | >96% Co extraction | 100% Li extraction | [67] |

and $Al_2S_3$ is generated during rotary furnace melting. In absence of flux, aluminium slags are generated. Another waste worth exploring is the aluminium dust which contains metallic aluminium apart from metal oxides, silicon and its derivatives (oxide, nitride, and hydride), zinc, iron, copper, fluorides, etc. This is generated during metal manufacturing and slag milling unit operations in centrifugal dust collection system [74].

The other common wastes are spent pot lining (SPL), Bayer's sludge, and red mud. Aluminium smelters generates a significant amount of spent pot lining (SPL), produced due to mechanical and chemical disintegration of refractory and insulating materials at high-temperature and stringent electrolysis. On average, SPL contains 18–40 kg/t Al [75] apart from fluorine compounds and cyanides terming this as a hazardous waste. It is anticipated that for every ton of metal generated, nearly 20–40 kg SPL is generated and gets accumulated to the tune of1-2 million tons worldwide per annum. India generates 0.7–1.4 mT of SPL per annum with the current annual primary metal production capacity of 3.426 million tons.

Vanadium is a critical metal being used in multiple applications like steel, catalysts and quite recently in energy storage grids. Vanadium exists in various primary resources like vanadinite, carnotite, patronite, and titaniferrous magnetite [76]. There are considerably vast secondary resources of vanadium like spent catalysts, red mud, Bayer's sludge, uranium tailings, etc. Vanadium content in the bauxite varies from 0.05–0.25% $V_2O_5$ depending upon the inception and nature of bauxite deposit. During the digestion of bauxite with caustic soda solution, about 30–35% of vanadium present in bauxite is extracted and remaining accumulates in Bayer's sludge ($V_2O_5$: 10–18%). This vanadium sludge is the potential source for the production of ammonium metavanadate and vanadium pentaoxide ($V_2O_5$), by hydrometallurgical processes [77].

During Bayer's process for alumina production, Bauxite residue is generated which is also called as red mud. To produce 1 ton aluminium, it requires 70,000 cans as compared to 2 metric tons of bauxite. But recycling aluminium cans does not result in wastes; however, 2 metric ton bauxite will also yield 1 ton red mud. Extensive efforts have been carried out worldwide to devise suitable applications of red mud, apart from the numerous flowsheets to extract metals by hydrometallurgical (acid/alkali leaching) as well as pyrometallurgical (smelting, carbothermic reduction, fluidized bed reaction, smelting) methods [78]. On the other hand, the presence of metals like Al, Mg, Si, P, Ca, etc., weighs down its holistic utilization. Alumina content in red mud increases the fluidity and alkalinity of slag terming it unsuitable for refractory manufacturing [78].

Pyrometallurgical processes often target iron content; however, hydrometallurgy has been reported targeting critical metals like vanadium, REEs, gallium, etc. Red mud samples in Russia, Jamaica, and China have been reported with high REE content [79, 80] in the range of 89–152 ppm Sc, 290- 360 ppm Y and La, upto 590 ppm Ce. The content of REEs is relatively lower in Indian red mud as reported by Abhilash et al. [10, 77, 82, 83] who have attempted to extract REEs from these red mud for synthesis of mixed REE oxides [81, 82]. Scandium content in red mud has caught worldwide attention, and efforts are underway to process red mud for generating high pure scandium oxide [80].

Various products like cement, glass ceramics, bricks, tiles, etc. have been tested by various groups from red mud, to maximize utilization and curtail its disposal [83]. Despite the use of red mud in water remediation, GHG sequestrations, and other civil works, the content of metals like Al, Fe, Ca, Mg, Si is a major concern.

### *4.3 Zinc Wastes*

Zinc wastes are valuable resources for base metals like Zn, Co, and Ni, apart from precious metals like Ge, Sb, Ag, etc. There have been many attempts to recuperate important metals from zinc tailings and residues [84]. The residue/zinc cake containing Zn, Pb, and Fe when digested in sulphuric acid followed by roasting and brine leaching can be used to extract 86% Zn and 89% Pb [85]. Alongside, there exists several other methods to process these zinc-based industrial wastes and residues. An example of abandoned mines in Turkey revealed prospects to recover metals like zinc, iron, and lead, from flotation tailings and slag followed by a two-stage acid leaching [86–88] for 77.5% Zn. Similarly, copper smelter slags and zinc hydrometallurgical process residues were also treated with sulphuric acid followed by roasting which selectively removed iron as hematite; and the residue on water leached to completely extract Zn, Cu, and Cd [87]. Applied. GEOCOAT™ recovers zinc from the low tenor ZnS concentrate (17–20% Zn, 3–6% Fe, 10–12% S and low copper) using the resource at a zinc mine in Namibia, via column leaching of 90 days to recover 91% Zn [84]. Although there have been numerous studies on the use of zinc mine wastes as backfill, the extraction of metals from them seems to be a more profitable option [85, 89].

## 5 Conclusions

Keeping given the evolving patterns of environmental remediation and sustainable growth, the review article attempts to deliberate on the sustainable substitutes of primary resources, otherwise termed as secondary resources through reprocessing of anthropogenic and industrial wastes. Anthropogenic wastes like CRTs, LCDs, PCBs, magnets, phosphors, and batteries contain huge proportions of quantities of base and critical metals namely In, Au, Ga, Ge, Ag, Zn, Cu, Pb, Mn, Nd, Y, Eu, Li, Ni, Co, etc. Mining and metallurgical operations in of ferrous and non-ferrous industries produce significant amounts of waste and contain metals like Fe, Zn, REEs, Al, etc. Notwithstanding the environmental threats concomitant with the processing of these wastes, their needs to be developed a circular economy model which promotes the zero-waste concept and ensures the generation of flowsheets that can address critical metal scarcity and extract them at reduced cost and cause less emissions.

The picture put forth in this chapter deliberates on the necessity for surplus research and generate outputs that can influence policy making thereby enabling investigations on the described raw materials. Technological innovations should be able to map such resources, quantify their worth based on metal value and pollution aspect using life cycle assessment, and empower mission mode programs to replenish metals from such wastes. The extent of funding from public organizations must be complemented in a bigger way from private ones as well, to ensure the practice and commercialization.

Keeping the changing scenario of primary metal scarcity and over-accumulation of secondary resources, and long-run influences of various recycling policies an important avenue for future research that can add to the metal repository in the country from secondaries can be developed. A cohesive methodology, encompassing multi-disciplinary processes, and unit operations with one common goal in alleviating critical metal demand and reduction of waste simultaneously must be developed.

## References

1. H.I. Abdel-Shafy, M.S.M. Mansour, Egypt. J Petro. **27**, 1275 (2018)
2. S. Dutta, D. Neela Priya, B. Chakradhar, T.S. Sasi Jyothsna, Value added by-products recovery from municipal solid waste. In *Waste Valorisation and Recycling*, ed. S. Ghosh (Springer, Singapore, 2019). https://doi.org/10.1007/978-981-13-2784-1_7
3. J. Buffington, R. Peterson, JOM **65**, 941 (2013)
4. G. Gaustad, E. Olivetti, R. Kirchain, Resour. Conserv. Recycl. **58**, 79 (2012)
5. V.Y. Risonarta, J.Anggono, Y.M.Suhendra, S.Nugrowibowo, Y.Jani, Strategy to Improve Recycling Yield of Aluminium Cans, E3S Web of Conferences 130, 01033 (2019)
6. S. Arya, S. Kumar, J Cleaner Prod. **271**, 122707 (2020)
7. V. Forti, C.P. Baldé, R. Kuehr, G. Bel. *The Global E-waste Monitor 2020: Quantities, Flows and the Circular Economy Potential* (Bonn, Geneva and Rotterdam: United Nations University/United Nations Institute for Training and Research, International Telecommunication Union, and International Solid Waste Association, 2020).
8. M.D. Rao, K.K. Singh, C.A. Morrison, J.B. Love, RSC Adv. **10**, 4300 (2020)
9. C.A. Lucier, B.J. Gareau, Electronic waste recycling and disposal: an overview. In *Assessment and Management of Radioactive and Electronic Wastes*, ed. Hosam El-Din Saleh (2019). https://doi.org/10.5772/intechopen.85983
10. S. Abhilash, A. Tabassum, P. Ghosh, E. Meshram, vanHullebusch. Metals (2021). https://doi.org/10.3390/met11020317
11. X. Liu, Q. Tan, Y. Li, Z. Xu, M. Chen, Front. Environ. Sci. Eng. **11**(5), 10 (2017)
12. H. Lee, B. Mishra, Miner. Process. Extrac. Metall. Rev. **41**(3), 153 (2020)
13. F. Pita, A. Castilho, Minerals **8**(11), 517 (2018)
14. E.Y. Kim, M.S. Kim, J.C. Lee, B.D. Pandey, J. Hazard, Mater. **198**, 206 (2011)
15. J.S. Niederkorn, S. Huszar, GoldBull. **17**(4), 128 (1984)
16. C.H. Lee, L.W. Tang, S.R. Popuri, Waste Manage. Res. **29**(7), 677 (2011)
17. L. Li, L. Jun, R. Yang, X.Z. Xiao, J.C. Ren, W. Feng, A. Khalil, J. Power Sour. **218**, 21 (2012)
18. L.S.S. de Oliveira, M.T. Carneiro, W.D. Lima, L.H. Yamane, R.R. Siman, Detritus **10**, 62 (2020)
19. P. Meshram, B.D. Pandey, Abhilash. Resour. Pol. **60**, 9 (2019)
20. S.A. Ismail, N.H. Jamil, H. Kamarudin, M.A.A. Mohd Salleh, Appl. Mechanics Mater. **754**, 567 (2015)

21. U. Jadhav, C. Su, M. Chakankar, H. Hocheng, Bioresour. Bioprocess. **4**, 42 (2017)
22. M.C. Hespanhol, P.R. Patrício, L.H.M. da Silva, S.J.R. Vargas, T.C.S. Rezende, R.A. Campos, J. Braz. Chem. Soc. **30**(11), 2376 (2019)
23. M.P. Asensio, E. Abas, J.L. Pinilla, M. Laguna, Eur. J. Inorg. Chem. **22**, 2203 (2020)
24. K. Zhang, Y. Wu, W. Wang, B. Li, Y. Zhang, T. Zuo, Resour. Conserv. Recycl. **104**, 276 (2015)
25. X. Zeng, F. Wang, X. Sun, J. Li, ACS Sustainable Chem. Eng. **3**(7), 1306 (2015)
26. K. Takahashi, A. Sasaki, G. Dodbiba, J. Sadaki, N. Sato, T. Fujita, Metall. Mater. Trans-A **40A**, 891 (2009)
27. J. Li, S. Gao, H. Duan, L. Liu, Waste Manag. **29**(7), 2033 (2009)
28. J. Ruan, Y. Guo, Q. Qiao, Procedia. Environ. Sci. **16**, 545 (2012)
29. B. Swain, C. Mishra, H.S. Hong, S. Cho, Waste Manag. **57**, 207 (2016)
30. L. Rocchetti, A. Amato, V. Fonti, S. Ubaldini, I. da Michelis, B. Kopacek, F. Vegliò, F. Beolchini, Waste Manage. **42**, 180 (2015)
31. P. Hadi, P. Gao, J.P. Barford, G. McKay, J. Hazard. Mater. **252**, 166 (2013)
32. H. Wang, S. Zhang, B. Li, D. Pan, Y. Wu, T. Zuo, Resour. Conserv. Recycl. **126**, 209 (2017)
33. W.A. Bizzo, R.A. Figueiredo, V.F. de Andrade, Mater **7**, 4555 (2014)
34. Y. Zhou, K. Qiu, J. Hazard. Mater. **175**, 823 (2010)
35. M. Kaya, Recovery of metals and nonmetals from waste printed circuit boards (PCBs) by physical recycling techniques. In *Energy Technology 2017. The Minerals, Metals & Materials Series*, ed. L. Zhang (Springer, Cham, 2017). https://doi.org/10.1007/978-3-319-52192-3_43
36. C. Hagelüken, Acta. Metall. Slovaca **12**, 111 (2006)
37. X. Wang, X. Lu, S. Zhang, J. Hazard. Mater. **244**, 342 (2013)
38. A. Anić-Vučinić, G. Bedeković, R. Šarc, V. Premur, J. Sustain. Dev. Energy Water Environ. Syst. **8**(3), 590 (2020)
39. L.H.Yamane, V.T. de Moraes, D.C.R. Espinosa, J. Alberto, S. Tenório, Waste Manag. **31**(12), 2553 (2011)
40. M.Sahan, M.Ali Kucuker, B.Demirel K.Kuchta, A.Hursthouse, Int. J. Environ. Res. Public Health **16**, 887 (2019)
41. M. Ghodrat, M. Rashidi, B. Samali, Int J. Waste Resour. **8**, 358 (2018)
42. D. Fontana, F. Forte, R. de Carolis, M. Grosso, Waste Manag. **45**, 325 (2015)
43. M. Annamalai, K. Gurumurthy, J. Air Waste Manage. Assoc., **71**(3), 315 (2020)
44. F. Liu, A. Porvali, J.Liang Wang, H. Wang, C. Peng, B.P.Wilson, M. Lundström, Miner. Eng. **145**(1), 106097 (2020)
45. J. Szałatkiewicz, Pol. J. Environ. Stud. **23**(6), 2365 (2014)
46. E. Yazici, H. Deveci, I. Alp, A. Akçil, R. Yazici, In. Proc. XXV International Mineral Processing Congress (IMPC) 2010, Australia, pp. 4009–4015 (2010)
47. U. Jadhav, H. Hocheng, Sci. Rep. **5**, 14574 (2015)
48. S.P. Kumar, S. Govindaradjane, T. Sundararajan, Int. J. Engg. Res. Appl. **3**(2), 469 (2013)
49. X. Xu, S. Sturm, Z. Samardzija, J. Scancar, K. Markovic, K.Z. Rozman, Green Chem. **22**, 1105 (2020)
50. M. Gergoric, C. Ekberg, M.R.S.J. Foreman, et al., J. Sustain. Metall. **3**, 638 (2017)
51. M. Gergoric, A. Barrier, T.J. Retegan, J. Sustain, Metall. **5**, 85 (2019)
52. T. Yingnakorn, P. Laokhen, L. Sriklang, T. Patcharawit, S. Khumkoa, Mater. Sci. Forum **1009**, 149 (2020)
53. X. Yin, Y. Wu, X. Tian, J. Yu, Y.N. Zhang, T. Zuo, A.C.S. Sustain, Chem. Eng. **4**, 7080 (2016)
54. J. Yang, T. Retegan, C. Ekberg, Hydrometallurgy **137**, 68 (2013)
55. A. Akcil, Y. Ibrahim, P. Meshram, S. Panda, Abhilash. J. Chem. Technol. Biotechnol. **96**, 1785 (2021)
56. S. Shaw, J. Chegwidden, Global drivers for rare earth demand (Roskill Information Services, 2012)
57. K. Binnemans, P.T. Jones, J. Rare Earths **32**(3), 195 (2014)
58. P.Meshram, Abhilash, B.D. Pandey, Global outlook on the availability of critical metals and recycling prospects from rechargeable batteries. In *Critical and Rare Earth Elements: Recovery from Secondary Resources*, ed. Abhilash and A. Akcil (CRC Press, Boca Raton, 2019), pp. 37–58

59. M. Joulié, R. Laucournet, E. Billy, J. Power Sourc. **247**, 551 (2014)
60. Y. Guo, F. Li, H. Zhu, G. Li, J. Huang, W. He, Waste Manag. **51**, 227 (2016)
61. Y.J. Li, G.S. Zeng, Hydrometallurgical process for recovery and synthesis of $LiCoO_2$ from spent lithium-ion batteries. IEEE Proc. Int. Conf. Electric Technol. Civil Engg, Lushan, China (2011), pp. 6009–6011
62. L. Chen, X. Tang, Y. Zhang, L. Li, Z. Zeng, Y. Zhang, Hydrometallurgy **108**, 80 (2011)
63. P. Meshram, B.D. Pandey, T.R. Mankhand, Chem. Engg. J. **281**, 418 (2015)
64. L. Li, R. Chen, F. Sun, F. Wu, J. Liu, Hydrometallurgy **108**, 220 (2011)
65. J.Y. Li, X.L. Xu, W.Q. Liu, Waste Mana. **32**(6), 1209 (2012)
66. G.P. Nayaka, K.V. Pai, G. Santhosh, J. Manjanna, Hydrometallurgy **161**, 54 (2016)
67. L. Li, L. Zhai, X. Zhang, J. Lu, R. Chen, F. Wu, K. Amine, J. Power Sourc. **262**, 380 (2014)
68. E. Matinde, G.S. Simate, S. Ndlovu, The J. South Afr. Inst. Mining Metall. **118**, 825 (2017)
69. P.J.W.K. deBuzin, N.C. Heck, A.C.F. Vilela, J. Mater. Res. Technol. **6**(2), 194 (2017)
70. X. Lin, Z. Peng, J. Yan, Z. Li, J.Y. Hwang, Y. Zhang, G. Li, T. Jiang, J. Cleaner Prod. **149**, 1079 (2017)
71. Z. Liu, Y. Zong, J. Hou, Adv. Appl. Ceramics **115**(3), 144 (2013)
72. M.Satish Reddy, D. Neeraja, Sådhanå, **43**, 124 (2018)
73. A. Meshram, R. Jha, S. Varghese, Materials Today: Proceedings **46**(3), 1487 (2021)
74. N. Unlu, M. Drouet, Resour. Conserv. Recycl. **36**(1), 61 (2002)
75. I.V. Flores, F. Fraiz, R.A.L. Junior, M.C. Bagatini, J Mater Res Technol **8**(1), 33 (2019)
76. P.Meshram, Abhilash, J. Kumari, B.D. Pandey, Russian J. Non-Ferrous Metals. **57**, 4, 338 (2016)
77. H.A. Abhilash, P. Meshram, R.B. Meshram, S. Jha, J.N. Patel, M.K. Soni, K. Rokkam, S. Mashruwala, Separation Sci. Tech. **56**(18), 3183 (2021)
78. Y. Liu, R. Naidu, Waste Manag. **34**(12), 2662 (2014)
79. K. Hammond, B. Mishra, D. Apelian, B. Blanpain, JOM **65**, 340 (2013)
80. M. Ochsenkühn-Petropulu, K.S. Hatzilyberis, L.N. Mendrinos, C.E. Salmas, Ind. Eng. Chem. Res. **41**(23), 5794 (2002)
81. A. Akcil, N. Akhmadiyeva, R. Abdulvaliyev, Abhilash, P. Meshram, Miner. Process. Extrac. Metall. Rev., **39**(3), 145 (2018)
82. S. Abhilash, M.K. Sinha, B.D. Sinha, Pandey. Int. J. Min. Proc. **127**, 70 (2014)
83. Abhilash, P.Meshram, S. Sinha, B.D. Pandey, V. KrishnaKumari, S. Kar, Metall. Res. Technol., **116**(2), 210 (2019)
84. S. Kumar, R. Kumar, A. Bandopadhyay, Resour. Conserv. Recycl. **48**(4), 301 (2006)
85. H. Fourie, P.H. van Rooyen, S. Rupprecht, T. Lund, N.M. Vegter, Exploitation of a massive low grade zinc-lead resource at Rosh Pinah Zinc Corporation, Namibia. In Proc. Fourth South Afr Conf Base Metals, Namibia, pp. 109–118 (2007)
86. M.D. Turan, H. Soner, A.F. Tümen, Hydrometallurgy **75**, 169 (2004)
87. C.S. Ek, Silver recovery from zinc hydrometallurgical residues. In *Proc. Int Symp sponsored by Copper, Nickel, Cobalt, and Precious Metals Committee of the Minerals, Metals and Materials Society and the International Precious Metals Institute*, ed. M.C. Jha, S.D. Hill (Las Vegas, Nevada, 1989), pp. 391–401
88. H. Kurama, F. Göktepe, Environ. Progress **22**(3), 161 (2003)
89. R.B. Ngenda, L. Segers, P.K. Kongolo, Base metals recovery from zinc hydrometallurgical plant residues by digestion method. In Proc. Hydrometallurgy Conf., SAIMM (2009) pp. 17–30

# Process Development and Stability Modeling of High-Speed Micromachining

**Rinku Kumar Mittal, Kundan Kumar Singh, and Ramesh Kumar Singh**

## 1 Introduction

Free-form surface features are increasingly used in precision manufacturing industries for telecommunications, electronics, defense and biomedical applications. Surface microtexturing used in various industries to enhance the essential functions such as tribological, wetting, biocompatibility, sustainability and cleanliness [1]. Optical free-form surfaces have wide applications in illumination, imaging, non-imaging, etc. [2]. Microneedles are microscopic applicators used to deliver vaccines or other drugs and have applications in pharmaceutical and biomedical research [3]. Microholes, slots, and channels are used for microfluidic applications in biomedical industries. Micromilling process is one of the micromanufacturing processes, which is widely used to produce 3D complex microscale components with an accuracy of sub-micron level. A variety of engineering materials with improved surface finish and higher material removal rate (MRR) can be processed using micromilling process, which cannot be accomplished from other micromanufacturing techniques, such as micro-EDM, lithography, laser machining, etc. [4].

Although the micromilling process has several benefits, this process has some limitations and challenges. The main limitation of the process is lower flexural stiffness due to the use of small diameters of the end mills. The limited stiffness can lead

R. K. Mittal
Department of Mechanical Engineering, Indian Institute of Technology Guwahati, Guwahati, Assam, India
e-mail: rkmittal@iitg.ac.in

K. K. Singh
Department of Mechanical Engineering, Birla Institute of Science and Technology, Pilani, India
e-mail: ksingh@hyderabad.bits-pilani.ac.in

R. K. Singh (✉)
Department of Mechanical Engineering, Indian Institute of Technology Bombay, Mumbai, India
e-mail: rsingh@iitb.ac.in

A. Shrivastava et al. (eds.), *New Horizons in Metallurgy, Materials and Manufacturing*,
Indian Institute of Metals Series, https://doi.org/10.1007/978-981-19-5570-9_6

to catastrophic tool failure, especially during machining of high-strength steels and titanium alloys which find widespread industrial use. The limitation of low flexural stiffness can be countered by the use of high rotational speeds, which will reduce the feed per flute (chip loads) and hence the cutting forces. However, the high rotational speeds in addition with lower flexural stiffness, could induce dynamic instability in the process. This dynamic instability called chatter is a self-excited vibration, which may deteriorate the surface quality and tool life. In addition, as the spindle operates over a wide range of rotational speeds (from 50,000 RPM to 150,000 RPM, sometimes even wider range), a dynamically stable structure is required to avoid vibration encountered due to resonance at higher order modes. Therefore, to create complex miniature features without chatter, it is important to design a high-speed micromachining structure which must possess static and dynamic stability for precise machining.

A significant amount of work has been reported in the literature on the investigation of chatter phenomena in the milling process at both macro and microscales. Tobias [5] and Tlusty [6] presented the mechanism of chip regeneration and developed a stability model for single point cutting operations. They determined the limiting depths of cut at different spindle speeds, which separate the stable and unstable operational regimes. Altintas and Budak [7, 8] suggested an analytical model to predict chatter of the milling process using zero-order approximation and multi-frequency method. A time-domain solution for a delay dynamic model based on semi-discretization was presented by Insperger et al. [9], to predict the stability in milling, which includes the time varying parameters directly. Vogler et al. [10] and Malekian et al. [11] considered the plowing and rubbing due to the minimum chip thickness effect in the micro-end milling force model and stability model. A stability model presented by Adetoro et al. [12] considered the cutting force coefficients and axial immersion angle as a function of axial depth of cut. Afazov et al. [13] included the effect of nonlinear cutting forces due to the run-out on the stability limits in micromilling. It may be noted that at very high rotational speeds, the misalignments and run-out amplification may change the dynamic behavior of the system during machining [14]. Li et al. [15] formulated a 2DOF model in rotational coordinates to see the rotational effects such as Coriolis and centripetal effects. They observed a significant difference in the stability with consideration of the tool rotation. Movahhedy et al. [16] incorporated the gyroscopic terms in a finite element model for the determination of the frequency response of the system. They investigated the effect of gyroscopic couple on the dynamic stability of a high-speed spindle system which resulted in lower stability limits in high-speed milling.

The gyroscopic effects become more prominent at high rotational speeds which can potentially affect the stability limits. Traditionally, only translational degrees of freedom have been used for stability modeling, which does not capture the effect of gyroscopic couples. Hence, it is imperative to incorporate the rotational degrees of freedom in the stability model for accurate identification of stability boundaries in high-speed micromilling. It is known that the minimum chip thickness effect and size effect significantly affect the cutting forces and stability of micromilling process [17]. In addition, the cutting velocity also affects the strain rate and heat generated,

**Table 1** Desired specifications for the linear stages

| Property | XY stages | Z stage |
|---|---|---|
| Accuracy | <±1 μm | <±1 μm |
| Resolution | 1 μm | 1 nm |
| Repeatability | 1 μm | 100 nm |

which can alter the machining behavior. Hence, it is important to include the cutting speed and the chip load (feed/flute) dependent cutting force coefficients for accurate prediction of the stability of the micromilling process. Consequently, this chapter is focused on the following aspects:

- Design and fabrication of a high-speed micromachining center.
- Development of single, two, and multiple degrees of freedom stability models.
- Creation of surface features for industrial applications.

## 2 High-Speed Micromachining System Development

### *2.1 Design Approach for Micromachining System*

The quality of a precision machine tool depends upon three main factors: accuracy, stability, and durability. All these features depend upon the quality of mechanical structure, guide way system, spindle, and control system. The specification of the linear stage is given in Table 1. These stages have brushless servo motor control, which is able to provide high acceleration for extremely smooth motion and accuracy without any wear, heating, and cogging. They use crossed roller guides and precision ground ball screws, which are driven by directly coupled brushless slot-less servo motors. The Z-stage is a linear motor with a pneumatic counterbalance.

An IBAG made spindle that can achieve a maximum speed of 140,000 RPM has been used. It contains ceramic bearings, which have anti-friction properties. Hence, very low friction and low wear at high-speed is achieved. The machine structure is very critical in high-speed micromachining. Static, modal, frequency response, transient dynamic, and impact analyses have been carried out for different structural configurations to obtain an optimal structure with suitable performance. The design methodology for the micromachine development is shown in Fig. 1.

### *2.2 Optimum Design of Micromilling Machine Tool*

The dimension of the base is 750 mm × 600 mm × 150 mm. This base contains two slots to fix the columns of the machine. These slots provide extra rigidity to the whole machine. The column structure is a bridge type frame used for mounting

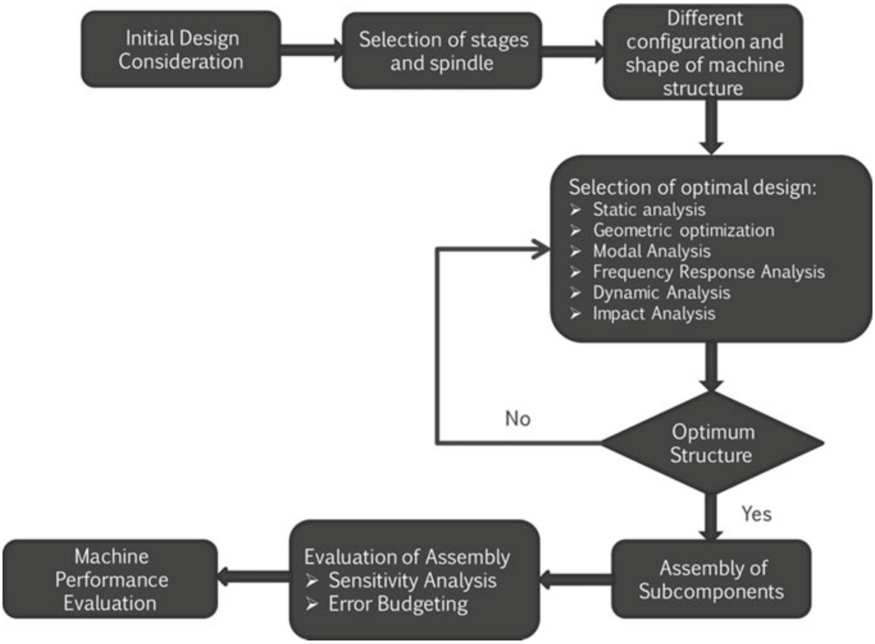

**Fig. 1** Flow chart for design and fabrication of high-speed micromachining center

the Z stage unit on it. The bases of the columns are kept in slots of the machine base. Two columns are 250 mm apart. The spindle holding fixture is designed to hold the spindle containing a flange. This is made of mild steel. This is designed to provide good rigidity (due to two ribs) while holding the spindle. Taper supports are provided to support column structure. These supports are provided to restrict the forward bending movement of the column structure of the machine. These supports are positioned such that they are in compression during bending of columns. These are made of granite to dampen the vibration. Fig. 2 shows the CAD model of the optimal geometry.

### 2.3 *Final Experimental Setup*

A high-speed micromachining center (Fig. 3) developed as per the optimal design at the Machine Tools Laboratory, Indian Institute of Technology Bombay, is used to conduct the experiments. The three-axis micromachining center has DC brushless servomotor driven stacked ball screw $x$–$y$ stages and linear motor driven $z$ stage. The positioning resolution and accuracy of $x$ and $y$ stages are 0.5 $\mu$m and $\pm$ 1 $\mu$m, respectively. The z stage is pneumatically counterbalanced at two ends with a positioning resolution of 5 nm. The micromachining center is equipped with a high-speed

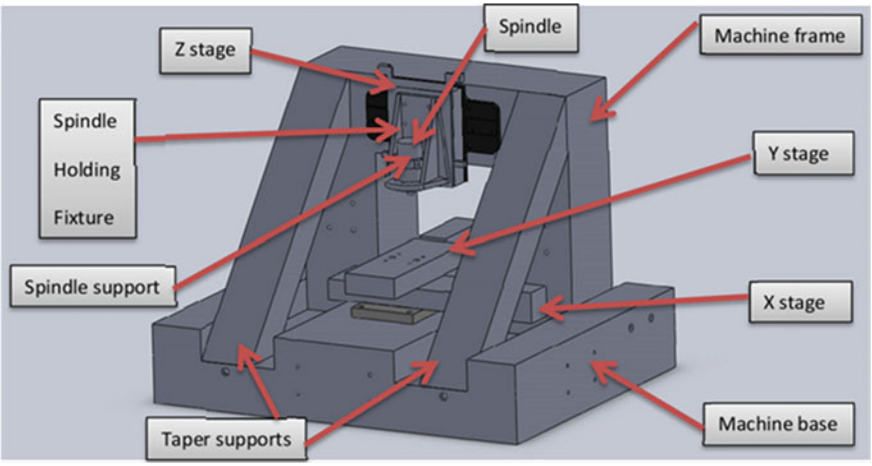

**Fig. 2** CAD model of micromachine

spindle mounted on the $z$ stage with a maximum speed of 140,000 rpm. The spindle is driven by AC synchronous electric motor. The average torque of this spindle is ~4.3 N-cm. All the stages are fixed on a granite structure which is placed on a vibration isolation table. Three component cutting forces were measured using a tabletop dynamometer (Kistler MiniDyn 9256C1). The two accelerometers made by Kistler® (model:8640A50) with a sensitivity of 97.3 mV/g were used for measurement of accelerations in two orthogonal directions (feed and normal to feed directions). The velocity of the cutting tool in the feed direction was measured by Laser Doppler Vibrometer (Polytec® model: NLV 2500). The topography of the machined surface has been analyzed using Alicona Infinite Focus® optical measurement system. A data acquisition (NI DAQ) system was used to collect the measurement data from all sensors and devices.

## 3 High-Speed Micromachining Process Modeling

### *3.1 Single Degree of Freedom (SDOF) Stability Model*

The machine tool structure is assumed as a spring-mass-damper system with single degree of freedom, as shown in Fig. 4. The lumped mass at tool tip can move into the $Y$ direction, which is normal to end mill feed direction. It may be noted that the tool deflection in the $Y$ direction will affect the workpiece surface significantly.

The machine tool system will be excited by cutting forces in $Y$ direction only. Therefore, the equation of motion of the SDOF model can be written in $Y$ direction as follows,

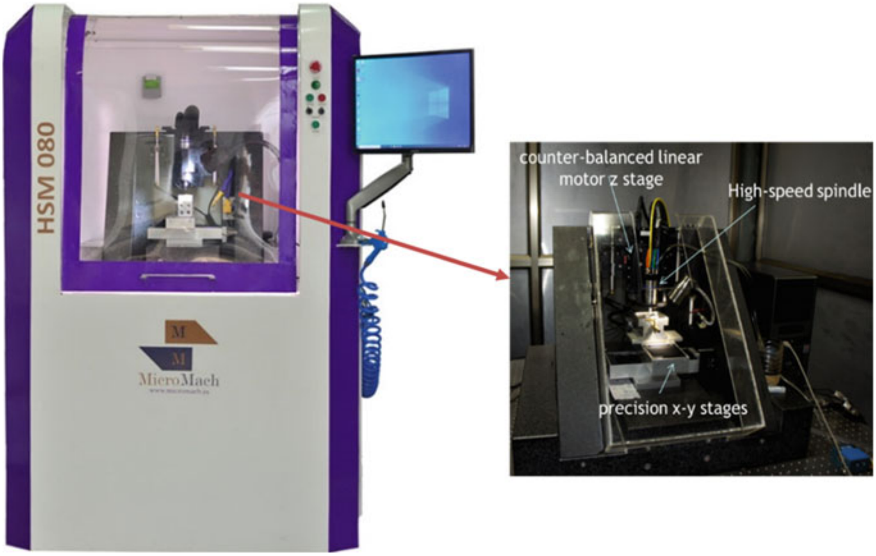

**Fig. 3** Three-axis high-speed micromachining center developed at Machine Tools Lab, IIT Bombay

**Fig. 4** Schematic of micromilling process

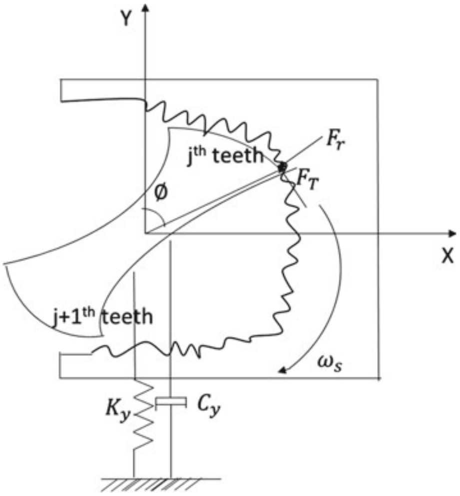

$$\ddot{y} + 2\zeta\omega_n\dot{y} + \omega_n^2 y = \frac{\omega_n^2}{k_y}\sum_{j=1}^{N} F_{yj} \tag{1}$$

where $k_y$ is the spring constant, $\omega_n$ is the natural frequency, and $\zeta$ is the damping coefficient at the tool tip. N is the number of flute of the microcutter. To capture the size effect and minimum chip thickness effect in micromilling process, the cutting force coefficients are assumed as a nonlinear function of cutting speed ($V$) and chip load ($f_t$) as,

$$K_{\mathrm{tc}} = K_1 V^{p1} f_t{}^{q1} \tag{2}$$

$$K_{\mathrm{rc}} = K_2 V^{p2} f_t{}^{q2} \tag{3}$$

where $K_1$, $K_2$, *p1, q1, p2,* and *q2* are constants which can be determined experimentally.

To determine the nonlinear cutting force coefficients as a function of cutting speed and chip load, experiments were conducted at different spindle speeds and feed rates. Cutting forces in $X$ and $Y$ directions were measured to determine the tangential and radial cutting forces via coordinate transformation. The root mean square (RMS) values of cutting forces were used to determine the tangential and radial cutting force coefficients. To estimate the nonlinear cutting force coefficients, the least square best fit approach (regression analysis) is used. The cutting velocity and chip load dependent cutting force coefficients are as follows [18].

$$\mathrm{K}_{\mathrm{tc}} = 665.2 V^{-0.1542} f_t{}^{-0.3972} \tag{4}$$

$$K_{\mathrm{rc}} = 418.8 V^{-0.0879} f_t{}^{-0.3709} \tag{5}$$

Following is the characteristic equation of the system obtained for an SDOF chatter model [10, 11].

$$\det[[I] - \frac{1}{2}\left(1 - e^{-j\omega_c T}\right) K_{\mathrm{tc}} a_{\mathrm{lim}} [A_0] H_y(i\omega_c)] = 0 \tag{6}$$

The limiting depth of cut for stable machining for a selected chatter frequency ($\omega_c$):

$$a_{\mathrm{lim}} = \frac{2\pi}{N\alpha_y \left(K_1 V^{p1} f_t^{q1}\right) \mathrm{Re}[H_y(i\omega_c)]} \tag{7}$$

where $N$ is the number of flutes, and $H_y(i\omega_c)$ is frequency response function in the y direction given by,

$$H_y(i\omega_c) = \frac{\omega^2}{k(\omega^2 - \omega_c^2 + 2i\zeta\omega\omega_c)} \tag{8}$$

where ω is the natural frequency, and $\omega_c$ is the chatter frequency.

The limited depth of cut, which will depend on the spindle rotational speed, can be determined from Eq. (7). However, estimation of modal parameters at tool tip such as: the natural frequency, spring constant, and damping constant is required. Methodology to determine the dynamic parameters at tool tip is shown in the following paragraph.

For stability analysis of the micromilling process, prediction of the tool tip dynamics is essential. Experimental modal analysis (EMA) has been performed to determine the modal parameters at the tool tip. The direct frequency response function (FRF) ($\Phi_{11}(\omega)$) and cross FRF ($\Phi_{21}(\omega)$) were determined experimentally by obtaining the displacement data at tool shank and tool tip by excitation of tool at shank using impulse hammer. Using the $\Phi_{11}(\omega)$ and $\Phi_{21}(\omega)$, direct FRF at the tool tip ($\Phi_{22}(\omega)$) can be estimated by using the reciprocity theory as follows,

$$\Phi_{22} = \frac{X_2(\omega)}{F_2(\omega)} = \frac{(\Phi_{21}(\omega))^2}{\Phi_{11}(\omega)} \tag{9}$$

where $\Phi_{11}(\omega) = \frac{X_1(\omega)}{F_1(\omega)}$ and $\Phi_{21}(\omega) = \frac{X_2(\omega)}{F_1(\omega)}$, where $X_1(\omega)$ and $X_2(\omega)$ are the displacement of the cutting tool in the frequency domain at shank and tool tip, respectively, due to excitation at the shank.

The curve fitting method is used to identify the dynamics parameters from the experimentally determined FRF, as shown in Fig. 5.

The stability lobe diagram has been generated by prediction of chatter free depths of cut at different spindle speeds by using Eq. (7). Stability limits were compared considering both cutting velocity and chip load dependent and constant cutting force

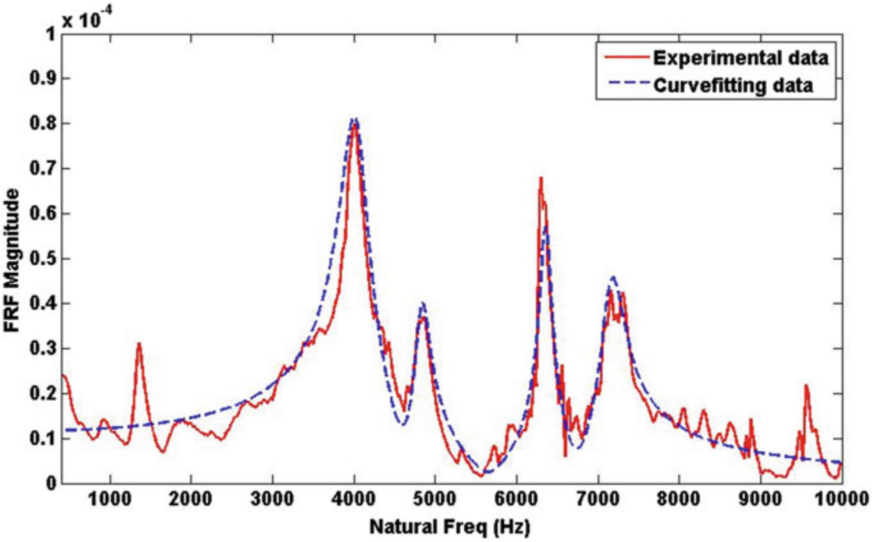

**Fig. 5** Experimental and curve fitted frequency response function at the tool tip

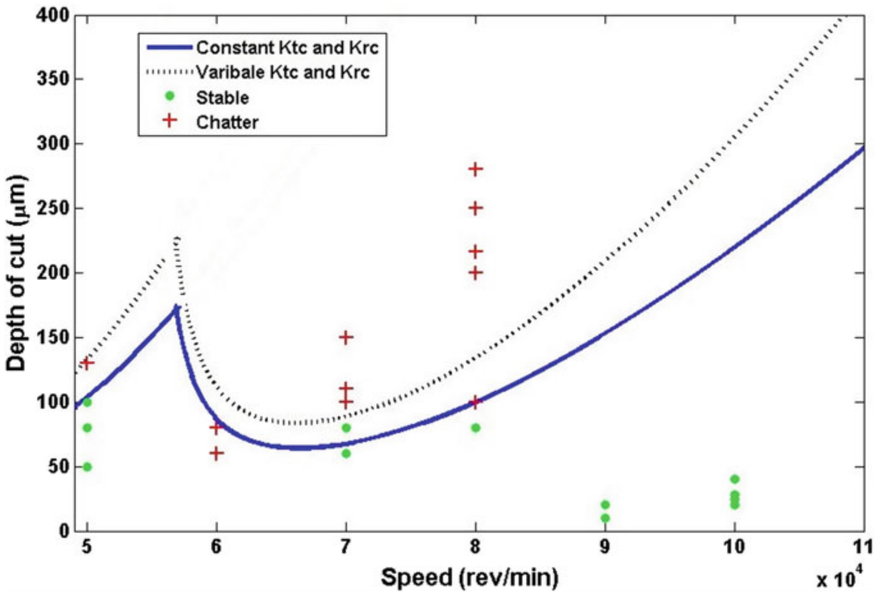

**Fig. 6** Theoretical stability boundaries with experimentally validated depths of cut for feed of 3 μm/flute

coefficients, as shown in Fig. 6. Experimental chatter onset was also shown in Fig. 6 to validate the predicted stability limits. At higher spindle speeds, stability limits are higher for cutting velocity and chip load dependent cutting force coefficients. This increase in the predicted stability boundaries can be attributed to fact that the cutting forces vary nonlinearly with cutting velocity and chip load. It can be seen that a SDOF model may not be appropriate at high spindle speeds; hence, higher order models may be required.

## *3.2 Two Degrees of Freedom Model*

Stability lobe diagrams can be generated using the following characteristic equation of the 2DOF machine tool system,

$$\det\left[[I]-\frac{1}{2}\left(1-e^{-i\omega_c T}\right)K_{\mathrm{tc}}a_{\mathrm{lim}}[A_0][\Phi(iw_c)]\right]=0 \tag{10}$$

where $A_0$ is the time invariant directional cutting coefficient vector dependent on immersion angle, $\omega_c$ is the chatter frequency, and $\Phi(\mathrm{i}\omega)$ is the FRF at tool tip.

A 2DOF machine tool system has been used in this formulation where the cutting force coefficients are function of the cutting speed and chip load. By solving Eq. (10), stable axial depth of cut can be calculated from,

$$a_{\lim} = -\frac{2\pi}{NK_{tc}(V, f_t)}\lambda_R(1 + \left(\frac{\lambda_I}{\lambda_R}\right)^2) \tag{11}$$

where $\lambda_I$ and $\lambda_R$ can be determined by assuming starting and exit immersion angle for slot milling operation in the characteristic equation (Eq. 10).

It may be noted that there is no closed-form solution for finding the spindle speed ($n$) as $K_r$ is also a function of $n$. Hence, a novel iterative scheme based on Newton–Raphson method has been developed to find the roots of the following transcendental equation [19].

$$\frac{60\omega_c}{2Nn} = 2\text{k}\pi + \cot^{-1}\left(\frac{\pm R - K_r I}{K_r R \pm I}\right) k = 1, 2, 3 \ldots. \tag{12}$$

Figure 7 shows the flow process for identifying the critical depth of cut as a function of rotational speed (stability lobe diagrams). For a selected chatter frequency, Eq. (12) is solved iteratively to determine the spindle speed, which will be a root of the transcendental equation. The limiting depth of cut is calculated using this spindle speed. The modal parameters of the tool tip ($k$, $\zeta$ and $\omega_n$) are required for the prediction of stability limits which can be determined from Fig. 5. Figure 8 shows the predicted stability limits for dry machining. Experimental chatter onset shows a good agreement with expected limiting depths of cut for 70,000, 80,000, 90,000, and 100,000 rpm. For very small diameter tools (~100 μm or lower), the extremely low flexural stiffness coupled with high rotational speeds can induce gyroscopic couple which can affect the stability limits.

## 3.3 Rotor Dynamics-Based Higher Order MDOF Stability Model for High-Speed Micromilling

The gyroscopic effects become more prominent at high rotational speeds, especially for very small diameter tools (~100 μm or lower). Hence, the effect of additional rotational degrees of freedom on prediction of stability limits has been investigated in this work [20]. In this proposed higher order stability model, rotational degrees of freedom have also been considered by using flexible bearing support at the ends of the tool, as shown in Fig. 9. The flexible bearing supports are assumed at the clamping end and tool tip end. A lumped mass is assumed at the center of mass, with four degrees of freedom: two displacements $x_G$ and $y_G$, and two rotations about the x and y axes which are $\theta_x$ and $\theta_y$, respectively.

The Lagrange method is used to derive the following equations of motion in the translational and rotational directions for lumped mass at the center of micro-end mill,

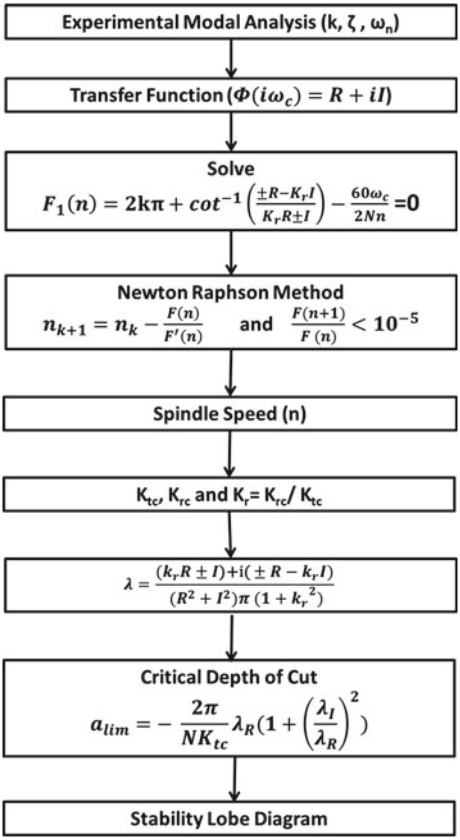

**Fig. 7** Flow process to generate the stability lobe diagram (SLD)

$$m\ddot{x}_G + \alpha_x^{'}\dot{x}_G + \alpha_x x_G - \gamma_x^{'}\dot{\theta}_{yG} - \gamma_x\theta_{yG} = F_x \tag{13}$$

$$m\ddot{y}_G + \alpha_y^{'}\dot{y}_G + \alpha_y y_G + \gamma_y^{'}\dot{\theta}_{xG} + \gamma_y\theta_{xG} = F_y \tag{14}$$

$$I_x\ddot{\theta}_{xG} + I_z\omega\dot{\theta}_{yG} + \gamma_y^{'}\dot{y}_G + \gamma_y y_G + \delta_y^{'}\dot{\theta}_{xG} + \delta_y\theta_{xG} = -bF_y \tag{15}$$

$$I_x\ddot{\theta}_{yG} - I_z\omega\dot{\theta}_{xG} - \gamma_x^{'}\dot{x}_G - \gamma_x x_G + \delta_x^{'}\dot{\theta}_{yG} + \delta_x\theta_{yG} = bF_x \tag{16}$$

where

$\alpha_q = k_{q,1} + k_{q,2}, \alpha_q^{'} = c_{q,1} + c_{q,2}$
$\gamma_q = k_{q,1}a - k_{q,2}b, \gamma_q^{'} = c_{q,1}a - c_{q,2}b$
$\delta_q = k_{q,1}a^2 + k_{q,2}b^2, \delta_q^{'} = c_{q,1}a^2 + c_{q,2}b^2; q = x, y$

The second term in Eqs. (15) and (16) is the linearized gyroscopic couple about the x and y axes, respectively. The equations of motion for a multiple degrees of

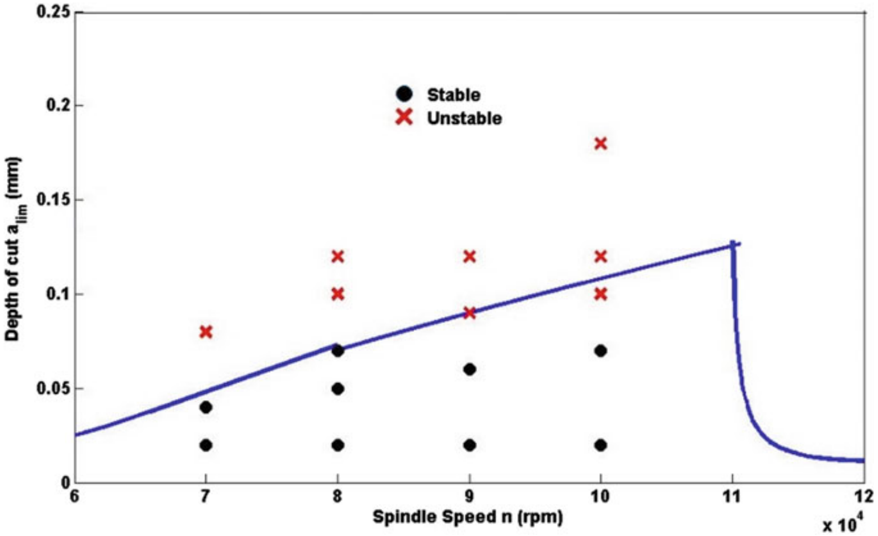

**Fig. 8** Experimentally validated stability lobe diagrams for 2DOF model

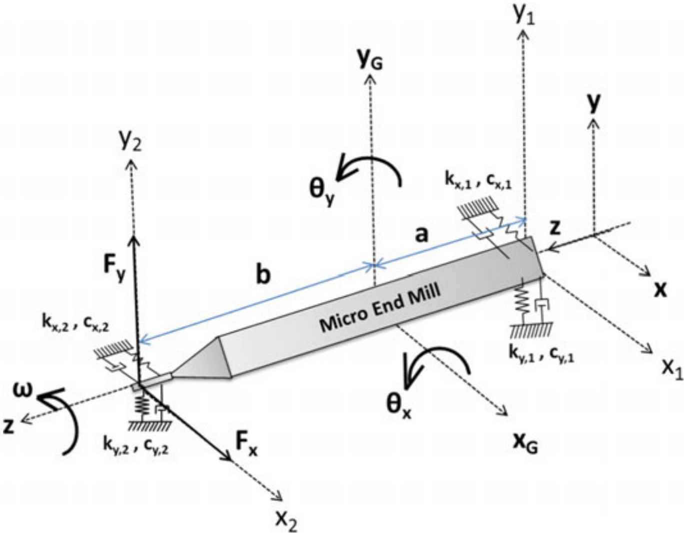

**Fig. 9** Micro-end mill as a rotor

freedom stability model consisting of both translational and rotational degrees of freedom can be written in the following matrix form:

$$M\ddot{\Phi} + C\dot{\Phi} + K\Phi = F \tag{17}$$

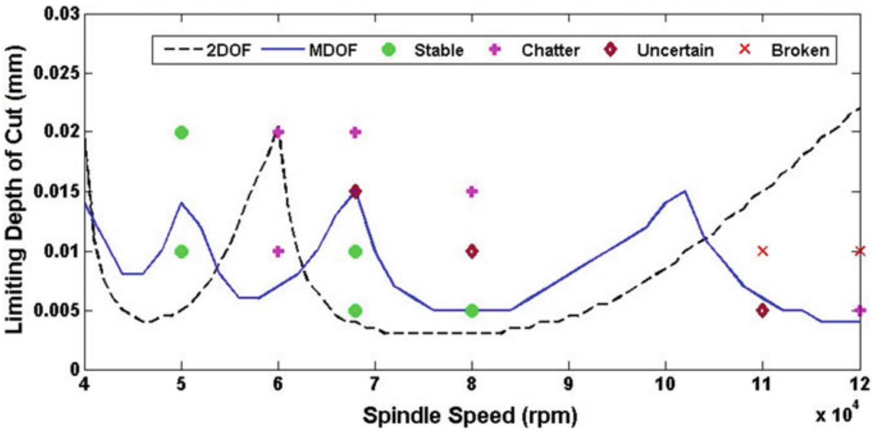

**Fig. 10** Stability lobe diagrams with experimental chatter onset

where $M$ is the mass matrix, $C$ is the damping matrix having the gyroscopic component and $K$ is the stiffness matrix. $\Phi$ is the vector of displacement variables, and $F$ is the force matrix determined using dynamic force modeling.

Figure 10 shows the stability lobe diagram with experimental chatter onset. It can be seen that at high spindle speeds (>100,000 rpm), the MDOF chatter model shows a much better agreement. Hence, using a higher order model is imperative to predict stability limits at very high rotational speeds as the effect of the gyroscopic couple becomes pronounced, especially for miniature tools (~100 μm in diameter). Using translational degrees of freedom alone at higher rotational speeds (>100,000 rpm) results in very high errors. However, at lower speeds, the two translational degrees of freedom can capture the stability limits with reasonable accuracy. There are additional lobes in the MDOF model, and a phase shift is observed between the stability lobes predicted by 2DOF and MDOF models. The MDOF also captures the location of islands of stability more accurately than the 2DOF model. The chatter onset experiments in one of the islands of stability (at ~68,000 rpm) show that limits predicted by MDOF are much closer to the experimental onset of chatter.

## 4 Creation of Features via High-Speed Micromachining

Demand of high precision components is growing in modern strategic sectors. Further, industries are facing challenges in developing new fabrication technologies for miniaturization of these components. Mechanical micromachining has several advantages over other MEMS processes due to its capability of producing complex, high-precision geometries with microfeatures in a wide range of materials. Micromilling has been shown to be a very versatile and rapid method for the removal of material and the creation of microcomponents. Figure 11a shows a surface

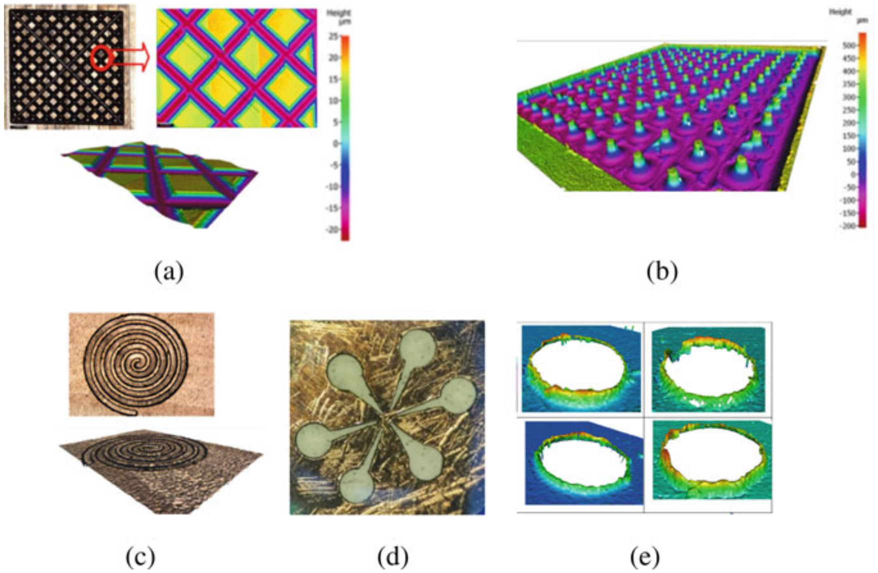

**Fig. 11** **a** textured surface; **b** array of microneedles; **c** spiral channel; **d** mask of thin film; **e** microholes

microtexture which is created using a ball end mill of 200 µm. Microtexturing finds various applications in various fields of engineering to enhance the functions such as tribological, wetting, biocompatibility, and sustainability. Microtextures on artificial biomedical implants enhance sustainability and life cycle by better implant-tissue interface, cell-adhesion, and cell proliferation [1].

Figure 11b shows an array of microneedles on Ti alloy which are formed using an end mill of size 300 µm. The upper diameter of the tapered needle is 20 µm, and the base diameter is 200 µm. The height of the needle is 500 µm. Microneedles have extensive scientific and industrial interests due to minimal invasion in the skin, low cost, excellent drug efficacy, and relative safety. The microneedles can offer a relatively low cost and minimally invasive tool for the treatment of multiple cosmetic and dermatologic conditions [21].

A spiral microchannel made by a 200 µm end mill is shown in Fig. 11c. Microchannels as a heat dissipation device have applications in diverse fields including: aerospace; automotive; bioengineering; cooling of gas turbine blades; micro-electronics; and thermal control of film deposition [22]. Spiral microchannels are used in size-based microparticles separation which is essential for many biomedical and chemical analysis [23].

Figure 11d shows the thin film copper mask which can be used in etching applications. These features are created on copper film of thickness 100 µm. These masks are usually used in photolithography and etching applications. Thin film copper masks are used to protect the substrate in the pulsed laser deposition process. Figure 11e show the microholes created using 100 µm microdrill. The size of microholes can be in range from 20 to 500 μm. Microholes have applications in various industries such as biomedical, automotive, and semiconductor industries.

## 5 Conclusions and Future Work

This chapter is primarily focused on process development and modeling the high-speed micromachining process and its dynamic stability. A higher order MDOF chatter model based on rotordynamics has also been developed to capture the effect of gyroscopic couple on the stability for low stiffness micro-end mills. It has been observed that machining stability is indeed affected by gyroscopic couple induced by rotational speeds. This work can potentially be extended in future to include the following issues:

- Extension of this process to other materials to create knowledge base for micromachining of other materials.
- Identification and modeling of nonlinearities in high-speed micromilling process.
- Development of a generalized stability model with minimal experimental inputs for a wide range of materials, tool geometries, and process conditions.

## References

1. D. Singh Patel, V. Agrawal, J. Ramkumar, V.K. Jain, G. Singh, J. Mater. Process. Technol. **282** (2020)
2. L. Nagdeve, V.K. Jain, J. Ramkumar, Manuf. Rev.
3. A.J. Guillot, A.S. Cordeiro, R.F. Donnelly, M.C. Montesinos, T.M. Garrigues, A. Melero, Pharmaceutics
4. J. Chae, S.S. Park, T. Freiheit, Int. J. Mach. Tools Manuf. **46**, 313 (2006)
5. B.N. Lewendon, Aspheric optics: design, manufacture, testing
6. J. Tlusty, M. Polacek, Int. Res. Prod. Eng. ASME, **465** (1963)
7. E. Budak, Y. Altintaş, J. Dyn. Syst. Meas. Control. Trans. ASME **120**, 31 (1998)
8. Y. Altintaş, E. Budak, CIRP Ann.-Manuf. Technol. **44**, 357 (1995)
9. T. Insperger, G. Stépán, Int. J. Numer. Methods Eng. **55**, 503 (2002)
10. M.P. Vogler, R.E. DeVor, S.G. Kapoor, J. Manuf. Sci. Eng. (2004)
11. M. Malekian, M.G. Mostofa, S.S. Park, M.B.G. Jun, J. Mater. Process. Technol. **212**, 553 (2012)
12. O.B. Adetoro, W.M. Sim, P.H. Wen, Mach. Sci. Technol. (2012)
13. S.M. Afazov, S.M. Ratchev, J. Segal, A.A. Popov, Int. J. Mach. Tools Manuf. **56**, 28 (2012)
14. M.B.G. Jun, R.E. DeVor, S.G. Kapoor, J. Manuf. Sci. Eng. Trans. ASME **128**, 901 (2006)
15. C.J. Li, A. Galip Ulsoy, W.J. Endres, J. Manuf. Sci. Eng. Trans. ASME **125**, 39 (2003)
16. M.R. Movahhedy, P. Mosaddegh, Int. J. Mach. Tools Manuf. **46**, 996 (2006)
17. F. Ducobu, E. Filippi, Rivière-Lorphèvre, in Proceedings of the 12th CIRP Conference on Modeling of Machining Operations (2009)
18. K.K. Singh, V. Kartik, R. Singh, Int. J. Mach. Tools Manuf. **96**, 56 (2015)

19. R.K. Mittal, S.S. Kulkarni, R. Singh, Int. J. Mech. Sci. 142–143 (2018)
20. R.K. Mittal, S.S. Kulkarni, R.K. Singh, Procedia Manuf. **26**, 607 (2018)
21. J. Yang, X. Liu, Y. Fu, Y. Song, Acta Pharmaceutica Sinica B
22. L. Shang, Y. Cheng, Y. Zhao, Chem. Rev.
23. G. Guan, L. Wu, A.A. Bhagat, Z. Li, P.C.Y. Chen, S. Chao, C.J. Ong, J. Han, Sci. Rep. 3 (2013)

# Materials Degradation: Metallic Materials

**Amulya Bihari Pattnaik and Smrutiranjan Parida**

## 1 Introduction

Corrosion of metals and alloys is an important concern for their application in various engineering and medical fields. The degradation of metallic materials can lead to various components and equipment failure, leading to direct and unaccountable indirect loss. In a recent report, the National Association of Corrosion Engineers International (NACE) has predicted a corrosion loss of 4.2% of GDP for India [1]. This corrosion loss is spread across all industries, agriculture, and service sectors. The industry sector constitutes a bulk of this corrosion loss. The corrosion loss of this magnitude is not surprising given the climate, geographical location, and pollution in India. However, this calls for a more concerted approach to the mitigation, prediction, and management of corrosion in various sectors. In this light of the environmental protection and optimized resource utilization, corrosion management falls rightly into the strategy of 3R—reduce, reuse, and recycle.

Metal and alloys corrode upon contact with water and air. When the corrosion process occurs in the presence of water, it is called aqueous corrosion (Fig. 1). The "water" can be in any form. The non-noble metals naturally react with water in the presence of oxygen, which is thermodynamically favorable. The thermodynamically driven corrosion process converts metals to metal oxides, resembling the ore from which it was extracted. Ironically, all of the engineering alloys behave in this manner. Due to the same rapid corrosion tendency, a protective oxide film may form on their surface as soon as the nascent surface is exposed. The cases in point are aluminum, titanium, tantalum, and stainless steel alloys. The tantalum is immune to the chemical

---

A. B. Pattnaik · S. Parida (✉)
Department of Metallurgical Engineering and Materials Science, IIT Bombay, Mumbai, India
e-mail: paridasm@iitb.ac.in

A. B. Pattnaik
e-mail: amulyapattnaik@iitb.ac.in

A. Shrivastava et al. (eds.), *New Horizons in Metallurgy, Materials and Manufacturing*,
Indian Institute of Metals Series, https://doi.org/10.1007/978-981-19-5570-9_7

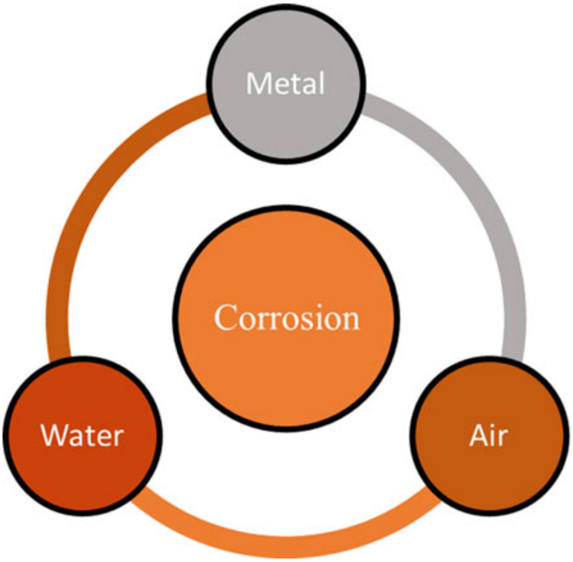

**Fig. 1** Process of aqueous corrosion of various metals and alloys

attack in nearly all environments within 150 °C temperature, due to the formation of a strongly adherent and highly protective passive film on its surface.

The oxide patina formation is one of the characteristics of metals and alloys, which is exploited as a strategy for corrosion protection and prevention. This strategy has been very well demonstrated by stainless steel and other nonferrous alloy systems. Continuous research, spanning over decades, focused on developing corrosion-resistant alloys based on this strategy.

Ferrous metals and alloys are the most widely used materials for engineering applications, 80% of which are carbon steel, low alloy steel, or mild steel [2]. In contrast to the stainless steels (obtained when 12% or more Cr is alloyed), these low alloy steels are not protected by passivity—the ability to form the protective passive oxide surface film. The battle against corrosion is perennial when protecting these alloys, widely used for economic reasons. Other corrosion protection strategies have also been developed and used appropriately, such as barrier coating and cathodic protection, for these alloys. They may be applied with due consideration to the cost, robustness, and convenience in various application conditions. However, a self-protective metallic structure requiring limited servicing is the desire of the industry and all users. The other important motivation for research in this field is to reduce the environmental load due to the synthesis and applications of passive protection methods, such as paint and coatings. It is pertinent to mention that much research is also being carried out to develop an environmentally benign formulation and impart multifunctionality to the paints.

The history of the research to develop the weather protection ability in low alloy steels is fascinating. It shows how the efforts are made to inculcate the inherent oxide formation capability in the low alloy steel by alloying addition at various points of time. The research to find the appropriate alloying combinations also led to the development of various low alloy steel compositions. These efforts underlie an understanding of the fascinating mechanism of oxide formation in low alloy steel. This chapter attempts to give a historical perspective on the alloy development of the low alloy steel for corrosion protection achieved by forming an adherent and protective oxide patina.

## 2 Alloy Development for Corrosion Resistance

The purpose of modifying the alloy composition is to impart oxide patina formation capability without affecting the desirable mechanical properties. The corrosion resistance in these alloys exploits the ability to form a protective oxide layer on the surface. The nature of the iron oxide layer formed depends on the composition of the alloy and the environmental conditions to which the alloy is exposed. The protectiveness of the rust/oxide layer depends on its chemistry, which is also influenced by environmental and alloying additions. For example, in iron and low/mild steels, the effect of composition and environmental condition are critical in determining the protectiveness of rust layers.

The development of weathering steels (WS) results from efforts to achieve self-protection in the ferrous alloy by imparting patina forming ability. The WS are low alloy steels that exhibit higher resistance to corrosion than plain carbon steel, due to an adherent protective oxide layer known as patina [3]. In these low carbon steels, the alloying elements such as Cu, Mn, Si, P, Ni, and Cr are added up to a total of no more than 5 wt% [4]. In certain environmental conditions, the corrosion rate is governed by the nature of the oxide layer formed on the steel surface [5]. Extensive research in this field has identified the formation of major iron oxides such as $\alpha$-FeOOH (Goethite), $\gamma$-FeOOH (Lepidocrocite), $\beta$-FeOOH (Akageneite), and Fe3O4 [6]. For these alloys, the existence of a wet/dry cycle is a very fundamental requirement for the formation of the protective layer [7]. For example, the steel surfaces sheltered from direct sunlight and rainfall tend to form loose, flaky protective patina than the surfaces exposed to sunlight and rainfall [8, 9]. It has also been seen that the presence of sulfur dioxide in certain industrial atmospheres accelerates the formation of a protective patina. However, the protective oxide layer does not form in extreme marine environments [10]. These examples underline the importance of the environment along with alloying addition in successful corrosion resistance alloy development. Therefore, an account of the mechanism of oxide layer growth, depending on the alloying elements and the environmental condition, provides an in-depth outlook and challenges in developing the oxide-forming low alloy steels.

## 3 Historical Development of Corrosion-Resistant Low Alloy Steels

Historically, the development of corrosion-resistant low alloy steels can be traced back to the research on copper steel and the WS. In 1910, Buck [11] carried out atmospheric corrosion studies of copper steel in rural, industrial, and marine atmosphere of the USA. He observed that the presence of copper in steel improves corrosion resistance. The copper-bearing steels were found to be 1.5–2 times more protective than the regular steels. In 1916, Buck and Handy [12] performed more detailed atmospheric corrosion studies on copper-bearing steels with copper contents varying from 0.004 to 2.12 wt%. The copper content up to 0.15 wt% resulted in a lower corrosion rate in most cases, and increasing the copper content further had a little effect on the corrosion rate. The ASTM Committee A-5 [13] also carried out large-scale studies on copper-bearing steels in rural, industrial, and marine environments. The alloy with as low as 0.04 wt% copper showed excellent atmospheric corrosion-resistant properties, and a copper level of 0.15 wt% has ample corrosion resistance. In 1926, ASTM Committee A-5 [14] carried out large-scale studies on corrosion of copper-bearing steels in various locations in the USA. The study concluded that copper is beneficial for the atmospheric corrosion resistance of low alloy steels. This finding led to the development of the first commercial WS by US Steel Corporation in 1933. The WS was named under the brand USS Cor-Ten steel, where Cor-Ten refers to corrosion resistance and good tensile properties.

The role of major alloying elements in the atmospheric corrosion-resistant behavior of the WS was first explained by two major studies. First study was conducted in 1941 by ASTM Committee A-5 [15], in which 71 low alloy sheets of steel were exposed to industrial and marine environments. The study found that the rust/oxide layer was more protective in the industrial atmosphere than in the marine atmosphere. The second study was carried out in 1942 by US Steel Co. [16], in which 270 different steel samples were exposed to semirural, marine, and industrial environments. The study also observed that the oxide layer formed in the industrial atmosphere after 4 years of exposure was more protective than in the marine atmosphere. The corrosion of three different steels—plain carbon steel, Cu-bearing steel, and Cor-Ten B, in the industrial atmosphere of Kearny, New Jersey, showed superior corrosion resistance of Cor-Ten B (~6 times increase) and Cu-bearing steel (~2.5 times increase) than the plain carbon steel [16]. These results were interesting, given the effects of relative humidity, pollution gas levels, and other parameters on the oxide-forming tendency in these atmospheres.

These extensive studies [15, 16] lead to the development of two different WS specifications, one with a higher phosphorus content designated as ASTM A-242 and another with a lower phosphorus content designated as ASTM A-588. The composition of the conventional weathering steel is given in Table 1 [17].

In 1992, the US Federal Highway Administration (FHWA), the American Iron and Steel Institute (AISI), and the US Navy developed a new variety of WS for structural applications. These were known as the high-performance steels (HPSs) designated

**Table 1** Chemical compositions of conventional WS [17]

| WS | C | Mn | P | S | Si | Cu | Ni | Cr | V | Al |
|---|---|---|---|---|---|---|---|---|---|---|
| ASTM A-242 | 0.11 | 0.31 | 0.092 | 0.020 | 0.42 | 0.30 | 0.31 | 0.82 | <0.01 | 0.08 |
| ASTM A-588 | 0.13 | 1.03 | 0.006 | 0.019 | 0.25 | 0.33 | 0.015 | 0.56 | 0.038 | 0.043 |

as HPS-70 W [18]. These steels exhibited excellent mechanical properties, good weldability, and a compact protective oxide layer with strong adherence [19].

# 4 Mechanism of Oxide Layer Growth in Low Alloy Steels

## *4.1 Nature and Structure of the Oxide Layer*

In 1964, Horton [20], in his Ph.D. dissertation, reported an atmospheric exposure test of WS in industrial and marine environments. Some critical observations were made on the nature and mechanism of growth of the oxide layers formed, such as:

(a) "The dual-layer structure: a loose outer portion and an adherent inner portion".
(b) "Rust layer grows by several mechanisms: (i) by iron ions diffusing outwards through the rust to form fresh rust at the air–rust interface; (ii) at the steel–rust interface; (iii) within the rust layer to fill the cracks and pores".

According to Horton, the $Fe^{2+}$ ion diffuses through the native oxide layer to the air–oxide interface and reacts with the dissolved oxygen to form fresh rust at the outer surface.

$$2Fe^{2+} + 1/2O_2 + 5H_2O = 2Fe(OH)_3 + 4H^+ \tag{1}$$

Figure 2 shows the schematic representation of the atmospheric corrosion mechanism (and hence oxide layer formation) suggested by Horton [21]. The "membrane"—as called by the author—is where the reaction takes place and moves gradually toward the steel surface with time.

Gradually, further studies on the oxide layer formation in copper and phosphorus-containing steels were carried out. Misawa et al. [22] studied the effect of copper and phosphorus on the rust formation mechanism of low alloy steel. The formation of fine amorphous ferric oxyhydroxide/feroxyhyte (δ-FeOOH) was observed, which might act as a protective barrier against corrosion. It was proposed that, at the beginning, the $SO_2$ from the atmosphere gets absorbed on the steel surface resulting in the formation of $H_2SO_4$. This accelerates the corrosion process by the formation of large amounts of $Fe^{2+}$ ions. The formation of $Fe^{2+}$ ions results in the dissolution of copper and phosphorus. The formation of fine particles of δ-FeOOH occurs due to the catalytic

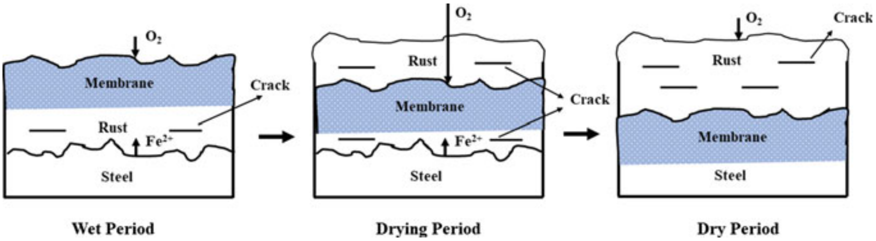

**Fig. 2** Schematic representation of atmospheric corrosion mechanism. Adapted from Horton [21]

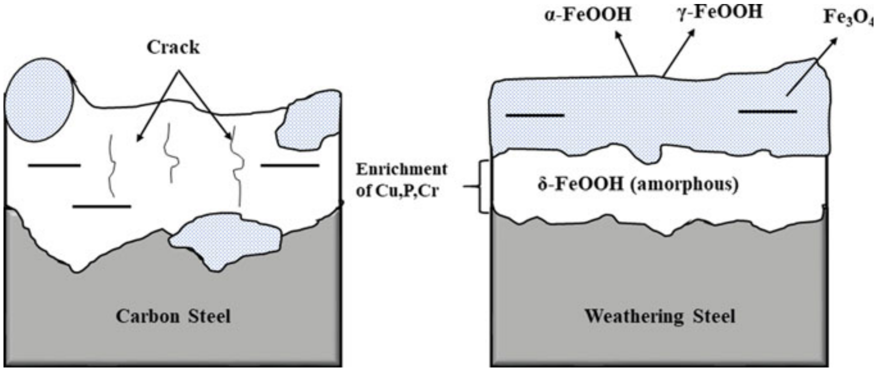

**Fig. 3** Mechanism of formation of rust layer suggested by Misawa **a** plain carbon steel **b** WS. Reproduced with permission from [22]

action of $Cu^{2+}$ and $PO^{3-}$ ions. The feroxyhyte phase forms a dense protective layer on the surface of WS, which reduces the corrosion rate by preventing the permeation of oxygen. A schematic below shows a representation of the mechanism of rust layer formed after long-term atmospheric exposure for (a) carbon steel and (b) WS, Fig. 3.

Later, Yamashita et al. [23] in 1994 studied the atmospheric corrosion behavior of mild steel and WS during 26 years of long-term exposure in the industrial atmosphere. In that study, the rust layer on the WS was found to be consisting of two layers—an outer layer which is loose and an inner layer of densely packed fine particles. The rust layer formed on the surface of mild steel consisted of many voids and microcracks. The most important observation made by Yamashita was that the outer layer mainly consisted of γ-FeOOH (lepidocrocite), and the inner layer is composed of α-FeOOH (goethite). They observed that the presence of chromium in the inner protective layer resulted in the formation of nano-size goethite, which is thermodynamically and electrochemically stable [24]. In this work, it was proposed that the initial rust layer consists of γ-FeOOH, which subsequently transformed to fine "Cr" substituted nano-size goethite particles via an amorphous ferric oxyhydroxide [$FeO_x(OH)_3$-2x] during long-term exposure. The schematic representation of the nature of the oxide layer formation proposed by Yamashita et al. is shown in Fig. 4.

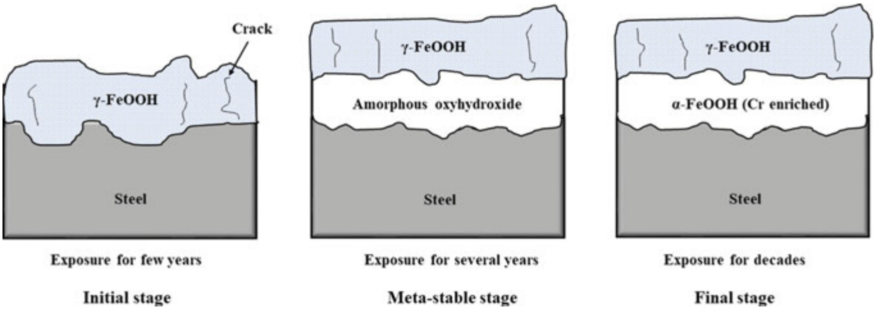

**Fig. 4** Schematic of the formation of oxide layer as proposed by Yamashita et al. Reproduced with permission from [23]

The figure depicts that the continuous wet/dry cycles during atmospheric exposure result in the dissolution of lepidocrocite and amorphous ferric oxyhydroxide precipitation. This amorphous substance transformed into a closely packed aggregate of Cr-substituted goethite. Subsequently, in 1996 Yamashita et al. [25] carried out a systematic investigation to study the compositional gradient and ion selectivity of Cr-substituted goethite. In this study, the Raman spectra of the protective oxide layer were recorded at several points with different distances from the rust/steel interface, both for the inner and the outer layers. The results of the Raman studies indicated that the outer layer mainly consisted of lepidocrocite ($\gamma$-FeOOH), and the inner layer is composed of goethite ($\alpha$-FeOOH). The outer lepidocrocite is thicker than the inner layer, which is consistent with the porous nature of the outer layer observed by others.

Yamashita et al. [25, 28] also studied the ion selectivity of the Cr-substituted goethite layer, to understand the corrosion resistance by the oxide layer. He reasoned that if the oxide layer is cation selective, it will not allow corrosive anions to ingress and cause corrosion. Therefore, the membrane potential of the Cr-substituted goethite was studied at varied KCl concentration of the solution. The variation of the transport number of $Cl^-$ ($t_{Cl^-}$) with the varied chromium content in the Cr-substituted goethite membrane was calculated. The $t_{Cl^-}$ decreased as the chromium content increased. It was concluded that at higher chromium content, the ion selectivity of the oxide layer changes from anion selective to cation selective. The iso-selectivity point (where $t_{Cl^-} = t_{K^+}$) was found to be at 3 wt% chromium. The Cr at the rust/steel interface was estimated to be around 5–10 wt%, making the Cr-substituted goethite layer cation selective. This, as proposed, prevented the ingress of $Cl^-$ and $SO_4^{2-}$ corrosive ions. Thus, the oxide layer/patina formed after long-term exposure, which was protective due to the dense aggregation of Cr-substituted fine goethite particles. The cation selective nature of the goethite layer does not allow aggressive corrosive anions to reach the steel surface.

In another study, Townsend et al. [26] of Bethlehem Steel Corporation, USA, studied the structure of the rust formed on WS exposed for 11 years in rural and industrial environments. The study found the inner layer to be porous, which comprises the mixture of lepidocrocite and goethite. The outer layer was found to be composed

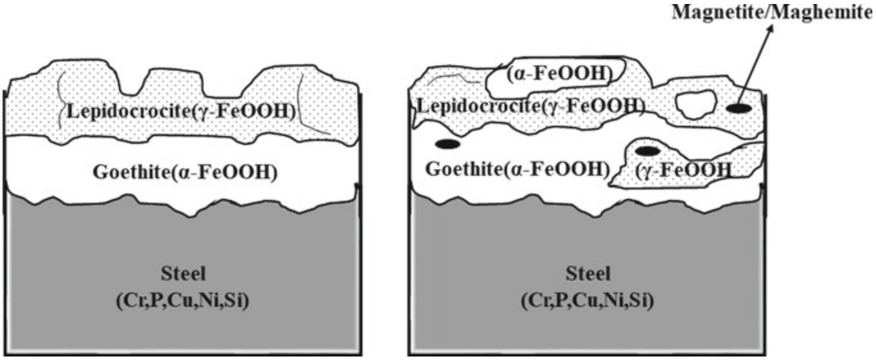

**Fig. 5** Schematic representation of the oxide layer formed on WS as proposed by Yamashita and Townsend **a** simple bilayer structure **b** irregular alternate band structure. Reproduced with permission from [27]

of hematite and magnetite. From the electrochemical measurements, they concluded that the outer layer was more passive. In contrast to the observations by Yamashita et al. [25], the study suggested that the outer layer, comprising of hematite and magnetite, continues to form as the exposure time increases and plays an important role in the protectiveness of the rust.

To resolve these differences in the observations, both groups' rust samples were exchanged between Yamashita and Townsend. They carried out parallel long-term exposure studies on similar WS samples. A common understanding was reached regarding the oxide layer structure for the samples exposed in Japan and USA. The schematic representation of the oxide layer formed is shown in Fig. 5 [27].

Yamashita and Townsend's collaboration resulted in the following conclusions on the structure of the oxide layer:

(a) The major components of the rusts were found to be Cr-substituted goethite, lepidocrocite, and a small amount of maghemite and/or magnetite.
(b) Lepidocrocite was observed in the outer layer, and Cr-substituted ultrafine goethite was observed in the inner layer. However, in some cases, goethite was also observed in the outer layer.
(c) The inner layer, consisting of densely packed Cr-substituted goethite, might be the reason behind the protectiveness of the rust layer.

Yamashita and Uchida have categorized [28] rust layer formed during prolonged exposure into three regions, such as.

(a) Region I: Initial lepidocrocite-rich region formed in few years.
(b) Region II: Amorphous phase-rich region formed after several years of exposure.
(c) Region III: Goethite-rich region formed after decades of exposure.

From all these studies, the general conclusion is that the rust layer formed on the mild steel atmospheric exposure has a bilayer structure. Both the layers are essential in overall corrosion protection, with α-layer being more compact and adherent. In the event of two layers formation, the descriptor of protectiveness must include α-FeOOH and γ-FeOOH layers, as discussed in the subsequent section.

### 4.2 Structure of the Oxide Phases

The structure and formation of ultrafine goethite particles due to the presence of chromium are explained by Yamashita et al. [29] in their work on the nanostructure of the rust using the X-ray absorption fine structure (XAFS) with X-ray synchrotron radiation. They showed that the goethite crystal structure is $FeO_3(OH)_3$ octahedron, where each $Fe^{3+}$ ion is surrounded by three $O^{2-}$ and three $OH^-$ ions. The goethite structure consists of an HCP array of anions ($O^{2-}$ and $OH^-$) stacked along the (001) direction with $Fe^{3+}$ ions occupying half the octahedral sites. It forms double chains of octahedra by edge-sharing and runs parallel to (001) direction. The double chains of octahedra are linked to the adjacent double chains by corner-sharing resulting in orthorhombic symmetry. There are two sites in the goethite structure for the Cr to substitute for (i) $Fe^{3+}$ site (ii) double chains of vacant sites. Yamashita et al. carried out extended X-ray absorption fine structure (EXAFS) on the rust samples and found that the $Cr^{3+}$ ion in the rust layer is coordinated with $O^{2-}$. It forms a complex anion ($Cro_x^{3-2x}$) with $O^{2-}$ and substitute in the double chains of vacant sites. This results in the breaking of the double chains of vacant sites as $Cro_x^{3-2x}$, which is larger in volume than $Fe^{3+}$ ions. Thus, the collapse of the double chains of vacant sites causes the formation of ultrafine crystals of goethite.

Kimura et al. [30] proposed another new concept of "Fe(O,OH)6 network" to explain the ultrafine structure of the goethite particles. The rust structure was studied using XAFS, XRD and TEM. The study found that the initial rust from the Fe(O,OH) network is similar in structure to γ-FeOOH. The Fe(O,OH) network subsequently transforms to α-FeOOH with the increase in the exposure time. They observed that the addition of chromium resulted in the formation of $Cr(O,OH)_6$ units with a different crystal structure to that of $Fe(O,OH)_6$. The formation of $Cr(O,OH)_6$ results in the distortion of the $Fe(O,OH)_6$ network. This results in the formation of ultrafine goethite particles.

### 4.3 The Protective Indices of the Oxide Film

From various studies, ample understanding was gained on the nature and structure of the protective oxide layer formed on low alloy steel and WS. Given the bilayer and composite structure of the protective film, quantifying the film's protectiveness cannot be ascribed to just one layer. In this regard, Yamashita et al. [31] showed that the ratio of goethite ($\alpha$) to lepidocrocite ($\gamma$) on the surface could be considered as an index to evaluate the protective ability of the rust layer. The study showed that the $\alpha/\gamma$ ratio increased proportionally with the exposure (Fig. 6a). Correspondingly,

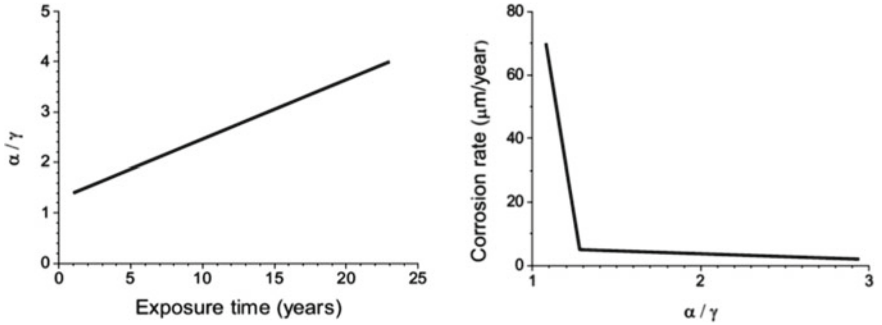

**Fig. 6** Variation of **a** $\alpha/\gamma$ ratio with the time of exposure **b** corrosion rate with $\alpha/\gamma$ ratio. Reproduced with permission from [31]

the relationship between corrosion rate and α/γ ratio (Fig. 6b). It was observed that the corrosion rate decreased as the $\alpha/\gamma$ ratio increased, and after $\alpha/\gamma$ ratio of ~ 1.4, the corrosion rate decreased by about 1/15th. Beyond $\alpha/\gamma > 2$, the rust layer was completely protective, and corrosion rate marginally varied with the $\alpha/\gamma$ ratio.

Later, Kamimura et al. [32] studied the protective ability of rust layer on weathering steels exposed to various industrial and rural environments with varied airborne salt concentrations. An increase was observed in the $\alpha/\gamma$ mass ratio of the rust layer on WS exposed to industrial and rural environments, with the exposure period. The dependence of the $\alpha/\gamma$ ratio on the exposure time is not linear for low airborne salt concentration. However, a good correlation was observed between α/γ ratio and exposure time (Fig. 7a).

At the high airborne salt concentration of 0.2 mdd and > 0.5 mdd, the correlation between α/γ ratio and exposure time is not entirely obvious. There is no correlation for > 0.5 airborne salt concentration, as shown in Fig. 7b. The relationship between the corrosion rate and the α/γ ratio (Fig. 8) in the environment with airborne salt concentrations of 0.2 and > 0.5 showed that, the corrosion rate is generally low when α/γ ratio is greater than 1; barring few cases where high corrosion rate was observed.

The results of the study show that the $\alpha/\gamma$ ratio is not always directly correlated to the corrosion rate when a large amount of airborne salts are present. The samples which do not show any correlation with the $\alpha/\gamma$ ratio contain large amounts of β-FeOOH and $Fe_3O_4$, indicating the oxide patina formation is strongly influenced by the environmental parameter, e.g., salt concentration.

Therefore, for the condition of high airborne salt, a new protective index, $\alpha/\gamma^*$ ratio, was proposed. The $\gamma^*$ represents the total mass of γ-FeOOH, β-FeOOH, and Fe3O4 phases.

However, the corrosion rate for different airborne salt concentrations showed a good correlation with the $\alpha/\gamma^*$ ratio (Fig. 9).

In another study, Hara et al. [33] investigated the protective ability of the rust layer formed on WS bridge. They proposed two protective ability indices: $\alpha/\gamma^*$ and $(\beta + s)/\gamma^*$, where $\alpha$ is the mass ratio of crystalline α-FeOOH, $\gamma^*$ is the total of

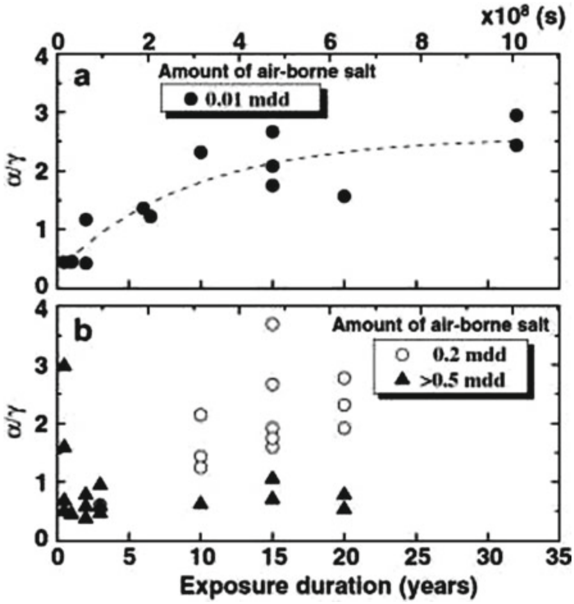

**Fig. 7** Correlation of $\alpha/\gamma$ ratio with exposure time for **a** 0.01 mdd (mg/dm$^2$/day) airborne salt concentration **b** 0.2 mdd and > 0.5 mdd airborne salt concentration. Reproduced with permission from [32]

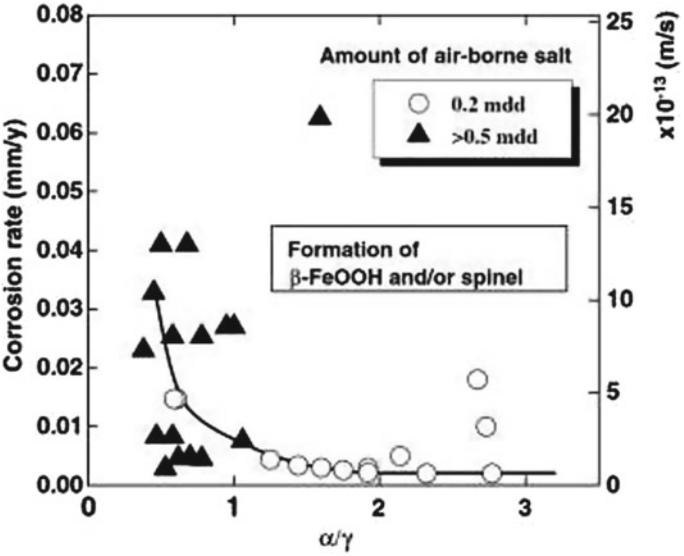

**Fig. 8** Variation of corrosion rate with α/γ ratio at high air borne salt concentration **a** 0.2 mdd and > 0.5 mdd [32]

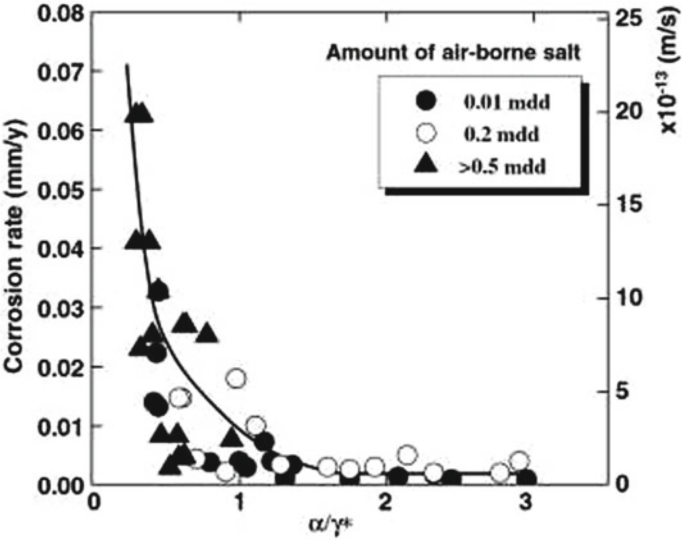

**Fig. 9** Variation of corrosion rate with $\alpha/\gamma^*$ ratio for different airborne salt concentrations. Reproduced with permission from [32]

γ-FeOOH, β-FeOOH, and $Fe_3O_4$, β is for β-FeOOH and "*s*" for spinel-type oxides. The authors have proposed a mass ratio, $(\beta + s)/\gamma^*$, along with $\alpha/\gamma^*$ to describe the protective ability of the rust layer. The β-FeOOH forms mostly in marine environments and can be reduced easily to $Fe_3O_4$; thus, it can accelerate corrosion rate [34, 35]. It was also found that in the chloride atmosphere, a spinel-type oxide ("*s*" phase) layer is formed along with that of β-FeOOH. However, the spinel-type oxide (especially Fe3O4) can accelerate the corrosion process due to their higher conductivity [36]. The relationship between the corrosion rate and $(\beta + s)/\gamma^*$ of the rust layer at various $\alpha/\gamma^*$ ratios is shown in Fig. 10.

The figure shows that the dependence of corrosion rate upon $(\beta + s)/\gamma^*$ is not independent of the $\alpha/\gamma^*$. For $\alpha/\gamma^* < 1$, the corrosion rate was never above 0.01 mm/year, when $(\beta + s)/\gamma^*$ was less than 0.5. However, the corrosion rate was more than 0.01 mm/year for $(\beta + s)/\gamma^*$ ratio greater than 0.5. If the $\alpha/\gamma^*$ was greater than 1, the corrosion rate was found to be independent of $(\beta + s)/\gamma^*$. This shows that $(\beta + s)/\gamma^*$ ratio can be used to describe the protective ability of the rust layer if $\alpha/\gamma^* < 1$. At $\alpha/\gamma^* > 1$, the corrosion rate was found to be independent of $(\beta + s)/\gamma^*$. As observed in previous studies $\alpha/\gamma^* > 1$ confirms that the rust layer is protective. This ratio can still be an appropriate descriptor of protectiveness of the rust layer in situations where mixed and complex oxide phases are formed.

Recent studies have shown that the α/γ ratio is critical in determining the protectiveness of the rust layer. The goethite (α-FeOOH) phase is thermodynamically and electrochemically stable in highly corrosive environments, making it the most stable and protective oxide [24]. The increase in the goethite content results in forming a

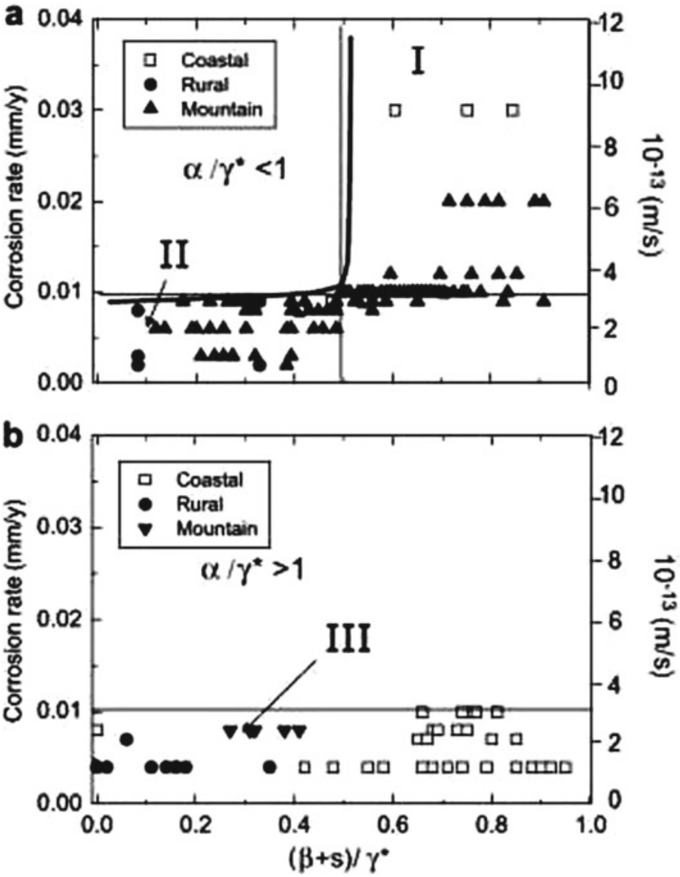

**Fig. 10** Variation of corrosion rate with $(\beta + s)/\gamma^*$ under the conditions of **a** $\alpha/\gamma^* < 1$ and **b** $\alpha/\gamma^* > 1$. Reproduced with permission from [33]

compact and adherent passive film that prevents the ingress of $Cl^-$ and $SO_4^{2-}$ ions. The lepidocrocite layer is highly porous, which makes it susceptible to higher corrosion [25]. The role of alloying elements on the protective ability indices of the rust layer has been summarized in Table 2, which is based on recent studies by various researchers in varying environmental conditions.

## 5 Outlook and Challenge

The formation of the protective oxide layer/patina in low alloy steels or WS is one of the defense mechanisms against corrosion. The oxide-forming ability gives these (and other nonferrous and ferrous alloys) self-healing abilities under various service

**Table 2** Protective ability indices with various alloying additions in the aqueous media

| Alloying element | Atmospheric conditions/electrolyte | Protective ability index (α/γ) | References |
|---|---|---|---|
| Ni (3.5 wt%) | $SO_2$ atmosphere (1 year exposure) | α/γ ratio = 0.15 | [37] |
| Cu, Cr | 5% NaCl | α/γ ratio = 23 (720 h) | [38] |
| Ni, Cr, Cu, V, N | (1.0 ± 0.05) × 10 − 2 mol L − 1 NaHSO3 | α/γ ratio = 2.25 (360 h) | [39] |
| Ni, Cu, Cr | 0.01 mol/L NaHSO3 | α/γ ratio = 0.785 | [40] |
| Cu, Ni, Mo | 1 wt.% NaCl<br>with 0.05 wt.% Na2SO4 | α/γ ratio = 1.87 | [41] |
| Cu, Ni, Mo, Cr | 1 wt.% NaCl solution | α/γ ratio = 0.55 (60 h) | [42] |

conditions. Nowadays, low alloy steels or WS are designed based on the following objectives [28].

(a) Higher corrosion resistance.
(b) Rapid growth of the protective layer.
(c) Applications in the marine environment.

The composition of low alloy steel or WS is optimized based on various mechanical properties, such as strength and ductility. In the literature, various low alloy steel or WS compositions have been studied by different research groups, but there is no definite trend on how the oxide layer formation depends on composition and environmental parameters. Further, the role of microalloying elements is also a new addition to the research in this area. Apart from the composition, the major challenge also lies in the generalization of the nature of the oxide layer developed under various environmental conditions. The atmospheric exposure tests of low alloy steel or WS take longer duration, as the formation of a "steady-state" protective oxide layer depends on the exposure time. Moreover, the laboratory wet/dry cyclic tests performed to study the effect of composition and environment on the nature of the protective oxide layer must be modified to mimic the natural corrosion environments [43]. So that, the discrepancy between the laboratory-based test and external exposure test is minimized or eliminated [44]. Some studies indicate that, whereas the Cebelcor test agrees well with the rural–urban atmosphere, the industrial atmosphere is well simulated by the Kesternich test, and the marine atmosphere is simulated by the Prohesion test [44]. However, more such studies are required in this direction to obtain any generalization. Given the complex nature of the alloying process, a generalized understanding of the correlation between the protective rust layer formation and the alloying addition is challenging. The complexity of the environment adds to this difficulty. However, the self-protective steel composition design requires the correlation between protective oxide formation, composition, and exposure environment.

## References

1. G. Koch, J. Varney, N. Thompson, O. Moghissi, M. Gould, J. Payer, International measures of prevention, application, and economics of corrosion technologies study. NACE Int. **1**, 216 (2016)
2. Z. Ahmad, *Principles of Corrosion Engineering and Corrosion Control* (Elsevier, 2006), Sep 18
3. X. Li, D. Zhang, Z. Liu, Z. Li, C. Du, C. Dong, Materials science: share corrosion data. Nature **527**(7579), 441–442 (2015)
4. M. Morcillo, B. Chico, I. Díaz, H. Cano, D. De la Fuente, Atmospheric corrosion data of weathering steels. A Rev. Corrosion Sci. **1**(77), 6–24 (2013)
5. ASTM A709/A709M, Standard Specification for Structural Steel for Bridges, American Society for Testing and Materials, Philadelphia (2009)
6. P. Keller, X-ray amorphous phases in rust. Mater. Corros. **22**(1), 32–35 (1971)
7. P. Dillmann, F. Mazaudier, S. Hœrlé, Advances in understanding atmospheric corrosion of iron. I. Rust characterisation of ancient ferrous artefacts exposed to indoor atmospheric corrosion. Corr. Sci. **46**(6), 1401–129, June 1 (2004)
8. T.E. Graedel, C. Leygraf, Atmospheric corrosion. Electrochem. Soc. Inter. **25** (2001)
9. C.P. Larrabee, Corrosion resistance of high-strength low-alloy steels as influenced by composition and environment. Corrosion (NACE) **9**, 259–271 (1953)
10. J. Zoccola, *Eight-Year Corrosion Test Report–Eight Mile Road Interchange* (Bethlehem Steel, Bethlehem, PA, 1976), April
11. D.M. Buck, Copper in steel-the influence on corrosion. Ind. Eng. Chem. **5**(6), 447–452 (1913)
12. D.M. Buck, J.O. Handy, Research on the corrosion resistance of copper steel. Ind. Eng. Chem. **8**(3), 209–216 (1916)
13. D.M. Buck, *The Influence of Very Low Percentages of Copper in Retarding the Corrosion of Steel* (American Sheet and Tin Plate Company, 1920)
14. C.P. Larrabee, Report of subcommittee XIV on inspection of black and galvanized sheets. Proc. ASTM **54**, 110–122 (1954)
15. H. R. Copson, in Atmospheric corrosion of low alloy steels. Proceedings-American Society for Testing and Materials (Vol. 52, 1952), Jan 1, pp. 1005–1026. 100 Barr Harbor Dr, W Conshohocken, PA 19428–2959: Amer Soc Testing Materials
16. C.P. Larrabee, S.K. Coburn, in The atmospheric corrosion of steels as influenced by changes in chemical composition. Proceedings 1st Int. Cong. Met. Corros (Butterworth, London, UK, 1962), p. 276
17. M. Morcillo, I. Díaz, H. Cano, B. Chico, D. De la Fuente, Atmospheric corrosion of weathering steels. Overview for engineers. Part I: Basic Concepts. Const. Build. Mat. **213**, 723–37 (2019), Jul 20
18. A. Azizinamini, High-performance steel: new horizon in steel bridge construction. TR News (1998), 194.
19. A.D. Wilson, in Properties of recent production of A 709 HPS-70 W bridge steels. International Symposium on Steel for Fabricated Structures (1999), pp. 41–49
20. J.B. Horton, The mechanism of rusting of low alloy steels in the atmosphere. Unpublished MS Thesis, Lehigh University, Bethlehem (1957)
21. J.B. Horton, *The composition, structure and growth of the atmospheric rust on various steels [Doctoral Thesis]* (Lehigh University, Bethlehem, 1964)
22. T. Misawa, T. Kyuno, W. Suetaka, S. Shimodaira, The mechanism of atmospheric rusting and the effect of Cu and P on the rust formation of low alloy steels. Corros. Sci. **11**(1), 35–48 (1971)
23. M. Yamashita, H. Miyuki, Y. Matsuda, H. Nagano, T. Misawa, The long term growth of the protective rust layer formed on weathering steel by atmospheric corrosion during a quarter of a century. Corros. Sci. **36**(2), 283–299 (1994)
24. J.T. Keiser, C.W. Brown, R.H. Heidersbach, The electrochemical reduction of rust films on weathering steel surfaces. J. Electrochem. Soc. **129**(12), 2686 (1982)

25. M. Yamashita, H. Miyuki, H. Nagano, T. MISAWA, Compositional gradient and ion selectivity of Cr-substituted fine goethite as the final protective rust layer on weathering steel. Tetsu-to-Hagane. **83**(7), 448–453 (1997), Jul 1
26. H.E. Townsend, T.C. Simpson, G.L. Johnson, Structure of rust on weathering steel in rural and industrial environments. Corrosion **50**(7), 546–554 (1994)
27. M. Morcillo, I. Díaz, B. Chico, H. Cano, D. De la Fuente, Weathering steels: From empirical development to scientific design. A Rev. Corrosion Sci. **1**(83), 6–31 (2014)
28. M. Yamashita, H. Uchida, Recent research and development in solving atmospheric corrosion problems of steel industries in Japan, in *Industrial Applications of the Mössbauer Effect* (Springer, Dordrecht, 2002), pp. 153–166
29. M. Yamashita, H. Konishi, I.M. Jun, H. Uchida, Nanostructure of protective rust layer on weathering steel examined using synchrotron radiation X-rays. Mater. Trans. **45**(6), 1920–1924 (2004)
30. M. Kimura, T. Suzuki, G. Shigesato, H. Kihira, S. Suzuki, Characterization of nanostructure of rusts formed on weathering steel. ISIJ Int. **42**(12), 1534–1540 (2002)
31. M. Morcillo, I. Díaz, H. Cano, B. Chico, D. De La Fuente, Atmospheric corrosion of weathering steels. Overview for engineers. Part II: Testing, inspection, maintenance. Const. Build. Mat. **222**, 750–765 (2019), Oct 20
32. T. Kamimura, S. Hara, H. Miyuki, M. Yamashita, H. Uchida, Composition and protective ability of rust layer formed on weathering steel exposed to various environments. Corros. Sci. **48**(9), 2799–2812 (2006)
33. S. Hara, T. Kamimura, H. Miyuki, M. Yamashita, Taxonomy for protective ability of rust layer using its composition formed on weathering steel bridge. Corros. Sci. **49**(3), 1131–1142 (2007)
34. T. Nishimura, K.I. Tanaka, Y. Shimizu, Effect of NaCl on rusting of steel in wet and dry corrosion cycle. Tetsu-to-Hagane. **81**(11), 1079–1084 (1995)
35. M. Yamashita, A. Maeda, H. Uchida, T. Kamimura, H. Miyuki, Crystalline rust compositions and weathering properties of steels exposed in nation-wide atmospheres for 17 years. Nippon Kinzoku Gakkaishi (1952) **65**(11), 967–971 (2001)
36. R.M. Cornell, U. Schwertmann, *The Iron Oxides: Structure, Properties, Reactions, Occurrences and Uses* (Wiley, 2003), Oct 17
37. X. Cheng, Z. Jin, M. Liu, X. Li, Optimizing the nickel content in weathering steels to enhance their corrosion resistance in acidic atmospheres. Corros. Sci. **1**(115), 135–142 (2017)
38. W. Wu, Z. Zeng, X. Cheng, X. Li, B. Liu, Atmospheric corrosion behavior and mechanism of a Ni-Advanced weathering steel in simulated tropical marine environment. J. Mater. Eng. Perform. **26**(12), 6075–6086 (2017)
39. Y. Liu, H.Y. Wu, L.X. Du, R.D. Misra, On the electrochemical behaviour of VN-8Cr weathering steel in simulated industrial atmosphere. Corros. Eng., Sci. Technol. **55**(2), 159–170 (2020)
40. W. Liu, J. Liu, H. Pan, F. Cao, Z. Wu, H. Lv, Z. Xu, Synergisic effect of Mn, Cu, P with Cr content on the corrosion behavior of weathering steel as a train under the simulated industrial atmosphere. J. Alloy. Compd. **5**(834), 155095 (2020)
41. Y. Fan, W. Liu, Z. Sun, T. Chowwanonthapunya, Y. Zhao, B. Dong, T. Zhang, W. Banthukul, X. Li, Corrosion Behaviors of Carbon Steel and Ni-Advanced Weathering Steel Exposed to Tropical Marine Atmosphere. J. Mater. Eng. Perform. **29**(10), 6417–6426 (2020)
42. Y. Fan, W. Liu, S. Li, T. Chowwanonthapunya, B. Wongpat, Y. Zhao, B. Dong, T. Zhang, X. Li, Evolution of rust layers on carbon steel and weathering steel in high humidity and heat marine atmospheric corrosion. J. Mater. Sci. Technol. **15**(39), 190–199 (2020)
43. J. Wang, Z.Y. Wang, W. Ke, Corrosion behaviour of weathering steel in diluted Qinghai Salt Lake water in a laboratory accelerated test that involved cyclic wet/dry conditions. Mater. Chem. Phys. **124**(2–3), 952–958 (2010)
44. P. Montoya, I. Díaz, N. Granizo, D. De la Fuente, M. Morcillo, An study on accelerated corrosion testing of weathering steel. Mater. Chem. Phys. **142**(1), 220–228 (2013)

# Frontiers in Multi-functional Biomaterials for Hip Joint Application

**Chinmayee Nayak and Kantesh Balani**

## 1 Introduction

Williams (1987) [1] has defined ***biomaterial*** as: '*A non-viable material used in a medical device, intended to interact with biological systems.*' Though the definition of biomaterial has evolved over time, and we must appreciate that inclusion of viable (instead of *non-viable* alone) materials (tissue scaffolds and organ transplants) makes the definition more encompassing in nature. Further, the removal of '*medical*' in the definition of biomaterial also opens up a range of applications to culturing cells, assessment, and qualification using assays, for sensing and diagnostic, monitoring, as well as therapeutic and aesthetic aspects.

***Biocompatibility***, on the other hand, is defined as: '*Ability of a material to perform with an appropriate host response in a specific application*' [1]. Here, it is important to highlight that the material must perform with '*an appropriate host response,*' i.e., the material should not lead to infection or should deter from blood clotting when implanted, or must ensure normal or assisted healing. Further, a material is being designed '*for a specific application,*' and in other biomedical conditions, the same material may not remain suitable. Thus, specific conditions also include not only the site of use (or functionality of the organ it must provide) but also the duration of contact. For example, a syringe needle may come in contact for only a few seconds, but it will penetrate the skin and comes in contact with blood. However, dialysis may last for few hours to purify the blood and catheters may remain in contact with the body for few days. Whereas the case of pacemakers or bone/dental implants is different as they may stay in the body for a lifetime.

C. Nayak · K. Balani (✉)
Department of Materials Science and Engineering, Indian Institute of Technology Kanpur,
Kanpur 208016, India
e-mail: kbalani@iitk.ac.in

C. Nayak
e-mail: cnayak@iitk.ac.in

A. Shrivastava et al. (eds.), *New Horizons in Metallurgy, Materials and Manufacturing*,
Indian Institute of Metals Series, https://doi.org/10.1007/978-981-19-5570-9_8

## *1.1 Material Classifications*

Materials may be classified based on: (i) their ***composition*** (e.g., metals, ceramics, polymers, and composites), (ii) ***biological response*** (e.g., bioinert, bioactive, bioresorbable, and toxic), and (iii) ***applications*** (structural or load-bearing, and non-structural), Fig. 1. As one may appreciate that one material will fit into one or more classes of these classifications. For example, a metal may be selected, which may be toxic, and fits into a category of structural material. Nonetheless, to take care of the material toxicity, a bioactive/bioinert coating may be deposited on the metal surface to retain its bulk properties (of high fracture strength and fatigue life), whereas surface ceramic coating can provide the functional biological (and cytocompatible) response.

### 1.1.1 Classification Based on Type of Material

***Metals such as*** stainless steel (say 316L grade), titanium alloys (e.g., Ti-6Al-4V), Co-Cr alloys, Ta scaffolds, Mg-based alloys, etc., are known for their high toughness and fatigue strength. ***Ceramics*** such as hydroxyapatite (HA), 3 mol.% yttria-stabilized zirconia (3YSZ), aluminum oxide ($Al_2O_3$), and bioglasses such as 45S5, 58S, 8625 are well known in various biomedical applications for their bioinert and bioactive nature. ***Polymers*** are needed as conduits for body fluids, drug-eluting carriers, and compliant tribological surfaces for joints, and typically include polyethylene, polyether ether ketone (PEEK), polytetrafluoroethylene (PTFE), polydimethoxysilane (PDMS), polyethylene glycol (PEG), polylactic acid (PLA), polyvinyl chloride (PVC), polyvinylidene fluoride (PVDF), ultra-high molecular weight polyethylene (UHMWPE), etc.

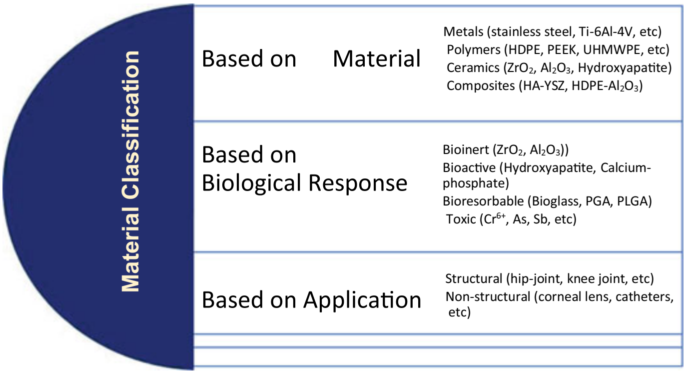

**Fig. 1** Classification and domains of biomaterials for tissue engineering

### 1.1.2 Classification Based on Type of Biological Response

Along the lines of biological response, a ***bioinert*** material will not have any biological interaction with the cells and will stay in the body without incurring any biological or chemical reaction. Examples of this type of materials are $Al_2O_3$, yttria-stabilized zirconia (YSZ), etc. Nonetheless, fibrous cells will form around the bioinert materials and encapsulate the same. Such an interface between the cells and material may allow interfacial movement and the joint may loosen out with time. On the other hand, a ***bioactive*** material allows chemical and biological reactions with the surrounding cells and binds to them strongly. Examples of this type are hydroxyapatite (HA), bioglass (BG), etc. Herein, the strong cell–material interaction keeps the interface strong and limits the cell damage by restricting their relative movement. These materials are suited best as coatings since the interfacial stability is obtained while restricting the damage of surrounding tissues. ***Resorbable*** materials degrade over time to allow their replacement by host cells. Herein, the cell–material interface keeps shifting with the resorption of material and the new cells taking its place. This is an ideal condition as the cell repair dominates and keeps replacing the artificial material, thus letting the regaining of blood vessels, and matching up of the original cell properties. One issue is that the resorption of material should possess a matching rate with that of new cell repair otherwise weakening of a portion may hamper the normal functionality of the organ. Additionally, the constant resorption mandates that the leached contents of resorbable materials must be metabolically acceptable. Examples of bioresorbable materials are tri-calcium phosphate, bioglass, polylactic acid (PLA), polyglycolic acid (PGA), etc. The last class of materials is called ***toxic***, i.e., when the material, directly or indirectly, hampers the key metabolic pathway of cells leading to their death. Such materials cannot be directly used as implants and must be coated or sealed and must not come in direct contact with the body. Examples of this can be the release of hexavalent Cr ions (say from Cr-coating), Hg (mercury), Antimony (Sb), etc.

### 1.1.3 Classification Based on Type of Applications

Based on the applications, biomaterials can be classified into ***structural*** and ***non-structural*** applications. ***Structural*** applications involve where the biomaterial must bear the load and sustain the functionality, examples of which are orthopaedic and dental applications, whereas ***non-structural*** applications involve the use of materials for regaining the functionality without the requirement of any structural loading, examples of which are corneal lens, catheters, etc.

## 2 Hip Joint Arthroplasty

Total hip joint replacement (THR) has been recognized as one of the most successful surgeries over the last decade. The Indian Society of Hip & Knee Surgeons (ISHKS) registry documented nearly 17,124 THR surgeries for over 10 years (January 1, 2006 to December 31, 2018) out of which 1306 underwent revision surgeries (Surgeons, 2019). Implant loosening is the major problem that limits the longevity of THR [2, 3]. There are two main parts to a total hip replacement implant. The femoral components, which include the femoral stem and head, fit into the femur bone and the acetabular cup sits in the pelvis region. Femoral stems are typically made up of metals (i.e., stainless steel grade SS316L, Ti-alloy (Ti-6Al-4V) or Co-Cr) to take up the impact and shock that an implant may experience. Polymeric and ceramic materials do not possess enough toughness to contain the damage and may fail catastrophically during service. The femoral stem is inserted by drilling a cavity followed by either press-fitting or cementing it with the surrounding bone (Fig. 2a). Typically press-fitting is done for patients less than 60 years old and the surgeon must ensure that the bones are strong enough to bear the impacting force of hammering the implant for it to snug fit. Press-fitting allows easy removal of the implant in case a revision surgery is needed after the implant has served its intended life of 15–20 years. On the other hand, cementing is done for elderly patients (80+ years of age) where the bone is cancellous (or porous) and may not handle the impact of fitting the implant. Thus, the bone cement (PMMA, polymethyl methacrylate) is used to keep the femoral stem glued to the surrounding bone. Though this cement permits the implant attachment, the revision surgery may demand the removal of nascent bone (along with the removal of the implant) and complicate the process as bone availability is anyway limited in elderly patients. Further, the non-biological interface between the bone cement and the surrounding bone triggers encapsulation of the implant by fibrous tissues and witnesses relative movement. Thus, with time, the cemented implant loosens and requires revision surgery. A remedy to this problem is to coat the implant with a bioactive material, and it is even better if the coating is porous (Fig. 2b, [4]).

### 2.1 *Femoral Stem Component*

The femoral stem component replaces a large portion of the bone in the femur and is, therefore, the load-bearing part of the implant. To bear this load, it must exhibit Young’s modulus comparable to that of cortical bone [5]. If the implant is not as stiff as bone, then the remaining bone surrounding the implant will be put under increased stress. If the implant is stiffer than the bone, then a phenomenon known as stress shielding will occur, and the bone will tend to resorb over time (known as Wulff’s law, [6, 7]). Steel has Young’s modulus (E~200 GPa) much higher than that of bone (cortical bone: 17 GPa, or cancellous bone: 1 GPa), meaning that stress shielding can become a serious issue. The cobalt–chromium–molybdenum alloy

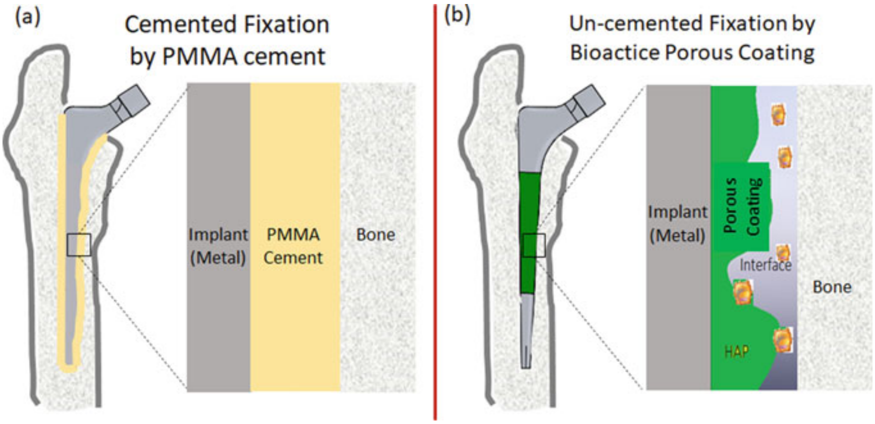

**Fig. 2** Different fixation methods of femoral stem **a** press fitting/by using PMMA bone cement **b** bio-active porous coating. Adapted from: https://www.healthpages.org/surgical-care/hip-joint-replacement-surgery/

(E~220 GPa) is harder than stainless steel, and, thus, more wear-resistant but its high cost and poor machinability limits its use. Titanium is also biologically inactive and resistant to creep deformation, and these advantages over stainless steel make it a very good choice for being used as the femoral stem component. It has almost double strength to elastic modulus ratio (than steel) and an impressive resistance to corrosion [8]. Even though the elastic modulus of titanium (E~116 GPa) is only half that of stainless steel, the bone surrounding the implant will undergo stress shielding. Thus, in order to match the stiffness, the implant is made porous or composites are designed to provide smooth stress transition between the surrounding bone and the implant material. Rather than using commercial purity (CP) titanium, the alloy Ti-6Al-4V (titanium alloy with 6% aluminum and 4% vanadium by weight, E~110 GPa) is often used as it improves the toughness and fatigue resistance. Controlling the porosity to 40% of Ti-6Al-4V alloy during the sintering process can further decrease the elastic modulus, which matches that of cortical bone extremely well.

A further advancement is to coat the implant with a layer of bioactive hydroxyapatite (HA) which has a similar chemical composition to that of bone minerals, the coating provides sites for bone cells in growth. The introduction of 40–70% porosity in HA coating encourages bonding by allowing bone to grow into the pores. The pores size must be in the range of 150–300 μm to ensure the penetration and ingrowth of cells. The plasma spraying is the only FDA-approved coating process that provides controlled porosity for earlier and greater fixation [9]. The large difference in thermal expansion coefficient between hydroxyapatite and Ti- alloy can generate thermal stresses and cause cracking and delamination of the coating, thus improving the fracture toughness of the coating is important. The functionally graded layer bioactive coating ensures a gradation of hardness and fracture toughness across the coating thickness. For example, the Hydroxyapatite (HA)–Alumina ($Al_2O_3$)–yttria-stabilized zirconia (YSZ) functionally graded composite consists of bulk YSZ to increase the toughness, $Al_2O_3$ interlayer provides crack resistance, and the top HA layer ensures the ingrowth of bone cells [10].

The incorporation of antibacterial Cu, Zn, and Co dopants for antibacterial efficacy in hydroxyapatite is well-established [11]. These agents provide antibacterial properties by the release of reactive oxygen species. Processing control was utilized to be able to trap the dopant at a specific site and control its release under simulated conditions for bacterial killing. Addition of reinforcements such as ZnO, Ag, $TiO_{2,}$ and $Fe_3O_4$ also attributes antibacterial behavior to the HA coating. The role of multi-functional ingredients, such as Ag, enhances antibacterial efficacy while simultaneously reinforcing with antioxidant $CeO_2$ result in expedited healing [12]. The presence of $Ce^{3+}$ allows capturing the reactive oxygen species (ROS) and is affirmed with enhanced $Ce^{4+}$ content after its exposure.

Fracture toughness is one of the important attributes for estimating the life span of the coating; therefore, strong improvement in fracture toughness (0.61 $MPam^{1/2}$) and crystallinity (80.4%) have been observed in plasma-sprayed HA-4wt% CNT coating [13]. The biocompatibility of CNT has been controversial over the years, however, literature also reports its nontoxic behavior in the biological system [14–16]. The bacteria culture test on HA, CNT, HA-Ag, and HA-CNT spark plasma sintered pellets suggested excellent viability of both gram-positive (*S. epidermidis*) and gram-negative (*E. coli*) bacteria on pure CNT pellet and the homogeneous clusters of *E.coli* bacteria [10]. Thereby, it was confirmed that CNT supports the growth of bacteria, and evidently does not show toxicity to bacteria cells. The suppression of bacterial growth can be explained by the anti-bacterial behavior of Ag when added in a modest amount (5 wt.%) into HA and CNT. A very sparse number of clusters of *E. coli* have been observed on the surface of CNT-Ag, due to the bacterial killing efficacy of silver particles. In parallel, CNT aids in the precipitation and mineralization of HA on its surface as shown in Fig. 3, which, in turn, enhances the tissue ingrowth. The uniform dispersion of CNTs provides direction for growing human osteoblast cells alongside [13].

## 2.2 Femoral Head Component

The femoral head component of the THR implant must be of accurate shape and smooth fit while exhibiting a low coefficient of friction ($<0.3$). Although metallic (Ti and Cr-based alloy) femoral heads were rampantly used in the late nineties and early twenty-first century, the hazardous reaction occurred by metal ions via metallosis led to its replacement by ceramic femoral heads [5]. Despite high brittleness, ceramic head components have outstanding tribological properties, including hardness (1200–2000 VHN), Young's modulus (210–380 GPa), and fracture toughness (4–8 $MPa.m^{1/2}$) [6]. Ceramic surfaces are hydrophilic (than the metallic surfaces) which contributes to exhibiting lower friction during articulation of a femoral head

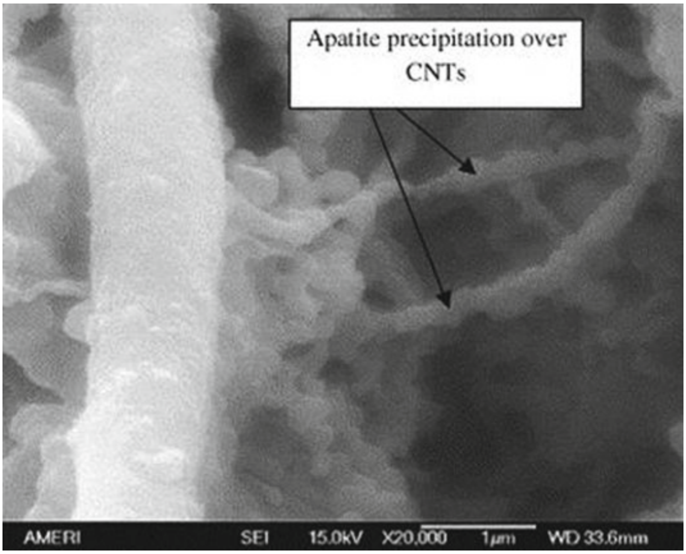

**Fig. 3** Mineralization of apatite over CNT surface. Reprinted with permission from Elsevier [13]

against cup liner. Alumina, zirconia, and zirconia-toughened alumina are the major ceramic materials used in the femoral head. An accurate dimension of the femoral head must be obtained in order to avoid developing point contacts with the mating softer polymeric cup-liner, which may build up higher pressure leading to severe wear and tear during articulation [17, 18]. Thus, processing parameters should be taken care of during sintering of the femoral head in order to ensure snug fitting between the femoral head and acetabular cup liner. The head and the cup liner must be manufactured as a pair to ensure exact fit with each other.

There are various combinations of materials for the femoral head and acetabular cup such as *hard-on-hard* and *hard-on-soft*, the former and latter indicate the material of liner and head, respectively [6]. Hard material includes metal or ceramic, soft material include polymer. Metal-on-metal (MoM) implants are the first choice of combination in the history of THR, but elevated levels of the metal ions in urine and the bloodstream have been a matter of concern [10, 19]. Then came up the possibility of ceramic on ceramic (CoC), wherein the main limitation of this pair is the generation of squeaking noise during joint articulation because of friction, which is socially not acceptable [20]. Thus, choosing ultra-high molecular weight polyethylene (UHMWPE) polymer as liner material along with a ceramic head, commonly referred to as ceramic on polymer (CoP), has become one of the most popular combinations due to the outstanding mechanical properties of UHMWPE [6].

## 2.3 Acetabular Cup Liner

The long hydrocarbon chain of UHMWPE provides ultra-high molecular weight of 2–6 × $10^6$ g/mol, high viscosity of ~ $10^7$ Pa.s ultimate tensile strength of 31–38 MPa, high impact energy (~1070 J/m), and extraordinary abrasion wear resistance to UHMWPE [21]. Few other polymers such as high-density polyethylene (HDPE) and polytetrafluoroethylene (PTFE) have also been used as acetabular cup liners. The ascending order of wear rate is UHMWPE-15.5 × $10^{-6}$ $mm^3$/Nm [22] < PEEK-31.7 × $10^{-4}$ $mm^3$/Nm [22] < HDPE- 2 × $10^{-4}$ $mm^3$/Nm [23] < PTFE-6 × $10^{-4}$ $mm^3$/Nm [24]. The comparison of wear among different polymers is shown in Fig. 4a. Though UHMWPE and HDPE belong to the same family, a comparative study as shown in Fig. 4b, establishing the superior wear resistance of UHMWPE over HDPE [25]. Being the most wear-resistant, UHMWPE has been recognized as the suitable material for THR. The main issue with this combination of materials is the wear of the acetabular cup, which can lead to the formation of small particles of the polymer and ensuing inflammation. This gears up the research to increase the wear resistance of UHMWPE by various methods. UHMWPE-based composites/nanocomposites dragged a huge interest of researchers due to significant improvement required in its mechanical and tribological properties. Thus, the mechanical and tribological properties have been improved by incorporating organic/inorganic reinforcements into UHMWPE, thereby restricting the wear debris formation. The addition of 20 wt.% $Al_2O_3$ to UHMWPE shows the hardness value of ~162.4 MPa which is 84% larger than UHMWPE (~88.4 MPa) [26]. Though the addition of $Al_2O_3$ as a reinforcement to UHMWPE shows excellent mechanical properties, still it also has some major disadvantages. The leached out aluminum ions show neurotoxic and cytotoxic behavior inside the body [27]. The addition of hydroxyapatite (HA) to UHMWPE shows an enhancement in the surface mechanical properties and enhances bioactivity [28]. CNTs being tough material help in effective load transfer and resist crack propagation in the UHMWPE matrix [29].

Zinc oxide (ZnO) exists in different morphologies, viz. micro-rods (R), nanoparticles (NP), and micro-disks (D) and when employed as a reinforcement in implants they can reduce the bacterial infection as ZnO exhibits antibacterial efficacy via the release of $Zn^{2+}$ and $H_2O_2$. Incorporation of ZnO (5–20 wt.%) in UHMWPE helps in reducing the bacterial growth as shown in the SEM images in Fig. 5. More specifically, all varieties of ZnO morphologies in the UHMWPE matrix elicit effective antibacterial characteristics on gram-positive bacteria (*Staphylococcus aureus*, Fig. 5a–d, or *Staphylococcus epidermidis*, Fig. 5e–h) but not for gram-negative bacteria (*Escherichia coli*, Figs. 5i-l). The bactericidal mechanisms were quantified for various ZnO morphologies. The UHMWPE-ZnO (R/NP/D) composites showcased nearly 60–80% lower antibacterial activity toward *E. coli* when compared to the gram-positive bacteria [31]. The gram-positive bacterium's cell wall has a teichoic acid consisting of protein receptors and ions that show higher affinity toward $Zn^{2+}$ ions and thus reflect higher antibacterial properties.

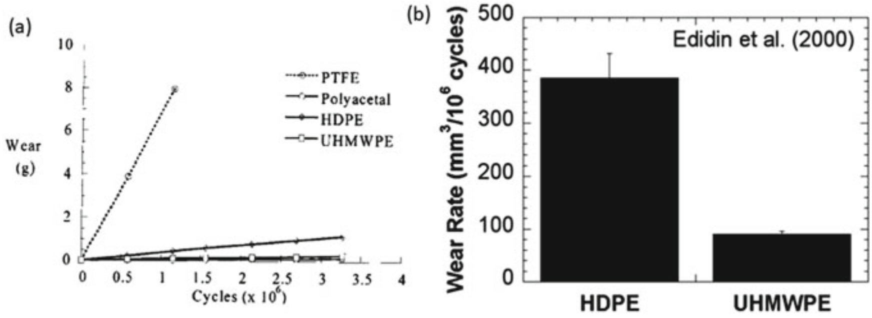

**Fig. 4** Comparison of **a** wear between polytetrafluoroethylene (PTFE), polyacetal, high-density polyethylene (HDPE), and ultra-high molecular weight polyethylene (UHMWPE) for acetabular cup liner. Reprinted with permission from Elsevier [30], **b** wear rates between UHMWPE and HDPE. Reprinted with permission from Elsevier [25]

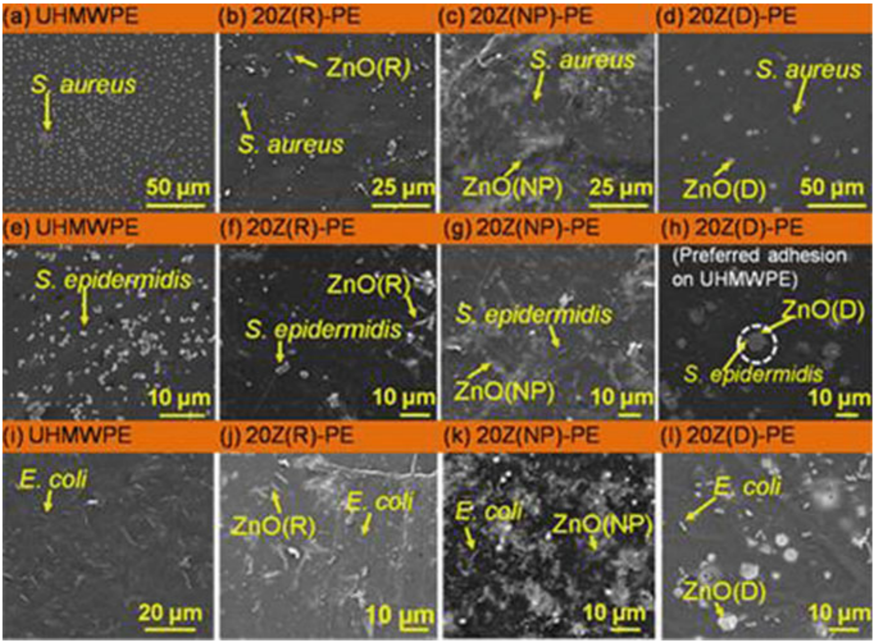

**Fig. 5** **a**–**d** *S. aureus*, **e**–**h** *S. epidermidis,* **i**–**l** *E. coli* grown on UHMWPE and ZnO–PE composites. Reprinted with permission from Elsevier [31]

## *2.4 Joint Articulation and Wear*

Lowering the wear rate of acetabular cup liner during articulation has become the greatest challenge in the field of hip joint arthroplasty, and hence, choosing a suitable material for the cup liner is important. The bioinert alumina ($Al_2O_3$), bioactive hydroxyapatite (HA), and toughening agent carbon nanotubes (CNT) have been added into the UHMWPE matrix to improve mechanical strength and tribological properties. However, the concentration of reinforcements is always a matter of concern as nanoscale dimensions tend to agglomerate and weaken the polymer–reinforcement interface. Addition of 20 and 6 wt.% $Al_2O_3$ (A) and CNT (C) in UHMWPE increased the hardness and elastic modulus due to secondary bonds O–Al-O bonds toughening action of CNT. The hydroxyapatite (H) (20 wt.%) aggregates contribute to decreased strength. However, synergistic improvements in hardness and elastic modulus were observed in the UHMWPE-Alumina-Hydroxyapatite-CNT (UAHC) composites. Similar observations are reported from fretting wear test, i.e., decreased CoF (0.17–0.21) and wear rate ($W_R$) (0.04 $mm^3/Nm$) of composites than neat UHMWPE (CoF: 0.23 and $W_R$: 0.05 $mm^3/Nm$). Thus, $Al_2O_3$, HA, and CNT can be potential fillers for polymeric acetabular cup liners [26].

Antibacterial agents, such as Ag and ZnO, also increase the wear resistance of UHMWPE when sliding against stainless steel as a counter-body. The schematic representation of various composites such as neat UHMWPE (U), U-3wt.% Ag (U3A), U-3wt.% ZnO (U3Z), and U-3wt.% Ag-3wt.% ZnO (U3A3Z) are shown in Fig. 6 (a-d) and the respective sliding wear mechanisms in Fig. 6**e**–**h**. Ag nanoparticles form a tribolayer (Fig. 6b and d) in contacting surfaces in sample U3A and U3A3Z and are evidenced in the inset of Fig. 6f and h. The 'Ag' layer acts as a lubricating layer and thus 59% and 35% reduced coefficient of friction (CoF) and wear rate ($W_R$) of U3A composite than neat U (CoF: $6.6 \times 10^{-2}$, $W_R$: $9.5 \times 10^{-5}$ $mm^3/Nm$) were observed. The fatigue wear mechanism changed to adhesive wear with no cracks/pits. The tendency of agglomeration with higher content of reinforcements (3 wt.% Ag/CNT) still limits the tribological properties which can be controlled with a modest amount (1 wt.% Ag/CNT) [32].

The coefficient of friction and associated wear rates for different reciprocating geometries depend on the shear stresses and strains during articulation. The finite element modeling (FEM) estimated the shear stresses on Ti6Al4V and SS using four reciprocating geometries (linear, square, circle, and eight/butterfly) during pin on disk tribology. Maximum shear stress ($\tau$) obtained from FEM showed the similar trend (Linear < Circular < Square < Eight) as experimental CoF and wear rate. The simulated profiles for maximum $\tau$ of SS 304 in dry condition with different traverse geometries are shown in Fig. 7. The highest values of maximum shear stress were observed for the eight/butterfly geometries in case of both Ti6Al4V and SS 304. Thus, it can be concluded that the shear stresses increase as the geometry or path of reciprocation/traverse gets complex.

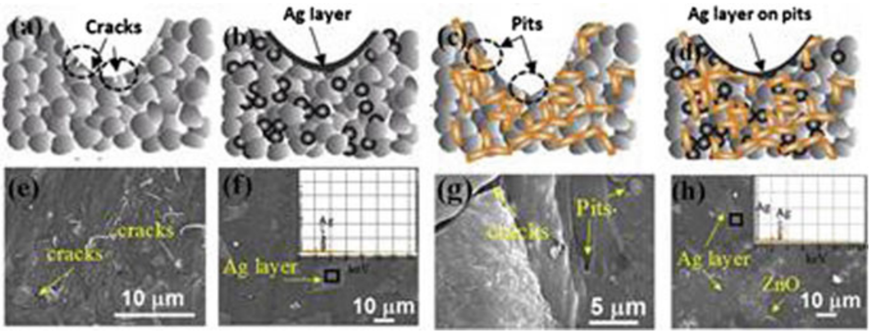

**Fig. 6** Schematic diagram representing the effect of Ag and ZnO reinforcements on wear mechanisms during sliding wear **a** UHMWPE, **b** U3A, **c** U3Z, and **d** U3A3Z. **g–h** are the corresponding SEM images to show the presence of cracks, pits, and tribolayer (inset are the corresponding EDS spectra, showing the presence of Ag layer). Reprinted with permission from Elsevier [32]

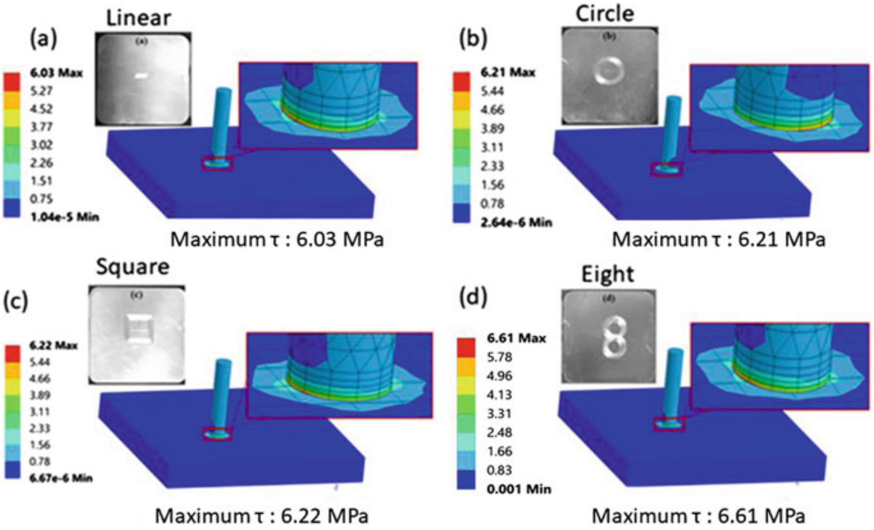

**Fig. 7** Maximum shear stress ($\tau$) of SS 304 substrates slides against zirconia pin in different geometries such as **a** linear, **b** circular, **c** square, and **d** eight in dry condition. Reprinted with permission from ICE Publishing [33]

## 3 Summary/Future Scopes

Total hip joint replacement (THR) is a very successful surgical procedure, which is being commonly accepted by elderly persons. The main challenge with hip replacements is to select a material that has mechanical properties similar to that of bone, must be wear-resistant, and must comply with an appropriate host response. The femoral stem is the skeleton of the THR implant that bears the major load. The hydroxyapatite (with 40–60% porosity) coated Ti-6Al-4V substrate has been the best suitable material for the femoral stem. The fixation of the implant via plasma-sprayed HA coating and the gradation functionality of the coating provide toughness by YSZ in the bulk, an intermediate cushioning bed by $Al_2O_3$ and with a porosous (40–70%, 150–300 μm) HA on the top enhance bone cell ingrowth. Further, the antibacterial properties of the coating can be ensured by the addition of ZnO, Ag, $TiO_{2,}$ and $Fe_3O_4$. The main requirement of the femoral head and acetabular cup is to minimize wear. The ceramic on polymer (CoP) combination is successful in hip arthroplasty with a ZTA femoral head and UHMWPE for acetabular cup liner. The advancements in improving the wear resistance of UHMWPE can be achieved by various reinforcements, such as $Al_2O_3$, HA, CNT, ZnO, and Ag. The various morphologies (Rod/Nanoparticle/Micro Disk) of ZnO can control the antibacterial properties of UHMWPE liner.

However, the field of hip joint arthroplasty needs serious research attention to improve the wear resistance of UHMWPE nanocomposites which can be explored in the future years. A thorough research can be extended to realistic bio-tribology wear tests on specific UHMWPE-based nanocomposites. Understanding the contact stresses during THR articulation by FEA simulation may also be approached in future studies. Further, packaging and sterilization may also compel the use of gamma irradiation or UV sterilization. So, an in-depth understanding of the effects of electron/UV/gamma irradiation on wear and tribological damage tolerance without compromising its cytocompatibility would be required.

**Acknowledgements** KB acknowledges funding from Swarnajayanti fellowship (DST/SJF/ETA-02-2016-17), Department of Biotechnology (BT/PR13466/COE/34/26/2015), and Science and Engineering Research Board (IMP/2018/000622), Government of India. Authors thank Ms. Suchi M. George for her kind assistance with language corrections.

## References

1. B. Albert, D. Bray, K. Hopkin, A. Johnson, J. Lewis, M. Raff, et al., Essential cell biology. in *Biochemistry and Molecular Biology Education*, 2nd ed. (2004). https://doi.org/10.1002/bmb.2004.494032049994
2. Y. Abu-Amer, I. Darwech, J.C. Clohisy, Aseptic loosening of total joint replacements: Mechanisms underlying osteolysis and potential therapies. Arthritis Res. Therapy **9**(SUPPL.1), 1–7 (2007). https://doi.org/10.1186/ar2170
3. P.H. Wooley, E.M. Schwarz, Aseptic loosening. Gene Ther. **11**(4), 402–407 (2004). https://doi.org/10.1038/sj.gt.3302202
4. B.H.S. Khanuja, J.J. Vakil, M.S. Goddard, M.A. Mont, *Cementless Femoral Fixation in Total Hip Arthroplasty* (2011), pp. 500–509. https://doi.org/10.2106/JBJS.J.00774
5. L. Kuncicka, R. Kocich, T.C. Lowe, Advances in metals and alloys for joint replacement. Prog. Mater Sci. **88**, 232–280 (2017). https://doi.org/10.1016/j.pmatsci.2017.04.002
6. S.G. Ghalme, A. Mankar, Y. Bhalerao, Biomaterials in hip joint replacement. Int. J. Mat. Sci. Eng. **4**(2), 113–125 (2016). https://doi.org/10.17706/ijmse.2016.4.2.113-125
7. K.S. Katti, Biomaterials in total joint replacement. Colloids Surf., B **39**(3), 133–142 (2004). https://doi.org/10.1016/j.colsurfb.2003.12.002

8. M. Geetha, A.K. Singh, R. Asokamani, A.K. Gogia, Ti based biomaterials, the ultimate choice for orthopaedic implants - A review. Prog. Mater Sci. **54**(3), 397–425 (2009). https://doi.org/10.1016/j.pmatsci.2008.06.004
9. L. Sun, C.C. Berndt, K.A. Gross, A. Kucuk, Material Fundamentals and Clinical Performance of Plasma-Sprayed Hydroxyapatite Coatings: A Review. J. Biomed. Mater. Res. **58**(5), 570–592 (2001). https://doi.org/10.1002/jbm.1056
10. M.A.F. Afzal, P. Kesarwani, K.M. Reddy, S. Kalmodia, B. Basu, K. Balani, Functionally graded hydroxyapatite-alumina-zirconia biocomposite: Synergy of toughness and biocompatibility. Mater. Sci. Eng., C **32**(5), 1164–1173 (2012). https://doi.org/10.1016/j.msec.2012.03.003
11. A. Bhattacharjee, R. Hassan, A. Gupta, M. Verma, P.A. Murugan, P. Sengupta, M. Saravanan, I. Manna, K. Balani, Effect of Zn and Co Doping on Antibacterial Efficacy and Cytocompatibility of Spark Plasma Sintered Hydroxyapatite. J. Am. Ceram. Soc. **103**(8), 4090–4100 (2020). https://doi.org/10.1111/jace.17077
12. A. Pandey, S. Midha, R.K. Sharma, R. Maurya, V.K. Nigam, S. Ghosh, K. Balani, Antioxidant and antibacterial hydroxyapatite-based biocomposite for orthopedic applications. Mater. Sci. Eng. **88**, 13−24 (2018). https://doi.org/10.1016/j.msec.2018.02.014
13. K. Balani, R. Anderson, T. Laha, M. Andara, J. Tercero, E. Crumpler, A. Agarwal, Plasma-sprayed carbon nanotube reinforced hydroxyapatite coatings and their interaction with human osteoblasts in vitro. Biomaterials **28**(4), 618–624 (2007). https://doi.org/10.1016/j.biomaterials.2006.09.013
14. P. Cherukuri, S.M. Bachilo, S.H. Litovsky, R.B. Weisman, Near-infrared fluorescence microscopy of single-walled carbon nanotubes in phagocytic cells. J. Am. Chem. Soc. **126**(48), 15638–15639 (2004). https://doi.org/10.1021/ja0466311
15. Q. Lu, J.M. Moore, G. Huang, A.S. Mount, A.M. Rao, Letters RNA polymer translocation with single-walled carbon nanotubes. (2004). https://doi.org/10.1021/nl048326j
16. D. Pantarotto, J.P. Briand, M. Prato, A. Bianco, Translocation of bioactive peptides across cell membranes by carbon nanotubes. Chem. Commun. **4**(1), 16–17 (2004). https://doi.org/10.1039/b311254c
17. P. Goebel, D. Kluess, J. Wieding, R. Souffrant, H. Heyer, M. Sander, R. Bader, The influence of head diameter and wall thickness on deformations of metallic acetabular press-fit cups and UHMWPE liners: A finite element analysis. J. Orthop. Sci. **18**(2), 264–270 (2013). https://doi.org/10.1007/s00776-012-0340-7
18. A. Tudor, T. Laurian, V.M. Popescu, The effect of clearance and wear on the contact pressure of metal on polyethylene hip prostheses. Tribol. Int. **63**, 158–168 (2013). https://doi.org/10.1016/j.triboint.2012.11.002
19. A.J. Hart, A. Matthies, J. Henckel, K. Ilo, J. Skinner, P.C. Noble, Understanding why metal-on-metal hip arthroplasties fail. J. Bone Joint Surgery (American) **94**(4), 1–10 (2012). https://doi.org/10.2106/JBJS.K.01266
20. C. Riviere, P. Vendittoli, Personalized hip and knee joint replacement.
21. B. Bhaskar, S. Arun, P. Sreekanth, S. Kanagaraj, Biomaterials in Total Hip Joint Replacements: The Evolution of Basic Concepts, Trends, and Current Limitations—A Review. Trends Biomater **1**, 175–210 (2016)
22. B.J. Briscoe, S.K. Sinha, Wear of polymers. Proceedings of the Institution of Mechanical Engineers, Part J: Journal of Engineering Tribology **216**(6), 401–413 (2002). https://doi.org/10.1243/135065002762355325
23. Y.J. Mahboba, M.A. Al-shammari, Enhancing wear rate of high-density polyethylene ( HDPE ) by adding ceramic particles to propose an option for artificial hip joint liner Enhancing wear rate of high-density polyethylene ( HDPE ) by adding ceramic particles to propose an option for artifi (2019). https://doi.org/10.1088/1757-899X/561/1/012071
24. D.L. Burris, W.G. Sawyer, A low friction and ultra low wear rate PEEK/PTFE composite. Wear **261**(3–4), 410–418 (2006). https://doi.org/10.1016/j.wear.2005.12.016
25. S.M. Kurtz, A Primer on UHMWPE. UHMWPE Biomaterials Handbook (2nd ed.) (2009). https://doi.org/10.1016/B978-0-12-374721-1.00001-8

26. C. Nayak, S. Ariharan, P. Kushram, K. Balani, Fretting of Aluminum Oxide, Hydroxyapatite and Carbon Nanotubes reinforced ultra high molecular weight polyethylene. J. Min. Mat. Eng. **4**, 22–34 (2018)
27. S. Polizzi et al., Neurotoxic effects of aluminium among foundry workers and Alzheimer's disease. Neurotoxicology **23**, 761–774 (2002). https://doi.org/10.1016/S0161-813X(02)00097-9
28. A. Gupta, G. Tripathi, D. Lahiri, K. Balani, Compression Molded Ultra High Molecular Weight Polyethylene-Hydroxyapatite-Aluminum Oxide-Carbon Nanotube Hybrid Composites forHard Tissue Replacement. J. Mater. Sci. Technol. (2013). https://doi.org/10.1016/j.jmst.2013.03.010
29. A.K. Patel, P. Trivedi, K. Balani, Processing and Mechanical Characterization of Compression-Molded Ultrahigh Molecular Weight Polyethylene Biocomposite Reinforced with Aluminum Oxide. J. Nanosci. Nanoeng. Appl. **4**, 1–11 (2014)
30. A.A. Edidin, S.M. Kurtz, Influence of mechanical behavior on the wear of 4 clinically relevant polymeric biomaterials in a hip simulator. J. Arthroplasty **15**(3), 321–331 (2000). https://doi.org/10.1016/S0883-5403(00)90647-8
31. R.K. Sharma, M. Agarwal, K. Balani, Effect of ZnO morphology on affecting bactericidal property of ultra high molecular weight polyethylene biocomposite. Mater. Sci. Eng., C **62**, 843–851 (2016). https://doi.org/10.1016/j.msec.2016.02.032
32. F. Alam, A. Kumar, V.R. Shukla, A. Nisar, K. Balani, Multi-length scale wear damage mechanisms of ultra-high molecular weight polyethylene nanocomposites. Polym. Testing **81**, 106210 (2020). https://doi.org/10.1016/j.polymertesting.2019.106210
33. C. Nayak, R. Kundu, R. Pandey, K. Balani, Tribological properties of SS 304 and Ti6Al4V using four reciprocating geometries on a bio-tribometer under dry and lubricated conditions. Nanomaterials and Energy (2020)

# Bacterial Cellulose for Drug Delivery: Current Status and Opportunities

**Shivakalyani Adepu, Sailaja Bodrothu, and Mudrika Khandelwal**

## 1 Introduction

There are various long-chain molecules or biopolymers naturally produced by the living cells. Among the various classes of naturally occurring polymers such as polysaccharides, polyamides, polyamines, and polyolefins, polysaccharides constitute the structural materials [1]. Cellulose (a polysaccharide) is the most common biopolymer and is present as the most important structural component across various living organisms such as prokaryotes, protists, animals, and plants. Cellulose is produced as a supramolecular hierarchical organization of polyglucan chains [2]. This means that the polyglucan chains are assembled into fibrous units which are then further assembled hierarchically into larger fibers and ribbons. The dimensions, composition, structure, and morphology vary with the source of cellulose. The various sources of cellulose include plants, trees, sea squirts (tunicates), algae, and certain species of bacteria [2].

Cellulose is used in a variety of common as well as advanced applications owing to its deep integration with our society, given its abundance, low cost, and suitable properties. It finds applications in paper, cotton, lubricants, fillers, adhesives, and also in form of fibers in clothes, membranes, and filters. Natural cellulosic fibers such as hemp, cotton, and linen have been used by our society as fuel, garments, and engineering materials for generations and their usefulness and acceptance in society are obvious by the volume of forest products, paper, and textiles across the globe. Cellulose derivatives, such as methyl cellulose, hydroxyl propyl methyl cellulose, ethyl cellulose, nitrocellulose, and cellulose nitrate, are used in lubricants, binder, explosives, lacquer, controlled release drug tablet, and detergents. Cellulose is also

---

S. Adepu · S. Bodrothu · M. Khandelwal (✉)
Cellulose and Composites Group, Department of Materials Science and Metallurgical Engineering, Indian Institute of Technology, Hyderabad, India
e-mail: mudrika@msme.iith.ac.in

A. Shrivastava et al. (eds.), *New Horizons in Metallurgy, Materials and Manufacturing*,
Indian Institute of Metals Series, https://doi.org/10.1007/978-981-19-5570-9_9

extensively used for technical applications such as tire cords, dialysis membranes, and reinforcements, substrates for sensors, packaging, and so on [2].

Plants and trees constitute the main resource for cellulose. In the process of cellulose extraction from plants and trees, it leads to massive deforestation, and thereafter the chemical treatments are required to remove non-cellulosic impurities such as lignin hemicelluloses causing pollution. Moreover, cellulose, when used in form of fibers, is often made by the regeneration of cellulose which involves chemical dissolution and regeneration. Due to these disadvantages, a lot of research is being pursued toward the utilization of other sources of cellulose. In particular, bacterial cellulose has received much attention owing to various advantages discussed below.

Many of the advanced applications can particularly benefit from the nano-dimensional aspect.

The cellulose obtained from bacterial origin is 100% pure, devoid of any impurities such as lignin and hemicelluloses (generally present in plants and trees). The cellulose chains are organized into semicrystalline (highly crystalline) nanofibrous three-dimensional network and produce a floating pellicle at the media–air interface. Cellulose is a supramolecular multi-level hierarchical organization of β-linked polyglucan chains into microfibrils. A comparison of celluloses obtained from bacteria and plants is compared in Table 1 with respect to the various attributes. It is evident from the table that bacterial cellulose offers various advantages in terms of dimensions, purity, and morphology [3].

**Table 1** Comparison of plant cellulose and bacterial cellulose [4]

| S. no | Properties | Plant cellulose | Bacterial cellulose |
|---|---|---|---|
| 1 | Purity | Impurities are present like lignin and hemicellulose | Pure |
| 2 | Crystallinity | 40–60% | 84–89% |
| 3 | Composition | 40–50% cellulose<br>15–20% hemicellulose<br>20–25% lignin<br>5–10% others | Ultra-fine network of highly uniaxially oriented cellulose nanofibers with high crystallinity |
| 4 | Aspect ratio | Low | High |
| 5 | Porosity | Low | High |
| 6 | Density | High | Low |
| 7 | Surface area | Low | High |
| 8 | Water absorption | Low | High |
| 9 | Ease of extraction of fibers from it | Cellulose fibers are prepared via chemical methods through acid digestion (amorphous area of the fibers is destroyed to get nanofibers) | No specific treatment required |

**Table 2** Various applications and relevant properties of bacterial cellulose [5–18]

| Application | Property |
|---|---|
| Food | Nata de coco—roughage content |
| Die absorption | Environment-friendly, cost-effective, the presence of surface hydroxyl groups and should be a good absorbent |
| Removal of heavy metal ions | Absorbent, porous structure |
| functional paper | Tensile strength, the presence of hydroxyl groups |
| binder for natural fiber and paper | High mechanical strength |
| facial scrub | Alignment of chains with shear = scrubbing action |
| Skin mask | Moisturizing ability, water retention |
| Cloth for fashion design | Ability to become hydrophobic by surface modification |
| Electronic paper display | Transparency, flexibility |
| Wound healing system | Moisturizing ability |
| Scaffold | Adhesiveness for cells, biocompatibility |
| Vascular graft | Shaping and morphological tuning abilities, biocompatibility |
| Drug delivery | Biocompatibility and microporous nature |
| Immobilization matrices | Immobilization of denitrifying bacteria<br>Urease immobilization<br>Glucoamylase immobilization<br>Yeast immobilization for ethanol fermentation |
| Sound transducing membrane | Dimensional stability at higher sonic velocities |
| Packaging | Low oxygen permeability, flexibility bacteriostatic sausage casing active food packaging |
| Emulsion thickener | Shear thinning behavior |
| Precursor for CNFs | Intrinsic nanofibrous network |

Also, Table 2 is presented below where some of the applications of bacterial cellulose are listed along with the property of bacterial cellulose which makes it suitable for that particular application.

Nanodelivery systems for therapeutic applications are being increasingly explored as efficient alternatives to the conventional systems. The conventional drug delivery systems suffer from significant issues such as poor loading efficiency, need for high dosage and dosing frequency, insufficient drug bioavailability, poorly controlled release behavior and fluctuations in plasma drug levels with associated toxicity [19]. Most of these issues can be tackled by nanodrug delivery systems as they offer a better control over drug absorption and distribution [20]. Nanomaterials can help overcome the challenges associated with the physicochemical properties of drug such as solubility/permeability and stability as well as biopharmaceutical aspects such as efficacy, bioavailability [21–23]. This in turn can enable the pharmacological translation of therapeutic agents (such as nanoparticles, herbal essential oils) which can play a vital role in management of some of the key challenges today such as treatment of chronic pain and issues of drug resistance as these agents suffer from poor aqueous solubility, low permeability, systemic cytotoxicity, and environmental sensitivity.

Various forms of nanodrug delivery systems have been developed which include nanoparticles, microcapsules, nanofibers, liposomes, niosomes, etc. [24, 25]. The choice of materials and nanocarrier is based on the specific therapeutic requirement, physicochemical characteristics of the drug, the kind of drug release required and release kinetics (immediate/ slow/ sustained/ delayed/ pulsatile) needed [26–28].

The nanofibrous materials are particularly preferred for the delivery of therapeutic agents owing to their high specific surface area, porosity, and high drug loading capacity [29]. Biomaterial-based nanofibrous hydrogels are further desirable due to their biocompatibility and integrated porous structure [30]. Bacterial cellulose (BC) is one such material, which is a pure form of cellulose, produced as an extracellular polysaccharide through a self-assembly process by certain types of bacteria (*Gluconobacter, Acetobacter, Agrobacter*, and *Sarcina*) as a dilute hydrogel (>90% water) with high water holding capacity [31, 32].

BC is superior to plant cellulose as it is devoid of impurities (lignin and hemicellulose) and consists of three-dimensional nanofibrous micro- and mesoporous structure with high mechanical strength [33]. The presence of 3D-nanofibrillar network with multidimensional porosity makes BC a suitable matrix for the inclusion of drugs and therapeutic agents (or formulations) of various types and sizes [26, 29, 34–36].

## 2 Synthesis

Various species of bacteria, such as Acetobacter and Rhizobium, are known to produce cellulose, with the possible reason of producing a protective environment against the adverse environment [4]. Typically, the bacterial cellulose is produced as a floating gelatinous pellicle by layered deposition at the liquid–air interface. This ensures the supply of media from below and the air from the top. The amount of layers/thickness of cellulose pellicle increases with time and reaches a maximum thickness. The production in terms of quality and quantity is dependent on the media as well as culture conditions. There is a huge body of work on using various sources of carbon and nitrogen and has led to the development of better cellulose-producing strains, better yield and has made it commercially possible [37]. Bacterial cellulose is a fact used as a dessert food ingredient for a long time in several East Asian countries and is commercially available as nata-de-coco. It is produced by the fermentation of coconut milk in food industries [38]. The biosynthesis and hierarchical organization of bacterial nanocellulose from *Gluconacetobacter xylinum* is schematically represented in Fig. 1.

The most popular media for the production of bacterial cellulose is the Hestrin–Schramm culture medium, which consists of distilled water with glucose (20 g/L), peptone (5 g/L), yeast (5 g/L), sodium phosphate ($Na_2PO_4$) (3.4 g/L), citric acid ($C_6H_8O_7$) (1.15 g/L) [39]. Bacterial cellulose (BC) pellicles are extracted from the media and treated with NaOH to kill the microbes present and subsequently washed

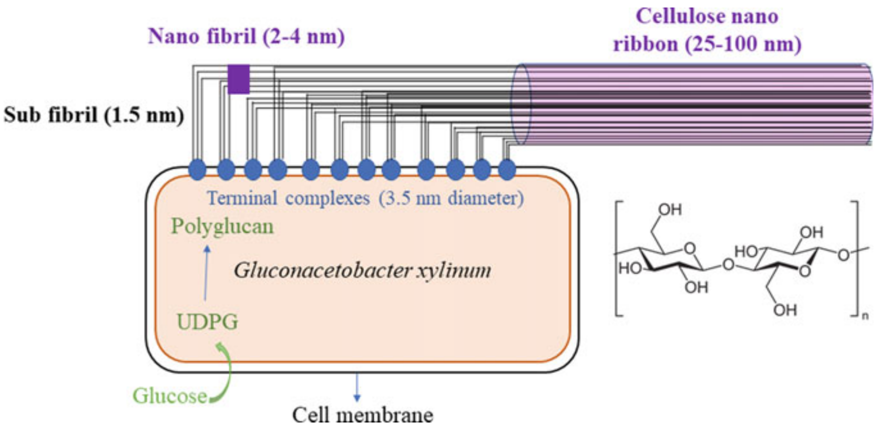

**Fig. 1** Schematic of the biosynthesis and hierarchical organization of bacterial cellulose

with distilled water to remove the cell debris and culture media contents. Commercially, BC is produced from coconut milk extracted from the freshly grated coconut. Sugar and acetic acid are added to the extracted coconut milk and fermented with the bacterial inoculum of *Acetobacter xylinum.* After 8–10 days of fermentation, a thick layer of hydrogel is formed on the surface of the fermentation tank. Ideally, the static culture method is used for the synthesis of bacterial cellulose. However, agitated cultures and other modifications to the culturing process are used to obtain modified celluloses which are discussed in this chapter in a later section. Therefore, of the biggest advantages of bacterial cellulose is the ability to produce it in the laboratory and deliberately modify the production to tune the bacterial cellulose properties.

Some of the most relevant properties for application as a drug delivery system are discussed below.

## 3 Structure

### i. Organization

Cellulose from all sources possesses a fibrous morphology produced by a supramolecular hierarchical organization. Particularly in the case of bacterial cellulose, polyglucan chains are produced as a polymerization product of glucose/sugars available to the bacteria in the nutrient medium. The polyglucan chains are produced by export pores of the bacteria which bundle up to register crystallinity leading to monoclinic or triclinic crystal structure. It has been observed that the contribution of a single bacterium may also comprise multiple crystalline fibrils to form a single polycrystalline fiber [40, 41]. Branching is also often observed in bacterial cellulose which is attributed to the cell division of bacteria; however, further work is needed to confirm this [42].

Cellulose is produced by the self-assembly process directed by the biosynthesis machinery of cell. The hierarchical organization of cellulose, its shape, and dimensions are determined by the biosynthesis machinery of that particular organism. Besides the physical machinery, alterations in the biosynthesis environment affect the cellulose structure, properties, and morphology.

ii. Crystallinity

Bacterial cellulose is produced by the bacterial cells in two steps—polymerization and crystallization. It has been studied using an interfering agent that the processes are independent. If crystallization is hampered or inhibited, polymerization is still seen to continue. It is perceived that the semicrystalline cellulose fibrils comprise of sequential arrangement of amorphous and crystalline regions [43, 44]. It is for this reason that the acid hydrolysis leads to the formation of nanocrystals/nanowhiskers as the acids attack the amorphous regions preferentially [45].

The crystallite sizes are different in all directions and depend on the H-bond and van der Waals interactions. Earlier reports from calculations of crystallite size from X-ray diffraction data have shown rectangular cross-sections with truncated ends [44].

iii. Chirality

Cellulose fibrils including those of bacterial cellulose are twisted and bundled. The twist in bacterial cellulose microfibrils can be attributed to the intrinsic chirality present in cellulose chains and/or to the rotation of bacterial cells. The latter is not applicable for the cellulose microfibrils obtained from non-bacterial sources. As the bacterium does not have flagella and any other phenomena of locomotion, the chirality of cellulose may be due to the intrinsic helicity of cellulose chains. Likewise, twists are also observed in plant tendrils (three to four times larger magnitude as compared to BC) in the form of spiral curls or helical coils. The helical coils can reverse their handedness. Further exploration is needed to understand the relationship between chirality at various morphological levels [46].

iv. Porosity

Bacterial cellulose owing to nanofibrous 3D interconnected network, it comprises of high degree of porosity. It is produced as a very dilute hydrogels with over 90% water. When water is extracted, depending on how water is extracted, the hydrogel is converted into aerogel or xerogels. The dried bacterial cellulose comprises micro (<2 nm), meso (2–50 nm), and macropores, relative distribution of which depends on the drying methods. It has been seen that freeze-dried bacterial cellulose is more porous and has larger pore size as compared to the oven-dried bacterial cellulose [47].

v. Biodegradability

Bacterial cellulose is not enzymatically biodegradable in vivo. However, it can be modified giving rise to better biodegradability. Biodegradable bacterial cellulose can be prepared with different oxidation degrees using sodium periodate. It can be modified by periodate oxidation forming 2,3-dialdehyde bacterial cellulose making it biodegradable. Modified nanonetwork can be degraded into porous network with micro-sized pores. The degradation begins with oxidized amorphous parts [48].

Also, bacterial cellulose can be incorporated with ingredients like cellulase and other buffer ingredient to maintain pH for the enzyme activation. The glucose released from degraded materials increased from 30% without incorporation of buffer ingredients to 97% when incorporated with these ingredients [49].

## 4 Bacterial Cellulose as a Matrix in Various Applications

The ideal structure, biocompatibility, and sustainability of bacterial cellulose have led to many studies and prompted its application in a variety of fields, such as medical, food, packaging, textiles, and electronics [23] (listed in Table 2). Due to exceptional properties bacterial cellulose-based composites have been employed in a wide range of applications including food [7], drug delivery [8], tissue engineering [9], cosmetics [10], clothing [11], conducting paper [12]. Bacterial cellulose-based materials are suitable for healthcare applications due to the structural similarity with the extracellular matrix. In wound healing materials, bacterial cellulose has been loaded with silver-sulfadiazine, silver nanoparticles [50]; bacterial cellulose as an artificial skin and blood vessels, scaffolds for tissue engineering have been produced by incorporation of hyaluronic acid, growth factors, and stem cells [15]. Bacterial cellulose has also been explored as a matrix for certain drugs which include Lidocaine hydrochloride, Methotrexate, Benzalkonium chloride, Diclofenac sodium, Amoxicillin, and tetracycline drug delivery [14, 16–18].

## 5 Bacterial Cellulose in Drug Delivery

Bacterial cellulose possesses nanofibrous micro- and mesoporous structure with high porosity and crystallinity, which makes it a suitable carrier for various therapeutics agents of different solubility and sizes. Given the natural fibrous morphology and semicrystalline nature of cellulose, bacterial cellulose can be used as nanofibers or processed to obtain nanowhiskers and nanocrystals. Bacterial cellulose nanofibers can also be pyrolyzed to obtain carbon nanofibers. For this chapter, the focus is kept on cellulose nanofibers.

Bacterial cellulose has been explored for the delivery of anaesthetics (Lidocaine Hydrochloride) [51], antibiotics (Tetracycline and Amoxicillin) [16, 17], anticancer drugs (Doxorubicin, methotrexate, and curcumin) [52–54], analgesics (Ibuprofen and Diclofenac sodium) [51, 55]. In most of these reports, a large burst release was observed in the first 15 min of release and entire drug released within 1 h. In case of immediate release dosage forms, such kind of release is appreciable; however, burst release is not always needed, and sustained release of drugs maintains drug level in therapeutic limits and decreases the dosage and dosing frequency of medicament. In order to achieve sustained release, various composites have been developed combining bacterial cellulose with other polymers such as Poly n-isopropyl acrylamide (PNIPAM) [56, 57], Polyvinyl alcohol (PVA) [58], Chitosan [59], sodium alginate [60], Zein [61], gelatin [62], pectin [63] for sustained, thermo- and pH-sensitive release. More details on these reports are tabulated in Table 3. The composites offered improvement by preventing the initial burst release to some extent and extended the release of drug to 2–5 h.

It is observed that bacterial cellulose in its native form offers high drug loading with burst release of therapeutic agents. Being a hydrogel, the rate and extent of swelling contribute greatly in loading as well as release. Further, the porosity also plays a significant role in determining the swelling index. Composite formation often leads to a reduced porosity and swelling capability, which helps in sustaining the release. However, in situ and ex situ modifications of bacterial cellulose are gaining attention due to the possibility of a better control over various properties of bacterial cellulose (such as fiber diameter, morphology, porosity, crystallinity, and degree of polymerization) and/or complement it with additional property or functionality [42].

## 6 Modifications of Bacterial Cellulose

Drug delivery depends on matrix parameters such as porosity, pore size distribution, density, flexibility. For example, porosity determines the extent of swelling, and ease of media ingress and release of drug. The fiber density and stiffness (which in turn may depend on the crystallinity of the fibers) determine the rate and extent of swelling. Similarly, pore size distribution can affect the rate of availability of drugs with time. Thus, it is important to focus on morphological and structural aspects of bacterial cellulose in order to obtain a reliable and tunable drug delivery system.

The bacterial cellulose biosynthesis involves two major steps: First step involves the synthesis of cellulose molecules by polymerization of uridine diphosphate glucose (UDP glucose) which is formed from the sugar precursor of medium and their subsequent exclusion into the medium. The second step involves the self-assembly process where the crystallization of cellulose molecules takes place to form nanofibrous network. The structural and morphological properties of bacterial cellulose are generally governed by the second step [68, 69].

Given this, two types of modifications are possible: in situ (pre-production, during production) and ex situ (post-production modifications). A schematic of in situ and ex situ modifications, used in the present work, is represented in Fig. 2.

### (A) In situ modification of bacterial cellulose in drug delivery

In situ modification can be carried out at different stages and with different objectives. Broadly, the strategies can be divided into one of the following ways:

**Table 3** Bacterial cellulose and its composites as carriers for drug release

| Matrix | Drug | Application | Observations | References |
|---|---|---|---|---|
| Bacterial cellulose | Tetracycline | Wound dressing | 90% of drug released in 1 h | [17] |
| Bacterial cellulose | Octenidine | Wound dressing | Initial burst (83%) within the first 8 h, reaching equilibrium conditions after 24 h and a total release of 92% | [64] |
| Bacterial cellulose-Alginate composite | Doxorubicin | Colorectal cancer | Sustained release for 14 days | [52] |
| Bacterial cellulose-Pectin films | Levofloxacin | Wound dressing | Burst release was reduced 20% when compared to pure bacterial cellulose (60%) | [63] |
| Bacterial cellulose-Gelatin | Methylene blue as model drug | | Drug release for 40 h | [62] |
| Bacterial cellulose in situ modified with CMC | Methotrexate | Topical treatment of Psoriasis | Burst release in first 15 min; 90% released in 1 h | [65] |
| Bacterial cellulose and PEO-co-PCL composite | Retinol | Cosmetics | 60% released in 6 h and sustained release for 24 h | [66] |
| Bacterial cellulose | Ibuprofen and Lidocaine | Transdermal patch | 90% permeation in 8 h | [51] |
| Bacterial cellulose–Polyaniline | Berberine hydrochloride | Controlled release at varying conditions | pH and electroactive drug release behavior<br>Slow release in acidic and fast release in alkaline and neutral conditions<br>Rapid directional release upon voltage application | [67] |

a. Pre-production modifications: involves addition of modifiers in the culture media, varying the cellulose-producing bacterial strain and carbon/nitrogen source.
b. During production modification: involves incorporation of patterns, substrates and altering the fermentation conditions (such as agitation, humidity, temperature) during biosynthesis/incubation.

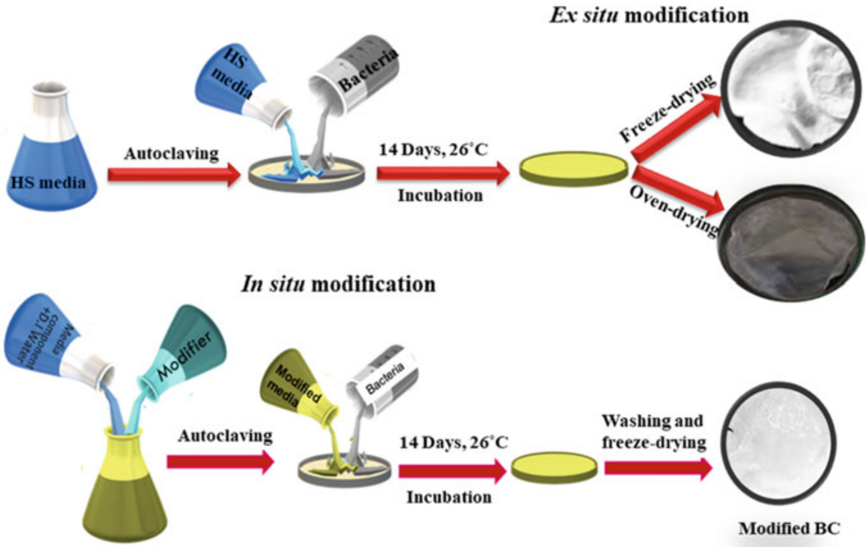

**Fig. 2** Schematic of in situ and ex situ modifications of bacterial cellulose

c. In situ composite formation: involves incorporating additives such as water-soluble additives, dispersed particles, etc., during fermentation to modify composition.

The additives which have been studied for in situ modification include synthetic polymers, proteins, polysaccharides, low molecular organic compounds, antibiotics, and metal oxides. The additives in the growth media, which are not specifically required for bacterial cell growth, can affect cellulose biosynthesis, either by binding directly to the cellulose in the course of production and interfering with the crystallization or co-crystallizing with the cellulose [70]. It is also possible that the inclusion of additives may alter the cellulose production indirectly by affecting the bacterial cells. Regardless of the method, the presence of an additive in the media affects the yield, microstructure, morphology, and physical properties.

The inclusion of water-soluble polymers in the cellulose culture media has displayed varying results. Some reported that the inclusion of such additives just resulted in altered cellulose structure [71, 72], while others have reported that the additives are incorporated into the growing cellulose fibrils, resulting in the formation of in situ composites [73, 74]. Polymers such as carboxymethyl cellulose (CMC) and methylcellulose (MC) interferes with the cellulose assembly, thus reducing the crystallinity and crystal size, as well as increase in pore size and thermal stability [71]. Inclusion of additives such as Poly(ethylene oxide) (PEO) [75], Poly(caprolactone) (PCL) [76], Poly(hydroxybutyrate) (PHB) [77], Poly(hydroxybutyrate-co-valerate) (PHBV) [78], Poly(vinyl alcohol) (PVA) [79–81], Tween 80 [82], Hydroxypropyl methylcellulose (HPMC) [83], and starches [84, 85] in the growth media have resulted in these additives being incorporated into the bacterial cellulose resulting in in situ composites, which causes variation in pore size, degree of polymerization, crystallinity, fiber diameter and mechanical strength and composition [74, 82, 83]. On the other hand, addition of certain low molecular weight water-soluble polymers such as PEG (Polyethylene glycol 4000 and 400), β-cyclodextrin, dyes (Calcofluor) and antibiotics (nalidixic acid) do not get incorporated in bacterial cellulose, but causes changes in morphology, fiber diameter, and crystallinity [42, 68]. The addition of PEG 400, as well as β-cyclodextrin, caused an increase of the bacterial cellulose pores, while PEG 4000 decreased the pore sizes without simultaneous integration of the additives into bacterial cellulose. A detailed literature review on in situ modification, indicating mechanism of modification and main observations is listed in Table 4.

BC has been explored for the delivery of anesthetics (Lidocaine Hydrochloride) [51], antibiotics (Tetracycline and Amoxicillin) [16, 17], anticancer drugs (Doxorubicin, methotrexate, and curcumin) [52–54], analgesics (Ibuprofen and Diclofenac sodium) [51, 55]. In most of these reports, a large burst release was observed in the first 15 min of release and entire drug released within 1 h. In case of immediate release dosage forms, such kind of release is appreciable; however, burst release is not always needed, and sustained release of drugs maintains drug level in therapeutic limits and decreases the dosage and dosing frequency of medicament. In order to achieve sustained release, various composites have been developed combining BC with other polymers such as Poly n-isopropyl acrylamide (PNIPAM) [56, 57], Polyvinyl alcohol (PVA) [58], Chitosan [59], sodium alginate [60], Zein [61], gelatin [62], pectin [63] for sustained, thermo- and pH-sensitive release. The composites offered improvement by preventing the initial burst release to some extent and extended the release of drug to 2–5 h.

In situ modification of bacterial cellulose with water-soluble non-incorporating additives seems to be an interesting line of research, where a modified bacterial cellulose structure can be achieved without change in composition. These additives act as removable auxiliaries. Adepu et al. [24] have tuned the drug loading and release kinetics of Diclofenac sodium from bacterial cellulose matrix by in situ modification by adding PEG2000 to the culture medium. As a non-incorporating in situ modifier, PEG2000 increased the overall porosity, pore volume and decreased the fiber density and specific surface area with no significant effect on crystallinity. A huge burst release was observed for PEG-modified bacterial cellulose as compared to pristine bacterial cellulose in the in vitro, drug release studies. The drug release was reported to be concentration-dependent and follows Fickian diffusion [26, 36]. In situ modifiers either increase or decrease the porosity of BC with or without altering the crystallinity significantly. If the i*n situ* modification increases the porosity of BC, a faster swelling rate with a quick and burst drug release is observed. If the in situ modification results in increased crystallinity, the BC nanofibers get wet slowly with low swelling rate that results in slower drug release. CMC as an in situ modifier was studied for the delivery of an anticancer drug, Methotrexate. In this, CMC coated the BC nanofibers by interacting with the cellulose self-assembly process which resulted in lesser porosity, denser structure, low crystallinity, and reduced water uptake. Reduced porosity of CMC-modified BC resulted in slower drug diffusion as

**Table 4** In situ modification of bacterial cellulose to tune drug release

| Modifier | Mechanism | Major observations | References |
|---|---|---|---|
| *Non-incorporating* | | | |
| Polyethylene glycol 4000 | Interfere with the association of microfibrils post-synthesis | Increase in total surface area | [68] |
| PEG 400 | Affects the self-assembly process | Inhomogeneous fiber structure; huge agglomerations | [68, 75] |
| Calcofluor | Interfere with the cellulose crystallization and assembly | Decrease crystallinity and crystallite size<br>Decrease in fiber diameter | [42] |
| Nalidixic acid | Affects the bacterial cell division | Decrease in crystallinity and crystallite size<br>Increase in fiber diameter<br>Decrease in surface area | [42] |
| B-Cyclodextrin | Inclusion complex and wash way | Increase in pore size<br>Increase in fiber diameter | [68] |
| *Incorporating agents* | | | |
| PEO | Interferes with the hydrogen bonding | Decrease in crystallinity and crystallite size<br>Increase in fiber diameter | [75] |
| Carboxymethyl cellulose (CMC)<br>HPMC<br>MC | Interfere with the cellulose crystallization and assembly | Decrease crystallinity and crystallite size<br>Decrease in fiber diameter<br>Decrease in total surface area<br>Reduced water uptake and swelling<br>Slower drug release | [82, 83] |
| PCL | Does not interfere with the network assembly and completely gets incorporated | Decrease in crystallinity<br>Increase in thermal stability | [76] |
| PHB | Does not interfere with the network assembly and completely gets incorporated | Decrease in Crystallinity<br>Increase in fibril dimension | [77] |
| PHBV | Does not interfere with the network assembly and completely gets incorporated | Increase in porosity<br>Decrease in crystallinity | [78] |
| PVA | Interferes with the hydrogen bonding<br>Influence the in situ growth of bacterial cellulose through the formation of spherulites | No significant difference in crystallinity and crystallite size<br>Increase in fiber diameter<br>Optical transparency increased | [81, 88] |

(continued)

**Table 4** (continued)

| Modifier | Mechanism | Major observations | References |
|---|---|---|---|
| Bamboo and sodium alginate | Enzymatic hydrolysate of glycerol-pretreated moso bamboo was used as a carbon source as replacement to glucose to get bamboo bacterial cellulose. Sodium alginate was added to bacterial cellulose by hydrogen bonding from 0.25 to 1 wt % | Poor release of BSA and faster release of lysozyme | [89] |

compared to pristine BC and degree of substitution of CMC plays a critical role on BC microstructure which in turn affects the drug release [86]. Sodium alginate as an in situ modifier, offered pH-responsive drug release with an increased swelling ratio at pH 7.4 and decreased swelling at pH 1.2. Slower release of BSA was observed due to the hydrophobic interaction of BSA with cellulose. Faster release of lysozymes was observed due to electrostatic interactions [87]. In situ modification of bacterial cellulose helped to achieve immediate release as well as sustained release. Depending upon the requirement one can choose specific modification to tune the release.

### (B) Ex situ modifications of bacterial cellulose in drug delivery

Ex situ modifications involve modification of bacterial cellulose post-production by making composites, by altering drying methods and/or by chemical/enzymatic hydrolysis to make cellulose nanocrystals and nanowhiskers. Most of the work targeted at using bacterial cellulose composites involve ex situ modification as illustrated in Table 5. Due to its highly porous nature, it is easy to incorporate additives post-production by simply dipping in their suspensions/solutions. Moreover, it also offers a possibility of in situ synthesis of nanoparticles and polymerization. Further, the chemical nature of bacterial cellulose can be modified by chemical grafting, given high porosity, surface area, and functional groups [68, 82, 90, 91]. However, the simplest way of modifying bacterial cellulose structure and morphology is using different drying methods as it affects the pore size, re-swellability, and crystallinity of bacterial cellulose [92, 93]. Very limited work has been carried out to use this simple strategy to tune bacterial cellulose properties for drug delivery [94, 95].

Typical techniques for the drying bacterial cellulose are freeze-drying, oven-drying, and critical point drying after the stepwise solvent exchange, water removal under pressure using water-absorbing materials and/or additional heating, as well as air-drying with or without water-binding additives [96–98]. Observed differences were mainly related to the degree of preservation of the 3D structure of bacterial cellulose, water uptake capacity and stability of loaded drugs, as well as the cost/time/environmental hazards. The importance of the drying process was shown by the lower uptake capacity of freeze-dried bacterial cellulose for proteins compared

**Table 5** BC and its composites used for drug delivery

| Matrix | Drug | Application | Observations | References |
|---|---|---|---|---|
| BC | Tetracycline | Wound dressing | 90% of drug released in 1 h | [17] |
| BC | Octenidine | Wound dressing | Initial burst (83%) within the first 8 h, reaching equilibrium conditions after 24 h and a total release of 92% | [64] |
| BC-Alginate composite | Doxorubicin | Colorectal cancer | Sustained release for 14 days | [52] |
| BC-Pectin films | Levofloxacin | Wound dressing | Burst release was reduced 20% when compared to pure BC (60%) | [63] |
| BC-Gelatin | Methylene blue as model drug | | Drug release for 40 h | [62] |
| BC in situ modified with CMC | Methotrexate | Topical treatment of Psoriasis | Burst release in first 15 min; 90% released in 1 h | [86] |
| BC and PEO-co-PCL composite | Retinol | Cosmetics | 60% released in 6 h and sustained release for 24 h | [66] |
| BC | Ibuprofen and Lidocaine | Transdermal patch | 90% permeation in 8 h | [51] |

with native bacterial cellulose [99, 100]. Freeze-drying is the most common method of drying bacterial cellulose. Recently, Pujitha et al. reported the effect of oven-drying and freeze-drying on the physical properties of bacterial cellulose such as morphology, porosity, and mechanical strength. Interestingly, fiber diameter, pore size, and porosity have been reduced in over-dried bacterial cellulose when compared to freeze-dried one. Crystallinity was also increased with oven-drying [95].

Ex situ modification of bacterial cellulose by changing drying method has been explored to photochromic films [101], improve toughness [102, 103], enhance adsorption [104], optically transparent films [94], and also for energy storage [105, 106] applications. Air-drying resulted not only in a structural collapse of bacterial cellulose but also in a very rapid release of the model drug azorubine compared with native bacterial cellulose [91, 99]. A comparative study of the effect of oven-drying versus freeze-drying technique on drug release behavior was reported recently studied using a water-soluble drug Diclofenac sodium [35]. Oven-drying offered a sustained zero-order release for 8 h while freeze-dried bacterial cellulose offered a burst release of 60% drug loaded within the first 1 h. These significantly different release profiles were attributed to the difference in compact microstructure, lesser porosity, higher crystallinity, and lesser swelling ratio of oven-dried bacterial cellulose as compared to freeze-dried [107].

## 7 Bacterial Cellulose in Other Forms for Drug Delivery

Regenerated bacterial cellulose has been gaining interest in the pharmaceutical sector to formulate various excipients (film-forming agents, rheology modifiers, enteric-coated formulations, microparticles, etc.). Bacterial cellulose was regenerated using n-morpholine oxide and loaded with two anti-ulcer drugs famotidine and Tizanidine. Burst release of about 90% drug release within first 30 min was observed through oral route [108]. Bacterial cellulose was defibrillated by ultra-refining to get bacterial cellulose nanofibrils, which are made into microparticles by spray-drying technique along with HPMC and mannitol. The microparticles of bacterial cellulose-HPMC-Mannitol were loaded with Diclofenac sodium and caffeine for enteric-coated drug release [109].

Herbal essential oil-loaded polymeric microcapsules were used as secondary drug carriers and incorporated in bacterial cellulose which was a primary carrier to further enhance the stability and control the release of herbal drugs [110].

Bioresorbable bacterial cellulose has also been researched for its enormous applications in drug delivery and implantable systems. Bacterial cellulose was oxidized with sodium iodate and loaded with a bactericidal agent, Chlorhexidine gluconate for treating dental infections. The drug was loaded directly in oxidized bacterial cellulose and also through inclusion complexes of β-cyclodextrin. The drug release from oxidized bacterial cellulose was 10 folds slower as compared to β-cyclodextrin [111].

## 8 Conclusion and Future Scope

In this chapter, bacterial cellulose as a carrier for therapeutic agents and modifications for tuning drug release are discussed. Bacterial cellulose, owing to its high surface area and multidimensional pores, has been an attractive and useful nanocarrier for drug release. Further, it is evident from the reported research papers that the properties of bacterial cellulose can be tuned to modulate the release of drugs. It is also reported that bacterial cellulose acts as a barrier to burst release enabling controlled and sustained activity by in situ and ex situ modifications with an alteration in the microstructure, porosity, and swellability. Various modifications (in situ and ex situ) of bacterial cellulose are found to play an important role in enabling the pharmacological translation of therapeutic agents (such as nanoparticles, herbal essential oils) which suffer from issues of poor aqueous solubility, low permeability, systemic cytotoxicity, and environmental sensitivity. Further, patterning and aligning could also be explored to tune release and dedicated research is required on understanding mechanisms of the possible interactions of therapeutic agents and bacterial cellulose for its efficient utilization as a safe drug delivery.

## References

1. S. Thomas, P. Visakh, A.P. Mathew, Advances in natural polymers. Adv. Struct. Mat. 255–312 (2013)
2. D. Lavanya, P. Kulkarni, M. Dixit, P.K. Raavi, L.N.V. Krishna, Sources of cellulose and their applications—A review. Int. J. Drug Formula. Res. **2**, 19–38 (2011)
3. M. Iguchi, S. Yamanaka, A. Budhiono, Bacterial cellulose—a masterpiece of nature's arts. J. Mater. Sci. **35**, 261–270 (2000)
4. R. Jonas, L.F. Farah, Production and application of microbial cellulose. Polym. Degrad. Stab. **59**, 101–106 (1998)
5. S.-P. Lin, I.L. Calvar, J.M. Catchmark, J.-R. Liu, A. Demirci, K.-C. Cheng, Biosynthesis, production and applications of bacterial cellulose. Cellulose **20**, 2191–2219 (2013)
6. H. Ullah, H.A. Santos, T. Khan, Applications of bacterial cellulose in food, cosmetics and drug delivery. Cellulose **23**, 2291–2314 (2016)
7. Z. Shi, Y. Zhang, G.O. Phillips, G. Yang, Utilization of bacterial cellulose in food. Food Hydrocolloids **35**, 539–545 (2014)
8. I. Almeida, T. Pereira, N. Silva, F. Gomes, A. Silvestre, C. Freire et al., Bacterial cellulose membranes as drug delivery systems: an in vivo skin compatibility study. Eur. J. Pharm. Biopharm. **86**, 332–336 (2014)
9. Lina F, Guang Y, Jin Z, Yue Z. Bacterial cellulose for skin repair materials: INTECH Open Access Publisher; 2011.
10. S. Bielecki, H. Kalinowska, A. Krystynowicz, K. Kubiak, M. Kołodziejczyk, M. de Groeve. Wound dressings and cosmetic materials from bacterial nanocellulose, in *Bacterial NanoCellulose: A Sophisticated Multifunctional Material* (CRC Press, 2012), pp. 157–174
11. B. Gupta, R. Agarwal, M. Alam, Textile-based smart wound dressings (2010)
12. J.A. Marins, B.G. Soares, K. Dahmouche, S.J. Ribeiro, H. Barud, D. Bonemer, Structure and properties of conducting bacterial cellulose-polyaniline nanocomposites. Cellulose **18**, 1285–1294 (2011)
13. J. Rajwade, K. Paknikar, J. Kumbhar, Applications of bacterial cellulose and its composites in biomedicine. Appl. Microbiol. Biotechnol. **99**, 2491–2511 (2015)
14. M.L. Cacicedo, M.C. Castro, I. Servetas, L. Bosnea, K. Boura, P. Tsafrakidou et al., Progress in bacterial cellulose matrices for biotechnological applications. Biores. Technol. **213**, 172–180 (2016)
15. G.F. Picheth, C.L. Pirich, M.R. Sierakowski, M.A. Woehl, C.N. Sakakibara, C.F. de Souza et al., Bacterial cellulose in biomedical applications: A review. Int. J. Biol. Macromol. **104**, 97–106 (2017)
16. R.-D. Pavaloiu, A. Stoica, M. Stroescu, T. Dobre, Controlled release of amoxicillin from bacterial cellulose membranes. Open Chem. **12**, 962–967 (2014)
17. W. Shao, H. Liu, S. Wang, J. Wu, M. Huang, H. Min et al., Controlled release and antibacterial activity of tetracycline hydrochloride-loaded bacterial cellulose composite membranes. Carbohyd. Polym. **145**, 114–120 (2016)
18. M.H. Perez, C. Zinutti, A. Lamprecht, N. Ubrich, A. Astier, M. Hoffman et al., The preparation and evaluation of poly ($\epsilon$-caprolactone) microparticles containing both a lipophilic and a hydrophilic drug. J. Control. Release **65**, 429–438 (2000)
19. J.K. Patra, G. Das, L.F. Fraceto, E.V.R. Campos, R.-T. del Pilar, L.S. Acosta-Torres et al., Nano based drug delivery systems: recent developments and future prospects. **16**, 1–33 (2018)
20. C. Pathak, F.U. Vaidya, S.M.J. Pandey, Mechanism for development of nanobased drug delivery system, 35–67 (2019)

21. O.M. Koo, I. Rubinstein, H.J.N.N. Onyuksel, Biology, medicine. Role of nanotechnology in targeted drug delivery and imaging: a concise review **1**, 193–212 (2005)
22. O.C. Farokhzad, R.J.A. Langer, Impact of nanotechnology on drug delivery. **3**, 16–20 (2009)
23. M. Kumar Teli, S. Mutalik, G.J.C. Rajanikant, Nanotechnology and nanomedicine: going small means aiming big. **16**, 1882–1892 (2010)
24. S. Adepu, S.J.M. Ramakrishna, Controlled Drug Delivery Systems: Current Status and Future Directions. **26**, 5905 (2021)
25. S. Adepu, H. Luo, S.J.I. Ramakrishna, Heparin-Tagged PLA-PEG Copolymer-Encapsulated Biochanin A-Loaded (Mg/Al) LDH Nanoparticles Recommended for Non-Thrombogenic and Anti-Proliferative Stent Coating 22, 5433 (2021)
26. S. Adepu, P. Kalyani, M.J.T. Khandelwal, Bacterial Cellulose-Based Drug Delivery System for Dual Mode Drug Release. **6**, 265–271 (2021)
27. A.P.J. Nikalje, Nanotechnology and its applications in medicine **5**, 81–89 (2015)
28. A.N. Zelikin, C. Ehrhardt, A.M.J. Healy, Materials and methods for delivery of biological drugs. **8**, 997–1007 (2016)
29. S. Adepu, M.J.C.P. Khandelwal, Ex-situ modification of bacterial cellulose for immediate and sustained drug release with insights into release mechanism. **249**, 116816 (2020)
30. A.M. Villalba-Rodriguez, K. Dhama, H.J.I. Iqbal, Biomaterials-based hydrogels and their drug delivery potentialities **13**, 864–873 (2017)
31. S. Adepu, M.J.M. Khandelwal, Bacterial cellulose with microencapsulated antifungal essential oils: A novel double barrier release system. **9**, 100585 (2020)
32. M. Khandelwal, A.H. Windle, N.J.J. Hessler, In situ tunability of bacteria produced cellulose by additives in the culture media. **51**, 4839–4844 (2016)
33. U. Römling, M.Y.J.T. Galperin, Bacterial cellulose biosynthesis: diversity of operons, subunits, products, and functions. **23**, 545–557 (2015)
34. S. Adepu, M.J.J. Khandelwal, Broad-spectrum antimicrobial activity of bacterial cellulose silver nanocomposites with sustained release. **53**, 1596–1609 (2018)
35. S. Adepu, M. Khandelwal, Ex-situ modification of bacterial cellulose for immediate and sustained drug release with insights into release mechanism. Carbohyd. Polym. **249**, 116816 (2020)
36. S. Adepu, M.J.P. Khandelwal, Drug release behaviour and mechanism from unmodified and in situ modified bacterial cellulose, 1–11 (2021)
37. K. Ramana, A. Tomar, L. Singh, Effect of various carbon and nitrogen sources on cellulose synthesis by Acetobacter xylinum. World J. Microbiol. Biotechnol. **16**, 245–248 (2000)
38. M. Phisalaphong, N. Chiaoprakobkij, M. Gama, P. Gatenholm, D. Klemm, Applications and products—Nata de Coco. Bacterial nanocellulose: a sophisticated multifunctional material, 143–156 (2012)
39. M. Schramm, S. Hestrin, Factors affecting production of cellulose at the air/liquid interface of a culture of Acetobacter xylinum. Microbiology **11**, 123–129 (1954)
40. R.E. Cannon, S.M. Anderson, Biogenesis of bacterial cellulose. Crit. Rev. Microbiol. **17**, 435–447 (1991)
41. M. Benziman, C.H. Haigler, R.M. Brown, A.R. White, K.M. Cooper, Cellulose biogenesis: polymerization and crystallization are coupled processes in Acetobacter xylinum. Proc. Natl. Acad. Sci. **77**, 6678–6682 (1980)
42. M. Khandelwal, A.H. Windle, N. Hessler, In situ tunability of bacteria produced cellulose by additives in the culture media. J. Mater. Sci. **51**, 4839–4844 (2016)
43. M. Khandelwal, A.H. Windle, Self-assembly of bacterial and tunicate cellulose nanowhiskers. Polymer **54**, 5199–5206 (2013)
44. A. Santmartí, K.-Y. Lee, Crystallinity and thermal stability of nanocellulose. Nanocellulose and Sustainability: Production, properties, applications, and case studies, 67–86 (2018)
45. M. Martínez-Sanz, A. Lopez-Rubio, J.M. Lagaron, Optimization of the nanofabrication by acid hydrolysis of bacterial cellulose nanowhiskers. Carbohyd. Polym. **85**, 228–236 (2011)
46. M. Khandelwal, A. Windle, Origin of chiral interactions in cellulose supra-molecular microfibrils. Carbohyd. Polym. **106**, 128–131 (2014)

47. A.M. Sokolnicki, R.J. Fisher, T.P. Harrah, D.L. Kaplan, Permeability of bacterial cellulose membranes. J. Membr. Sci. **272**, 15–27 (2006)
48. J. Li, Y. Wan, L. Li, H. Liang, J. Wang, Preparation and characterization of 2, 3-dialdehyde bacterial cellulose for potential biodegradable tissue engineering scaffolds. Mater. Sci. Eng., C **29**, 1635–1642 (2009)
49. Y. Hu, J.M. Catchmark, In vitro biodegradability and mechanical properties of bioabsorbable bacterial cellulose incorporating cellulases. Acta Biom. **7**, 2835–2845 (2011)
50. S. Adepu, M. Khandelwal, Broad-spectrum antimicrobial activity of bacterial cellulose silver nanocomposites with sustained release. J. Mater. Sci. **53**, 1596–1609 (2018)
51. E. Trovatti, C.S. Freire, P.C. Pinto, I.F. Almeida, P. Costa, A.J. Silvestre et al., Bacterial cellulose membranes applied in topical and transdermal delivery of lidocaine hydrochloride and ibuprofen: in vitro diffusion studies. Int. J. Pharm. **435**, 83–87 (2012)
52. M.L. Cacicedo, I.E. León, J.S. Gonzalez, L.M. Porto, V.A. Alvarez, G.R. Castro, Modified bacterial cellulose scaffolds for localized doxorubicin release in human colorectal HT-29 cells. Colloids Surf., B **140**, 421–429 (2016)
53. C. Subtaweesin, W. Woraharn, S. Taokaew, N. Chiaoprakobkij, A. Sereemaspun, M. Phisalaphong, Characteristics of curcumin-loaded bacterial cellulose films and anticancer properties against malignant melanoma skin cancer cells. Appl. Sci. **8**, 1188 (2018)
54. F.M. de Lima, A.B. Meneguin, A. Tercjak, J. Gutierrez, B.S.F. Cury, A.M. dos Santos et al., Effect of in situ modification of bacterial cellulose with carboxymethylcellulose on its nano/microstructure and methotrexate release properties. Carbohyd. Polym. **179**, 126–134 (2018)
55. N.H. Silva, A.F. Rodrigues, I.F. Almeida, P.C. Costa, C. Rosado, C.P. Neto et al., Bacterial cellulose membranes as transdermal delivery systems for diclofenac: in vitro dissolution and permeation studies. Carbohyd. Polym. **106**, 264–269 (2014)
56. M.C.I. Mohd Amin, N. Ahmad, M. Pandey, X.C. Jue, Stimuli-responsive bacterial cellulose-g-poly (acrylic acid-co-acrylamide) hydrogels for oral controlled release drug delivery. Drug Dev. Ind. Pharm. **40**, 1340–1349 (2014)
57. N. Ahmad, M.C.I.M. Amin, S.M. Mahali, I. Ismail, V.T.G. Chuang, Biocompatible and mucoadhesive bacterial cellulose-g-poly (acrylic acid) hydrogels for oral protein delivery. Mol. Pharm. **11**, 4130–4142 (2014)
58. R.-D. Pavaloiu, A. Stoica-Guzun, M. Stroescu, S.I. Jinga, T. Dobre, Composite films of poly (vinyl alcohol)–chitosan–bacterial cellulose for drug controlled release. Int. J. Biol. Macromol. **68**, 117–124 (2014)
59. W.-C. Lin, C.-C. Lien, H.-J. Yeh, C.-M. Yu, S.H. Hsu, Bacterial cellulose and bacterial cellulose–chitosan membranes for wound dressing applications. Carbohydrate Poly. **94**, 603–611 (2013)
60. X. Shi, Y. Zheng, G. Wang, Q. Lin, J. Fan, pH-and electro-response characteristics of bacterial cellulose nanofiber/sodium alginate hybrid hydrogels for dual controlled drug delivery. RSC Adv. **4**, 47056–47065 (2014)
61. Y.-H. Tsai, Y.-N. Yang, Y.-C. Ho, M.-L. Tsai, F.-L. Mi, Drug release and antioxidant/antibacterial activities of silymarin-zein nanoparticle/bacterial cellulose nanofiber composite films. Carbohyd. Polym. **180**, 286–296 (2018)
62. W. Treesuppharat, P. Rojanapanthu, C. Siangsanoh, H. Manuspiya, S. Ummartyotin, Synthesis and characterization of bacterial cellulose and gelatin-based hydrogel composites for drug-delivery systems. Biotechnology reports **15**, 84–91 (2017)
63. M.L. Cacicedo, G.A. Islan, M.F. Drachemberg, V.A. Alvarez, L.C. Bartel, A.D. Bolzán et al., Hybrid bacterial cellulose–pectin films for delivery of bioactive molecules. New J. Chem. **42**, 7457–7467 (2018)
64. S. Moritz, C. Wiegand, F. Wesarg, N. Hessler, F.A. Müller, D. Kralisch et al., Active wound dressings based on bacterial nanocellulose as drug delivery system for octenidine. Int. J. Pharm. **471**, 45–55 (2014)
65. M. Ramos, A. Beltrán, M. Peltzer, A.J. Valente, G.M. del Carmen, Release and antioxidant activity of carvacrol and thymol from polypropylene active packaging films. LWT-Food Science and Technology **58**, 470–477 (2014)

66. Y. Numata, L. Mazzarino, R. Borsali, A slow-release system of bacterial cellulose gel and nanoparticles for hydrophobic active ingredients. Int. J. Pharm. **486**, 217–225 (2015)
67. S. Li, A. Jasim, W. Zhao, L. Fu, M.W. Ullah, Z. Shi et al., Fabrication of pH-electroactive bacterial cellulose/polyaniline hydrogel for the development of a controlled drug release system. ES Materials & Manufacturing **1**, 41–49 (2018)
68. N. Heßler, D. Klemm, Alteration of bacterial nanocellulose structure by in situ modification using polyethylene glycol and carbohydrate additives. Cellulose **16**, 899–910 (2009)
69. T.R. Stumpf, X. Yang, J. Zhang, X. Cao, In situ and ex situ modifications of bacterial cellulose for applications in tissue engineering. Mater. Sci. Eng., C **82**, 372–383 (2018)
70. K.I. Uhlin, R.H. Atalla, N.S. Thompson, Influence of hemicelluloses on the aggregation patterns of bacterial cellulose. Cellulose **2**, 129–144 (1995)
71. K.-C. Cheng, J.M. Catchmark, A. Demirci, Effect of different additives on bacterial cellulose production by Acetobacter xylinum and analysis of material property. Cellulose **16**, 1033–1045 (2009)
72. C. Tokoh, K.J. Takabe, M. Fujita, Cellulose synthesized by Acetobacter xylinum in the presence of plant cell wall polysaccharides. Cellulose **9**, 65–74 (2002)
73. D. Klemm, D. Schumann, F. Kramer, N. Heßler, M. Hornung, H.-P. Schmauder et al., *Nanocelluloses as innovative polymers in research and application* (Springer, Polysaccharides Ii, 2006), pp.49–96
74. M. Seifert, S. Hesse, V. Kabrelian, D. Klemm, Controlling the water content of never dried and reswollen bacterial cellulose by the addition of water-soluble polymers to the culture medium. J. Polym. Sci., Part A: Polym. Chem. **42**, 463–470 (2004)
75. E.E. Brown, M.P.G. Laborie, Bioengineering bacterial cellulose/poly (ethylene oxide) nanocomposites. Biomacromolecules **8**, 3074–3081 (2007)
76. A.R. Figueiredo, A.J. Silvestre, C.P. Neto, C.S. Freire, In situ synthesis of bacterial cellulose/polycaprolactone blends for hot pressing nanocomposite films production. Carbohyd. Polym. **132**, 400–408 (2015)
77. D.R. Ruka, G.P. Simon, K.M. Dean, In situ modifications to bacterial cellulose with the water insoluble polymer poly-3-hydroxybutyrate. Carbohyd. Polym. **92**, 1717–1723 (2013)
78. C. Zhijiang, H. Chengwei, Y. Guang, Poly (3-hydroxubutyrate-co-4-hydroxubutyrate)/bacterial cellulose composite porous scaffold: Preparation, characterization and biocompatibility evaluation. Carbohyd. Polym. **87**, 1073–1080 (2012)
79. K.H. Hong, J.L. Park, I.H. Sul, J.H. Youk, T.J. Kang, Preparation of antimicrobial poly (vinyl alcohol) nanofibers containing silver nanoparticles. J. Polym. Sci., Part B: Polym. Phys. **44**, 2468–2474 (2006)
80. S. Gea, E. Bilotti, C. Reynolds, N. Soykeabkeaw, T. Peijs, Bacterial cellulose–poly (vinyl alcohol) nanocomposites prepared by an in-situ process. Mater. Lett. **64**, 901–904 (2010)
81. A. Kai, T. Kobayashi, Influence of poly (vinyl alcohol) on the structure of bacterial cellulose spherulite. Polym. J. **24**, 131 (1992)
82. H.-C. Huang, L.-C. Chen, S.-B. Lin, C.-P. Hsu, H.-H. Chen, In situ modification of bacterial cellulose network structure by adding interfering substances during fermentation. Biores. Technol. **101**, 6084–6091 (2010)
83. H.-C. Huang, L.-C. Chen, S.-B. Lin, H.-H. Chen, Nano-biomaterials application: In situ modification of bacterial cellulose structure by adding HPMC during fermentation. Carbohyd. Polym. **83**, 979–987 (2011)
84. J. Yang, X. Lv, S. Chen, Z. Li, C. Feng, H. Wang et al., In situ fabrication of a microporous bacterial cellulose/potato starch composite scaffold with enhanced cell compatibility. Cellulose **21**, 1823–1835 (2014)
85. C.J. Grande, F.G. Torres, C.M. Gomez, O.P. Troncoso, J. Canet-Ferrer, J. Martínez-Pastor, Development of self-assembled bacterial cellulose–starch nanocomposites. Mater. Sci. Eng., C **29**, 1098–1104 (2009)
86. F.M. de Lima, A.B. Meneguin, A. Tercjak, J. Gutierrez, B.S.F. Cury, A.M. Dos Santos et al., Effect of in situ modification of bacterial cellulose with carboxymethylcellulose on its nano/microstructure and methotrexate release properties **179**, 126–134 (2018)

87. L. Ji, F. Zhang, L. Zhu, J.J.I. Jiang, An in-situ fabrication of bamboo bacterial cellulose/sodium alginate nanocomposite hydrogels as carrier materials for controlled protein drug delivery. **170**, 459–468 (2021)
88. H.S. Barud, S.J.L. Ribeiro, C. Carone, R. Ligabue, S. Einloft, P. Queiroz et al., Optically transparent membrane based on bacterial cellulose/polycaprolactone. Polímeros **23**, 135–142 (2013)
89. L. Ji, F. Zhang, L. Zhu, J. Jiang, An in-situ fabrication of bamboo bacterial cellulose/sodium alginate nanocomposite hydrogels as carrier materials for controlled protein drug delivery. Int. J. Biol. Macromol. **170**, 459–468 (2020)
90. B.V. Mohite, S.V. Patil, A novel biomaterial: bacterial cellulose and its new era applications. Biotechnol. Appl. Biochem. **61**, 101–110 (2014)
91. Y. Pötzinger, D. Kralisch, D. Fischer, Bacterial nanocellulose: the future of controlled drug delivery? Ther. Deliv. **8**, 753–761 (2017)
92. C.J. Zhang, L. Wang, J.C. Zhao, P. Zhu, *Effect of drying methods on structure and mechanical properties of bacterial cellulose films* (Trans Tech Publ, Advanced Materials Research, 2011), pp.2667–2670
93. B. Wei, G. Yang, F. Hong, Preparation and evaluation of a kind of bacterial cellulose dry films with antibacterial properties. Carbohyd. Polym. **84**, 533–538 (2011)
94. S.C. Fernandes, L. Oliveira, C.S. Freire, A.J. Silvestre, C.P. Neto, A. Gandini et al., Novel transparent nanocomposite films based on chitosan and bacterial cellulose. Green Chem. **11**, 2023–2029 (2009)
95. M.P. Illa, C.S. Sharma, M. Khandelwal, Tuning the physiochemical properties of bacterial cellulose: effect of drying conditions. J. Mat. Sci., 1–12 (2019)
96. F. Liebner, E. Haimer, M. Wendland, M.A. Neouze, K. Schlufter, P. Miethe et al., Aerogels from unaltered bacterial cellulose: application of scCO2 drying for the preparation of shaped, ultra-lightweight cellulosic aerogels. Macromol. Biosci. **10**, 349–352 (2010)
97. M. Ul-Islam, T. Khan, J.K. Park, Water holding and release properties of bacterial cellulose obtained by in situ and ex situ modification. Carbohyd. Polym. **88**, 596–603 (2012)
98. M.V. Zimmermann, C. Borsoi, A. Lavoratti, M. Zanini, A.J. Zattera, R.M. Santana, Drying techniques applied to cellulose nanofibers. J. Reinf. Plast. Compos. **35**, 628–643 (2016)
99. A. Müller, M. Zink, N. Hessler, F. Wesarg, F.A. Müller, D. Kralisch et al., Bacterial nanocellulose with a shape-memory effect as potential drug delivery system. RSC Adv. **4**, 57173–57184 (2014)
100. A. Müller, Z. Ni, N. Hessler, F. Wesarg, F.A. Müller, D. Kralisch et al., The biopolymer bacterial nanocellulose as drug delivery system: investigation of drug loading and release using the model protein albumin. J. Pharm. Sci. **102**, 579–592 (2013)
101. W. Hu, S. Liu, S. Chen, H. Wang, Preparation and properties of photochromic bacterial cellulose nanofibrous membranes. Cellulose **18**, 655–661 (2011)
102. Y. Nishi, M. Uryu, S. Yamanaka, K. Watanabe, N. Kitamura, M. Iguchi et al., The structure and mechanical properties of sheets prepared from bacterial cellulose. J. Mater. Sci. **25**, 2997–3001 (1990)
103. H.A. Khalil, Y. Davoudpour, M.N. Islam, A. Mustapha, K. Sudesh, R. Dungani et al., Production and modification of nanofibrillated cellulose using various mechanical processes: a review. Carbohyd. Polym. **99**, 649–665 (2014)
104. X. Yin, C. Yu, X. Zhang, J. Yang, Q. Lin, J. Wang et al., Comparison of succinylation methods for bacterial cellulose and adsorption capacities of bacterial cellulose derivatives for Cu2+ ion. Polym. Bull. **67**, 401–412 (2011)
105. G. Zu, J. Shen, L. Zou, F. Wang, X. Wang, Y. Zhang et al., Nanocellulose-derived highly porous carbon aerogels for supercapacitors. Carbon **99**, 203–211 (2016)
106. M.P. Illa, M. Khandelwal, C.S. Sharma, Bacterial cellulose-derived carbon nanofibers as anode for lithium-ion batteries. Emergent Materials **1**, 105–120 (2018)
107. S. Adepu, P. Kalyani, M. Khandelwal, Bacterial cellulose-based drug delivery system for dual mode drug release. Trans. Indian National Academy of Eng., 1–7

108. M. Badshah, H. Ullah, F. He, F. Wahid, U. Farooq, M. Andersson et al., Development and Evaluation of Drug Loaded Regenerated Bacterial Cellulose-Based Matrices as a Potential Dosage Form. Frontiers Bioeng. Biotech. **8**, 1389 (2020)
109. A.B. Meneguin, B.H. da Silva, R.M. Sábio, P.Z. de Sousa, K.F. Manieri, L.A.P. de Freitas et al., Spray-dried bacterial cellulose nanofibers: A new generation of pharmaceutical excipient intended for intestinal drug delivery. Carbohyd. Polym. **249**, 116838 (2020)
110. S. Adepu, M. Khandelwal, Bacterial cellulose with microencapsulated antifungal essential oils: a novel double barrier release system. Materialia **9**, 100585 (2020)
111. B.S. Inoue, S. Streit, A.L. dos Santos Schneider, M.M. Meier, Bioactive bacterial cellulose membrane with prolonged release of chlorhexidine for dental medical application. Int. J. Biol. Macromol. **148**, 1098–1108 (2020)

# An Odyssey from High Entropy Alloys to Complex Concentrated Alloys

**Jitesh Kumar, Saumya R. Jha, N. P. Gurao, and Krishanu Biswas**

## 1 Introduction

Materials have been an integral part of human civilization since ancient time. In the Stone Age, ancient people used naturally occurring materials such as stone, rawhide, bone, wood and some indigenous metals like gold, silver and copper, which were mechanically shaped into tools and weapons. The Stone Age came to an end with the discovery of bronze (3000 BC), which was the greatest gift to humankind. Bronze was the accidentally discovered alloy of copper and tin with superior properties in terms of strength, castability and durability than those of naturally occurring materials [1–3] (Fig. 1).

Thus, the discovery of bronze gave the birth of the tradition of alloying in quest of new alloys with improved properties than those of the constituent elements. This serendipitous strategy of alloy design has provided the route to headway of several engineering alloys based on a principal element with the addition of other components albeit, in a dilute amount, to balance the properties. For example, steels contain iron as a principal component into which secondary elements; carbon, silicon, nickel and chromium are added in minute amounts to obtain high strength, ductility and corrosion resistance [4]. High-strength aluminium alloys, where aluminium is the main component due to its lower density is alloyed with copper and magnesium to enhance the strength [5]. This fundamental concept of alloy design based on the primary element has remained unchanged over millennia which can even be understood that these alloys were designated after their principal constituents such as ferrous alloys, aluminium alloys, copper alloys and nickel-base superalloys. Superalloys are an earlier example of a multi-component system where 10–12 elements are mixed to adjust the properties. In this context, the bulk metallic glass is another example of

---

J. Kumar · S. R. Jha · N. P. Gurao · K. Biswas (✉)
Department of Materials Science and Engineering, Indian Institute of Technology Kanpur, Kanpur 208016, India
e-mail: kbiswas@iitk.ac.in

A. Shrivastava et al. (eds.), *New Horizons in Metallurgy, Materials and Manufacturing*, Indian Institute of Metals Series, https://doi.org/10.1007/978-981-19-5570-9_10

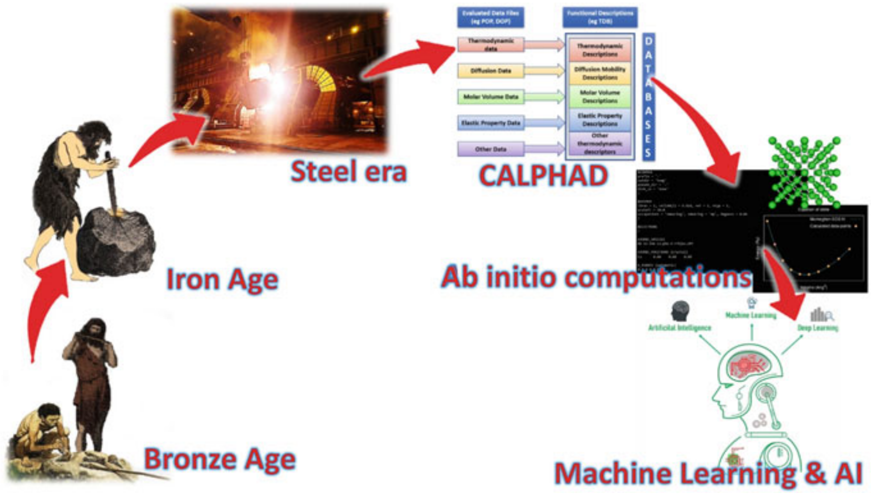

**Fig. 1** Evolution of materials through the civilizations and advancements in materials development research

a multi-component system in terms of number and concentration. Nonetheless, the primary element-based design concept limits the number of alloys systems, which is primarily accumulated at the corner and edge of the phase diagram. Therefore, a new approach of alloys design is needed to expand the compositional space to explore more number of alloys systems to meet the technological challenges, which have almost been exhausted by the design of the conventional alloy approaches.

One such approach involves mixing the multiple principal elements in equiatomic or near equiatomic compositions, which is an entirely new concept of alloy design, altering the course of the traditional alloys design practice and receiving worldwide attention by the material science community. The main idea of this concept is to unlock the vast compositional space of phase diagrams that offer several alloys systems without any design constraint in terms of the number of elements and their compositions. With this compositional flexibility, a large number of papers have been published across the globe, and extensive research is in progress across the continents. The first paper on this concept was simultaneously published by Cantor et al. [6] and Yeh et al. [7] in 2004. A new terminology ‘high entropy alloys (HEAs)’ was given by Yeh, which has been defined as for any alloys having at least five elements whose concentration varies between 5 to 35 atom%. Yeh and co-workers provided a hypothesis that mixing five or more elements in the equiatomic composition leads to maximize the configurational entropy and thus facilitates the formation of solid solution over the intermetallic phase/s at higher temperatures. The initial concept of HEAs is mainly focused on mixing the elements in equiatomic compositions to obtain a single-phase solid solution with simple microstructure and desired properties. Recently, some attention has been shifted to investigate the multicomponent system with a non-equiatomic composition such as $Fe_{42}Mn_{20}Ni_{30}Co_{6}Cr_{2}$ and

$Fe_{40}Mn_{27}Ni_{26}Co_5Cr_2$ quinary alloys [8, 9], $Cr_{10}Mn_{40}Fe_{40}Co_{10}$ and $Cr_4Mn_{28}Fe_{40}Ni_{28}$ quarternary alloys [10, 11]. The main idea behind this is to expand the central portion of the phase diagram, which is limited by the constraint of equiatomic concept. Thus, it leads to the modification of the original definition, which is at least three-element and whose concentration must be greater than 35 atomic%. Therefore, embracing the new concept, several nomenclatures like multi-metallic cocktails, high entropy materials, complex concentrated alloys (CCAs), 100% solute alloys and multiprincipal elemental alloys have made their way in the literature [12]. This new definition further opens vast compositional space with a cosmic number of alloys systems with promising properties such as excellent cryogenic temperature strength–ductility [13] fracture toughness [14] and improved wear resistance [15, 16]. These promising properties are mainly attributed to the four core effects that include high entropy effect, severe lattice distortion, sluggish diffusion and cocktail effect. It is to be mentioned here these core effects need not necessarily have to be present in complex, concentrated alloys. Still, at least one of them plays an important role in distinguishing a complex concentrated alloy from a conventional alloy apart from the presence of multiple principal elements.

The conjecture that the diffusion is sluggish in HEMs is not always true and has been much debated in the literature. Few studies have shown the diffusivity in Cantor alloys lies in between the Fe–Cr-Ni steels and its pure constituents [17, 18]. Similarly, the cocktail effect that predicts the unexpected properties of MPEAs is not a direct result of the linear superposition of the properties of individual elements but can be the manifestation of an unusual combination, microstructure and interaction among them. The high entropy effect, which is a signature effect states that the high configurational entropy of mixing due to the mixing of five or more elements in equiatomic composition promotes the formation of solid solution over intermetallics. However, Deng et al. [19] reported non-equiatomic $Cr_{10}Mn_{40}Fe_{40}Co_{10}$ alloy that has only four elements and configurational entropy of mixing 1.19R is surprisingly a single-phase solid solution. With these examples, it is concluded that the MPEAs need a thorough investigation and scientific study to establish a universal concept for a better understanding of these novel classes of materials and their design, development and deployment for actual engineering applications.

Due to the cosmic number of possible combinations in HEAs, these classes of alloys need to be screened through high throughput experimental techniques aided with multi-length and timescale simulations to achieve the desired properties. One of the methods to achieve better mechanical properties of FCC MPEAs is to alter the stacking fault energy (SFE) of the alloys system. As the stacking fault energy decreases, the corresponding twin energy concomitantly decreases, leading to overcoming strength–ductility trades off through work hardening and delayed necking by introducing 'twinning' as a deformation mode (TWIP effect) [14, 20, 21]. SFE also plays a vital role in the transformation from FCC to ε-martensite by reducing the onset of activation barrier of FCC to ε-martensite transformation and thus triggers the transformation-induced plasticity (TRIP) [14, 17, 20] causing interfacial hardening. The properties of MPEAs can also be enhanced through lattice distortion by introducing a large atom in a matrix of elements with similar size to cause lattice to be severely distorted locally to promote solid solution strengthening. Microstructural engineering through severe plastic deformation (SPD) such as equal channel angular pressing (ECAP), high-pressure torsion (HPT) and friction stir processing (FSP) has been used for grain refinement to increase the strength through Hall–Petch effects. However, all aforementioned processes are widely used for FCC base HEMs but not used in BCC HEMs due to their limited room temperature ductility.

In the above, the present review is intended to provide our journey through the multi-component phase space in search of the betterment of properties needed for structural applications. The review has been divided into four different sections. In the first section, we describe various alloy design strategies for the prediction of MPEAs through the parametric process, thermodynamic modelling and various computational simulations at different lengths and timescales because the multi-element space offers a cosmic number of alloys systems requiring screening to avoid error-and-trial method. The second section discusses different routes of alloy synthesis. The third part of the review examines the mechanical properties of MPEAs and also discusses the underlying deformation mechanisms required to develop the scientific understanding of these alloys. We conclude our review by highlighting some challenges and future scope of this new class of materials.

## 2 Design Strategy

Due to the vast compositional space offered by this new class of materials where alloys can be developed in the astronomical figures, it is necessary to screen out the alloys with promising properties, and some approaches must be improvised that minimizes our time and resources to avoid cumbersome ‘trial-and-error’ method. Contrary to the preliminary assertions based on the booming field of high entropy alloy systems, the relaxed definition of multicomponent systems or complex, concentrated alloys is inclusive of ternary and quaternary systems which have proven better than their ‘high entropy’ counterparts, thus unlocking a whole new platform for the exploration of alloy systems with better properties. Recent investigations of ternary systems have unearthed specific alloy combinations with excellent combinations of strength and ductility, besides offering outstanding tunability with microstructural modification techniques. A significant advantage of MEAs over HEAs is their potency to exploit strengthening mechanisms of complex alloy systems with less compositional extensiveness of a large number of components. Thus, several approaches to unearth-specific alloy systems are based on the theoretical aspects that might be employed to revise the phase and the mechanical properties of MPEAs/HEAs. Some of these are discussed briefly here.

**Parametric approach**: The prediction of a stable solid solution phase is the key area of interest in MPEAs/HEAs community. A most common practice utilizes the empirical rule of Hume-Rothery [22, 23] along with thermodynamic quantities that form parametric criterion to predict the solid solution phase in MPEAs/HEAs.

The essential phase selection parameters in HEAs are enthalpy of mixing ($\Delta H_{\text{mix}}$) and entropy of mixing ($\Delta S_{\text{mix}}$) which are given as

$$\Delta H_{\text{mix}} = \sum_{i,j;i\neq j}^{n} \Omega_{ij} c_i c_j \tag{1}$$

$$\Delta s_{\text{conf}} = -R\sum_{i=1}^{n} X_i ln X_i \tag{2}$$

where $\Omega_{ij} = 4\,\Delta H_{\text{mix}}^{AB}$ and $\Delta H_{\text{mix}}^{AB}$ are the enthalpy of mixing of binary A-B calculated by Miedema's semiempirical model [24, 25]. '*R*' is the universal gas constant. The Hume-Rothery rule for the formation of stable solid solutions alloys depends on three factors: (1) the difference in atomic size (δ) of the solvent and solute must be less than or equal to 6.6%, (2) the electronegativity difference ($\Delta\chi$) between alloys components will be more in the presence of intermetallic compounds and (3) the valence electron of two elements should be similar. However, in HEAs, where there is no solvent and solute, the Hume-Rothery parameters have been modified. For 'δ' the modified formula is given by:

$$\delta = \sqrt{\sum_{i=1}^{n} c_i \left(1 - \frac{r_i}{\overline{r}}\right)^2} \tag{3}$$

where *n* is the total number of components of species *i*, having concentration $c_i$ and atomic radius $r_i$. $\overline{r}$ is the average atomic radius of alloy. For $\Delta\chi$:

$$\Delta\chi = \sqrt{\sum_{i=1}^{n} c_i (\chi_i - \overline{\chi})^2} \tag{4}$$

And valence electron concentration (VEC) is given by:

$$\text{VEC} = \sum_{i=1}^{n} c_i (\text{VEC})_i \tag{5}$$

The enthalpy of mixing (calculated based on Miedema's model using enthalpies of formation or Ω) is also a major characterizing parameter for predicting the alloy characteristics based on thermodynamic data. Attempts have been made to coin better descriptors than the previously used configurational entropy term such as the $\Delta H_{\text{mix}}$ vs $\delta$ ratio for the screening of HEAs and MPEAs. Zhang et al. [26] first plotted $\Delta H_{\text{mix}}$ *vs* $\delta$, which predicts the regime for a stable solid solution phase, along with intermetallics and amorphous phases as shown in Fig. 2. Such parametric approaches

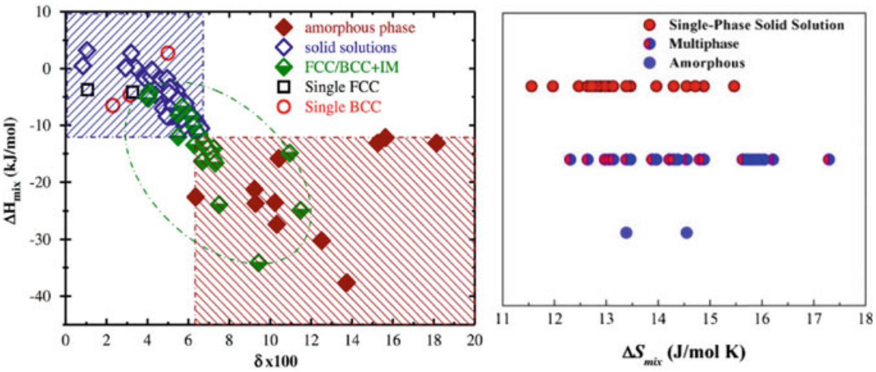

**Fig. 2** A graph between $\Delta H_{\text{mix}}$ vs $\delta$ representing the classification of HEAs that form only solid solutions along with intermetallic compounds and amorphous phase against a configurational entropy-based classification [30, 31]. Reprint with permission

have also been efficiently used to design other path-breaking high entropy materials such as high entropy metallic glasses (HE-MGs) [27–29].

For rationalizing the solid solution formation-based approach built upon the Hume-Rothery rules, Eshelby's micromechanical model was developed based on continuum elasticity concept, considering the solute atoms as analogues of inclusions in an elastic medium. This, however, is not applicable to HEAs directly owing to the inherent difference in nature of HEAs as compared to conventional alloys, *i.e.,* having solutes in minor proportions and solvents as base elements. In order to address this issue, a geometric model has been formulated for HEAs taking into consideration, the formation of voids or atomic overlap in the lattice as subtractive factors for the calculation of dense atomic packing as revealed by the sharp diffraction peaks obtained in most HEAs (single as well as multiphase). The atomic size difference arises from intrinsic residual strains, deduction of which is possible by minimization of atomic packing misfit. However, they arise owing to phase formations and cannot be detected in X-ray diffraction, similar to residual strains which decrease upon thermal annealing. The fluctuation can be correlated with the stored elastic energy in an HEA, lowering the free energy for phase formation. In consistency with Lindemann's criteria for lattice stability, the fluctuation in lattice strain must be $<$ 5% for single-phase solid solutions and between 5 and 10% for multiphase solid solutions.

**Calculation of Phase diagram (CALPHAD) approach**: The CALPHAD [32] modelling approach is the most potent tool to design the materials. Unlike the first principal calculation method, CALPHAD does not face any size limitation to be modelled for the prediction of the phase equilibria. They provided the key information for an alloy such as phases present, their stability with temperature and composition as well as their volume fraction. The phase equilibria predicted by the

CALPHAD are based on Gibbs free energy minimization which utilizes the computational software integrated with the thermodynamic database. It also provides a path to collect the pieces of information of the higher-order alloy system with the help of the lower-order system; for example, the phase equilibria in the ternary alloys system as a function of pressure, temperature and composition can be obtained from their subset of binary and unary systems. This approach can further be extended to HEAs making the CALPHAD a cogent methodology to predict the phase stability in HEAs. In such method, Taazuddin et al. [33] and Raturi et al. [34] predicted the single-phase multicomponent multiprincipal elemental alloys in conjugation with the parametric approach where the six alloys system with single-phase have been predicted from the pool of 1287 alloys systems. Thus, this approach reduces the tedious experimental process of trial and error, providing breakthrough solutions with relatively low computation power. One should be cautious about predicting the phase stability in HEAs because it is based on the extrapolation from our traditional understanding of the binary and ternary systems. It requires a robust database to predict the phase stability. In such an approach, Miracle, et al. [12] suggested that as many experimental data must be fed back to predict the phase stability with maximum accuracy. The design process for the database must include the intermetallic along with the solid solution phase, which could be used as a tool to develop the alloys with the hard phase in the final microstructures.

**Ab initio Method**: Ab initio, *i.e.* the first principal calculation is an important computational tool to decipher the phase stability and properties of the materials, which is based on the quantum mechanical theories along with natural constant without any empirical input. Ab Initio calculation is performed in the framework of density functional theory [35] using Kohn–Sham formalism [36]. The key variable in DFT calculation is the electron density in which the quantum mechanical Schrodinger wave equation for multi-electron is superimposed upon the single electron problem. Ab initio method has been used profusely in theoretical solid-state physics to explore the properties of the material and later move into the field of HEAs/MPEAs [37, 38]. The applicability of different ab initio in the area of HEAs/MPEAs is very challenging because of a large number of atoms involved whose atomic positions are uncertain. DFT provided the ground state energy at 0 K in real sense. Still, with the integration of the thermodynamic concept, one can predict the phase stability and properties of materials at finite temperatures. However, DFT calculation is the most robust technique which has a solid founding principle of physics that requires less experimental input and empirical approach. Oh et al. [39] recently demonstrated general design rules based on atomistic simulations combined with the parametric approach to enable optimum utilization of atomic-level information to reduce the immense degree of freedom in the compositional space to achieve mechanical property-driven alloy design [39].

**Machine Learning (ML)**: The advancement of computing power and availability of vast algorithms have created opportunities for thermodynamic modelling of complex systems using the tool of machine learning. The ML attracted worldwide attention due to its versatility in several fields such as atomic forces [40, 41], interatomic potentials

[42–44] and formation energies [45, 46]. One of the most significant advantages of ML lies in its adaptability of the available new data and can readily correlate between input data and output target in comparison with existing models. In the past few years, the ML technique has emerged as a useful tool in designing new materials with the estimation of several properties [47–50]. Choudhury et al. [51] used several machine learning algorithms such as logistic regression, decision tree, K-nearest neighbour (KNN), support vector machine (SVM), Naïve-based approach and neural networks to classify HEAs. Huang et al. [52] and Zhuang's group [52] have attempted to predict the phase formation in HEAs based on ML methods with great accuracy. Zhang et al. [53] used machine learning to reveal the significant role of formation enthalpy and atomic topology in the phase formation in HEAs.

Besides these, targeted parameter-based studies on these alloys are being performed to probe the microstructural aspects to correlate them with strength and toughness. A concept of microstructural entropy has been coined which dictates the grain boundary and defects-induced strengthening characteristics of a multimodal single-phase microstructure, which, with further exploration and validation, could prove as an essential basis for grain-scale studies for property prediction and tunability analyses. Advanced pattern predictive capabilities of ML-based approaches could not only be exploited based on arrays of extrapolative information but also coupled with derived parameters for property estimations. Other advanced artificial intelligence tools, including deep learning, mimicking human brain to process data, are expected to be used in screening the vast compositional landscape to search for materials with optimum mechanical properties.

## 3 Synthesis Route

### *3.1 Liquid State Processing Route: Melting and Casting*

The vacuum arc melting and vacuum induction route are the most popular technique to produce HEAs/MPEAs. All constituent components are thoroughly mixed in the liquid state and then solidified in the water-cooled copper mould. The temperature in the arc melting is around 3000 °C, which is enough to melt almost all the metals. Multiple and repetitive melting has been performed to ensure chemical homogeneities. However, there is the disadvantage of compositional control in this technique as some low boiling points of metals may get vapourized during melting. Thus, induction and resistance heating furnaces are generally used to avoid weight loss during melting. Generally, alloys were prepared in the form of a button on bowl-shaped copper mould. Another arrangement has been made by drop-casting of liquid alloys into the pre-machined cylindrical copper mould. This shape of ingots is useful for further processing by hot or cold working to break the solidification microstructure or to directly test the cast alloy [54].

This technique can achieve high cooling rates. However, the solidification rate cannot be controlled in this route that leads to the microstructural inhomogeneities from the centre to the periphery of a cylindrical specimen. There are always chances of having casting defects, elemental segregation, pores and residual stress that deteriorate the mechanical properties. It is necessary to eliminate these defects for further processing.

One of the techniques to reduce the casting defects is via the Bridgman solidification casting, which is useful for controlling the microstructure and properties optimization. Two processing parameters can govern microstructure morphology and size, namely temperature gradient and growth rate, which are adjusted by heating power and extracted velocities of rod-shaped samples.

### *3.2 Solid-State Processing Route*

Solid-state route is as popular as melting casting route to synthesize the HEAs/MPEAs, which is quite time-consuming due to the processing parameters and time-consuming. This involves the mechanical alloying (MA) followed by consolidation. In MA, the high energy ball mill produces the composite powders by continuous cold welding of particles and their fragmentation into fine particles; as a result, homogeneous alloys have been obtained by diffusing one species into each other. The first equiatomic BCC single-phase AlFeTiCrZnCu HEAs was reported by Varalakshmi et al. [55]. via MA with excellent compositional homogeneities.

This mechanically alloyed powder composite is needed to sinter to obtain a dense component. Field-assisted sintering route, especially spark plasma sintering (SPS), is most popularly used to consolidate the alloyed powders. SPS involves simultaneous action of heating through pulse current at particles interface which causes incipient melting of particle surface and pressure (50–100 MPa) and leads to the high degree of compactness. SPS offers the sintering in a short period, thus inhibiting the grain growth and avoiding swelling and spring back, which is are generally observed in a conventional sintering process. In this regard, Yadav et al. [56] prepared a dual-phase $(CuCrFeTiZn)_{100\text{-}x}Pb_x$ HEAs via MA followed by SPS. The alloy exhibited excellent mechanical as well as wear properties.

## 4 Mechanical Properties of High Entropy Alloys

### *4.1 Experimental Observation*

In this present section, the mechanical properties of HEMs and CCAs will be discussed in correlation with its deformation mechanism, with respect to classical structural alloys. However, direct comparison of these new classes of materials with the present structural materials is just to find the scientific understanding of the deformation mechanism since the majority of data is available in uniaxial deformation. Only a few data points for properties like fracture toughness [13, 57, 58] and fatigue resistance [14, 59, 60, 61] are available. In this context, the most widely investigated alloy is the equiatomic CoCrFeMnNi (Cantor) alloy which has a single-phase FCC microstructure and exhibits a low yield strength. Still, a significant amount of work hardening has been observed at room temperature. The Cantor alloy shows the strong dependency of the yield strength as a function of temperature and almost increase in strength by fourfold as temperature decreased to 77 K from 500 K for grain size 155 um [62, 63]. The Cantor alloy has low yield strength at room temperature, which is mainly considered due to low lattice friction as its constituents elements are nearly similar in size. The increase in strength and ductility (Fig. 3) at 77 k is primarily attributed to the formation of nanoscale twins throughout the grains at the strain level of 9% which provides additional strain hardening as a result of dynamic Hall–Petch strengthening [21]. This deformation-induced twinning delayed the onset of necking at higher strain. As a result, the strength and ductility both increase due to twin-induced plasticity (TWIP) effect.

The temperature dependency of yield strength in Cantor alloys is unlikely and different from that pure FCC metals and alloys which show no or insignificant temperature dependency of yield strength for same temperature range. However, it does not mean that HEAs have unique features of temperature dependency when compared to FCC alloys. For instance, Brass (Cu-70/Zn-30) shows the same fourfold increase in strength from 500 to 77 K [65]. An obvious question arises that despite similar behaviour of conventional FCC alloys why we go for HEAs and MPEAs. The reason is that the HEAs and MPEAs encompass almost the entire spectrum of steel, aluminium, titanium, nickel and magnesium alloys, as shown in Fig. 4, and offer design flexibility to explore multiple strengthening and strain hardening regimes in the context of structural properties that can be better tuned by exploring the

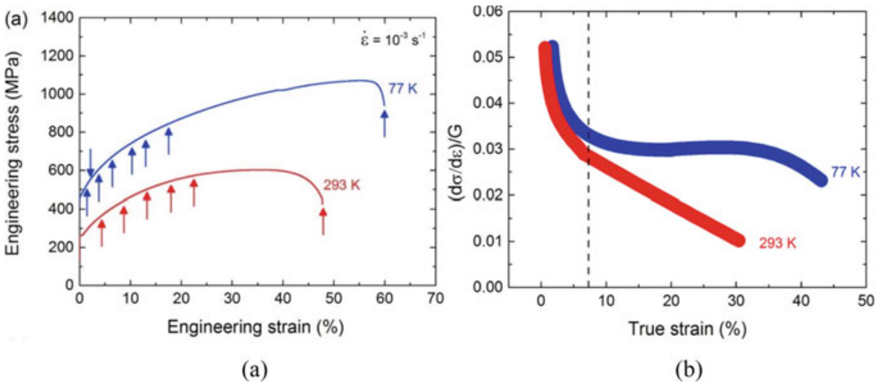

(a) (b)

**Fig. 3** **a** Engineering stress–engineering strain and **b** strain hardening–true strain curves for CoCrFeMnNi HEA tested at different temperatures [64]. Reprint with permission

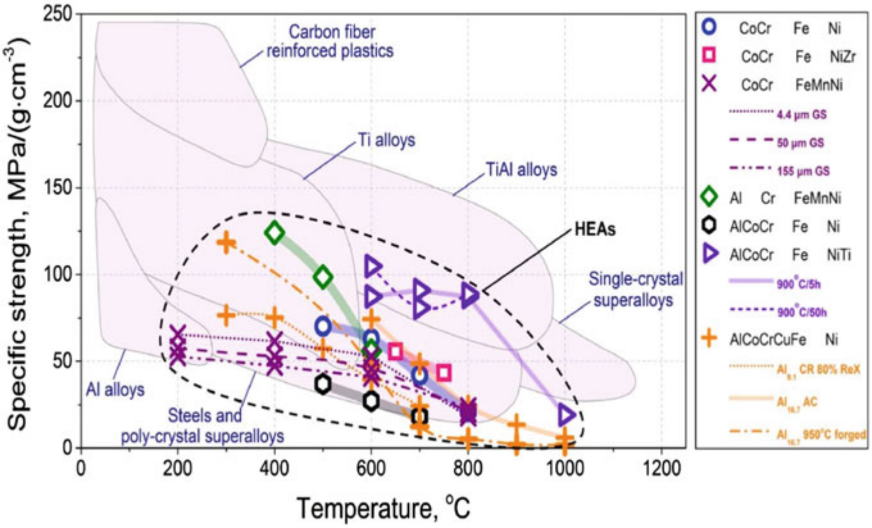

**Fig. 4** Plot between Specific strength vs temperature of HEA and CCAs group studied till date, compared to conventional high-temperature materials [66]. Reprint with permission

synergy between multiple mechanisms. For instance, the plain carbon and alloy steel, stainless steel, twinning and transformation-induced plasticity steel and dual-phase steel explore different mechanisms like solid solution strengthening, twinning and transformation-induced plasticity as second phase martensitic hardening. However, the non-equiatomic dual-phase $Fe_{50}Mn_{30}Co_{10}Cr_{10}$ high entropy alloy exploits all the four mechanisms to achieve extraordinary properties [11].

Similarly, equiatomic CoCrNi, which is a medium entropy alloy (MEA), possesses the ultimate tensile strength of 890 MPa and tensile ductility of 73% [67]. This alloy has shown a significant amount of strain hardening as compared to the conventional TWIP steels. This is a result of the formation of nanoscale twin/HCP lamellae during deformations [68].

Various attempts have been made to improve the mechanical properties (yield strength) of the Cantor alloy as well as its subset through the addition of interstitial elements. In this regard, Wu et al. [56] reported an improved yield strength of Cantor alloy by introducing 0.5% carbon. The yield strength increases from 165 to 225 MPa, while ductility decreases from 65 to 40%, which can primarily be attributed to shear field introduced by carbon atom and its interaction with dislocations. The latter shows a fair amount of work hardening due to the formation of nanotwins at higher strain. Luo et al. [69] reported simultaneously increase in strength and ductility when Cantor alloys exposed to hydrogen, which lower the stacking fault energy of Cantor alloys and thus enabled the formation of nanotwin. However, hydrogen doesn't contribute to interstitial hardening as there is no increase in strain hardening. However, hydrogen became boon for Cantor alloy, whereas almost all materials are prone to hydrogen embrittlement. In contrast to interstitial solid solution strengthening some work also has been published showing the substitutional solid solution strengthening in HEMs. For example, when vanadium is doped in Cantor alloy, there is significantly improved in yield strength (~76%) while around the twofold increase in strength of quarternary FeCoCrNi when it is doped with Pd [70] atom which is mainly attributed to large atomic misfit volume induced by Pd and same effect has been observed when vanadium is introduced [71]. In such an approach, Kumar et al. [72, 73]. studied the effect of Al addition on the Cantor alloy, and they reported that there is an increase in yield strength (calculated from hardness data) with an increase in Al concentration. Al causes the lattice of Cantor alloy to be severely distorted because of its larger atomic size. It also suggests that the absolute number of the component does not dictate strengthening rather depends on the choice of element. In such an approach, Gao et al. [74] studied the precipitation strengthening in Cantor alloys by introducing NbC. The yield strength increases from 353 to 732 MPa while ductility decreased by 13%. The strengthening came from precipitation of NbC within the grain (precipitation hardening) as well as at the grain boundary, thus retard the grain growth (Hall–Petch strengthening). In another approach, Seol et al. [75] described the significant increase in tensile strength of Cantor alloys (920 MPa, 58%) and FeNiCoCr (880 MPa, 73%) on the addition of boron (10 ppm). Boron segregates at grain boundary thus reducing the grain size and also contributing to interfacial hardening. Some researchers have shifted their attention to the concept of non-equiatomic composition of CCAs. Y Denge et al. [19] developed a non-equiatomic $Fe_{40}Mn_{40}Co_{10}Cr_{10}$ with tensile properties (YS-240 MPa, UTS-489 MPa and 58% ductility) comparable to Cantor alloy; however with a greater degree of work hardening as a result of TWIP effect. Despite the decrease in strength, the absence of Ni and lean amount of Co and Cr makes them cheaper than Cantor alloys. In continuation of this Li et al. [11]. developed a metastable dual-phase TRIP HEA which shows a better combination of strength and ductility than those of low entropy alloys. The strengthening comes from significant amounts of solid solution strengthening and interfacial hardening as a result of the transformation of metastable FCC phase into ε-HCP phase. At 40% strain, a lot of mechanical nanotwin were observed during deformation, which contributes to the dynamic Hall–Petch strengthening. The beauty of these alloys is that it offers multiple mechanisms; solid solution strengthening, interfacial hardening (cause strengthening), TRIP, TWIP and dislocation slip (cause ductility) and thus enable them to overcome the strength–ductility paradox.

In comparison with FCC-based HEAs and MPEAs BCC-based HEAs are not widely studied. They mostly consist of refractory elements. They attracted worldwide attention due to their ability to retain strength up to 1873 K temperature first reported by Senkov et al. [76] in 2010. The single-phase BCC HEAs mostly consist of refractory elements and with some amount of Al and Si to modify the properties, such as high-temperature corrosion resistance, room temperature ductility and decrease the density of the alloy [77–80]. Their properties are comparable to DP steel and TRIP steel but with measured differences in the microstructure. The latter contains several interphase boundaries. The interfacial hardening causes a high degree of work hardening, which cause ductility in these alloys. However, in single-phase BCC HEAs only Taylor hardening and extensive solid solution hardening from the whole solute matrix with severely distorted lattice have been observed. Recently, Juan et al. [81] reported a single-phase equiatomic HfNbTaTiZr refractory HEAs having BCC structure which has a tensile strength of 974 MPa with elongation of 20% at ambient temperature having grain size 38 µm. Lei et al. [68] reported a refractory element-based alloy with outstanding properties. They developed an alloy via doping of oxygen into the equiatomic TiZrHfNb which possesses a tensile strength of 1300 MPa and ductility about 30%. These type of alloys are considered the alternative of Ni-base superalloys for high-temperature application. The uniqueness of refractory elements lies in their various properties such as melting temperature (2128–3695 K), density (4.5–19.4 g/cm$^3$) and elastic moduli (68–114GPa) which can be used to develop refractory-based MPEAs with improved properties.

However, the post-synthesis process has been conducted to improve the mechanical properties of HEAs/MPEAs via microstructural engineering such as ECAP, HPT and FSP. They not only cause of the grain refinement but also invoke the other strengthening effect such as TWIP, TRIP and sometimes dissolution of the second phase (precipitate, nanocluster) into the matrix causing enhanced solid solution strengthening. For example, Sonkusare et al. [82] reported grain refinement by three orders of magnitude from an average grain size of after 5 turns of high-pressure torsion at room temperature at 5 GPa. There was more than three times increase in the hardness which was not fully accounted for Hall–Petch strengthening due to decrease in grain size and Taylor hardening by increase in dislocation density and was attributed to non-equilibrium solid solution strengthening due to partial dissolution of copper-rich nanoclusters. Nene et al. [83] reported a simultaneous increase in the strength and ductility of $Fe_{50}Mn_{30}Co_{10}Cr_{10}$ dual-phase non-equiatomic HEAs when subjected to FSP technique, which led to a substantial decrease in grain size from the average size of 100–5.5 µm. In addition to that it led to the transformation of FCC-$\gamma$ phase into the HCP-$\varepsilon$ phase which contributes to interfacial hardening.

## *4.2 Deformation Mechanisms*

### 4.2.1 FCC-Based MPEAs

**Solid Solution Effects—Lattice distortion**: Pure FCC metals practically do not show any temperature dependency on yield strength in the temperature range of 500–77 K [84]. In comparison, Cantor alloy shows a strong temperature dependence of yield strength in the same temperature range, which almost increases by fourfold from 500 to 77 K, as shown in Fig. 5 [85]. This is different from pure FCC metals, but it does not mean that it has unique properties than the FCC-based alloys. For example, the yield strength of Brass shows a similar increase in yield strength by fourfold for the same temperature. A critical query arises that the temperature-dependent of yield strength of MPEAs is the result of the temperature dependence of shear modulus.

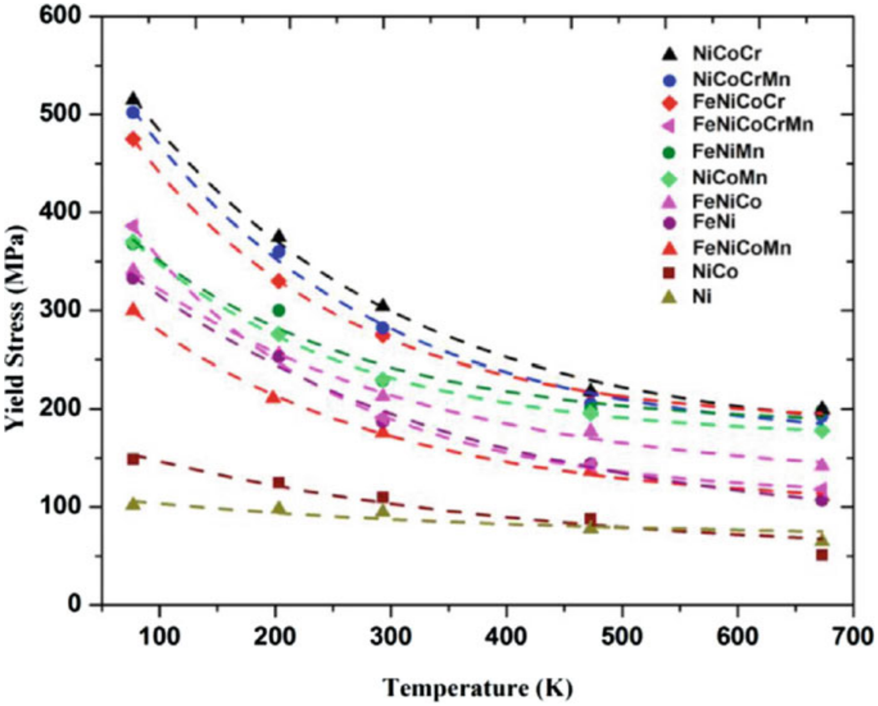

**Fig. 5** Graph showing the temperature dependence of yield strength for Cantor alloy with respect to its different equiatomic subset along with pure Nickel [85]. Reprint with permission

Nevertheless, the shear modulus of Cantor alloys and its several subsets of equiatomic MEAs show weak temperature dependency between 500 and 77 K [86–88].

However, this thermally activated phenomenon is attributed to the standard solid solution strengthening inherent with the MPEAs caused by the volume misfit [89]. However, quantification of volume misfit is no easy task in MPEAs where there is no concept of the solvent and solute. In dilute alloys, the volume misfit is directly calculated from the lattice parameter of alloys which is generally increasing in increase with solute content in the solvent lattice [90] which has been practised for a long time. However, it is not the same in case of MPEAs because the effective atomic radii of the constituents element in MPEAs are different from the corresponding pure element radii [91]. So, atomic radii of the pure element cannot be used directly to calculate the misfit volume. One way to quantify the misfit volume which contributes to solid solution strengthening, is by the concept of simple averaging. Medium entropy or concentrated alloys in general possess all macroscopic properties of dilute alloys, thus nullifying the problem of solvent and solute concept [92]. However, this needs high throughput computational simulation in the framework of first principle calculation.

It is a common perception that HEAs are stronger than conventional alloys as a consequence of enhanced solid solution strengthening due to the large number of constituent elements. However, the ternary CrCoNi MEA shows a higher strength in comparison with Cantor alloy (quinary), along with their quaternary subset and FeMnNi for almost the same grain size under the same thermo-mechanically processing condition. This mainly indicates that the number of the elements does not determine the strength but the type of the element is important. For instance, the introduction of Pd into the FeCoCrNi increases the strength almost 2.5 times because Pd has large atomic radius than other elements and thus induced large misfit volume. Hence, it contributes to enhanced solid solution strengthening. Similar observations were made by Agrawal et al. [93]. who carried out detailed investigation on subset alloys of CoCuFeMnNi alloy to study the contribution of alloying element to solid solution strengthening. They studied the deformation behaviour of equiatomic FeMn, FeMnNi, FeMnNiCo subset alloys to clearly establish the link between solid solution strengthening and overall yield strength in MPEAs to show that the size of the alloying element vis-a-vis the average size of the solvent atom decides the yield strength of the MPEA.

**Role of Stacking Fault Energy (SFE)**: The strain hardening in FCC metals due to dislocation interaction only decreases with increasing strain till necking criterion is reached. Detailed TEM analysis shows that there is no change in dislocation densities of FCC metals from room temperature to 77 K, which is evident of no dependency of work hardening rate in most FCC metals at low strain rate [65]. This indicates that there must be another operative mechanism other than Taylor hardening, which causes a further increase in strength and ductility simultaneously. The mechanism that invoked is the deformation-induced twinning which begins at a strain of 6% in the grain and consistently in all grains at strain level about 9% [20, 94]. SFE plays an essential role in the formation of twining by reducing the critical stress for twinning. It is now well-reported that Cantor alloy has low SFE (15–30 mJ/m$^2$) at room temperature and continuously decreases with decreasing temperature [95–97]. Lower SFE corresponds to lower activation energy for twinning. Thus, there is increase in ductility, work hardening capacity and resistance to fracture by delayed necking in Cantor alloy by twin deformation mechanism at cryogenic temperature. This effect is known as TWIP due to which strength and ductility both increase [68, 89, 98]. Twins are also observed in Cantor alloys at room temperature but at higher strain level that is material is almost about to break. Introduction of twin within the grains leads to grain fragmentation (dynamic Hall–Petch strengthening), and twin boundary also acts as a barrier to the dislocation motion, thus contributing to strengthening. Sometimes certain twin boundaries also serve as pathways to the partial dislocation relieving the local stress and further promoting the deformations. Agrawal et al. [93] determined SFE of CoCuFeMnNi and subset alloys, FeMn, FeMnNi, FeMnNICo to show that the SFE of all the alloys is in a narrow range similar to that of Cantor alloy. However, detailed microstructural investigation using electron backscatter diffraction showed extensive deformation twinning in FeMnNi alloy that also exhibited high strength compared to other subset alloys but lower than the quinary alloy. Thus, it is worth pondering if the concept of global SFE is valid for MPEAs which are 100% solute alloys as local change in chemistry can strongly affect the separation between partials and it may not be prudent to classify MPEAs as high, medium or low SFE materials like nickel, copper and silver, respectively [96]. Experimental investigations show that most MPEAs have low SFE as per the classical definition but it is only for few compositions like CoCrNi and FeMnNi that strengthening mechanisms like TWIP or stacking fault strengthening contribute to significant strengthening.

Nonetheless, lower SFE is also commensurate to the lower activation energy barrier for the transformation from the FCC-$\gamma$ phase to HCP $\varepsilon$-martensite phase. As a result, $\gamma$-$\varepsilon$ interphase acts as an additional barrier to the dislocation motions besides grain boundaries and twin boundaries which results in high work hardening effect and thus contributes to increase in strength and ductility. This effect is known as transformation-induced plasticity (TRIP). The stacking fault, twin and HCP phase are different entities, but they are all related to change in the stacking sequence of the underlying FCC structure. The stacking fault in FCC phase forms by gliding of Shockley partials of $1/6\langle 112\rangle$ Burgers vectors which constitute the thin region of HCP. In other words, the stacking faults in FCC metals is a region of stacking sequence in HCP which act as nuclei during deformation, and thus, the FCC-$\gamma$ phase to HCP $\varepsilon$-martensite phase takes place.

**Grain size effect**: Initially, the grain size effects were investigated by the Vickers microhardness measurements at room temperature [99]. The hardness, as well as the corresponding Hall–Petch slope of equiatomic CoCrFeMnNi alloy, was reported to be higher than those of the FCC metals [100] indicating that much slip resistance offered by MPEAs at grain boundaries. Subsequently, hardness measurements were performed on the lower subset of Cantor alloys, and their slops were found to be lower than Cantor alloys. However, the hardness-based yield strength determination is not sufficient to predict the mechanical properties because it is just a preliminary stage of testing performed at room temperature for screening out the properties of the alloys. Eventually, the tensile tests of Cantor alloy were conducted at various temperatures for different grain sizes in the range of 4 to 155 $\mu$m [20]. The Hall–Petch slope was found in the range of 530–420 MPa $\mu\text{m}^{-1/2}$ for the temperature of 77–873 K. The room temperature Hall–Petch slope (494 MPa $\mu\text{m}^{-1/2}$) for the Cantor alloys is significantly higher than those of FCC metals (90–230 MPa) measured by tensile test. The Hall–Petch slope (494 MPa $\mu\text{m}^{-1/2}$) is even identical for the grain size [65] ranges 0.5–89 $\mu$m. However, the direct comparison of this data to present FCC-based alloys is not appropriate because of the limited number of experimental data is available, and detailed studies are required to understand the underlying mechanism. There is a decrease in the Hall–Petch slope in the nanocrystalline grain size regime for Cantor alloy similar to that for conventional FCC metals and alloys which is attributed to non-equilibrium nature of grain boundaries produced by high-pressure torsion. Sonkusare et al. [101] showed that the strengthening in nanocrystalline CoCuFeMnNi MPEA could not be explained by dislocation strengthening and Hall–Petch strengthening and attributed to non-equilibrium solid solution strengthening. Thus, it is important to study the effect of grain size over a wide range in different MPEAs to develop a fundamental understanding of grain size strengthening in MPEAs [102].

**Effect of strain rate**: The Cantor alloys show an approximately weak effect of strain rate on the yield strength at the quasi-static strain rate ($10^{-1}$–$10^{-5}$ $s^{-1}$) for the grain size of ~ 35 μm [51] which is the representative of almost all the FCC metals and alloys in agreement with the immense activation volume at room temperatures that correspond to solid solution strengthening effect. At the intermediate strain rate (100 $s^{-1}$), there is an increase in yield strength from 484 to 650 MPa for the grain size around ten μm [103]; besides, the overall elongation is higher at higher strain rate. Still, there is a decrease in uniform elongation. This is mainly attributed to the transition from slip-assisted deformation (at $10^{-3}$ $s^{-1}$) to the mixed mode of dislocation slip and twinning (100 $s^{-}1$) as well as a higher dislocation density. However, deformation at the dynamic strain rate of around 5000 $s^{-1}$ was exclusively performed in compression using a split Hopkinson bar at room temperature for Cantor alloy. There is an increase in the strength from 360 MPa (at $10^{-3}$ $s^{-1}$) to 680 MPa (4700 $s^{-1}$). This strong dependency of strain rate is due to the viscous phonon drag effect [104].

### 4.2.2 BCC-Based MPEAs

**Solid solution effect**: Unlike FCC HEAs, BCC HEAs are not widely studied probably because of low or negligible ductility at low homologues temperature. Among several single-phase BCC HEAs which were investigated thoroughly, the TiZrNbHfTa possesses tensile ductility at room temperature. Detailed TEM analyses of the tensile tested sample revealed that at the initial stage of strain (~0.85% stage I) the substructures contain an abundant of screw dislocations of ½<111> type, which is typical in metals and alloys having BCC structure. They are arranged heterogeneously with several distinct bands containing dislocation dipoles, dislocation of opposite sign, jogged section screw dislocation and loops surrounding dislocation free region thus forming hard zone and soft zone [105]. At the intermediate stage of strain (2.3%, at the end of stage I), the heterogeneities are maintained with increasing density of dislocations. Dislocation tangle started to form in the bands besides dislocation dipoles in the band [106]. At the latter stage of strain (10%, stage III), the band structure almost disappeared, and homogeneous distribution of dislocations was observed. The strain hardening rate in BCC TiZrNbHfTa HEAs/MPEAs has shown the modest dependency on the strain. The hardening characteristic is determined by Taylor hardening model for a given dislocation density. The hardening parameter 'α' for this alloy is 0.16, which is same as of the BCC metals. This indicates that Peierls stress is the prime factor that contributes to strengthening in this class of alloys.

**Grain size effects**: The grain size has no significant impact on the tensile yield behaviour of TiZrNbHfTa HEAs/MPEAs. The yield strength (~950 MPa) is roughly the same for the grain size 38, 81 and 128 μm [107]. Even the yield strength (1145 MPa) does not vary significantly for the same alloy having grain size 22 μm and cannot be judged as a Hall–Petch effect. However, to investigate the Hall–Petch effect, second phase effect [105, 108, 109, 110], texture effect due to thermomechanical processing and the effect of the interstitial element must be taken into consideration [111].

**Effect of strain rate**: There is a significant increase (~40%) in the yield strength of equiatomic TiZrNbHfTa alloys when strain rate increase from quasi-static (0.001 $s^{-1}$) to dynamic strain rate (3400 $s^{-1}$) [112]. The detailed EBSD analysis revealed that at low strain rate, deformation is governed by the formation of a homogeneously distributed band of dislocations cell. In contrast at a higher strain rate level, a bunch of macroscopic localized shear bands forms. However, strain-softening has been observed after the immediate onset of yielding, which is mainly attributed to extensive strain localization at a higher strain rate.

The effect of intrinsic parameters like solid solution strengthening, stacking fault energy and grain size as well as extrinsic parameters like strain, temperature and strain rate on FCC and BCC MPEAs clearly indicates that we have simply explored the tip of the iceberg of the compositional space. More efforts are required to perform detailed mechanical testing experiments on a few model systems that show sufficient potential in terms of excellent mechanical properties.

## 5 Summary and Future Scope

An Odyssey through the alloy design landscape from the high entropy alloys to the multiprincipal element alloys over the last decade and a half has been exhilarating. We indeed are lucky to belong to these times where the very fundamentals of a five-thousand-year-old phenomenon have been challenged. The new kid on the block has made us all take notice and go back to our drawing boards to redefine concepts of physical and mechanical metallurgy we thought we have put to good use to create an industrialized world dominated by steels, aluminium alloys and superalloys. The advent of new materials characterization tools like atom probe tomography, correlative microscopy techniques, advanced processing tools like additive manufacturing and rapid alloy prototyping, high throughput nanoindentation and the availability of exceptional computing power to perform simulations at different length and time scales coupled with machine learning approach has catalysed the development of MPEAs. Efforts should now be directed to develop not just structural materials with high strength and ductility but MPEAs with a combination of much desired but least compatible properties like excellent high and low cycle fatigue resistance, high-temperature strength with good oxidation resistance, lightweight, high strength and modulus alloys, low-density high-temperature alloys for turbine blade applications, next-generation corrosion-resistant alloys for severe conditions using the aforementioned methodology comprising of simulations and high throughput experiments. These techniques are expected to play an essential role in the advancement of the field of multi-property targeted alloy development but the curiosity and imagination of the individual who will be handling these tools and techniques will set the horizons of our civilization. We started the review on a philosophical note with the poem of Bach and would like to end it with a quote from Graham Bell. He stated that great discoveries and improvements invariably involve the cooperation of many minds. We hope that many minds in India and the world come together to enrich the field of MPEAs in the near future.

## References

1. B. Murty, J.-W. Yeh, S. Ranganathan, in *High-Entropy Alloys* (Butterworth-Heinemann, 2014)
2. E.P. George, D. Raabe, R.O. Ritchie, Nat. Rev. Mater. **4**(8), 515–534 (2019)
3. A.S. Sharma, S. Yadav, K. Biswas, B. Basu, Mater. Sci. Eng. R. Rep. **131**, 1–42 (2018)
4. J. Farrer, in *The Alloy Tree: A Guide to Low-Alloy Steels, Stainless Steels, and Nickel-base Alloys* (CRC Press, 2004)
5. J.R. Davis, Aluminum and aluminum alloys. ASM Int. (1993)
6. B. Cantor, I. Chang, P. Knight, A. Vincent, Materials Science Engineering: A **375**, 213–218 (2004)
7. J.W. Yeh, S.K. Chen, S.J. Lin, J.Y. Gan, T.S. Chin, T.T. Shun, C.H. Tsau, S.Y. Chang, Adv. Eng. Mater. **6**(5), 299–303 (2004)
8. D. Ma, M. Yao, K.G. Pradeep, C.C. Tasan, H. Springer, D. Raabe, Acta Mater. **98**, 288–296 (2015)
9. M. Yao, K.G. Pradeep, C.C. Tasan, D. Raabe, Scripta Mater. **72**, 5–8 (2014)
10. N. Stepanov, D. Shaysultanov, M. Tikhonovsky, G. Salishchev, Mater. Des. **87**, 60–65 (2015)
11. Z. Li, K.G. Pradeep, Y. Deng, D. Raabe, C.C. Tasan, Nature **534**(7606), 227–230 (2016)
12. D.B. Miracle, O.N. Senkov, Acta Mater. **122**, 448–511 (2017)
13. B. Gludovatz, A. Hohenwarter, D. Catoor, E.H. Chang, E.P. George, R.O. Ritchie, Science **345**(6201), 1153 (2014)
14. B. Gludovatz, A. Hohenwarter, K.V. Thurston, H. Bei, Z. Wu, E.P. George, R.O. Ritchie, Nat. Commun. **7**(1), 1–8 (2016)
15. S. Yadav, A. Kumar, K. Biswas, Materials Chemistry Physics **210**, 222–232 (2018)
16. A.S. Sharma, S. Yadav, K. Biswas, B.J.M.S. Basu, E. R. Reports **131**, 1–42 (2018)
17. K.-Y. Tsai, M.-H. Tsai, J.-W. Yeh, Acta Mater. **61**(13), 4887–4897 (2013)
18. M. Vaidya, S. Trubel, B. Murty, G. Wilde, S.V. Divinski, Journal of Alloys Compunds **688**, 994–1001 (2016)
19. Y. Deng, C.C. Tasan, K.G. Pradeep, H. Springer, A. Kostka, D. Raabe, Acta Mater. **94**, 124–133 (2015)
20. F. Otto, A. Dlouhý, C. Somsen, H. Bei, G. Eggeler, E.P. George, Acta Mater. **61**(15), 5743–5755 (2013)
21. G. Laplanche, A. Kostka, O. Horst, G. Eggeler, E. George, Acta Mater. **118**, 152–163 (2016)
22. W. Hume-Rothery, Indian J. Phys. **11**, 74–74 (1969)
23. E. Pickering, N. Jones, Int. Mater. Rev. **61**(3), 183–202 (2016)
24. F.R. De Boer, W. Mattens, R. Boom, A. Miedema, A. Niessen, *Cohesion in Metals* (Netherlands, North-Holland, 1998)
25. A. Takeuchi, A. Inoue, Mater. Trans. **46**(12), 2817–2829 (2005)
26. Y. Zhang, Y.J. Zhou, J.P. Lin, G.L. Chen, P.K. Liaw, Adv. Eng. Mater. **10**(6), 534–538 (2008)
27. A. Bajpai, J. Bhatt, K. Biswas, N.P. Gurao, Physica B **595**, 412350 (2020)
28. J. Bhatt, W. Jiang, X. Junhai, W. Qing, C. Dong, B.S. Murty, Intermetallics **15**(5), 716–721 (2007)
29. S. Guo, C.T. Liu, Progress in Natural Science: Materials International **21**(6), 433–446 (2011)
30. S. Guo, Q. Hu, C. Ng, C.T. Liu, Intermetallics **41**, 96–103 (2013)
31. Y.F. Ye, Q. Wang, J. Lu, C.T. Liu, Y. Yang, Mater. Today **19**(6), 349–362 (2016)

32. N. Saunders, A.P. Miodownik, *CALPHAD (calculation of phase diagrams): A Comprehensive Guide* (Elsevier, 1998)
33. N. Gurao, K. Biswas, J. Alloy. Compd. **697**, 434–442 (2017)
34. A. Raturi, J. Aditya, N.P. Gurao, K. Biswas, J. Alloys Comp. **806**, 587–595 (2019)
35. L. Hedin, B.I. Lundqvist, J. Phys. C: Solid State Phys. **4**(14), 2064 (1971)
36. W. Kohn, L.J. Sham, Phys. Rev. **140**(4A), A1133 (1965)
37. J. Hafner, C. Wolverton, G. Ceder, MRS Bull. **31**(9), 659–668 (2006)
38. E. Gross, R. Dreizler, in *Density Functional Theory*. Vol. 337 of NATO ASI Series B' (Plenum Press, New York, 1995)
39. H.S. Oh, S.J. Kim, K. Odbadrakh, W.H. Ryu, K.N. Yoon, S. Mu, F. Körmann, Y. Ikeda, C.C. Tasan, D. Raabe, T. Egami, E.S. Park, Nat. Commun. **10**(1), 2090 (2019)
40. S. Chmiela, A. Tkatchenko, H.E. Sauceda, I. Poltavsky, K.T. Schütt, K.-R. Müller, Sci. Adv. **3**(5), e1603015 (2017)
41. Z. Li, J.R. Kermode, A. De Vita, Phys. Rev. Lett. **114**(9), 096405 (2015)
42. V.L. Deringer, G. Csányi, Phys. Rev. B **95**(9), 094203 (2017)
43. A.P. Bartók, J. Kermode, N. Bernstein, G. Csányi, Phys. Rev. X **8**(4), 041048 (2018)
44. Q. Gao, S. Yao, J. Schneider, M. Widom, arXiv preprint arXiv:.09110 (2015)
45. A.R. Natarajan, A. Van der Ven, npj Computational Materials **4**(1), 1–7 (2018)
46. W. Ye, C. Chen, Z. Wang, I.-H. Chu, S.P. Ong, Nat. Commun. **9**(1), 1–6 (2018)
47. G.B. Olson, Science **288**(5468), 993–998 (2000)
48. A.R. Oganov, C.W. Glass, J. Chem. Phys. **124**(24), 244704 (2006)
49. S. Curtarolo, G.L. Hart, M.B. Nardelli, N. Mingo, S. Sanvito, O. Levy, Nat. Mater. **12**(3), 191–201 (2013)
50. R.E. Newnham, *Properties of Materials: Anisotropy, Symmetry, Structure* (Oxford University Press on Demand, 2005)
51. A. Choudhury, T. Konnur, P. Chattopadhyay, S. Pal, Engineering Comp. (2019)
52. W. Huang, P. Martin, H.L. Zhuang, Acta Mater. **169**, 225–236 (2019)
53. L. Zhang, H. Chen, X. Tao, H. Cai, J. Liu, Y. Ouyang, Q. Peng, Y. Du, Mat. Des., 108835 (2020)
54. T. Srivatsan, M. Gupta, in *High Entropy Alloys: Innovations, Advances, and Applications* (CRC Press, 2020)
55. S. Varalakshmi, M. Kamaraj, B.S. Murty, J. Alloy. Compd. **460**(1), 253–257 (2008)
56. S. Yadav, S. Sarkar, A. Aggarwal, A. Kumar, K. Biswas, Wear **410**, 93–109 (2018)
57. U. Roy, H. Roy, H. Daoud, U. Glatzel, K. Ray, Mater. Lett. **132**, 186–189 (2014)
58. C. Chen, S. Pang, Y. Cheng, T.J.J.A. Zhang, J. Alloys Comp. **659**, 279–287 (2016)
59. Z. Tang, T. Yuan, C.-W. Tsai, J.-W. Yeh, C.D. Lundin, P.K. Liaw, Acta Mater. **99**, 247–258 (2015)
60. M.A. Hemphill, T. Yuan, G. Wang, J. Yeh, C. Tsai, A. Chuang, P. Liaw, Acta Mater. **60**(16), 5723–5734 (2012)
61. D.L. Mohsen Seifi, Z. Yong, P.K. Liaw, J.J. Lewandowski, JOM **67**, 2288–2295 (2015)
62. A. Gali, E.P. George, Intermetallics **39**, 74–78 (2013)
63. G. Miyamoto, H. Usuki, Z.-D. Li, T. Furuhara, Acta Mater. **58**(13), 4492–4502 (2010)
64. G. Laplanche, A. Kostka, O.M. Horst, G. Eggeler, E.P. George, Acta Mater. **118**, 152–163 (2016)
65. P. Paufler, Crystal Res. Tech. **20**(5), 634–634 (1985)
66. E.P. George, W.A. Curtin, C.C. Tasan, Acta Mater. **188**, 435–474 (2020)
67. D. Raabe, D. Ponge, O. Dmitrieva, B. Sander, Scripta Mater. **60**(12), 1141–1144 (2009)
68. Z. Lei, X. Liu, Y. Wu, H. Wang, S. Jiang, S. Wang, X. Hui, Y. Wu, B. Gault, P. Kontis, Nature **563**(7732), 546–550 (2018)
69. H. Luo, Z. Li, D. Raabe, Sci. Rep. **7**(1), 1–7 (2017)
70. B. Yin, F. Maresca, W. Curtin, Acta Mater. **188**, 486–491 (2020)
71. B. Yin, W. Curtin, Mat. Res. Lett. **8**(6), 209–215 (2020)
72. J. Kumar, N. Kumar, S. Das, N. Gurao, K. Biswas, Trans. Indian Inst. Met. **71**(11), 2749–2758 (2018)

73. J. Kumar, A. Linda, M. Sadhasivam, K.G. Pradeep, N.P. Gurao, K. Biswas, Acta Mater. **238**(118208) (2020). https://doi.org/10.1016/j.actamat.2022.118208
74. N. Gao, D. Lu, Y. Zhao, X. Liu, G. Liu, Y. Wu, G. Liu, Z. Fan, Z. Lu, E. George, J. Alloy. Compd. **792**, 1028–1035 (2019)
75. J.B. Seol, J.W. Bae, Z. Li, J.C. Han, J.G. Kim, D. Raabe, H.S. Kim, Acta Mater. **151**, 366–376 (2018)
76. O. Senkov, G. Wilks, D. Miracle, C. Chuang, P.J.I. Liaw, Intermetallics **18**(9), 1758–1765 (2010)
77. C. Liu, H. Wang, S. Zhang, H. Tang, A. Zhang, J. Alloy. Compd. **583**, 162–169 (2014)
78. D. Dimiduk, C. Woodward, D. Miracle, O. Senkov, S. Senkova, Oxidation behavior of a refractory NbCrMo0. 5Ta0. 5TiZr alloy (2014)
79. O. Senkov, S. Senkova, C. Woodward, Acta Mater. **68**, 214–228 (2014)
80. O. Senkov, C. Woodward, D. Miracle, Jom **66**(10), 2030–2042 (2014)
81. C.-C. Juan, M.-H. Tsai, C.-W. Tsai, W.-L. Hsu, C.-M. Lin, S.-K. Chen, S.-J. Lin, J.-W. Yeh, Mater. Lett. **184**, 200–203 (2016)
82. R. Sonkusare, N. Khandelwal, P. Ghosh, K. Biswas, N.P. Gurao, J. Mater. Res. **34**(5), 732–743 (2019)
83. S.S. Nene, K. Liu, M. Frank, R.S. Mishra, R.E. Brennan, K.C. Cho, Z. Li, D. Raabe, Sci. Rep. **7**(1), 1–7 (2017)
84. P. F. Koshelev, Strength Mater. **3**(3), 286–291 (1971). https://doi.org/10.1007/BF01527440
85. Z. Wu, H. Bei, G.M. Pharr, E.P. George, Acta Mater. **81**, 428–441 (2014)
86. A. Haglund, M. Koehler, D. Catoor, E.P. George, V. Keppens, Intermetallics **58**, 62–64 (2015)
87. G. Laplanche, P. Gadaud, C. Bärsch, K. Demtröder, C. Reinhart, J. Schreuer, E.P. George, J. Alloy. Compd. **746**, 244–255 (2018)
88. G. Laplanche, P. Gadaud, O. Horst, F. Otto, G. Eggeler, E. George, J. Alloy. Compd. **623**, 348–353 (2015)
89. N. Mott, F.N. Nabarro, Proceedings of the Physical Society **52**(1), 86 (1940)
90. R. Fleischer, Acta Metall. **8**(1), 32–35 (1960)
91. N.L. Okamoto, S. Fujimoto, Y. Kambara, M. Kawamura, Z.M. Chen, H. Matsunoshita, K. Tanaka, H. Inui, E.P. George, Sci. Rep. **6**, 35863 (2016)
92. C. Varvenne, A. Luque, W.A. Curtin, Acta Mater. **118**, 164–176 (2016)
93. R. Agarwal, R. Sonkusare, S.R. Jha, N. Gurao, K. Biswas, N. Nayan, Mater. Des. **157**, 539–550 (2018)
94. Y. Zhu, X. Liao, X. Wu, Prog. Mater Sci. **57**(1), 1–62 (2012)
95. S. Liu, Y. Wu, H. Wang, J. He, J. Liu, C. Chen, X. Liu, H. Wang, Z. Lu, Intermetallics **93**, 269–273 (2018)
96. A. Zaddach, C. Niu, C. Koch, D. Irving, Jom **65**(12), 1780–1789 (2013)
97. J.-W. Yeh, Jom **67**(10), 2254–2261 (2015)
98. S. Mridha, S. Das, S. Aouadi, S. Mukherjee, R.S. Mishra, JOM **67**(10), 2296–2302 (2015)
99. W. Liu, Y. Wu, J. He, T. Nieh, Z. Lu, Scripta Mater. **68**(7), 526–529 (2013)
100. Z.C. Cordero, B.E. Knight, C.A. Schuh, Int. Mater. Rev. **61**(8), 495–512 (2016)
101. R. Sonkusare, K. Biswas, N. Al-Hamdany, H. Brokmeier, R. Kalsar, N. Schell, N. Gurao, Mat. Sci. Eng.: A, 139187 (2020)
102. J. Moon, Y. Qi, E. Tabachnikova, Y. Estrin, W.-M. Choi, S.-H. Joo, B.-J. Lee, A. Podolskiy, M. Tikhonovsky, H.S. Kim, Sci. Rep. **8**(1), 11074 (2018)
103. M. Kang, J.W. Won, J.B. Kwon, Y.S. Na, Mater. Sci. Eng., A **707**, 16–21 (2017)
104. J.M. Park, J. Moon, J.W. Bae, M.J. Jang, J. Park, S. Lee, H.S. Kim, Mater. Sci. Eng., A **719**, 155–163 (2018)
105. B. Schuh, B. Völker, J. Todt, N. Schell, L. Perrière, J. Li, J. Couzinié, A. Hohenwarter, Acta Mater. **142**, 201–212 (2018)
106. J.-P. Couzinié, L. Lilensten, Y. Champion, G. Dirras, L. Perrière, I. Guillot, Mater. Sci. Eng., A **645**, 255–263 (2015)
107. C.-C. Juan, K.-K. Tseng, W.-L. Hsu, M.-H. Tsai, C.-W. Tsai, C.-M. Lin, S.-K. Chen, S.-J. Lin, J.-W. Yeh, Mater. Lett. **175**, 284–287 (2016)

108. O. Senkov, S. Semiatin, J. Alloy. Compd. **649**, 1110–1123 (2015)
109. S. Maiti, W. Steurer, Acta Mater. **106**, 87–97 (2016)
110. N. Stepanov, N.Y. Yurchenko, S. Zherebtsov, M. Tikhonovsky, G. Salishchev, Mater. Lett. **211**, 87–90 (2018)
111. A. Kumar, B.L. Eyre, Proceedings of the Royal Society of London. A. Mathematical Physical Sciences **370**(1743), 431–458 (1980)
112. O. Myslyvchenko, M. Krapivka, O. Makarenko, V. Nazarenko, J. Superhard Mater. **37**(1), 21–26 (2015)